Chemistry of Non-Planar Polycyclic Aromatic Hydrocarbons on Metal Surfaces

---

Dissertation

zur

Erlangung der naturwissenschaftlichen Doktorwürde
(Dr. sc. nat.)

vorgelegt der

Mathematisch-naturwissenschaftlichen Fakultät

der

Universität Zürich

von

Anaïs Marie Manuelle Mairena

aus Frankreich

Promotionskommission

Prof. Dr. Karl-Heinz Ernst (Vorsitz)

Prof. Dr. Karl Gademann

Prof. Dr. Anthony Linden

Zürich, 2018

Table of contents

Abstract

Molecular recognition in surface chemistry is of paramount importance for many applications such as heterogeneous catalysis, crystallization and the design of interfaces for new devices. Resolution of chiral compounds into pure enantiomers via crystallization is for example the most important approach in pharmaceutical and fragrance industries in order to obtain pure drugs and scents from racemic solutions. Chiral recognition also plays an important role for the design of non-linear optics or spin filters as well as for the understanding of biological systems and the origin of homochirality of life. Our current understanding of intermolecular interactions is still incomplete and calls for the study of adequate model systems. Modern methods of surface science are applied in ultrahigh vacuum: mainly scanning tunneling microscopy (STM), but also X-ray photoelectron spectroscopy (XPS) and temperature desorption spectroscopy (TDS). The results are justified with theoretical models using extended Hückel theory (EHT), molecular mechanics (MM) or density functional theory (DFT). Non-planar polycyclic aromatic hydrocarbons (PAH) are particularly interesting because they offer a complex chemistry with a wide range of properties useful for different applications. Two different molecular classes were studied on single crystal metal surfaces: chiral (helical) and curved (bowl-shaped) aromatic molecules.

Helicenes, a class of PAH with a helical backbone, are perfect candidates to investigate the chemistry and the interactions between chiral molecules. We present an elucidation of chiral recognition of different helicenes in monolayer and multi-layer films on a Cu(111) surface. At low coverages, racemic pentahelicene ([5]H, $C_{22}H_{14}$) forms non-covalently-bonded homochiral dimers, i.e. both molecules have the same handedness. Close to monolayer coverage, a transition from a 2D racemate, which means that it is composed of homochiral pairs with opposite handedness, to a conglomerate of homochiral mirror domains is observed in the first layer. It is found that this phenomenon is induced by second layer nucleation and indicates a long-range chiral communication between second layer islands and other areas on the surface. It also shows a drastic transformation of the self-assembly due to a small enantiomeric bias.

Molecular functionalisation, interesting for surface patterning and for the tunability of molecular functionality, will be discussed by comparing enantiopure 1-azahexahelicene (aza[6]H) with previous results obtained on heptahelicene ([7]H) and amino[6]H on Au(111) and Cu(100).

Surfaces provide an up–down asymmetry which might induce stereochemical effects during chemical reactions of chiral molecules. This is investigated through the study of Ullmann coupling, which

has become very popular for the carbon–carbon coupling of organic molecules on surfaces. The Ullmann coupling of bromo[4]H on Cu(100) gives rise to the formation of homochiral bis[4], which self-assemble into homochiral mirror domains. The diastereoselectivity is rather based on the low inversion barrier of the [4]H subunits than any selectivity during coupling which is performed at 200 °C. In comparison, the study of bromo[7]H, having substantially higher inversion barriers shows no diastereoselectivity. On Au(111), the coupling of two Br[7]H produces both heterochiral and homochiral bis[7]H, arranging in two different long-range ordered structures. On Cu(111), the formation of an intermediate organometallic compound is observed but the presence of Br affects the self-assembly after covalent coupling. Br desorbs only in the presence of atomic hydrogen, requiring at least a partial dehydrogenation of the molecules. This observation is usually neglected in the now wide field of covalent on-surface chemistry and has significant consequences on the reaction products of halogenated molecules.

Novel reaction products can also be produced by fragmentation or recombination during thermal decomposition of molecules. When thermodynamically favored, decomposition can proceed autocatalytically on surface, as often observed for oxygen-containing molecules such as carboxylic acids. A better understanding of the mechanisms leading to this reaction, called “surface explosion”, is achieved by studying for the first time the autocatalytic decomposition of PAH which do not contain oxygen on O/Cu(100). Br[7]H undergoes an autocatalytic decomposition. On the contrary, non-brominated heptahelicene does not show autocatalytic behavior during decomposition. Consequently, the “anchoring” via the organometallic bond due to scission of the halogen-carbon bond during thermal annealing is a necessary condition for the surface explosion. Measurements on different types of PAH lead to the conclusion that in addition steric overcrowding induced (cyclo) dehydrogenation, is necessary for the initiation of the autocatalytic process. Such insight into the mechanism of this autocatalytic process could be beneficial for the understanding of heterogeneous catalysis.

Buckybowls, a class of curved PAH are discussed in the second part of this thesis. They generated great attention due to their opto-electronic properties induced by specific intermolecular π-π interactions. Thus understanding the self-assembly of buckybowls is attractive for various applications in organic electronics (organic semiconductors, photovoltaics, light-emitting diodes and thin film transistors). Spontaneous ordering was studied for several corannulene derivatives on Cu(111): pentaindenocorannulene (PiC), monoindenocorannulene (MiC), the C_{70} fragment $C_{38}H_{14}$ and terphenylcorannulene (TpC). The single-molecule adsorption footprints are justified by a complex balance between vdW and Pauli interactions between surface and molecules often inducing a large charge redistribution at the interface. Peculiar self-assembled motifs can be explained by attractive π-π and CH-π non-covalent bonding forces between the molecules.

Buckybowls such as pentaindenocorannulene (PiC) are also considered for hydrogen storage, to act as fullerene receptors and for medical applications (toxin inhibitors, drugs-encapsulation or nano-membranes fabrications). To reach this goal, the thermally induced on-surface chemistry of PiC, is studied on Cu(100). At low coverage ($\theta < 0.3$ ML), when intermolecular interactions are negligible, PiC adsorbs bowl opening-up with its C_5 symmetry axis perpendicular to the surface. At larger coverage, molecules tilt due to intermolecular CH-π and π-π intermolecular interactions. Annealing at 503 K leads to the formation of flat star-shape molecules.

Zusammenfassung

Wechselwirkungen zwischen Molekülen an Oberflächen sind für viele Prozesse entscheidend. Beispiele sind die heterogene Katalyse, die Kristallisation und neuartige Elektrodengrenzflächen in elektronischen Bauteilen. Die Trennung von Enantiomeren von chiralen Molekülen mittels Kristallisation ist der wichtigste Ansatz in der Pharma- und Duftstoffindustrie, um aus razemischen Lösungen enantiomeren-reine Wirk- und Duftstoffe zu erhalten. Chirale Moleküle spielen auch eine wichtige Rolle beim Design von nichtlinearen Optiken und Spinfiltern, dem Verständnis biologischer Systeme und der Entstehung der Homochiralität des Lebens. Unser derzeitiges Verständnis intermolekularer Wechselwirkungen ist noch unvollständig und erfordert das Studium adäquater Modellsysteme. Zu Anwendung kommen moderne Methoden der Oberflächenphysik im Ultrahochvakuum. Den Schwerpunkt bildet hier die Rastertunnelmikroskopie (STM), unterstützt durch Röntgenphotoelektronenspektroskopie (XPS) und Themodesorptionsspektroskopie (TDS). Die Resultate werden mit theoretischen Modellen unter Verwendung der erweiterten Hückel-Theorie (EHT), der Molekularmechanik (MM) und der Dichtefunktionaltheorie (DFT) erklärt. Nicht-planare polyzyklische aromatische Kohlenwasserstoffe (PAH) sind besonders interessant, weil sie eine komplexe Chemie mit einer breiten Palette von Eigenschaften bieten, welche für verschiedene Anwendungen nützlich sind. In dieser Arbeit werden zwei verschiedene Molekülklassen auf einkristallinen Metalloberflächen behandelt: chirale (helikale) und gekrümmte (korbförmige) aromatische Moleküle.

Helicene, eine Klasse von PAH mit helikalem Rückgrat sind perfekte Kandidaten um die Chemie und die Wechselwirkungen zwischen chiralen Molekülen zu studieren. Wir präsentieren eine Aufklärung der Wechselwirkung zwischen Helicenen in Mono- und Multilagen auf einer Cu(111) Oberfläche. Bei geringen Bedeckungen bildet racemisches Pentahelicene ([5]H, $C_{22}H_{14}$) nicht-kovalent gebundene homochirale Dimere, d.h. beide Moleküle haben die gleiche Händigkeit. In der Nähe der Monoschicht wird in der Monolage ein Übergang von einem 2D-Razemat zu einem Konglomerat aus homochiralen Domänen beobachtet. Die Razematphase ist dabei aus homochiralen Paaren mit entgegengesetzter Händigkeit aufgebaut. Der Übergang von Razemat zu Konglomerat wird durch Nukleation der zweiten Schicht bewirkt, die in der Doppellage oder zumindest in der zweiten Lage homochiral ist. Der dadurch bewirkte lokale Mangel eines Enantiomers führt dazu, dass nun anstatt des Razemats, homochirale Nukleation und Wachstum in der ersten Lage induziert wird. Eine bisher unbekannte drastische Transformation der Selbstorganisation aufgrund eines geringen lokalen Überschusses eines Enantiomers. Des Weiteren wird der Einfluss vom Modifizierungen der Moleküle auf die Oberflächenstrukturierung anhand

der Selbstorganisation von 1-Azahexahelicene (Aza[6]H) diskutiert und mit früheren Resultaten aus der Literatur, d.h. mit Heptahelicene ([7]H) und Amino[6]H auf Au(111) und Cu(100) verglichen.

Die Ausrichtung von Molekülen auf Oberflächen induziert eine Asymmetrie, die stereochemische Effekte bei chemischen Reaktionen an chiralen Molekülen bewirken könnte. Es werden Ergebnisse für die C-C Kopplung von Helizenen mittels Ullmann-Kupplung präsentiert. Die Kupplung von Bromo[4]H auf Cu(100) liefert fast ausschliesslich homochirales Bis[4]H, das sich spontan in homochirale Spiegeldomänen auftrennt. Die beobachtete Diastereoselektivität beruht allerdings eher auf der niedrigen Inversionsbarriere der [4]H-Untereinheiten als auf einer Selektivität bei der C-C Kupplung, die bei relativ hohen Temperaturen (ca. 200°C) durchgeführt wird. Die Studie von Bromo[7]H mit wesentlich höheren Inversionsbarrieren zeigt daher keine Diastereoselektivität. Auf Au(111) erzeugt die Kupplung von zwei Br[7]H sowohl heterochirales als auch homochirales Bis[7]H, das in zwei verschiedenen geordneten Strukturen angeordnet ist. Auf Cu(111) wird die Bildung einer metallorganischen Zwischenverbindung beobachtet, aber die Gegenwart von Brom beeinflusst die Selbstorganisation nach der kovalenten Kopplung. Br desorbiert nur in Gegenwart von atomarem Wasserstoff, wofür mindestens eine partielle Dehydrierung der Moleküle erforderlich ist. Diese Beobachtung wurde bisher im Bereich der kovalenten Oberflächenchemie vernachlässigt und hat erhebliche Auswirkungen auf die Reaktionsprodukte von halogenierten Kohlenwasserstoffen.

Neue Reaktionsprodukte können auch durch Fragmentierung oder Rekombination während der thermischen Zersetzung von Molekülen hergestellt werden. Die autokatalytische thermische Zersetzung auf einer Oberfläche wird oft bei dichtgepakten Monoschichten von Karbonsäuren beobachtet, wobei freiwerdende Vakanzen in der Monolage die Zersetzung stark beschleunigen. Durch Studien der thermischen Zersetzung von nicht sauerstoffhaltigen PAHs auf der oxidierten Cu(100) Oberfläche haben wir weitere Faktoren, die eine autokatalytische "Oberflächenexplosion" bewirken, gefunden. Br[7]H unterliegt einer autokatalytischen Zersetzung während nicht bromiertes Heptahelizen kein autokatalytisches Verhalten zeigt. Folglich ist die "Verankerung" über die metallorganische Bindung aufgrund der Spaltung der Halogen-Kohlenstoff-Bindung während des Heizens eine notwendige Bedingung für die Oberflächenexplosion. Messungen an verschiedenen PAH-Typen führen zu der Schlussfolgerung, dass zusätzlich ein sterischer Verdrängunseffekt von Wasserstoffen am aromatischen Gerüst notwendig ist, um den autokatalytischen Prozess einzuleiten. Ein besseres Verständnis der Mechanismen dieses autokatalytischen Prozesses sollte für das Verständnis der heterogenen Katalyse von Vorteil sein.

Im zweiten Teil dieser Arbeit werden Buckminsterfullerene („Buckybowls") behandelt. Diese aromatischen Kohlenwasserstoffschalen haben spezielle optoelektronische Eigenschaften. Daher ist das

Verständnis der Selbstorganisation von solchen Molekülen für verschiedene Anwendungen in der organischen Elektronik interessant. (Organische Halbleiter, Photovoltaik, Leuchtdioden und Dünnschichttransistoren). Spontane Selbstanordnung wurde für verschiedene Corannulen-Derivate behandelt: Pentaindenocorannulene (PiC), Monoindenocorannulene (MiC), das C_{70}-Fragment $C_{38}H_{14}$ und Terphenylencorannulene (TpC). Deren Wechselwirkung mit der metallischen Oberfläche werden durch komplexes Zusammenspiel von zwischen van der Waals (vdW) und Pauli-Repulsion bestimmt. Als intermolukulare Wechselwirkungen sind hauptsächlich attraktive π-π und CH-π Bindungungen am Werk.

Einige „Buckybowls", wie Pentaindenocorannulene (PiC), sind beispielsweise auch als Wasserstoffspeicher, als Fullerenrezeptoren, für medizinische Anwendungen (Toxininhibitoren, Arzneimitteleinkapselung, Nano-Membranen-Herstellung) nützlich. Motiviert durch diese Anwendungen wird die thermisch induzierte Oberflächenchemie von PiC auf Cu(100) untersucht. Bei geringer Bedeckung ($\theta < 0.3$ ML), wenn intermolekulare Wechselwirkungen praktisch nicht vorkommen, adsorbiert PiC mit der Öffnung der Schale senkrecht zur Oberfläche. Bei einer größeren Bedeckung neigen Moleküle aufgrund intermolekularer CH-π und π-π Wechselwirkungen zu gekippten Adsorbatkomplexen. Nach Heizen auf 503 K kann man sternförmige planare Moleküle beobachten.

Nomenclature

Acronyms

CNT	carbon nanotube
CVD	chemical vapor deposition
DFT	density functional theory
DOS	density of states
e.e.	enantiomeric excess
Fcc	face centered cubic
EHT	extended Hückel theory
ESCA	electron spectroscopy for chemical analysis
GGA	generalized gradient approximation
HOMO	highest occupied molecular orbital
HREELS	high-resolution electron energy loss scattering
IS	intermediate state
LDA	local density approximation
LEED	low energy electron diffraction
LT	low temperature
LUMO	lowest unoccupied molecular orbital
ML	monolayer
MM	molecular mechanics
PAH	polycyclic aromatic hydrocarbons
PES	potential energy surface
Rac	racemic
RT	room temperature
SEXAFS	surface-extended X-ray absorption fine structure
STM	scanning tunneling microscope/ microscopy
TDS	thermal desorption spectroscopy
θ	coverage, 1 corresponds to a saturated ML of adsorbates
UHV	ultrahigh vacuum
vdW	van der Waals
VT	variable temperature
XPD	X-ray photoelectron diffraction
XPS	X-ray photoelectron spectroscopy
2D,3D	two and three dimensional respectively

Compounds

[4]H	tetrahelicene
[5]H	pentahelicene
[6]H	hexahelicene
[7]H	heptahelicene
[n]H	n-helicene with $n > 7$
dB[5]H	dibenzopentahelicene
DBA	dibromoanthracene
DBBA	dibromobianthracene
MiC	monoindenocorannulene
PiC	pentaindenocorannulene
TA	tartaric acid
TpC	terphenylcorannulene

I. Introduction

Constant improvement of new materials and novel technologies is indispensable for the sustainable development of our modern society, e.g. in the field of information storage and processing technologies or energy and chemical conversion methods. Nanoscience, a booming research area focusing on the understanding, manipulation and fabrication of structures at the nanoscale, has a tremendous potential. In particular, many different phenomena are governed by the surface properties of materials such as friction and wetting. Thin-films growth, catalysis at surfaces and coatings are for example crucial for new technological applications.

Surfaces are the topmost layers of a solid (thickness ≤ 1 nm) and their behavior differs from that of the bulk in many ways. To minimize the surface energy, i.e. the necessary energy to create surfaces, and because of the asymmetric environment of surface atoms, several effects which are not found in the bulk are observed[1,2]. For instance, atoms at surfaces can form bonds with the species in the adjacent phase (liquid, gaseous or solid) and new electronic states, i.e. surface states, can be created due to the transition from bulk material to vacuum. In addition, atoms near the surface plane can undergo relaxation or even reconstruction due to bonding imbalances[2]. Moreover, real surfaces have atomic steps, atoms vacancies or adatoms, which may become favored adsorption sites for atoms[1]. Such defects can break or make bonds between atoms and are catalytically active. About forty years ago, these peculiar properties led pioneers such as Gabor Somorjai and Gerhard Ertl to study surface-assisted chemistry on well-defined model systems. The advantages of investigating on-surface chemical reactions are numerous. At first, the absence of solvent, the steric constraints induced by the 2D dimensionality as well as the possible catalytic activity of the surface can lead to novel reaction products. In an ultrahigh vacuum (UHV) environment, the confinement in 2D also allows the precise control of reaction parameters[3]. By using advanced methods, such as scanning tunneling microscopy, allowing investigation at sub-molecular spatial resolution, or X-ray photoelectron spectroscopy, offering a surface-sensitive spectroscopic analysis of the elemental composition and chemical state of the elements at the surface[3]. The reaction products which desorb from the surface can be identified by thermal desorption spectroscopy. To improve our fundamental understanding of chemical reactions, all these techniques are used in this work on single crystal metal surfaces with well-defined surface geometries.

This thesis will focus on a specific family of organic molecules, namely, polycyclic aromatic hydrocarbons (PAH). These molecules are made of hydrogen and carbon atoms and have at least two aromatic rings. They are interesting because they allow studying a wide range of intermolecular interactions including van der Waals (vdW) interactions[4], CH-π interactions, π-π stacking[5], substrate-mediated interactions (e.g. via electronic surface states) and sometimes metal-coordinated bonds (with metallic adatoms of the surface for example)[4]. On one hand, this project deals with chemical reactions between PAH, triggered by thermal energy. On the other hand, it discusses their self-assembly, i.e. their spontaneous assembly into ordered patterns due to weak intermolecular forces when adsorbed on a surface[4]. Self-assembly is challenging because the molecular recognition processes often involve cooperative effects[6]. In addition, it is not only controlled by intermolecular interactions but by a complex balance between them and the molecule-substrate interactions. Consequently, the physical and chemical properties of adsorbates and substrate play an important role. Thermodynamic conditions also have a strong impact on the spontaneous organization of molecules on metal surfaces[7,8]. A better understanding of self-assembly will help to get fundamental insights into the physics and chemistry of adsorption, crystallization and heterogeneous catalysis. Furthermore, self-assembly is used as a 'bottom-up' manufacturing approach in nanotechnology and has therefore a significant importance for the interface design of new devices. Non-planar PAH are particularly interesting because they offer a much more complex chemistry than their planar counterparts. Two families are treated in this work: chiral and curved PAH.

Intrinsically chiral PAH, such as helicenes, which will be presented in chapter III, offer the possibility to study molecular recognition and reactions between chiral molecules. Non-covalent interactions between chiral molecules are of paramount importance for the understanding of biological systems[9] (e.g. assembly of lipids forming membranes), drugs development (more than half of the world-wide produced drugs currently are chiral) and for fragrance industries. Since life itself is chiral, different enantiomers generally have different physiological effects on the human body. Information on their self-assembly is extremely valuable since crystallization is still the most important means for separation of chiral compounds. Chiral PAHs at surfaces serve as model systems which are tremendously less complex than biologically relevant systems. The self-assembly of pentahelicene will be presented in the paragraph III.2. The effect of functional groups, will be investigated on 1-aza[6]H in the paragraph III.3. It is interesting for the bottom-up functionalization of surfaces and for the tunability of 2D nanostructures and molecular functionality for applications. Novel molecules can also be created by on-surface chemistry, but because of the confinement in two dimensions, the exclusion of certain symmetry elements can have an impact on the reaction products of chiral molecules. This will be investigated with bromohelicenes using a reaction leading to covalent C-C coupling, called Ullmann coupling[10,11] (paragraph III.4). Thermal annealing induces decomposition of molecules into new molecular fragments by the formation and breakage of covalent bonds. Decomposition may proceed autocatalytically on surfaces, as often observed for oxygen-containing molecules such as carboxylic acids[12]. Here we present the first case of an autocatalytic decomposition of oxygen-free molecules on an oxygen-reconstructed Cu(100) surface (paragraph III.5). Bromohelicenes will be compared to other planar PAH to explain the mechanisms leading either to standard decomposition or to autocatalytic 'surface explosion'.

Finally, buckybowls, which are curved PAH fullerene fragments, will be discussed in chapter IV. The self-assembly of buckybowls allows to study π-π and CH-π interactions between concave and convex sides of the bowls or the rim hydrogens and convex sides. Due to their interesting thermal and electrical conductivity, understanding the self-assembly of buckybowls would also be beneficial for various applications, especially in organic electronics: organic semiconductors[13], photovoltaics[14,15], light-emitting diodes[16,17] and thin film transistors[18]. For these applications, metallic substrate-molecules interactions which impact the work function, must be carefully tuned to allow a good injection of charge carriers at the devices' electrodes[19–22]. Penta-, monoindenocorannulene, (paragraphs IV.2.1and IV.3.1), the corannulene derivative $C_{38}H_{14}$ (paragraph IV.3.2) and terphenylcorannulene (paragraph IV.3.3) will be presented. Some buckybowls such as pentaindenocorannulene (PiC) have significant potential for applications in hydrogen storage[23] or as fullerene receptors[24]. They can be useful for medical applications (toxin inhibitors[25], drugs-encapsulation[26,27], nano-membranes fabrications[28]) or as a precursor for controlled carbon-nanotubes (CNT) growth[29,30]. Thermally-induced bond breaking/formation of PiC in order to evaluate the suitability as new precursor for graphene nanoribbon or carbon nanotubes formation is studied in the paragraph IV.2.

In order to understand the complex phenomena occurring between organic molecules and a metal surface, theoretical and computational treatments are required and will be used in this thesis to support the experimental results. Because the physical and chemical laws involved are far too complex, approximations are required. The limitations of the theoretical approaches will be discussed.

II. Experimental aspects

In this chapter, the experimental set-up (section II.1), the materials used (section II.2) and the data processing routine (section II.3) are described. Finally, a brief introduction to the theoretical methods which will be used in this work can be found in section II.4. All the experiments presented in this thesis were performed in the Molecular Surface Science Group (Nanoscale Material Science Laboratory) and its facilities at Empa in Dübendorf.

II.1. Experimental set-up

1.1 Ultrahigh vacuum chamber

For studying molecules on surfaces, a clean environment is required in order to offer good measurement conditions. The number of gas particles in the chamber with P = 5×10^{-8} Pa[i] at room temperature is, according to gas kinetics, still 1.24×10^{7} molecules/cm^3 [ii]. For determination of how long a surface can stay clean under these conditions, the flux F of molecules colliding the surface per second must be calculated. According to kinetic theory of gas, F can be calculated as follows:

$$F = \frac{P}{\sqrt{2\pi mkT}} \tag{1}$$

where k is the Boltzmann constant (1.38×10^{-23} J K^{-1}), m is the molecular mass, P is the pressure and T the temperature. Assuming the remaining gas in the chamber is only hydrogen, a cm^2 of surface is hit by more than 5.30×10^{15} particles per second when the partial pressure is P = 5×10^{-8} Pa at room temperature. It does not mean that all incoming particles will stick on the surface. This is defined by the sticking coefficient. Assuming a sticking coefficient of 10%[1,2] on a copper surface which has 2×10^{15} atoms cm^{-2}, it takes about 37700 seconds to form a molecular layer (less than a day). Hence, ultrahigh vacuum (UHV) conditions are required in order to have sufficient time for investigation.

Most of the results presented in this work were obtained in the single chamber shown in (Figure 1). It is equipped with a variable temperature-STM (Omicron Nanotechnology) mounted on a vibration isolation system suspended by a spring. To achieve the required UHV (P ≤ 5×10^{-8} Pa) conditions, an ion getter pump and a Ti-sublimation pump were attached on the chamber. Samples and tips were inserted

---

[i] 1 mbar = 100 Pa, 1 atm = 1.01 hPa, 1 Torr = 133 Pa

[ii] Under ambient conditions, there are about 2.7×10^{19} particles/cm^3.

on their holders using a load lock, pumped with turbo-molecular pump, supported by a rotary vane pump. The samples were manipulated using a wobble stick in the main chamber.

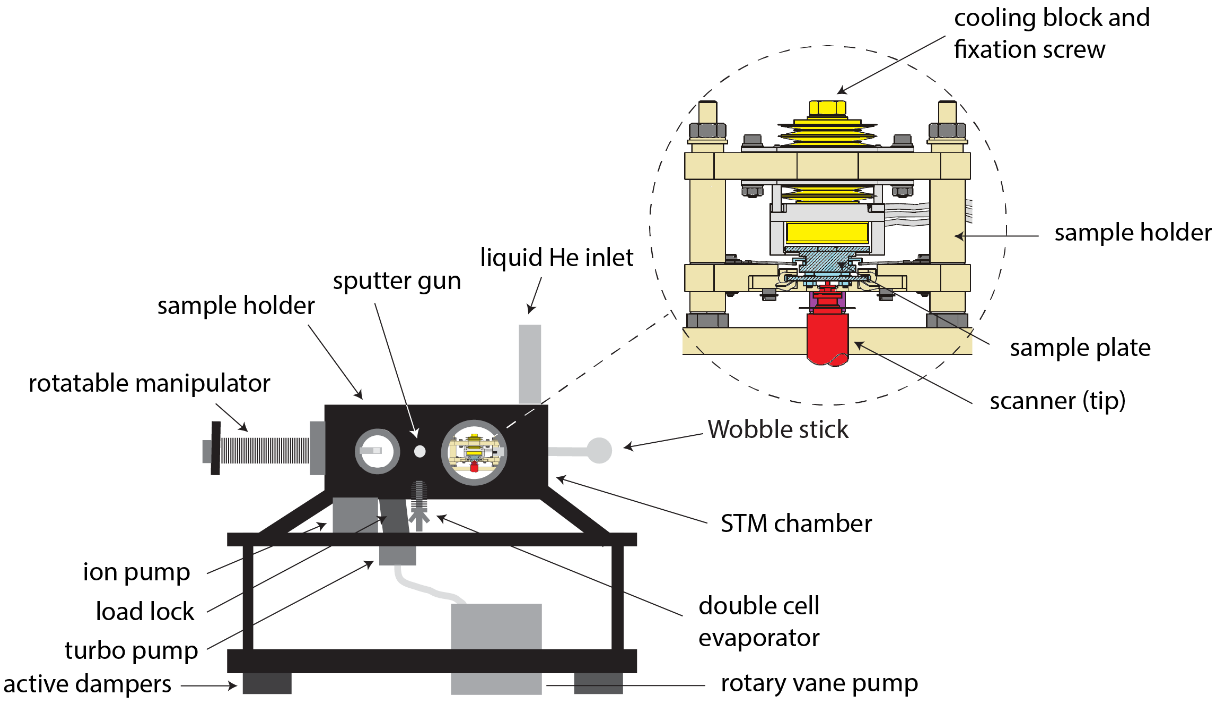

Figure 1: Sketch of the VT-STM chamber[iii]

Standard preparation tools were available: a sputter gun, a gas inlet for Argon and a molecular evaporator with two cells. Using these tools, the metallic single crystals were cleaned by cycles of Ar^+ sputtering and annealing at 673 K. Then, the molecules were deposited by means of sublimation on the clean metallic surface kept at room temperature. During the preparation, the sample was placed on a rotatable manipulator having contact brushes allowing a direct annealing of the sample (via the sample holder's internal heater). The sample was positioned upside down in the STM holder and scanned from below (see inset in Figure 1). The tip used is made from tungsten because of its great mechanical strength, its low cost and its simplicity of fabrication using electrochemical etching[31]. The sample could be cooled down to about 50 K by using a liquid He continuous flow cryostat or heated using either a direct heating system or an indirect resistive heater. The microscope stage remained at constant temperature during the measurements. The vibration isolation of the whole system was achieved by active dampers.

[iii] The drawing of the STM holder in the inset is inspired from the VT-STM User's Guide, Omicron (version 6.1, 2013).

A few experiments were conducted in a second system equipped with the same tools. The STM was a Specs Aarhus 150 which had a mechanically cut and in-situ sputtered Pt/Ir (with 90% Pt) tip. X-ray photoelectron spectroscopy (XPS) and temperature desorption spectroscopy (TDS) were also available. XPS measurements (Specs PHOIBOS 100 electron analyzer) were conducted in normal-emission using non-monochromatic Al K_α X-rays. The binding energy scale was calibrated with the $Cu2p_{3/2}$ peak (932.7 eV) (resp. the Au $4f_{7/2}$ (84.0 eV) peak) and the Fermi level (0.0 eV) of the Cu (resp. Au) crystal. The intensities were normalized with respect to the $Cu2p_{3/2}$ (resp. Au $4f_{7/2}$) signal. TD spectra were obtained using a quadrupole mass spectrometer (Balzers QME 200). A special housing with a pinhole (so-called Feulner cup) was installed to avoid collecting material from the sample holder.

1.2 Scanning tunneling microscopy

One of the most powerful tools to investigate molecular self-assembly at surfaces is scanning tunneling microscopy. It is the principal method used in this work and will thus be discussed in detail. G. Binnig and H. Rohrer invented the first STM[32] and got the Nobel Prize in 1986 for its conception. An STM (Figure 2a) can be used under UHV condition but also in air, at a liquid-solid interface[33], etc. It is used to study atoms and molecules at surfaces and can be operated at different temperatures[2]. This device can achieve a resolution of a few pico-meters vertically and atomic resolution laterally.

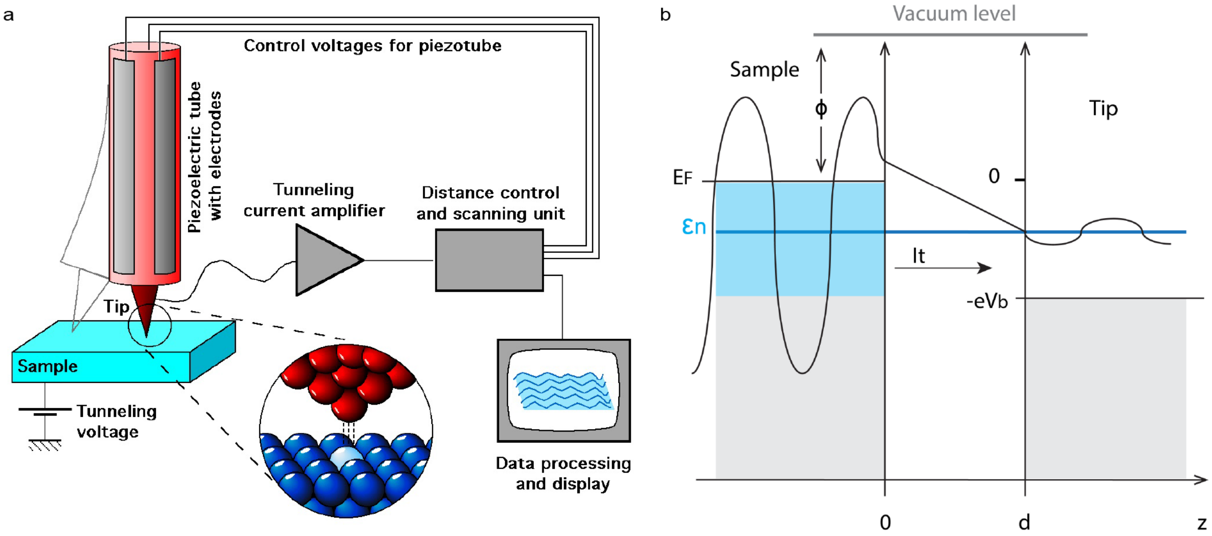

Figure 2: (a) STM set-up[iv] (b) Representation of a 1D wave function in the STM tunneling junction, with a negative voltage applied to the sample with respect to the tip (inspired by ref. [2])

[iv] STM drawing from Michael Schmid, TU Wien.

An STM is composed of a sharp metallic tip which is brought very close to the surface of the conductive sample to analyze. A voltage (up to a few volts) is applied between the tip and the sample allowing a tunneling current to flow. This tunnel current (typical values in the range of few pA to a few nA) depends strongly on the tip sample distance (typical values: 5-10Å). Quantum mechanics tells us indeed that there is a finite probability for electrons to tunnel through the vacuum barrier[34] between the tip and the sample due to the overlap between their wave functions. Nevertheless, when both the tip and sample are held at the same electrical potential, there are no available unoccupied states for the electrons to travel to. By applying a bias voltage V_b between the tip and the sample, their Fermi energy levels shift (Figure 2b), unoccupied states can be reached and a current can flow[2,35].

To obtain an image with the STM used in this work, the surface is scanned line by line by the tip (area between 1 nm^2 and 1µm^2) using a piezoelectric tube on the tip holder (Figure 2a). In the constant current feedback mode applied here, the height of the tip is adjusted via a feedback loop allowing to maintain a constant current. The tip has a considerable influence on the observed images. If the tip apex is made of several atoms (instead of only a single atom ideally), the tunneling current spread across these atoms and the obtained images can be distorted. Hence, tips must be as sharp and clean as possible. It can be done in situ in the STM chamber either by annealing, by using a voltage pulse to cause field-induced evaporation of tip atoms or by a contact between the tip and the sample. It is in theory possible to achieve atomic resolution, however the atomic and electronic structure of the tip is often not known precisely[36].

1.2.1 Theory

The theory behind the operation principle of the STM can be simply understood by using a simplified one dimensional model[2] (Figure 2b). The gap between the tip and sample is represented as a 1D potential barrier of height U and width d. In this potential, the wave function of one electron of mass m and energy E is given by the Schrödinger equation (2). Its classically allowed and forbidden solutions $\phi(z)$ are given by the equations (3).

$$-\frac{\hbar^2}{2m}\frac{d^2}{dz^2}\phi(z) + U(z)\phi(z) = E\phi(z) \tag{2}$$

$$\begin{cases} E > U : \phi(z) = \phi(0)e^{\pm ikz} with\ k = \frac{1}{\hbar}\sqrt{2m(E-U)} \\ E < U : \phi(z) = \phi(0)e^{-\kappa z} with\ \kappa = \frac{1}{\hbar}\sqrt{2m(U-E)} \end{cases} \tag{3}$$

where $\hbar = h/2\pi$ and h is the Planck constant and m is the electron mass.

The tunneling current I_t, (equation (4)) depends exponentially on the distance d between the tip and the sample. It allows the distance to be precisely controlled[33]. This exponential dependence comes from the exponential decays of the wave functions in the gap.

$$I_t \propto \sum_{\varepsilon_n = E_F - eV_b}^{E_F} |\phi_n(0)|^2 \, e^{-\frac{2}{\hbar}\sqrt{2m\phi}d} \tag{4}$$

where ϕ_n are the sample states with energy ε_n, E_F is the Fermi energy and V_b is the bias voltage between the tip and the sample.

The STM can be used in two different modes. The most common mode, used in this thesis, is the constant current mode. The voltage used to adjust the piezo-drives to keep a constant current is measured. This mode is mainly used for surfaces composed of the same atoms. The obtained image is often identified as the surface topography. This is not always true because the tunneling current is in fact proportional to the local density of states (DOS) ρ, i.e. the number of electrons per unit energy ε and per unit volume z. It therefore gives information about the electronic structure of the sample. This dependency is visible in the expression of the current (5), which is a function of the DOS (equation (6)) at the Fermi level.

$$I_t \propto V_b \rho(0, E_F) e^{-\frac{2}{\hbar}\sqrt{2m\phi}d} \tag{5}$$

$$\rho(z, E) = \frac{1}{\varepsilon} \sum_{\varepsilon_n = E - \varepsilon}^{E} |\phi_n(z)|^2 \tag{6}$$

Hence the variation in the surface electronic structure has to be taken into account for image interpretation[2,33]. A topographic interpretation of a STM scan assumes a constant DOS of the sample above equivalent surface states[35]. Note that the STM is only sensitive to the electron states close to the Fermi level[37].

The second principle scanning mode of the STM is the constant height mode in which the variation in the tunneling current is measured. It is used on flat surface to reveal the surface composition (due to the different work functions of different surface atoms) or the defects. It will not be discussed further because it will not be used in this work. More information about the constant height mode can be found in ref.38,39, together with a real 3D description of the tunneling effect which is much more complicated that the simplified 1D model presented here.

1.2.2 Study of organic molecules on surfaces with STM

Probing an organic/metal surface system implies understanding its electronic structure. As already mentioned, when imaging molecules on metal surfaces, one should keep in mind that the images correspond to the electronic states contributing to the tunneling and not simply to the position of the atoms within the molecules[35] (equation (5)). Depending on the polarity of the applied voltage, it might be that molecules or atoms on metal surfaces appear differently in STM[v]. For instance, on Ag(100), oxygen atoms appear as protrusions under negative bias and as depressions under positive bias[35]. Depending on the polarity of the applied bias, pentacene also shows different contrasts on NaCl/Cu(111)[40] [vi]. To understand this behavior, it is important to look at the orbital structure. This thesis is about organic/metal surface systems so we will focus on this case. A metal is a continuum of energy levels occupied up to the Fermi level. On the contrary, a π-conjugated molecule has discrete energy levels. The core levels (at higher binding energies) are spatially confined on the atoms[4] but at lower binding energies, the molecular levels are spatially homogeneously distributed over the molecule (the molecular band gap being defined by the HOMO-LUMO difference).

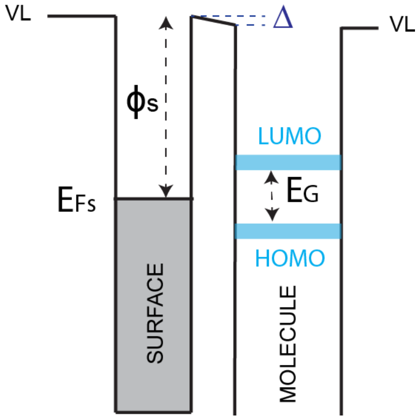

Figure 3: Energy diagram of an organic molecule and a metal surface after adsorption. The molecular frontier orbitals (HOMO and LUMO), the corresponding band gap E_G of the molecule and the Fermi level of the surface E_{Fs} are indicated. Δ is the difference between the vacuum level (VL) of the molecule and the substrate due to the presence of an interface dipole. ϕ_s is the surface work function.

When the molecule adsorbs on the surface, the position of the molecular energy levels can be approximately estimated because the vacuum level of the isolated molecule will align to that of the substrate (Figure 3)[4] [vii]. Applying a negative (respectively positive) bias on the sample (molecule + metal

---

[v] It can also be influenced by the last atom at the tip apex, e.g. CO- or O-terminated tip.

[vi] Using a thin insulator layer is useful for studying orbitals and electronic structures because it decouples the molecules from the metal surface and reduces hybridization and broadening of the molecular orbitals[40].

[vii] This is called the Schottky-Mott rule. It is an approximate position because this rule is exact only for few systems (e.g. a spin-coated polymer on metal surface). In the case of adsorption of molecules on atomically flat metal surfaces, the molecular orbitals are often shifted, and broadening is often observed due to the hybridization of the respective electronic states when molecules and metal are brought in contact. In this case, no alignment of the vacuum levels occurs (Δ in Figure 3) due to charge transfer (to/from polaronic states or gap states created by the

surface) with respect to the tip implies that the Fermi level of the sample raises (respectively decreases) compared with the Fermi level of the tip (Figure 4). Hence, the occupied (respectively unoccupied) states of the sample close to the Fermi level (HOMO, resp. LUMO) contribute the most. The contribution of different states in the different cases can create a difference in contrast for certain molecules.

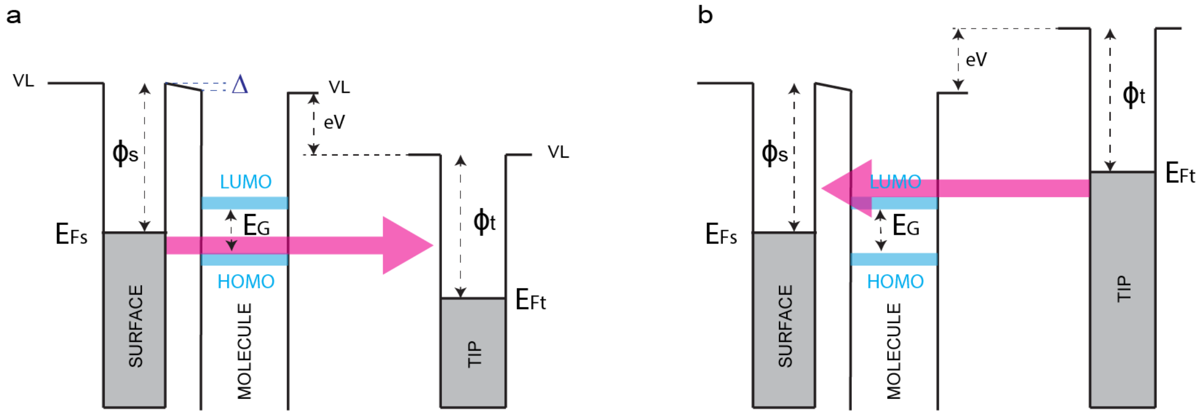

Figure 4: Energy diagram of an STM junction with a sample made of organic molecules on a metal template when the sample is biased by a (a) negative or (b) positive voltage V with respect to the tip. The molecular frontier orbitals (HOMO and LUMO) of the molecule and the Fermi levels of both tip E_{Ft} and surface E_{Fs} are indicated. Δ is the difference between the vacuum level (VL) of the molecule and the substrate due to the presence of an interface dipole. ϕ_s and ϕ_t are the surface work functions of the surface and the tip respectively.

In this work, the impact of HOMO and LUMO contributions for the studied molecules will be presented in the contour maps of the charge density of the frontiers orbitals.

1.3 X-ray photoelectron spectroscopy

X-ray photoelectron spectroscopy (XPS), also known as ESCA (electron spectroscopy for chemical analysis) is a surface sensitive technique used to identify the chemical composition of a sample qualitatively and quantitatively (except H and He). In XPS, the material to analyze is irradiated with X-rays and the kinetic energy of the emitted photoelectrons is measured. When an atom is irradiated with ionizing electromagnetic radiation, three phenomena can occur. Firstly, the photon can go through the material without interaction. Secondly, it can be inelastically scattered by an electron from the atomic orbitals. Finally, it can interact and transmit all its energy to an electron which is then excited to an unoccupied level or emitted out of the atom[41]. This last phenomenon is called photoelectric effect[42]. For it to occur, the incoming photon must have enough energy to eject the electron from the core levels to

---

shift in the molecular orbital frontiers), which generates a dipole layer across the interface. This subject goes far beyond the scope of this work and does not fundamentally change the explanation of the different contrasts observed when changing the polarity of the bias. The interested reader can find additional information in ref.4.

the vacuum (Figure 5a, d). The kinetic energy of the emitted electron (E_k) is therefore given by the following formula[41,43,44]:

$$E_k = h\nu - E_b - \phi \tag{7}$$

where $h\nu$ is the energy of the incoming photon (ν is its frequency and h is the Planck constant), E_b is the binding energy of the electron atomic orbital with respect to the Fermi level and ϕ is the work function, i.e. the energy between the Fermi level and the vacuum level (Figure 5d).

The energy of the photon is known: Al K_α ($h\nu$ = 1486.7 eV) and Mg K_α ($h\nu$ = 1253.7 eV) are typical anode materials[43]. By measuring the kinetic energy and the work function, the binding energy can therefore be determined. This quantity, E_b, depends on the type of element and on the chemical environment[41,44]. Thus, it gives chemical information about the elements at the sample surface but also about the covalent or ionic bonds between atoms in a molecule.

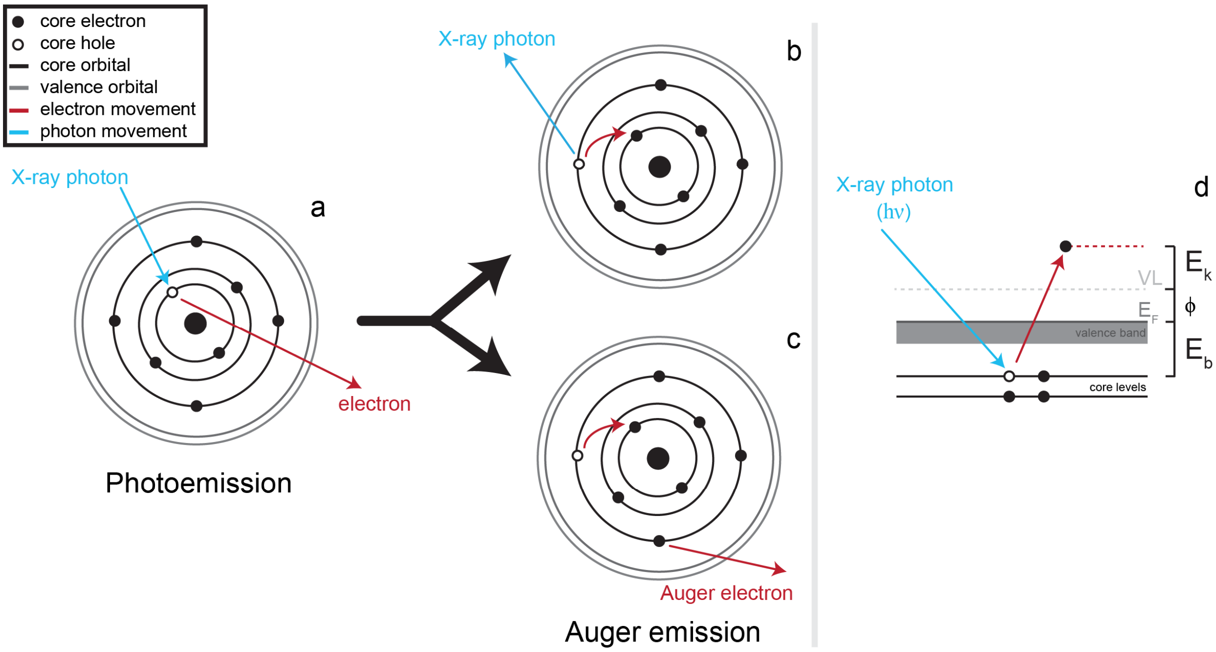

Figure 5: (a) Scheme of the photoelectric effect in an atom: a photon impact knocks out an electron from the core levels which then leaves the atom. (b, c) An electron from a higher energy level can fill the core hole. The excess of energy is released either through the emission of a photon (b) or by ejecting an electron from the same or an outer shell of the atom, the so-called Auger electron (c). (d) Energy diagram depicting the photoelectric effect: an incoming photon can eject an electron from a core level into the vacuum if its energy $h\nu$ is larger than $E_b+\phi$.

An XP spectrum displays the number of electrons emitted as a function of the binding energy. Note that in addition to the photoelectron emitted *via* the photoelectric effect, Auger electrons are also detected. The emission of a photoelectron creates an empty core level which can be filled by an electron from a higher energy level. Energy is transferred during this process, leading to the emission of an X-ray photon or the ejection of an Auger electron[41,43] (Figure 5b, c).

In addition to the photoelectrons and Auger electrons, a few undesired contributions to the signal are often measured. For instance, because the mean free path of electrons in matter is few tens of Ångströms, some of them will undergo inelastic collisions and will contribute to the background signal. Another often encountered example, is the presence of satellite peaks observed at lower binding energies, which are characteristic from the X-ray source used (Al or Mg) which are not entirely monochromatic[43,44]. Additional details about this technique can be found in refs. 41,43,44.

1.4 Thermal desorption spectroscopy

Thermal desorption spectroscopy (TDS), also called temperature programmed desorption, is a technique which gives information on the kinetics and thermodynamics of desorption. The sample is heated gradually up to a certain temperature with a defined heating rate. With enough thermal energy, atoms or molecules adsorbed on the surface start to desorb and can be detected by a quadrupole mass spectrometer. The signal measured by the spectrometer is proportional to the partial pressure of the desorbed molecular fragments or gas components. The temperature T and coverage θ dependence of the desorption rate is described by the so-called Polanyi-Wigner[45,46] equation (8), a type of Arrhenius equation.

$$\mathrm{r(t)} = -\frac{d\theta}{dt} = \nu_n\, \theta^n e^{-E/RT} \tag{8}$$

where ν_n is the rate constant, E is the desorption energy, n is the order of the desorption reaction (typically 0, 1 or 2) and R is the gas constant. More information about the desorption process and TDS can be found in refs. 45,46.

II.2. Materials

Most of the organic molecules were synthetized by colleagues from various chemistry groups (Table 1). The molecules were all sublimated from a Knudsen cell on a sample which was kept at room temperature. Most of the molecules were mobile at room temperature on surfaces of Cu or Au. To observe a self-assembly, a dense packing of the molecules was often required. To quantify the number of molecules on the surface, the coverage is expressed as a percentage of the so-called monolayer coverage (ML). We defined the ML coverage as the most densely packed single layer of molecules.

Metal single-crystals (MaTeck GmbH, purity 99.999%) were used as substrates because their surface geometry is well known. In addition, they are flat (roughness smaller than 0.03 µm and orientation precision better than 0.1°).

Argon and oxygen gases (Messer, purity 99.999%) were used for Ar ion sputtering and to obtain O/Cu(100) layers, respectively.

Molecule	**Synthesized by**	**Sublimation temperature [K]**
Rac-pentahelicene ([5]H)	group of Prof. Andreas Terfort, University of Frankfurt	363
Pentaindenocorannulene (PiC)	Samuel Lampart (Prof. Jay S. Siegel's group, University of Zürich)	593
Monoindenocorannulene (MiC)	Prof. Jay S. Siegel's group, University of Zürich, according to ref. 47.	423
(M)-1-azahexahelicene (aza[6]H)	group of Dr. Matthew Fuchter, Imperial College London, with their own method described in ref. 48.	408
$C_{38}H_{14}$	group of Yao-Ting Wu, National Chang Kung University, using a reaction path described in ref. 49.	583
Rac-2-bromotetrahelicene (Br[4]H)	Kévin Martin (Prof. Narcis Avarvari group), University of Angers, using the procedure described in ref. 50.	373
Rac-2,3-dibromotetrahelicene (diBr[4]H)	Prof. Narcis Avarvari group, University of Angers	373
Terphenylcorannulene (TpC)	group of Yao-Ting Wu, National Chang Kung University,	493
Rac-9-bromoheptahelicene (Br[7]H)	Dr. M. Wienke, University of Hamburg	443
Rac-bisheptahelicene (bis[7]H)	group of Prof. Andreas Terfort, University of Frankfurt	573
4,4'-dibromoterphenyl 1-Br-pyrene 10,10'-diBr-9,9'-bianthracene (DBBA) 9,10'-dibromoanthracene (DBA)	commercial compounds obtained from Sigma Aldrich	363 343 433 373

Table 1: Synthesis and sublimation details about the molecules used in this work.

II.3. Data processing

The obtained STM images were processed using WSxM 5.0. They were flattened and (if necessary) low-pass filtered (using Fourier transform filters) to remove the noise due to vibrations or due to a change in the He flux used for cooling the sample. For having a good contrast to see clearly the structures on all terraces, large scale STM images were sometimes flattened with a parabola filter which suppresses the height differences between the steps. As an example, the flattened Figure 29 and the original non-flattened Figure A. 7 in the appendix can be compared. For XPS, the spectra obtained on the clean samples were subtracted from the measurements containing molecules. The spectra were fitted using Origin 2017. For TDS, a special housing (so-called Feulner cap) with a pinhole was installed to avoid collecting material from the sample holder. Nevertheless, a monotonously rising background was sometimes observed in particular for CO. For each mass spectrum, the background intensity which was obtained before starting the temperature ramp, was subtracted from the TD spectra. 2D drawings of molecular structures were realized using the ChemBioDraw Ultra 13.0 software.

II.4. Theoretical methods

In order to better understand the complex interactions between organic molecules and metal surfaces, an experiment can be supported by computational models. Different methods were used in this work to predict certain properties of molecular systems (adsorption configuration, binding energy between several molecules, etc.). Dr. Laura Zoppi performed all the Density Functional Theory (DFT) calculations presented here, which were computationally quite expensive. The program package HyperChem allows molecular mechanics (MM) modelling and the use of Extended Hückel Theory (EHT) for orbital calculations and corresponding STM simulation. As shown in this work, such modelling can be sufficient to explain the experimental data.

It is not the goal of this work to go too deep into the theoretical details, but a simple overview is necessary to understand what was done in this work. The chemical and physical laws involved in the description of molecular systems are often too complex and each theory has indeed its own hypothesis, simplifications and limitations. In quantum methods (DFT, EHT), several choices can be made to find an approximate solution to the Schrödinger equation for a many-electron system, still impossible to solve exactly. Likewise, MM, a method based on classical mechanic to find minimum energy configurations for molecules, has its limitations. It uses a sum of simple analytical empirical functionals, included in a so-called force-field, to calculate the potential energy of the system. Each force-field is specific to certain molecules and will work only under certain conditions. MM does not allow studying chemical reactions for example. Moreover, modelling metals is always something complicated (electrostatic and polarization effects) and calls for an appropriate force field to describe the interactions between organic molecules and metal surfaces.

4.1 Density Functional Theory

DFT is the most successful method in modern chemistry to compute the electronic structure and predict the properties of molecules. The goal of DFT is to investigate the electronic structure of a many-body system (atoms, molecules, solids, surfaces) of interest, which is characterized (for N nuclei and M electrons) by the following Hamiltonian:

$$\hat{H}(\vec{R},\vec{r}) = \hat{T}_n^{kin}(\vec{R}) + \hat{T}_e^{kin}(\vec{r}) + \hat{U}_{ee}(\vec{r},\vec{r}) + \hat{V}_{ne}(\vec{R},\vec{r}) + \hat{V}_{nn}(\vec{R},\vec{R}) \tag{9}$$

where $\vec{R}$ and $\vec{r}$ are vectors describing respectively the nuclei (with 3N Cartesian x, y, z components) and electrons (with 3M Cartesian x, y, z components) positions, $\hat{T}_n^{kin}$ and $\hat{T}_e^{kin}$ are respectively the kinetic energies of nuclei and electrons. $\hat{U}_{ee}(\vec{r},\vec{r})$ is the potential energy of interactions between electrons, $\hat{V}_{nn}(\vec{R},\vec{R})$ is the potential energy of interactions between nuclei and $\hat{V}_{ne}(\vec{R},\vec{r})$ is the potential energy of interactions of the nuclei with the electrons. To obtain the electronic structure, the corresponding Schrödinger equation must be solved:

$$\hat{H}(\vec{r_1},\dots,\vec{r_M};\ \vec{R_1},\dots,\vec{R_M})\psi_i = E_i\psi_i(\vec{r_1},\dots,\vec{r_M};\ \vec{R_1},\dots,\vec{R_M}) \tag{10}$$

This Hamiltonian can be simplified by using the Born-Oppenheimer approximation[51]. Because nuclei are much heavier and slower than electrons, they are assumed to be motionless and to have a constant potential energy. Therefore, we can consider the electrons as moving in the field of fixed nuclei and simplify the Schrödinger equation:

$$\hat{H}\Psi = (\hat{T} + \hat{U} + \hat{V})\Psi = E\Psi \tag{11}$$

where $\hat{T}$ is the kinetic energy operator for the electrons, $\hat{V}$ is the external potential felt by the electrons and $\hat{U}$ is the electron-electron interaction potential. The solution of this Schrödinger equation, the electronic wave function (function of the 3M coordinates of the M electrons), can then be used to compute the electron density $n(\vec{r})$. In quantum mechanics, the electronic density is a measure of the probability for an electron to occupy an infinitesimal element of space surrounding any given point. It is defined as the integral over the spin coordinates of all electrons and over all but one of the spatial variables[52–57]:

$$n(\vec{r}) = M \sum_{spin} \int |\Psi(\vec{r},\vec{r_2},\dots,\vec{r_M})|^2 \, d\vec{r_2},\dots,d\vec{r_M} \tag{12}$$

It is a scalar quantity depending only on three spatial variables. It would therefore be convenient to use it to describe the ground states properties of a many electrons system instead of using the M-electrons wave function which has much more coordinates[52–57]. This is what DFT does.

The foundations of DFT come from two theorems of Hohenberg and Kohn. The first theorem[58] states that the ground state electron density n_0 uniquely determines the ground state electron wave-function Ψ_0, i.e. Ψ_0=$\Psi[n_0]$, and the external potential (within a constant). As the external potential defines $\hat{H}$, it means that all observables are also functionals of the ground state electron density. The idea is therefore to be able to compute this density. Then, all the properties of the system can be determined. The second theorem of Hohenberg and Kohn (also called variational principle[2]) says that the energy is a unique functional of the electron density and its minimization with respect to $n(\vec{r})$ leads to the ground state energy of the system[58]. The problem is therefore reduced to the minimization of the energy functional E[n]= T[n] +U[n] +V[n][52–57], where (according to the notations of equation (11)) T is the kinetic energy functional and U is the electrons-electrons interactions potential. The external potential V depends on the system under study and can be re-written as V[n] $= \int V(\vec{r})n(\vec{r})d^3r$. Nevertheless, it is not possible to solve the many-interacting electrons system analytically and in particular it is impossible to find the analytic expression of the kinetic energy[52–57]. The Kohn-Sham ansatz suggests a solution by replacing this system by a system of independent electrons in an external potential[59]. It means that the energy functional is replaced by the following expression:

$$E_s[n] = T_s[n] + V_s[n] \tag{13}$$

where $T_s[n]$ is the kinetic energy of electrons without interactions and $V_s[n]$ is the external effective potential in which the electrons are moving, and which is defined such as $n_s(\vec{r}) = n(\vec{r})$.

Consequently, the Schrödinger equation (10) can be simplified as a system of mono-electronic equations (called Kohn-Sham equations) [52–57]:

$$[T_s + V_s(\vec{r})]\phi_i(\vec{r}) = \epsilon_i\phi_i(\vec{r}) \tag{14}$$

where ϕ_i are the orbitals which account for the original density $n\overrightarrow{(r)}$ of the problem such as $n_s(\vec{r}) = \sum_{i=1}^{M}|\phi_i(\vec{r})|^2 = n(\vec{r})$. On a developed form the equation (14) can be rewritten, as a function of the orbital energy ϵ_i, as follow:

$$\left[-\frac{1}{2m}\nabla^2 + V(\vec{r}) + \int \frac{e^2 n\vec{r}}{|\vec{r} - \vec{r}'|}d^3r' + V_{exc}(n(\vec{r}))\right]\phi_i(\vec{r}) = \epsilon_i\phi_i(\vec{r}) \tag{15}$$

where the first term corresponds to T_s and V_s is made of the three following terms: the external potential of the nuclei V, the electrostatic potential between electrons (the third term of equation (15)) and the exchange correlation potential V_{exc} accounting for the many-particle interactions. As the different potentials depend on $n(\vec{r})$, which depends on ϕ_i, this problem must be solved iteratively. Theoreticians usually start with a guess for the density and compute the different potentials allowing them to find the orbitals ϕ_i which are then used to compute a new density. This process continues until convergence[52–57].

The most difficult task in this simplified problem, is to determine the exchange correlation potential[60]. V_{exc} includes the many-particle interactions and therefore depends on the density at each $\vec{r}$. It must be approximated. Different approximations exist[61] such as the local density approximation (LDA), which is the simplest approximation but underestimates the bond length and band gap. Another example of a more complicated approximation is the generalized gradient approximation (GGA) which slightly overestimates the bond length but gives better results for different important parameters such as the band-gap. Depending on the level of accuracy that one wants to reach, it might be computationally demanding.

DFT is nowadays the most commonly used computational method in chemistry to compute the electronic structure and to predict various properties of molecules. However, one should keep in mind that it still faces many challenges. In particular, it needs to improve the description of weakly bonded systems (e.g. hydrogen bonding or VdW forces) and reaction barriers[60] which can be problematic with the systems under study in this work. For the molecules presented in this work, Dr. L. Zoppi, from the university of Zürich, used a optB86-VdW functional[62,63], which accounts for dispersion effects, and ultra-soft pseudo-potentials. She used a periodic four-atom-layer slab where the bottom two layers were fixed and all other atoms could relax unconstrained until the forces on each atom are less than 0.013 eV/Å.

4.2 Extended Hückel Theory

Depending on the properties of interest, DFT might not be required. Simpler and low-cost methods such as EHT may be sufficient. EHT is a semi-empirical method, faster than DFT and gives good qualitative results concerning the computation of molecular orbitals (number of levels, degeneracy) and the charge distribution of conjugated hydrocarbons. Because of the high level of approximation, it cannot be used for geometry optimization[54] or spectral predictions[64]. Therefore, geometry optimization is performed with molecular mechanics (see next section).

EHT attempts to solve the Schrödinger associated to the molecular Hamiltonian (equation (11)). The resulting many-electrons wave function can be rewritten as an anti-symmetrized product (Slater determinant) of single-electron wave functions or molecular orbitals. In addition, each molecular orbital can be approximated as a linear combination of n atomic orbitals ϕ_j[64]:

$$\Psi_i = \sum_j c_{ij}\phi_j \qquad j = 1, \dots, n \tag{16}$$

Then, according to the variational principle, this simplified problem can be solved by minimizing the energy[64]. It gives rise to a set of n Hückel equations[65]:

$$\sum_i c_{ij}[H_{ij} - ES_{ij}] = 0 \tag{17}$$

where $H_{ij} =< \phi_i|\hat{H}|\phi_j >$ such as $H_{ij} = H_{ji}$ (hermitian operator) and $S_{ij} =< \phi_i|\phi_j >$ such as $S_{ij} = \begin{cases} 1 & i = j \\ S_{ji} & i \neq j \end{cases}$ Moreover, S_{ij} are the overlap integrals and characterize the probability of presence of an electron i and an electron j in the same area. If the atomic orbital basis set ϕ_j is known, H_{ii} and S_{ij} can be computed in the same basis set. Equation (17) has non-zero solutions when the associated determinant $|H_{ij} - ES_{ij}|$ is equal to zero. The value of H_{ii} is related to the energy needed to ionize an electron from the ith orbital. It is determined by the atom nature and the orbital type considered (that is why EHT is a semi-empirical method)[65]. H_{ij} when $i \neq j$ is approximated by $H_{ij} = kS_{ij}(H_{ii} + H_{jj})/2$ where k is defined experimentally. The Hamiltonian matrix and the different parameters as well as the eigenvalues (energies) can be computed and the eigenvectors are then calculated[54]. Note that a general many-electron wave function cannot be expressed exactly as a single determinant. As a result, EHT do not fully incorporate electronic correlation (repulsive part) and the resulting energies tend to be too high. Consequently, EHT should not be used for geometry optimization[54] or spectral predictions[64] [viii].

In this thesis, EHT is performed in HyperChem 8.0 directly on a force-field optimized structure and the output file contains the previously mentioned parameters, eigenvalues and eigenvectors. The related charge density contours of the frontier orbitals, which can be compared with the STM contrasts, were displayed using Igor code from Dr. Oliver Gröning from EMPA, Dübendorf. Note that the surface was included in the MM optimization which serves as basis for the electronic structure calculation but it is not included in the EHT calculations.

[viii] In general, all Hartree-Fock methods have this problem. A solution, offered by post-Hartree-Fock methods is to find a basis of single electron wave functions and express the many-electron wave function as a linear combination of all their possible determinants. Nevertheless, such techniques tend to be computationally demanding and cannot be used for large systems.

4.3 Molecular Mechanics

Three-dimensional models are calculated in order to present the most energetically favorable configuration of molecules under certain conditions. To reach this goal, the potential energy surface (PES) which is the potential energy (including nuclear repulsion) as a function of a given conformation of the molecule must be minimized. The PES is found by solving, for many nuclear configurations (different inter-nuclear distances and angles), the Schrödinger equation[54,66]. Nevertheless, it is a difficult problem for many computational techniques. In addition, for large many body systems, sophisticated molecular modelling methods are computationally too demanding to be routinely used. When only equilibrium geometry and transition states or relative energies between different molecules or conformers are of interest, molecular mechanics is a perfect alternative for qualitative descriptions.

The simplicity of MM lies in the fact that, to estimate the potential energy surface and the physical properties of molecules, molecular mechanics methods do not solve the Schrödinger equation but assume that atoms are heavy enough to obey classical mechanics rules. This method does not explicitly treat electrons but consider a molecule as a collection of atoms interacting with each other by simple analytical empirical functionals implemented in a so-called force field. The bonding between atoms (considered as spheres) is modelled as harmonic oscillators. Compared to semi-empirical quantum methods, it is faster and allows considering larger systems for molecular dynamics or for conformational energy investigations. Because electrons are not treated explicitly, it does not allow studying bond-breaking/forming reactions or systems strongly affected by electron delocalization or molecular orbitals interaction. Therefore, energies obtained with molecular mechanics have no meaning as absolute quantities. It is only the differences in energy between several conformations of the same system which are relevant[66–69].

In order to gain a clearer idea of the level of approximations used in this method, let us consider the easily understandable example of the PES of a diatomic molecule[54], as considered with the AMBER force field. In a diatomic molecule, there is only one nuclear coordinate, namely the interatomic distance. Thus, the PES describes the potential energy of the system as the distance between the two atoms distance varies. MM methods such as AMBER are based on the Hooke's law approximation (harmonic oscillator model) for the PES. Figure 6 shows the deviation from the Morse potential that is considered as a good model for the PES of a diatomic molecule. Even though both functions have by definition the same minimum (because the equilibrium distance is an empirical parameter), the Morse potential is a better approximation because it explicitly includes certain effects like the anharmonicity of real bonds. Nevertheless, the harmonic potential used in MM such as AMBER is faster to compute and easier to parametrize than the Morse function. Furthermore, at ambient temperature only the bottom of the potential is populated.

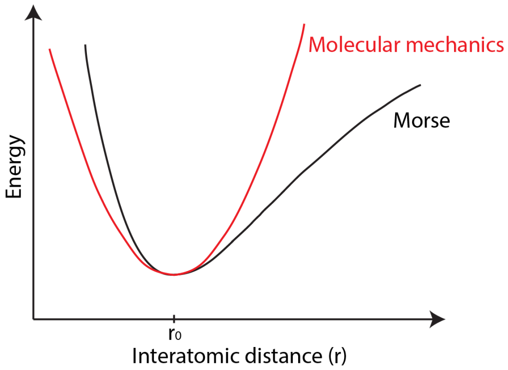

Figure 6: Energy functions, depending on the interatomic distance. Black: Morse potential, which is considered as a very good approximation of the diatomic potential. Red: PES of a diatomic molecule when computed by molecular mechanical methods, like AMBER. Adapted from ref. 54.

A force field allows calculating the molecular system's PES, E_{total}, associated with a given conformation of the molecule, as a sum of individual energy terms:

$$E_{total} = E_{non-covalent} + E_{bending} + E_{torsion} + E_{stretching} \tag{18}$$

$E_{non\text{-}covalent}$ includes electrostatic interactions of charge distributions, hydrogen bonding and vdW interactions (long-range attraction and short-range repulsion). In addition, $E_{bending}$ is the energy corresponding to angle deformations, $E_{torsion}$ describes intramolecular rotations about bonds and $E_{stretching}$ describes bond deformation[54,60]. Many different force-fields are available. Some of them contain additional energy terms to improve the accuracy of the modelling. Each force-field is defined via experimental data and via the choice of different functionals for each energy term. It is only designed for an ensemble of a molecular system[54] for which the chosen functionals are adapted[54]. For instance, in order to model the vdW interactions included in $E_{non\text{-}covalent}$, one could use a Lennard-Jones potential (AMBER) or a combination of an exponential repulsion (supposed to be more accurate for repulsive forces) with an attractive $1/R^6$ dispersion interaction (MM+)[70].

The 3D models of molecules were obtained via HyperChem™ 8.0. using AMBER or MM+ force-fields for geometry optimization calculations[ix]. AMBER is popular for geometry optimization and is widely used in academics resulting in a constant improvement of its parameters. It was already used with success to explain self-assembly phenomena of helicenes and buckybowls on metal surfaces[7,29]. It was

---

[ix] Energies computed in this software are given in kcal/mol. 1.0 kcal/mol corresponds to 4.3×10^{-2} eV per particle.

originally developed for proteins and nucleic acid computations[71]. As both the covalent bonds description (for relaxed structures) as well as the dispersion and dipolar forces (for molecular interactions) are important for protein simulations, this force field tries to combine the best of "both worlds". That is the reason why, it is the most used force-field method in this thesis. Nevertheless, it might lack explicit parameters for small organic systems that are then replaced by parameters from the default MM force field in HyperChem. MM+ on the other side was developed based on the MM+ force field developed by Allinger[72]. It is specifically designed for small organic molecules and peptides but only with single or few functional groups[72]. It has certain advantages when working with this type of molecules. Because of the functional it uses, it is more precise to simulate the vdW interaction than AMBER[73]. It works well for small organic molecules including those that show conjugation. It should be used with caution when working with heteroaromates or fullerenes. MM+ is a united atom force field[x], whereas AMBER is an all atom force field[xi].

Periodic boundary conditions were used (with the automatic cutoff computed by the program to avoid discontinuities in the potential energy surface). For geometry optimization of the molecular structure, a conjugate gradient method, called Polak-Ribiere, was used[54]. The termination condition was to get a RMS gradient smaller than 0.001 kcal/(Å mol). For all molecular models in this work, the surface is made of four layers of metal atoms fixed in their bulk configuration. If another constraint is added, it is specified in the text. The binding interaction between two molecules will always be determined by comparing the energy of the optimized configuration with the energy of the two molecules far away from each other on the surface.

---

[x] It decomposes the molecules into groups of atoms that can represent the molecular properties on larger scale than atomic scale. It is a good approximation for systems in which the intermolecular motion predominates compared with intramolecular motion.

[xi] It provides parameters for every type of atom in a system, including hydrogen.

III. Chiral polycyclic aromatic hydrocarbons

III.1. Introduction

1.1 Chirality

Chirality is the spatial property of an object to be incongruent, i.e. not coinciding exactly when superimposed, with its mirror image[74]. Chiral (also called enantiomorphous) objects are devoid of symmetry elements of the second kind (mirror planes, centers of inversion, rotation-reflection axis)[75]. Common examples are shoes, crooked spires, gastropod shells, hands. The latter is the origin of the term chirality which comes from the Greek word Χειφ (hand). This term was mentioned for the first time in a lecture[xii] given by Lord Kelvin in 1893[76,77]. The Figure 7 presents examples of chirality in everyday life.

Figure 7: Chirality in everyday life. From left to right: the spiral staircase at the Lighthouse in Glasgow, a snail shell, the crooked spire in Rochechouart, a fern frond unfurling[xiii].

On a molecular scale, chirality is present in the biological world which is literally single-handed (e.g. amino acids are only left-handed in the human body)[74]. Chirality can be used, for example, to determine the age of bow-head whales[78]. The method is based on measuring the degree of aspartic acid handedness switching (called racemization). As physiological properties of mirror image isomers, (so-called enantiomers) differ most of the time, chirality is also of interest in pharmaceutics. Many drugs are chiral, but ibuprofen, for example, is administered as a racemic mixture[xiv]. Chirality is also important in fragrance industry. The two enantiomers of limonene smell for example differently (one like orange and the other like turpentine).

[xii] The lecture was published in 1894[77].

[xiii] From left to right: Pictures by George Gastin, Kabir Bakie, Babsy and Jon Radoff

[xiv] The *R*-enantiomer undergoes extensive interconversion to the *S*-enantiomer in vivo which is believed to be the more pharmacologically active enantiomer[259].

The concept of molecular chirality was first discussed in 1848 by L. Pasteur who manually separated right and left handed ammonium sodium tartaric acid crystals (Figure 8a) and observed opposite optical activities for their aqueous solution, whereas a racemate, i.e. a mixture containing the same quantity of both enantiomers showed no optical rotation[79]. In achiral environment, enantiomers have the same physico-chemical properties except for their equal but opposite optical rotations. Note that Pasteur was helped in his discovery by two important aspects. At first, the TA precipitated into a conglomerate of homochiral crystals, i.e. each single crystal contained only molecules with the same handedness. Secondly, the handedness of the molecular assembly was transferred to the macroscopic shape of the TA crystal[80]. Twenty-six years later, H. van't Hoff and J. A. Le Bel proposed independently the model of the asymmetric carbon atom as chiral entity (Figure 8b). Whenever a molecule has a carbon atom with four different substituents and if their arrangement around the carbon is not planar, then this carbon atom is a chiral center. Two non-superimposable mirror configurations are therefore possible. The discovery of the asymmetric carbon atom allowed to explain the chiral nature of the molecules in optically active substances[81].

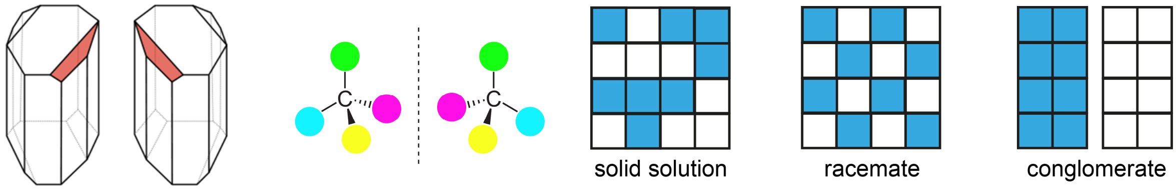

Figure 8: From left to right: Left and right handed tartaric acid crystals (usually found at the bottom of a wine bottle); asymmetric carbon atom and its mirror image; three possible outcomes of the crystallization of a racemic compound

Both discoveries are fundamental in the history of chirality especially at a time when molecular structure and atomic bonding were not well understood[81]. Nowadays, the complex non-binding interactions between chiral molecules, also called chiral recognition, are still poorly understood: we are neither able to predict the outcome of a crystallization based on the molecular structure nor to explain why only 10% of all racemates crystallize into conglomerates[xv] [82] (Figure 8c). Such complexity mostly comes from cooperativity[83]. Extremely small structural influences can indeed strongly impact the macroscopic structure when they are amplified by several cooperating units[80,84]. The study of chirality at surfaces is consequently motivated by the development of meaningful model systems which can improve our current understanding of the topic.

[xv] If they do not crystallize as conglomerates, the vast majority of racemic mixtures of chiral molecules will crystallize as a racemate and less than 1% form a solid solution, i.e. both enantiomers are distributed randomly in the crystal in contrast to a racemate where both enantiomers are present in the same proportions.

As explained earlier, pharmaceutical and agrochemical industries aim at getting pure products and are interested in enantioselective catalysis. In 2001 W.S. Knowles, R. Noyori and K.B. Sharpless have been awarded with the Chemistry Nobel Prize for their work on chirally catalyzed reactions. Another strong motivation for studying chiral molecules on surfaces came in the 1990's from heterogeneous catalysis[33]. In this process, the use of a chiral modifier on a catalytically active metallic surface confers enantioselectivity to the catalyst. By selecting the modifier properly, the reaction allows to produce an enantiomeric excess of one enantiomer[85]. Nevertheless, the mechanism of these reactions is still not completely understood. Moreover, the study of surface chirality could foster our actual understanding of biomineralization[80]: chiral molecules such as proteins can interact with achiral minerals during crystal growth and induce chirality in macroscopic crystals[xvi].

A promising approach towards chiral model systems for better understanding molecular recognition is to investigate two-dimensional self-assembly of chiral molecules on single-crystal substrates by means of STM. At first, the spatial arrangement of the molecules is much simpler than in 3D crystals. Due to the in-plane confinement giving rise to the preclusion of certain symmetry elements, enantioseparation on a surface has been predicted to occur more frequently[7,86]. However, in a recent review overlooking literally all published chiral surface science work, this claim was not substantiated[87]. In addition, STM allows the direct study of molecular recognition with sub-molecular resolution in monolayers and multilayers[88,89].

Note that chirality in 2D systems depends on two main aspects: 1) The chirality of the molecules and their mutual interactions are important. 2) The geometry of the surface has also an impact on binding of the molecules to the surface and therefore on the self-assembly[90]. The chirality in self-assembled motifs can therefore be induced by the intrinsic chirality of the surface and molecules or during the adsorption of prochiral molecules. This thesis focusses on a class of intrinsically chiral molecules called helicenes.

1.2 Helicenes

As helicenes are usually ortho-fused polycyclic aromatic hydrocarbons denoted in which steric overcrowding leads to the non-planar helical molecular backbone[91]. Helicenes are intrinsically chiral due

---

[xvi] The interested reader can find more information about biomineralization in ref.[260].

to their helical shape. This is called axial chirality. They have neither a chiral center nor an asymmetric carbon atom. One complete pitch of a screw is obtained with six benzene rings[91].

R. S. Cahn et al. defined a notation[92] in order to identify the two types of helices: a right-handed helix is designated by a *P* ("plus") whereas a left-handed helix is denoted by a *M* ("minus"). This notation will be used throughout this thesis. An example is given for pentahelicene enantiomers in Figure 9.

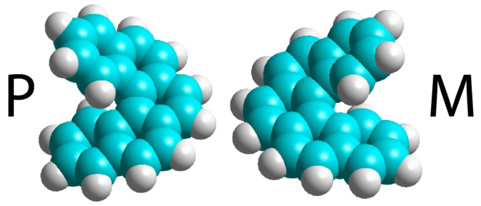

Figure 9: Ball models of a (*M)*- and (*P)*-pentahelicene

Helicenes purely made of benzo groups are called carbohelicenes. If at least one of the carbon atoms of the backbone is replaced by another element, the molecule belongs to the hetero-helicene family. Nomenclature notations of helicenes can be complicated. For example, the molecule with five ortho-fused benzene rings (Figure 10) should be called 3,4,5,6-Dibenzophenanthren[93]. For simplification, M. S. Newman and D. Lednicer introduced a new notation. The number of aromatic rings of a helicene is indicated in brackets before the name. Therefore 3,4,5,6-Dibenzophenanthrene is designed as [5]helicene and the same molecules with a nitrogen atoms in position 7 and 8 (Figure 10) is called 7,8-diaza[5]helicene[94].

An inversion of handedness of the molecules requires overcoming the so-called racemization barrier. The Gibbs free energy for the thermal racemization of [5]H (24.1 kcal/mol at 293 K[95], or 22.9 kcal/mol at 300 K), [6]H (36.2 kcal/mol at 300 K), [7]H (41.7 kcal/mol at 300 K), [8]H (42.4 kcal/mol at 300 K) and [9]H (43.5 kcal/mol at 300 K[96]) has been experimentally determined. The inversion barrier for [4]H was calculated as 4.0 kcal/mol with semi empirical and ab initio methods[97]. As can be seen, the inversion barrier raises rapidly with the number of rings until [7]H. Its values are similar for longer helicenes.

The first hetero-helicene (7,8-diaza[5]helicene in Figure 10 is one of them) was discovered in 1903 by J. Meisenheimer and K. Witte[91] and fifteen years later the first pentahelicene was synthesized by R. Weitzenböck and A. Klingler[91,98]. Since then, the interest for these molecules has continuously increased due to their special properties. For example, they can form charge-transfer complexes with many π acceptors. Furthermore, helicenes are often fluorescent molecules and can therefore be used for optoelectronics. Nevertheless, their quantum yield being not very good, they need functionalization, such as [5]H was functionalized with nitrile groups and are used as emissive material for OLED[99]. Helicenes are interesting for other applications, such as liquid crystals[98], molecular motors[100,101] or switches[102], asymmetric catalysts[103], optical active polymers[104,105] or sensing materials[106]. An extensive list of helicene applications (mainly for carbohelicenes) is given in ref.[98].

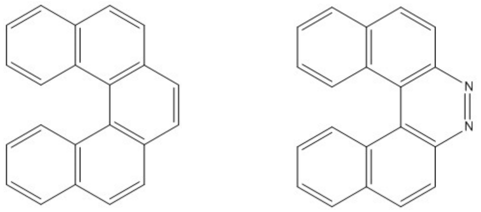

Figure 10: From left to right: molecular structure of a [5]helicene and a 7,8-diaza[5]helicene

An important aspect, which makes helicenes suitable to be used for experiments described in this thesis, is the possibility of sublimation at reasonable temperatures. They can be functionalized and their length can be varied[xvii]. It allows studying a wide range of intermolecular interactions: vdW, CH-π, π-π stacking or interactions between functional groups.

1.3 Previous work

A good overview of all the studies realized with helicenes in various fields (biochemistry, opto-electronic, surface science,…) was written by M. Gingras[98]. This paragraph will only discuss the studies of helicenes on metal surfaces which are relevant for this work.

1.3.1 Self-assembly of racemic and enantiopure carbohelicenes on surfaces

Rac-[7]H ($C_{30}H_{18}$) was meticulously studied with STM by Ernst and co-workers on several single metal crystals to determine the influence of the template on the self-assembly. On each surface a specific adsorption footprint is indeed adopted by the molecule upon deposition. In the case of *rac*-[7]H on Cu(111), X-ray photoelectron diffraction (XPD) revealed that the molecule binds to the surface with their three first C_6 rings (terminal phenanthrene group) oriented parallel to the (111) plane[107]. From the fourth rings on, the molecules spiral away from the surface. The fact that identical adsorption sites (Figure 11) are occupied has only recently been established by DFT calculations (L. Zoppi, Empa, unpublished results). This is expected because the length of the unit cell of Cu(111) fits the size of benzene rings in

---

[xvii] There are numerous synthesis procedures to obtain helicenes. For more details about them, the interested reader can consult ref. [261] and ref. [262] for non-stereoselective and stereoselective syntheses respectively.

planar aromatic hydrocarbons, allowing the molecule to adsorb on top of identical adsorption sites[108]. This is not the case on Au(111) and Ag(111) due to their larger lattice constant. A Cu(100) with a C_4 symmetry does not allow the three first ortho-fused benzene rings of a helicene being located above identical adsorption sites (Figure 11).

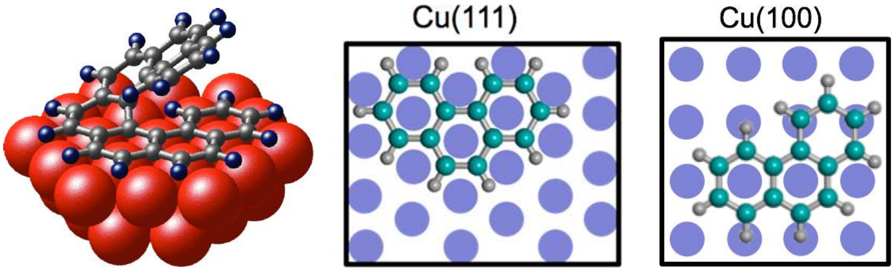

Figure 11: Schematic drawing of the molecular orientation of (*M)*-heptahelicene on the Cu(111) surface with the corresponding adsorption footprint of [7]H on Cu(111) as measured in ref.[107]. The expected adsorption footprint of the three lowest C_6 rings of [7]H on Cu(100) is displayed on the right (see refs. [107,109]).

On Cu(111), at low coverage, *rac*-[7]H forms heterochiral pairs as determined by STM manipulation[110]. Close to ML coverage, Ernst and co-workers observed the formation of non-superimposable mirror domains made of racemic rows composed of heterochiral dimers[7,111]. On Au(111) and Ag(111), similar heterochiral zigzag rows were observed with minor structural changes (orientation with respect to the substrate, spacing between the rows…) induced by the different lattice parameters of the metal substrates[112]. However, on Cu(100), with a completely different adsorption footprint, the assembly is different. At low coverage, homochiral quadruplets were observed, arranged in a conglomerate of homochiral domains at saturated ML coverage[113]. These studies allowed to demonstrate that the geometry of the surface is indeed important.

Enantiopure *M*-[7]H forms almost identical self-assemblies at ML coverage on Cu(111), Au(111) and Ag(111)[112,113]. The dense packing at full ML coverage is in all three cases responsible for the formation of an ordered motif made of lines of triangles. Each triangle consists of a triplet of molecules. Note that the stress induced by a larger lattice parameter of the substrate can reduce the stability of the self-assembly. For instance, on Au(111) at around 0.95 ML coverage, *M*-[7]H forms an ordered structure made of lines of small squares[112]. Each square is made of four molecules closely packed together due to the intermolecular interactions in the dense layer. Increasing coverage leads to the modification of the self-assembly: squares now coexist with triangles. At saturated ML coverage, squares are not observed anymore and the surface is fully covered with triangles. In both motifs, the molecules are positioned so that their three upper-most C_6 rings is in the center of a rectangle or of a triangle. In all cases, the squares and triangles are the result of dense packing. Note that the adsorption of enantiopure compounds often leads to enantiomorphism of the adsorbate lattice, i.e. the molecular lattice vectors have a tilt angle with respect to the substrate lattice vectors and this angle is the same in opposite directions for the opposite enantiomers[109].

Rac-dibenzopentahelicene (*rac*-dB[5]H) was investigated on Au(111)[114]. It is an isomer of [7]H which also has a helical shape but with a larger opening angle and a different footprint on surface. Only 50% of the surface was covered by an ordered structure at ML coverage. The molecules formed a conglomerate of homochiral 2D domains[114].

1.3.2 Excess experiments

A small chiral bias can induce a cooperative response leading to single enantiomorphism. This effect is either called sergeant-and-soldiers or majority-rule effect, depending on if the majority compound is chiral or not. It was first observed for polymers and was then observed in 2D for carboxylic acids and for helicenes. For *rac*-[7]H on Cu(111), Parschau and co-workers[115], used the "sergeant-and-soldiers" effect to show that the second layer formation gives rise to a transition from a 2D racemate (racemic zigzag rows) into a 3D racemate, where the layers are enantiomerically pure. In fact, at a certain coverage between 1 ML and 2 ML, a coexistence between second layer islands and diluted domains made of racemic zigzag rows in the first layer was observed. The second layer islands were, however, much larger than would be expected for this coverage. They explained this dilution by a higher nucleation temperature for the double layer phase with respect to the first layer and a transport of molecules from the first to the second layer. The mobility of the molecules being still high enough to allow them to travel over large distances and supporting both the growth of the homochiral second layer and the dilution in the 1st layer. At lower coverage, the 1st layer started to nucleate but the coverage was too low in the ML to give rise to the formation of well-ordered zigzag row domains. In order to determine the composition of the ML when two complete layers of *rac*-[7]H are crystallized, Parschau *et al.*[115] performed an excess experiment. By adding a small amount of *M*-[7]H to the racemic mixture, they demonstrated that the second layer is only made of *(P)*-[7]H, the majority enantiomer must therefore be in the first layer: the double layer is made of homochiral layers with alternating handedness.

1.3.3 Self-assembly of functionalized helicenes

Self-assembly of functionalized helicenes is important to understand how to tune the properties at the metal/organic interfaces for applications. Studies performed on helicenes functionalized with heteroatoms or polar groups deposited on metal single crystals will be briefly discussed.

Racemic 6,13-dicyanoheptahelicene spontaneously forms a conglomerate of homochiral domains on Cu(111)[116]. According to DFT, the intermolecular interactions which drive the self-assembly are hydrogen bonding and CN-CN dipolar interactions. At low coverage and on Cu(111), enantiopure 6,13-dicyanoheptahelicene forms chains which are linked by H-bonding at 90 K and which, upon the release of Cu adatoms at RT, form metal-coordinated chains[117]. In the H-bonded case, the opposite enantiomers lead to chains of inverted symmetry. However, organometallic chains are not chiral.

On Cu(100), *(M)*-5-amino[6]helicene forms duplets, triplets and squares[118]. These quadruplets completely cover the surface close to saturated coverage. For *rac*-5-amino[6]helicene, the same structures are observed at low coverage with additional heterochiral clusters and duplets with shorter intermolecular distances[119]. Close to saturated ML, *rac*-5-amino[6]helicene does not self-assemble, except for a few rows, embedded in the disordered structure[119]. On Au(111), at the liquid solid interface, *rac*-5-amino[6]H forms racemic polymorphs coexisting with a similar structure as the triangles made of three molecules observed for [7]H on Au(111)[120]. In vacuum, *(M)*-5-amino[6]H forms double rows[118]. C_6 rings-surface interaction dominates in the case of Cu(100) but the amino-surface interaction dominates on Au(111). In both cases no polar interactions mediated by hydrogen bonding was observed. The assembly was only driven by the maximization of vdW forces.

Racemic hexathia[11]heterohelicene on Au(111), forms a hexagonal lattice which is apparently made from a random distribution of (*P*)- and (*M*)- enantiomers[121–123]. On Au(110), the molecules form chains running along the high symmetry axes of the sample. Their chirality could not be determined except in multistep regions where the rows were homochiral.

Finally, racemic 7-bromopentahelicene was studied on Ag(001). No ordered-structure was observed, due to the limited mobility of the molecules on this surface[124].

1.4 Goals and outline

The influence of the metallic substrate geometry on the self-assembly of carbohelicenes, which in turn is dominated by vdW interactions, is on its way to become well understood. However, a lot of work needs still to be done to understand the effect of different intermolecular interactions on the self-assembly. This problem calls for the study of well-defined models which can be meticulously compared to each other to understand the influence of various functionalities on chiral recognition.

As discussed previously, *rac*-dB[7]H and *rac*-[7]H, two isomers with a different helix opening showed completely different structures on the surface. The study of *rac*-[5]H will be presented in the paragraph III.2. In the paragraph III.3, enantiopure *(M)*-aza[6]H will be studied at low coverage on Cu(100) and Au(111) which induce different adsorption footprints. The results will be compared to the one obtained on *(M)*-5-amino[6]helicene[118] on the same surfaces in order to determine the influence of different polar group on the outcome of the self-assembly.

In a second part, on-surface covalent chemistry will be performed with bromohelicenes. Because surfaces provide an up–down asymmetry, excluding certain symmetry elements, such as centers of inversion, they may induce stereochemical effects during chemical reactions of chiral molecules. Ullmann coupling, a successful reaction for the C–C coupling of organic molecules on surfaces, is the perfect candidate to verify this hypothesis. Ullmann coupling was not yet performed on chiral molecules and will be presented for *rac*-Br[4]H and *rac*-Br[7]H on copper and gold in the paragraph III.4. Thermally-induced decomposition of helicenes will also be studied in the paragraph III.5. This on-surface chemical reaction will be performed with various PAH on oxygen-reconstructed copper. The goal is to induce an autocatalytic decomposition using oxygen-free helicenes, a phenomenon which was until now only observed for oxygen-containing molecules.

III.2. Coverage-mediated chiral phase transition: pentahelicene on Cu(111)

The study of pentahelicene ($C_{22}H_{14}$, [5]H) was performed to observe the influence of the length of a helicene on the self-assembly. Due to its relatively low racemization barrier around room temperature (24.1 kcal/mol at 293 K[95]), [5]H can only be studied as a racemate (*rac*). Both enantiomers are illustrated in the Figure 9. The 2D crystallization of *rac*-[5]H was studied with STM on a face centered cubic (fcc) Cu(111) surface at about 50 K[xviii].

[xviii] Most of the results presented in this paragraph were published in ref. 67.

2.1 Low coverage

2.1.1 Dimer formation

The coverage has an important impact on the self-assembly. At low coverage (θ << 1 ML), single molecules as well as dimers were observed (Figure 12). The EHT calculations of the frontiers orbitals allow determining unambiguously the handedness of every molecule. The dimers are homochiral: they are made of two [5]H having the same handedness, rotated by 180° with respect to each other. It means that as soon as the molecules are close enough to each other, it is energetically better for the adsorbed molecules to form pairs. This tendency to form pairs was already observed in the case of [7]H[7]. Nevertheless, the [5]H form homochiral dimers whereas [7]H forms only heterochiral dimers[110]. R. Amemiya and co-workers[125] studied the non-covalent bonding interactions between helicenes in 3D. They observed that configurations of molecules with the same handedness form more stable complexes than pairs of enantiomeric helicenes. On Cu(111), this seems to be the same in 2D for the [5]H but not for the [7]H.

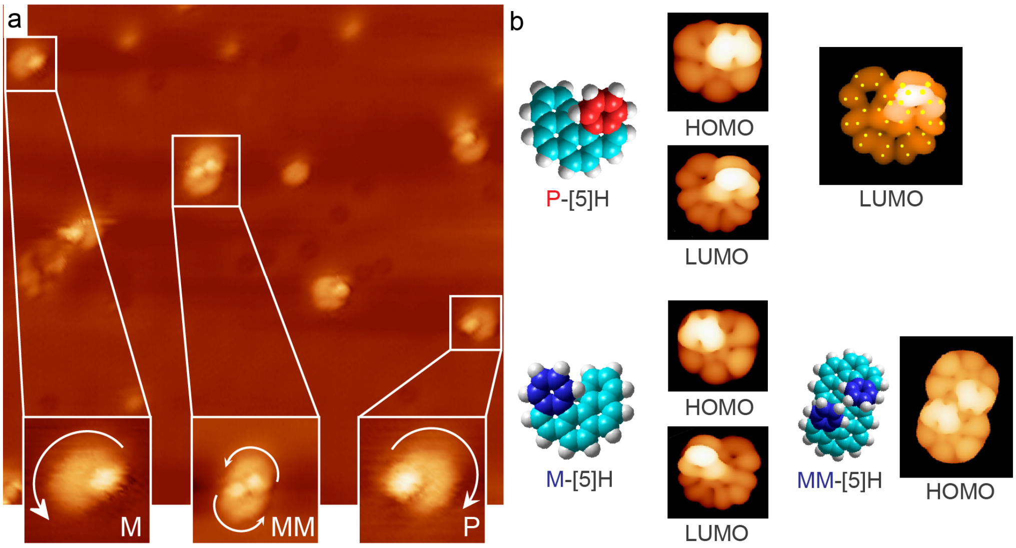

Figure 12: (a) Low-temperature STM image (15.3 nm × 15.3 nm, 89 mV, 40 pA) of [5]H on Cu(111) at low coverage (obtained by Dr. J. Seibel with a home-built LT-STM at 7 K). The insets (2 nm × 2 nm) display magnifications of a single *(M)*-[5]H molecule, a *(M,M)* homochiral dimer, i.e. made of two *(M)*-[5]H) and a single *(P)*-[5]H molecule. Circular arrows indicate the molecular handedness: they go from the bright uppermost part to the lowest part of the molecules. (b) Ball models of [5]H and corresponding electron density maps of the frontier orbitals (electron density: 0.0001 e/Å^3) calculated with EHT. Density maps of the HOMO (states 47-51) and LUMO (states 52-54) for a *(P)*-[5]H (top), a *(M)*-[5]H (bottom left) as well as a *(M,M)* dimer (bottom right) with their corresponding models are visible. In all cases, the molecules appear round with a brighter off-centered protrusion corresponding to their upper part as emphasized by the superposition of the atoms (in yellow) on the *(P)*-[5]H LUMO image in the top right corner. The Hückel calculations support the handedness assignment of the molecules in (a).

2.1.2 Modelling

To learn more about the interactions between two molecules in a dimer, MM was used (with AMBER and MM+ force fields which can both be used for [5]H, as justified in the paragraph II.4.3). Such force field calculations were already used with success for explaining self-assembly phenomena of helicenes on metal surfaces[7]. The helicenes were relaxed freely on the surface.

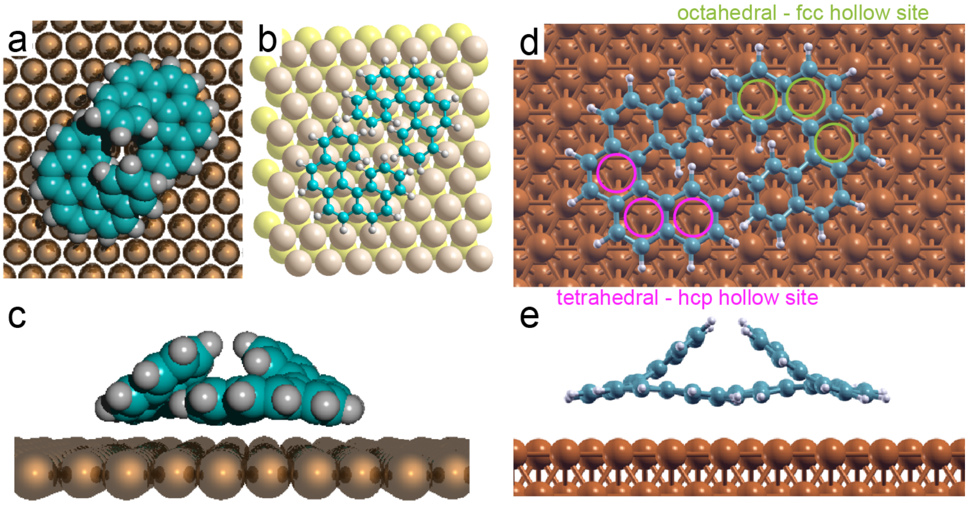

Figure 13: Molecular modelling of homochiral [5]H dimers on Cu(111). (a) Ball model of fully optimized lowest energy configuration resulting from AMBER force field calculations. (b) Ball-and-stick model of the dimer with the three lowest rings of both molecules located above different threefold hollow sites. (c) Side view on the optimized geometry of the AMBER force field calculations, showing that for both molecules, the three lowest rings are almost parallel to the surface. (d) Ball-and- stick model of the optimized dimer according to DFT calculations. The three lowest rings of both molecules are located above different threefold hollow sites. (e) Side view of a dimer, obtained from DFT: as for MM, the three lowest rings are almost parallel to the surface. The DFT calculations were performed by Dr. L. Zoppi.

The structure of the homochiral dimer at minimum energy (Figure 13a-c), obtained when two [5]H with the same handedness are deposited on the surface, reflects well the STM result presented in Figure 12. The attractive interaction energy between the two molecules is about 5.6 kcal/mol (AMBER, 5.7 kcal/mol with MM+). The value lies in the typical range of vdW interactions. The model indicates a partial overlap of upper and lower terminal rings of the two molecules in the dimer. The partial overlap of the terminal rings suggests π-π interactions as binding mechanism for the dimer. It is larger than calculated for π-π stacking interactions of benzene dimers (2-3 kcal/mol[126]), but here all four terminal rings of both molecules are involved in the interaction.

Similar evaluations were performed with DFT which was in this case very sensitive about local energy minima and depended strongly on the initial conditions before relaxation. The relaxed configuration (Figure 13d, e) was obtained only when the molecules were initially placed so close from each other that repulsion dominated, pushing both molecules apart until they reach this energy minimum. Starting with both molecules further apart, as for the force field approach, the optimization stopped with both molecules at a larger distance and with a lower intermolecular binding energy. The lowest-energy dimer arrangement is identical to the one found with the force field calculation. Both MM and DFT deliver an adsorption geometry such that 5[H] adsorbs with its three lowest rings more or less parallel to the surface (Figure 13c). It is the same adsorption footprint as found with XPD for heptahelicene by Fasel *et al.*[107] (Figure 11 and paragraph III.1.3.1). However, the surface binding sites resulting from the two modelling approaches are different. According to MM, the three low-lying C_6 rings are located above on-top sites. This is usually not the case for aromatic rings on Cu(111)[127–130]: they usually adsorb above a threefold hollow site. If the complete dimer is shifted such that the lowest rings are above three-fold hollow sites, the two molecules in the pair will be located on top of different hollow sites (Figure 13b). The lowest rings of one molecule are above tetrahedral coordination sites (hcp hollow sites) and the lowest rings of the other molecule are above octahedral coordination sites (fcc hollow sites). According to DFT, the two [5]H adsorb with their three lower benzene rings above surface hollow sites, again different for both molecules of a dimer, but both sites (hcp and fcc) have almost the same energy. The distance between the 2nd lowest ring plane and the perpendicular top most Cu atom of the surface is 3.1 Å in DFT for the monomer and for the dimer (3.07 Å with MM+ and 3.6 Å with AMBER). This distance is actually identical to the one determined for 5-aminohexahelicene on Cu(100)[118]. The DFT-derived intermolecular binding energy is 6.0 kcal/mol which is similar to the value obtained with MM.

The intermolecular interaction between [7]H molecules is different than the interaction between [5]H molecules. It was confirmed with MM (Figure 14) for the optimized heterochiral dimer of 7[H] that an attractive interaction of only 3.0 kcal/mol results. The two additional rings in the helical backbone of a single helicene modify the respective position of the terminal benzene rings. The repulsion between them is spread over different numbers of bonds, which has an influence on the interplanar angle of the molecule. This angle is equal to 48.9° for [5]H[131] and 30.7° for [7]H[91] (Figure 14 d). A large interplanar angle allows two [5]H to adsorb "face to face" (Figure 13 a), leading to attractive π-π interactions between their overlapping terminal ends. However, two [7]H can only interact from the side (Figure 14 c), weakening the vdW interaction between each other. [5]H acts like dB[5]H[114], which also formed homochiral dimers rotated by 180° with respect to each other due to their larger opening compared to [7]H.

The take home message of the comparison between DFT and MM is that, except for the adsorption site, the force field approach already confirms well the experimental observation of homochiral dimers formation. The exact binding site on the surface requires intense DFT calculations with many different initial conditions to identify the lowest energy configuration.

As a comparison with the homochiral dimer, a heterochiral *(P,M)* pair was optimized with MM (Figure 14a, b). The optimization gives rise to two different configurations and consequently two different interaction sites, equivalent in energy, with a binding interaction of 3.7 kcal/mol (AMBER). Therefore, the heterochiral dimer has a total energy higher than the homochiral dimer, i.e. it is less favorable.

DFT calculations can also give additional information concerning the charge distribution when one molecule or the dimer adsorbs on the surface. It this case, the Pauli repulsion between the molecule and the surface implies an important charge redistribution at the interface (Figure A. 1 in the appendix). Charge depletion is observed in the molecular region whereas the charge accumulates underneath and around the molecule. This effect is known as cushion effect[132–137]. The dipole moment of a single [5]H on the surface was found to be 4.5 D[xix]. It is 7.3 D for a dimer which is high: it is the magnitude range of the dipole created during the adsorption of alkali metal on metal surfaces[138–140].

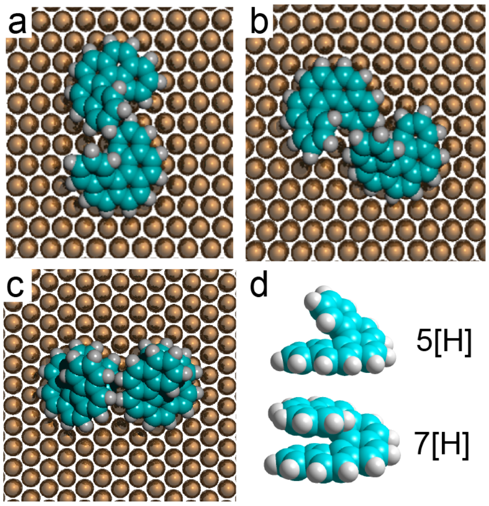

Figure 14: Molecular modelling of heterochiral [5]H and [7]H dimers on Cu(111). (a, b) Ball models of lowest-energy configurations of *(P,M)*-[5]H (AMBER force field). The two configurations are equivalent in energy. The binding interaction between the two heterochiral molecule is equal to 3.7 kcal/mol. It is much lower than the energy computed for a homochiral dimer (5.6 kcal/mol). (c) Ball model of the lowest-energy configuration of *(P,M)*-[7]H (AMBER force field). The binding interaction between two [7]H is only 3.0 kcal/mol in this case. (d) Side view of a [5]H and [7]H molecules, showing the interplanar angles between the terminal ends of each molecule.

In summary, *rac*-[5]H and *rac*-[7]H on Cu(111) adsorb with their three first C_6 rings parallel to the surface, as confirmed with theoretical modelling (Figure 11 and paragraph III.1.3.1). The surface-molecule interaction is consequently similar in both cases.

[xix] 1D = 3.34 × 10^{-30} C.m

2.2 Long-range ordered structures

2.2.1 Evolution of the self-assembly with the coverage

The formation of long-range ordered structures only starts close to ML coverage (Figure 15a). The relatively high mobility of the molecules, even at 50 K, does not allow the formation of self-assembly at a lower coverage. At θ = 0.97 ML (Figure 15a), a long-range ordered structure with a checkerboard pattern starts to form. The checkerboard completely fills the 1st layer (Figure 15b) at a coverage that we assigned as one ML (according to the definition of a ML in paragraph II.2). This coverage has indeed the highest observed lateral density in the first single layer. A structure with a honeycomb pattern appears and its proportion raises with the coverage until the complete disappearance of the checkerboard pattern in the 1st layer (Figure 15c, d). Exceptionally, a small patch of the honeycomb structure can be observed below ML (Figure 15a). However, usually, the honeycomb pattern is only seen above ML coverage.

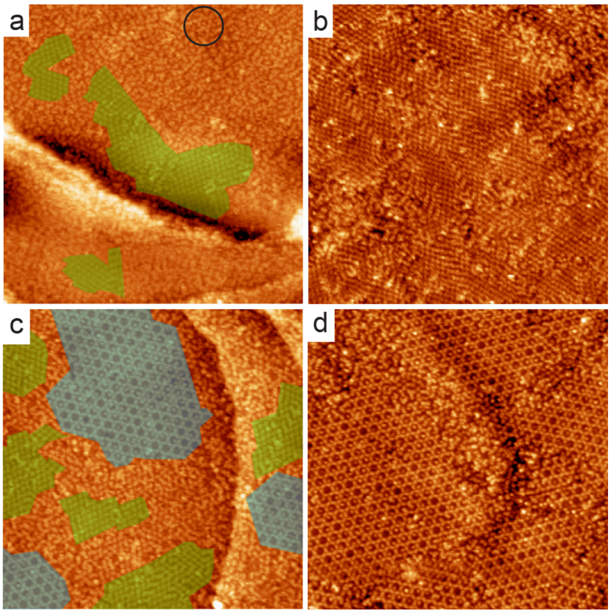

Figure 15: STM images (80 nm × 80 nm) of the 1st layer at different coverages. (a) θ = 0.97 ML: checkerboard domains are observed. A small patch of honeycomb domain is highlighted with a black circle (20 pA, 1.78 V) (b) θ = ML: only the checkerboard structure is present on the surface (20 pA, 2.27 V) (c) θ = 1.01 ML: both structures are observed (35 pA, 3.27 V) (d) At higher coverages (1.03 ML ≤ θ < 2.0 ML): only the honeycomb structure is observed in the 1st layer (20 pA, 2.84 V).

2.2.2 Characterization of the two long-range ordered structures

To explain the transition between both structures, the determination of the patterns composition is important (Figure 16). Identifying the handedness of the molecules is not as straightforward as at low coverage due to the interaction of adjacent molecules, which lowers corrugation and therefore STM contrast, but it is still possible. Ignoring the defects, the contrast of every molecule (bright off-centered protrusion and faint tail) allows to conclude that both long-range ordered structures are built-up by homochiral dimers (Figure 16).

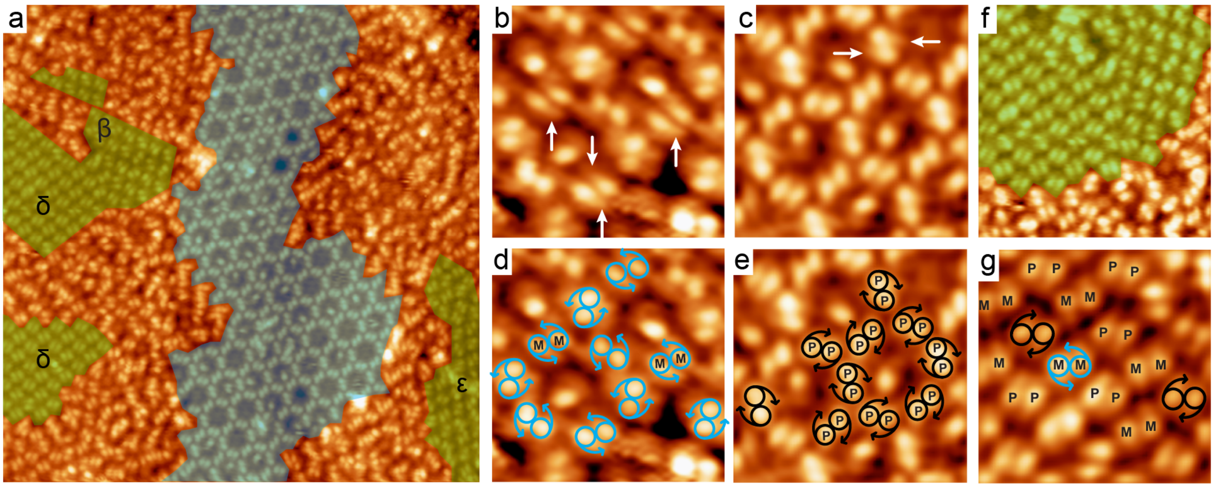

Figure 16: STM images of different ordered structures in the 1st ML of [5]H on Cu(111). (a) Long-range STM image ($\theta = 1.02$ ML, 50 nm × 50 nm, 35 pA, 2.50 V) showing the coexistence of the checkerboard (green) and honeycomb (blue) structures. β, δ and ε correspond to the three rotational domains of the checkerboard structure. (b, c) Magnified images of the two mirror domains of the honeycomb phase. Arrows indicate features corresponding to the lower part of a molecule near the bright protrusion (upper part of the molecule). (b: 5.8 nm× 5.8 nm, 95 pA, 1.12 V; c: 7.7 nm × 7.7 nm, 35 pA, 2.50 V). (d, e) Same STM images as (b, c) but with indications of the handedness of the molecules. Circles (blue for M, black for P) mark the bright protrusions and the associated curved arrows follow the lower molecular part spiraling down. Each domain of the honeycomb phase is homochiral. (f, g) Images of the checkerboard structure. (f) Within a single domain (green) two different apparent alignments of the dimers are observed (16.6 nm × 16.6 nm, 35 pA, 2.50 V). (g) Image (7.5 nm × 7.5 nm, 35 pA, 2.5 V) highlighting the composition of the checkerboard phase: a regular alternating arrangement of homochiral dimers with opposite handedness.

Checkerboard structure

The checkerboard structure (Figure 16f, g) is made of a succession of homochiral pairs with opposite handedness *(M,M)* and *(P,P)*: it is therefore a racemate. Three rotational domains (β, δ and ε in Figure 16a) are observed. They are explained by the symmetry of the Cu(111) surface. Indeed, the metal substrate acts as a grid which allows only certain molecular patterns and certain distances between the molecules. According to DFT (Figure 13b), each molecule in a dimer adsorbs only on one type of hollow sites (hcp for one of the molecule and fcc for the other molecule of the dimer), i.e. only half of the sites of the six-fold symmetric topmost Cu(111) layer are available. It leads to a three-fold symmetry. Accordingly, the racemic structure can only have three different orientations.

Honeycomb structure

The honeycomb structure forms mirror domains which are identified by α and $\overline{\alpha}$ in Figure 17. The matrix notations and associated parameters are displayed in Table 2. The mirror domains are rotated by the same angle in opposite directions with respect the $[1\bar{1}0]$ axis of the Cu lattice: respectively 14°±2° for the $\overline{\alpha}$ domain and −14°±2° for the α domain. Because both mirror domains are oriented parallel to the three-equivalent high-symmetry $[1\bar{1}0]$ axes of the copper surface and have a C_6 symmetry, a rotation of 60° applied to a mirror domain will leave it unchanged. It explains the absence of rotational domains for this structure.

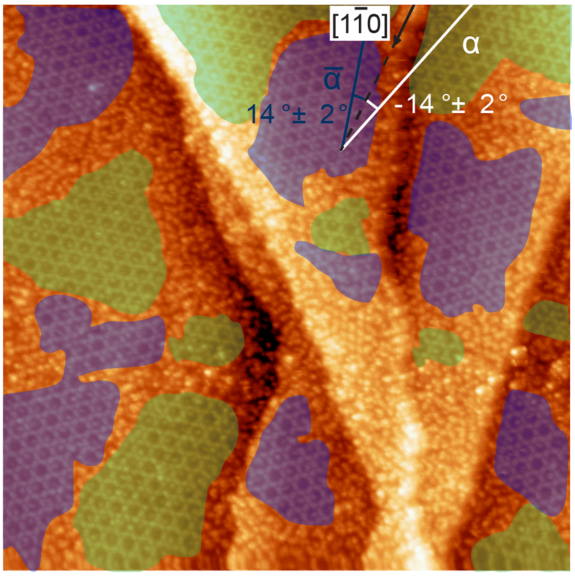

Figure 17: STM image of the honeycomb structure: α (green) and $\overline{\alpha}$ (blue) mirror domains and their respective angles with respect to the $[1\bar{1}0]$ direction of the Cu(111) surface. (100 nm × 100 nm, 20 pA, 2.05 V)

In both domains, a hexagon is made of six dimers having three distinct orientations (Figure 16b-e), which can once again be justified by the C_3 symmetry of the system. Nevertheless, mirror domains have opposite handedness: α domains are only made of *(M,M)* pairs (Figure 16b, d) whereas $\overline{\alpha}$ are only made of *(P,P)* dimers (Figure 16c, e). The honeycomb structure is therefore a conglomerate of homochiral domains.

Modelling

To model both structures, several parameters must be determined. At first, to express the position of the molecular lattice with respect to the copper lattice, the so-called matrix notation is determined based on the STM images of the substrate and of the molecular self-assembly[xx]. The matrix notation relates the molecular adlayer lattice vectors $\vec{a}$, vectors $\vec{b}$ and the substrate unit cell vectors vectors $\overrightarrow{a_s}$, $\overrightarrow{b_s}$ as follows:

[xx] Another way to define the relation between the adlayer and the substrate lattices (when they have common periodicity) is to express it as a function of the basis vectors' length and of the angle of rotation between the two lattices[263]. It is called the Wood notation[264]

$$\begin{pmatrix} a \\ b \end{pmatrix} = \begin{pmatrix} m_{11} & m_{12} \\ m_{21} & m_{22} \end{pmatrix} \times \begin{pmatrix} a_s \\ b_s \end{pmatrix} \tag{19}$$

The choice of the unit cells of substrate and molecular lattices is established by several detailed rules[141]. The different matrix notations of the two structures as well as number of molecules per unit cell and the occupied area per molecule are given in the Table 2. The matrix notation, the molecular models and the known chiral composition of each structure allow to model the two long-range ordered structures (Figure 18). In both cases, the models agree well with the STM images.

Structure	Chiral composition of a domain	Master matrix[141]	Molecules / unit cell	Occupied area / molecule [Å^2]
Honeycomb	homochiral	$\begin{pmatrix} 12 & -3 \\ 3 & 15 \end{pmatrix}$	6	177.4
Checkerboard	racemic	$\begin{pmatrix} 14 & 4 \\ -4 & 10 \end{pmatrix}$	4	123.9

Table 2: Structural parameters of the structures formed by *rac*-[5H] on Cu(111). The area per unit cell was calculated from the matrix notation.

The area per molecule (Table 2) for the honeycomb structure (177.4 Å^2) is higher than for the checkerboard structure (123.9 Å^2). A molecule is often observed in the middle of the pore of the honeycomb structure (Figure 16). Even when considering an additional molecule in every honeycomb pore, the area per molecule decreases only to 152.0 Å^2. It is not sufficient to counterbalance the fact that the racemic structure is denser than the conglomerate. This observation follows partly the empirical "Wallach's rule"[142] which states a higher density for racemic crystals than for their homochiral counterparts[143]. In the case of [5]H on Cu(111), when the coverage increases, the surface is indeed increasingly covered with the denser racemic structure. Nevertheless, this process is reversed with further deposition of molecules when the diluted conglomerate starts to form. It is an intriguing phenomenon since, as the racemic mixture is denser than the conglomerate, adding more molecules should give rise to a complete layer of the checkerboard structure. To explain it, one must have a closer look at the transition from the dense racemate to the less dense conglomerate. It is quite “fast” as the coexistence of both phases is observed only within a few percent excess above ML coverage. More importantly, the formation of the honeycomb phase occurs when the coverage is higher than a monolayer, i.e. only as the 2nd layer forms. The observed racemate–conglomerate transition must be therefore induced by the 2nd layer nucleation. In addition, when the 2nd layer starts to grow, a dilution in the 1st layer is observed (from dense racemate to less dense conglomerate): hence, there must be a transport of molecules from the 1st to the 2nd layer. A similar transport of molecules in a multilayer was already observed for [7]H (see paragraph III.1.3.2).

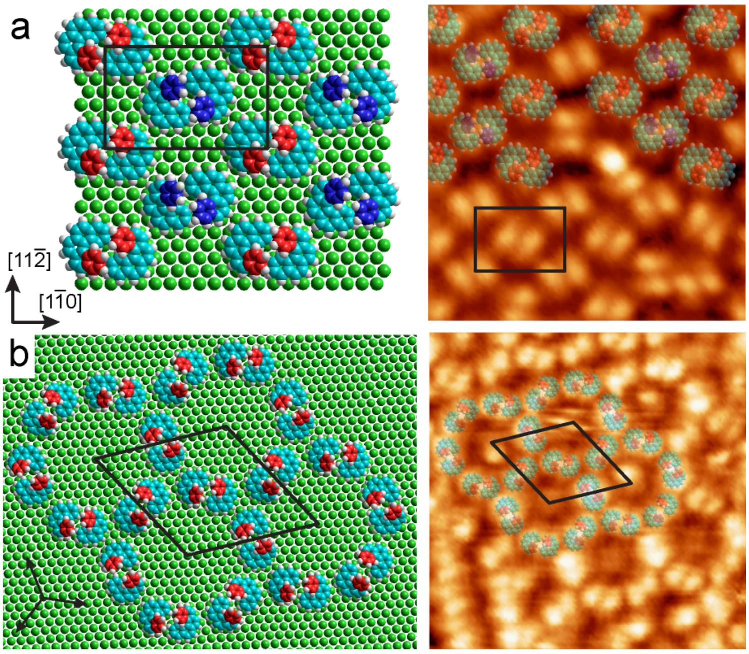

Figure 18: (a) Molecular model and superposition of the model on a STM image (9.5 nm × 9.5 nm, 35 pA, 2.50 V) for the checkerboard structure. The uppermost ring of the molecule is highlighted in red and blue for a *(P)*-[5]H and a *(M)*-[5]H, respectively. The high-symmetry directions of the Cu surface are indicated in the lower left corner and the molecular unit cell is indicated with a rectangle. The models for the two other rotational domains can be found in Figure A. 2 in the appendix. (b) Molecular model and superposition of the model on a STM image (8.5 nm × 8.5 nm, 30 pA, 2.30 V) for a *(P)*-[5]H domain of the honeycomb structure. The long axes of the dimers point into three symmetry-equivalent directions (indicated by three arrows with same origin). The molecular unit cell is indicated with a parallelogram. The model of the mirror domains is presented in the appendix in the Figure A. 3.

2.3 Heterochiral to homochiral transition in the 1st layer induced by 2nd layer nucleation

2.3.1 Second layer

By increasing the coverage ($\theta > 1$ ML), larger areas of the 2nd layer, covered with a new structure can be observed. Unfortunately, the STM resolution was not sufficient to allow determining the chiral configuration of the molecules in the second layer. However, a few observations could still be made. Firstly, this structure forms two mirror domains distinguishable by their orientations (Figure 19). Their tilt angle with respect to the [1$\bar{1}$0] substrate direction is, as observed for the 1st-layer honeycomb structure ±(14±2)°. Secondly, the periodicity of the 2nd layer is identical to the one of the honeycomb phase (hexagonal symmetry in Figure 20). The 2nd layer therefore seems to grow epitaxially on the 1st layer.

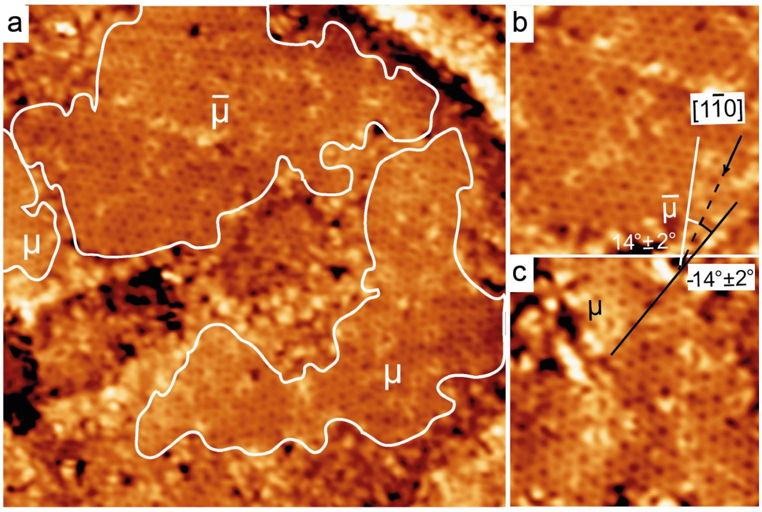

Figure 19: STM images of the 2nd layer. (a) For $\theta > 1$ ML, two mirror domains μ and $\bar{\mu}$ with different orientations are observed (100 nm × 100 nm, 20 pA, 4.00 V). (b, c) STM images of both mirror domains ($30 \times 30\ nm^2$, $I = 20$ pA, $U = 4.00$ V). Their relative alignment with respect to the $[1\bar{1}0]$ direction (dashed line and arrow) of the Cu(111) surface is indicated by white and black lines. The mirror domains are rotated by 14 ± 2° in opposite directions with respect to a high symmetry direction of the copper substrate.

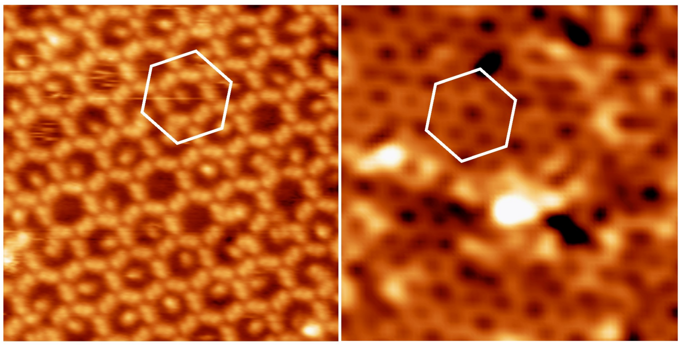

Figure 20: Comparison of equal-area-STM images of the honeycomb structure in the 1st layer (left) with a 2nd layer domain (right). In both images, the structures have the same periodicity, as indicated by the hexagons (left image: 21nm × 21 nm, 2.05 V, 20 pA, 1st layer $\theta = 1.03$ ML; right image: 21 nm × 21 nm, 4.00 V, 20 pA, 2nd layer $\theta = 1.7$ ML).

2.3.2 Origin of the transition: the homochiral double-layer nucleation mechanism

The transition from the dense racemate to the conglomerate can be explained using the above-mentioned observations. At low temperature (~50 K) and ML coverage (Figure 21a), the 1st layer is made of the dense racemic structure. In order to increase the coverage by a few percent above ML, i.e. to deposit more molecules, the sample is warmed up to room temperature (Figure 21b). After deposition, the sample is again cooled down to about 50 K: the STM shows a diluted 1st layer with honeycomb domains. The dilution is induced by a transport of molecules from the 1st into the 2nd layer (paragraph

2.2.2). The transport can only happen if the double layer phase nucleates before the 1st layer upon cooling, i.e. at higher temperature (Figure 21c). The transport creates locally an enantiomeric excess (*e.e.*) in the 1st layer which is required to explain the nucleation and further growth of the homochiral honeycomb structure (Figure 21c, d). This mechanism is supported by the epitaxial growth of the second layer on top of the first layer (Figure 20). In addition, homochiral nuclei are observed experimentally already at $\theta = 1.01$ (Figure 22). They are formed because locally, there is an *e.e.* and due to the lack of the other enantiomer, the racemic checkerboard phase in not viable for further growth. Thus, the homochiral dimers arrange into hexagons to optimize their energy by vdW inter-dimers interactions. The hexagons might serve as nuclei for the growth of the honeycomb phase.

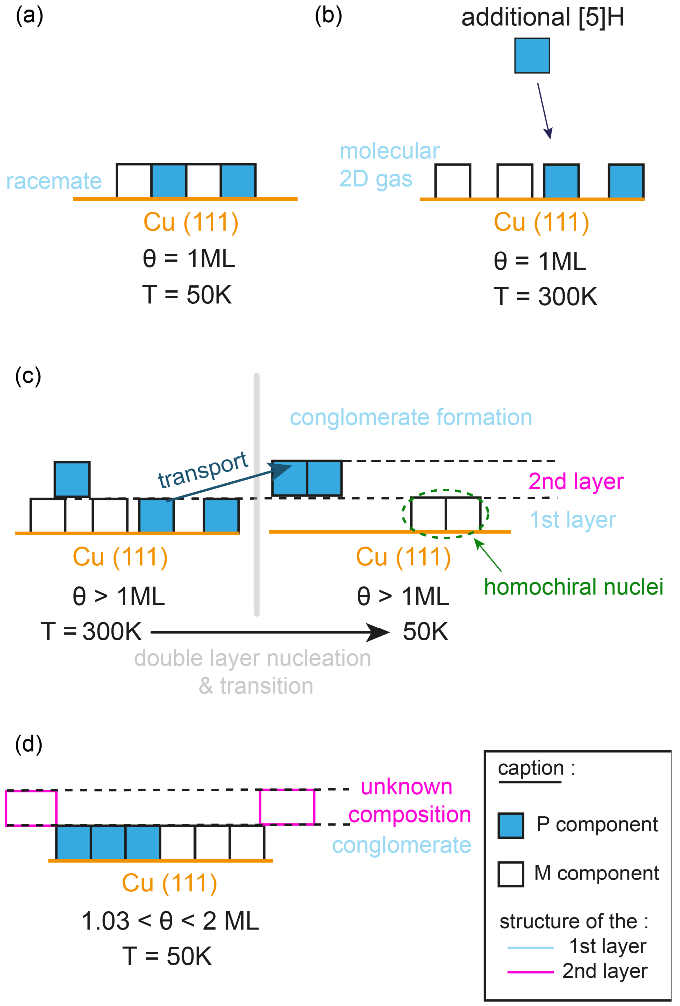

Figure 21: Sketch of the double-layer nucleation mechanism explaining the racemate-conglomerate transition. (a) At ML, coverage and low temperature, the 1st layer is made exclusively of the racemic checkerboard structure. (b) To add more molecule, the sample must be at room temperature, the molecules of the 1st layer are moving due to thermal agitation and form a 2D molecular gas. (c) At $\theta > 1$ ML, upon cooling, the homochiral double layer nucleates before the 1st layer inducing molecular dewetting. A local enantiomeric excess is created acting as a nucleus for the honeycomb phase growth. (d) At $\theta > 1.03$ ML, the 1st layer is made of a conglomerate of the homochiral honeycomb structure. The 2nd layer composition is unknown.

The kinetics plays an important role in this process. Because the 1st layer is overall racemic, the diffusion of the molecules must be limited. It allows the formation of homochiral nuclei which act as a chiral chemical potential and are the driving force for the transition from the racemate to conglomerate. In other words, it is an additional term of the free Gibbs energy which drives the transition due to enantioselective mass change in the 1st layer.

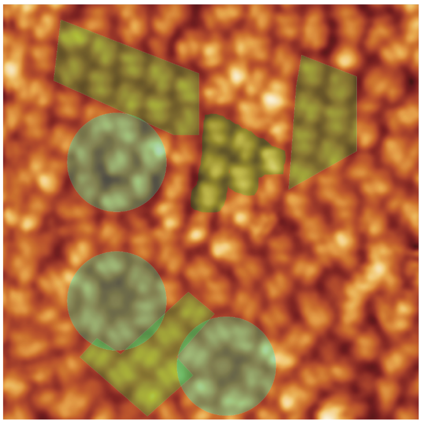

Figure 22: STM image of the initial stage of the transition from racemate to conglomerate induced by 2nd layer nucleation (θ = 1.01, 21.4nm × 21.4 nm, 1.90 V, 30 pA). The checkerboard structure domains are highlighted in green. Homochiral nuclei of the honeycomb phase are highlighted with blue filled circles.

Note that it is mandatory to have molecules in the disordered 2nd layer ($\theta > 1$ ML) to initiate double layer nucleation. As long as there are only molecules in the first layer, only first layer nucleation and growth occur. The lateral density of the conglomerate phase is only 70% of the racemate phase but at the nominal sub-monolayer coverage equivalent to the honeycomb phase ($\theta = 0.7$ ML), no ordered structures have been observed at all.

A similar process was already observed for [7]H on Cu(111)[115] (paragraph III.1.3.2): a chiral bias transformed the system from a 2D racemate into a 3D racemate, in which the structure in each layer was homochiral. In both cases, a molecular dewetting was observed. What is different in our case, is that a new structure, including a heterochiral – homochiral transition, appears in the 1st layer. On the contrary, for [7]H, the principle 1st layer's motif (heterochiral zigzag rows) is still observed until the 2nd layer completely forms. The change of chiral composition in the 1st layer was only revealed by excess experiments. The coexistence of racemate and conglomerate as well as the homochiral-racemic transition within the monolayer have been reported previously for prochiral molecules[144–146], chiral tartaric acid[147], and helicenes[120,148]. What is new in this case is the transition from racemate to conglomerate which is only induced by 2nd layer nucleation. In addition, there is no example of racemate crystals made by homochiral vdW dimers in 2D or in 3D.

2.4 Conclusion

On Cu(111), *rac*-[5]H forms completely different structures than *rac*-[7]H. At all coverages, the dimers formed by the molecules were homochiral for [5]H and heterochiral for [7]H. Even if the molecule-substrate interactions are the same in both cases, the addition of two ortho-fused benzene rings and subsequent modification of the interplanar angles of the molecules have a strong impact on the pairing of molecules at low coverage. It modifies the interaction site and weakens the attractive vdW interaction in a dimer, as confirmed by MM and DFT calculations. Considering that the helix interplanar angle is equal to 48.9° for [5]H[131] and 30.7° for [7]H[91] (Figure 14d), [4]H with an interplanar angle[91] of 26.7° should not be able to form homochiral dimers interacting face to face. It would be interesting to verify it experimentally. Different short-range structures have a huge impact on the self-assembly (Table 3) and results in the formation of completely different pattern close to ML coverage. Note that the geometries of the observed long- and short-range structures also showed a strong dependency on the Cu(111) surface symmetry.

Molecule	[7]H, $C_{30}H_{18}$	[5]H, $C_{22}H_{14}$
Ortho-fused benzene rings	7	5
Short-range structure	*(P,M)* dimers[7]	*(P,P)* or *(M,M)* dimers
Long-range structure	Racemic zigzag rows in mirror domains [7,111]	Racemate & conglomerate
Binding interaction dimer	3.0 kcal/mol	5.6 kcal/mol

Table 3 : Structural parameter of the two long-range ordered structures observed in the 1st layer of *rac*-[5]H on Cu(111)

For *rac*-[7]H[115], a chiral bias in a form of a small *e.e.* (addition of one of the enantiomer to the racemic mixture on surface), leads to single enantiomorphism in multilayered sample, i.e. to the presence of only one of the enantiomer in each layer. The majority enantiomer is only allowed to exist in the bottom layer. The top layer consists exclusively of the minority enantiomer. In the case of [5]H, the chiral bias is due to a kinetic effect. This is the addition of molecules above ML coverage and the transport of molecules from the 1st to the 2nd layer which create locally a small *e.e.*. Nevertheless, the diffusion of the molecules must be limited to allow the formation of homochiral nuclei. Because the first layer is overall racemic, a higher diffusion of the molecules would prevent the formation of homochiral nucleus which act as a chiral chemical potential and is the driving force for this transition from the racemate to conglomerate. Our results reveal that the majority rule effect, i.e. chiral amplification due to an enantiomeric excess is not only possible in 2D on surface but also in 3D (multilayers). A small excess in coverage is sufficient to completely change the first layer structure and therefore its properties. This observed new effect is promising for organic electronics: for example, to tune the molecular structure at electrode interfaces of devices. Functionalized pentahelicene should be investigated in the future because more and more helicenes-based applications use functionalized helicenes. For instance, aza[6]H or dicyano[5]H could be investigated to see the impact of polar interactions on the self-assembly and on the double layer nucleation and growth. On a more fundamental point of view, this work proved that STM can be successful to provide insights into fundamental processes of crystallization even though this technique is rather slow.

III.3. Influence of functionalization on the self-assembly of carbohelicenes: *(M)*-azahexahelicene

Enantiopure *(M)*-1-aza[6]H ($NC_{25}H_{15}$) was studied on Cu(100) and Au(111) to determine the influence of replacing a C atom by a N atom in the helicene backbone. In addition, various studies exist on non-functionalized-helicenes on different metal surfaces[7,67,111,113,115] but not so many about functionalized-carbohelicenes[118]. *(M)*-5-amino[6]H have already been studied by H. Ascolani *et al.*[118,119] on the same surface. The difference between an aza- or an amino-helicene is the position of the N atom (Figure 23). In the first case, the N atom replaces a C atom and in the second case, a H atom is replaced by a NH_2 group. Comparing the two molecules can therefore determine the impact on the intermolecular interactions of the presence of a N atom in the backbone or at the rim of a helicene.

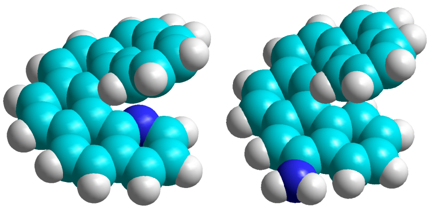

Figure 23: *(M)*-1-aza[6]H and *(M)*-5-amino[6]H

3.1 On Cu(100)

On Cu(100), single molecules and squares made of four molecules are observed at low coverage (Figure 24a). At higher coverage (0.5 ML < θ < 1 ML), the molecules are mostly disordered, but a few single and double rows of ordered molecules appear (Figure 24b). *(M)*-amino[6]H also formed squares at low coverage but duets and triplets were observed additionally[118]. Close to saturated coverage, the quadruplets completely cover the surface. At intermediate coverage (0.5 ML < θ < 0.9 ML), for both molecules, the formation of an ordered motif made of rows and double rows is observed. However, the composition of these rows cannot be compared because the resolution is not elevated enough in both cases. The formation of enantiopure squares was already observed for 0.95 ML coverage of enantiopure [7]H on Au(111)[112] and for *rac*-[7]H on Cu(100)[113] (paragraph III.1.3). In all the mentioned cases[112,113,118], the molecules are interacting with their upper part oriented toward the center of the square. It seems to be the case here too (Figure 24a, inset) because the brighter part each molecule is in the center of each square.

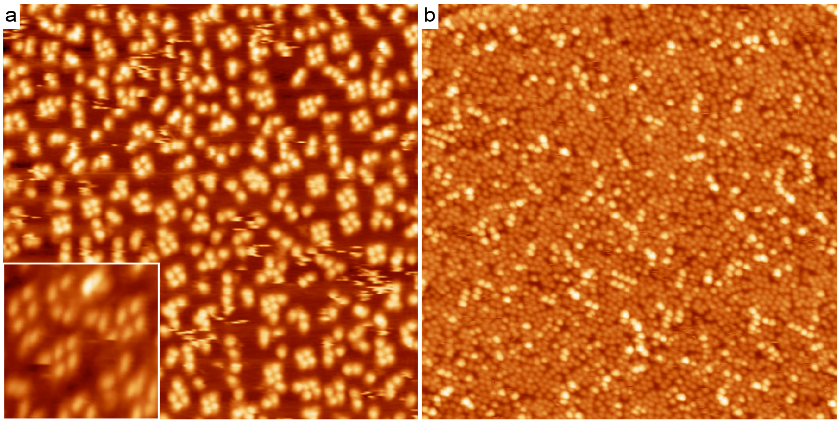

Figure 24: STM images of 1-aza[6]H on Cu(100) at different coverages. (a) At low coverage, the molecules are mostly isolated or arrange in squares made by four molecules. (b) At higher coverage (0.5 ML < θ < 0.9 ML), single row and double rows are observed among disordered molecules. (Measuring parameters: a: large image: 54.9 nm × 54.9 nm, –3.0 V, 30 pA; inset: 12.3 nm × 12.3 nm, –2.9 V, 25 pA, b: 87.9 nm × 87.9 nm, –2.9 V, 31 pA).

The addition of a N atom in the molecular backbone or at the molecular rim does not have much influence on the self-assembly on Cu(100), which are still dictated by vdW attractive interactions between the upper C_6 rings of the molecules. It should nevertheless be noted that for both 1-aza[6]H and 5-amino[6]H, the nitrogen atom is placed on the external part of a square and does not prevent the regular intermolecular interactions already observed for *rac*-[7]H on Cu(100)[113]. To determine if there is any difference between the two molecules above 0.9 ML coverage, the assembly at full ML should be investigated.

3.2 On Au(111)

On Au(111), the aza[6]H occupy at first the herringbones (Figure 25a). Close to ML coverage, more triangles made of three molecules are observed (Figure 25b). The more the coverage increases, the more these triplets arrange into ordered domains (Figure 25c). The structures observed for aza[6]H on Au(111) are completely different than the ones observed for amino[6]H on Au(111) (paragraph III.1.3)[118]. This might be induced by different intermolecular interactions. Note that for enantiopure [7]H on Au(111), the triplets are also observed[112]. They appear at a coverage of 0.98 ML, where they coexist with quadruplets until 1 ML coverage. At 1 ML, only triplets fill the surface. It means that the replacement of one C atom by a N atom in the molecular backbone at the position 1 (Figure 23) does not have much influence on the small-range ordered structures formed by the molecules. Once again, it has to be taken into account that according to a model of a triplet made by J. Seibel *et al.*[112], the molecules interact via their three upper-most C_6 rings and the position of the N atom is far away from the upper most ring. The replacement of a H atom at the rim by an amino group has however a strong influence both on the small-range ordered building-block and on the self- assembly on the Au(111) despite his position. This difference is noticeable only on Au(111) and not on Cu(100) probably because the molecular interactions with the surface are weaker on gold and the intermolecular interactions have therefore more impact on the self-assembly.

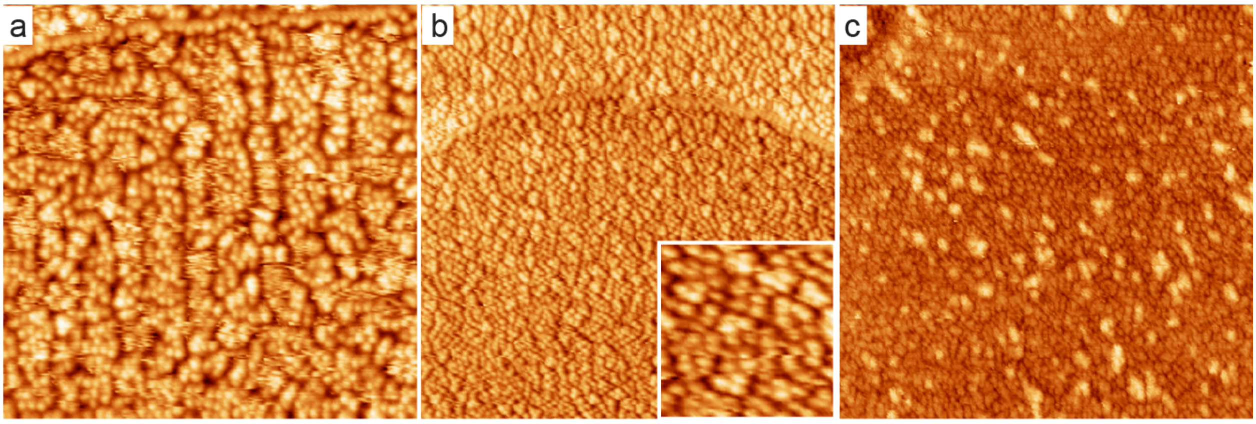

Figure 25: STM images of 1-aza[6]H on Au(111) just below ML coverage. The molecules aggregate first in the herringbones (a) and when the coverage is dense enough, they then form triangles made of three molecules (b). When the coverage increases, these triangles start to assemble into ordered domains (c). (Measuring parameters: a: 44.5 nm × 44.5 nm, 4.6 V, 25 pA; b: 74.1 nm × 74.1 nm (large) and 9.3 nm × 9.3 nm (inset), 3.1 V, 30 pA; c: 92.9 nm × 92.9 nm, 3.1 V, 30 pA).

3.3 Conclusion

In conclusion, on both Cu(100) and Au(111), the short-range ordered structures formed by *(M)*-1-aza[6]H and [7]H are similar. It suggests a small influence of the aza-moiety on the intermolecular interactions on both surfaces. Note that this result might be different if the N atom would be placed somewhere else on the molecular backbone. It would be for example interesting to place a N atom in the upper-most C_6 ring of an aza[6]H to verify if it has a stronger impact on the intermolecular interactions.

5-amino[6]H forms the same structures as 1-aza-[6]H and [7]H on Cu(100). However on Au(111), the replacement of a H atom at the rim by an amino group has, despite his position at the outer side of the molecule, a big impact on the small-range and large-range ordered structures' formation. This difference, observed on Au(111) and not on Cu(100), is probably induced by different intermolecular interactions due to the amino groups, which have more impact on gold due to the weaker surface-molecules interactions.

Note that pentahelicene can be only obtained as a racemate due to its low racemization barrier but it is not the case for hexahelicene. It makes them suitable candidate for a mixing experiment with racemic aza[6]H. Mixing experiments are promising because it gives insights into the chiral intermolecular recognition process and it involves cooperative effects. A chiral modifier can indeed involve a kind of "sergeant-and-soldiers" or "majority rule" effect on the surface[149,150] and induce homochirality for example.

III.4. On-surface Ullmann coupling of Br-helicenes: bishelicenes formation

In 2010, the Nobel Prize in Chemistry was awarded to Richard F. Heck, Ei-ichi Negishi and Akira Suzuki for palladium-catalyzed cross couplings in organic synthesis[151]. The principle of a transition metal-catalyzed cross-coupling reaction is the following: two molecules which are going to be coupled, attach to the metal catalyst via metal-carbon bonds (intermediate state). In a further step, they couple to one another by forming a carbon-carbon single bond[152]. The discovery of cross-couplings reactions between a nucleophilic compound (organometallic species for example) and an electrophilic organohalide (organic compound with a halogen atom bonded to a carbon atom) is of paramount importance because it is a new way of constructing molecules for chemists, by providing an efficient method for the formation of carbon-carbon bonds[153]. This led to the discovery of new cross-coupling reactions generating other bonds[154] (e.g. C-N,C-O,C-S, etc.)[xxi]. These reactions work with various catalysts such as Pd[153], Ni[153] or Cu[155]. Variations are based on the identity of the two reactants (which can be identical or not) and on the metal catalyst used.

[xxi] The interested reader can learn more about the history of this discovery in ref. [154].

Many decades after this discovery in solution, cross couplings are nowadays studied with success on surface because they can allow the bottom-up formation of tailor-made covalently bonded molecular networks[156,157] and subsequent functionalization of the surface, e.g. spintronics[158]. The covalent linking of two aryls via copper-catalyzed reaction is called Ullmann coupling. It was first shown to be successful on copper by Bent *et al.*[10,11] in the 90s and was then extended on various metal surfaces[29,159–161].

As surfaces provide an up–down asymmetry excluding certain symmetry elements such as centers of inversion, they might induce stereochemical effects during chemical reactions on chiral molecules. This hypothesis will be tested on the Ullmann-coupling of bromo-terminated carbohelicenes, which belong to both organohalides and aromatic hydrocarbons families. They are good candidates for Ullmann coupling reactions due to their relatively weak Br-C bond. To the best of our knowledge, Ullmann coupling was not yet performed on chiral molecules and will be presented for the first time in this work on different surfaces and with different molecules.

We therefore present the study of 9-Br[7]H on Au(111) and on Cu(111) and the study of 2-Br[4]H on Cu(100). These systems were chosen for multiple reasons. Firstly, the comparison between Br[7]H and Br[4]H can give information on the impact of three additional benzene rings on the coupling and on the possible induced stereochemical effects, e.g. different interplanar angles, inversion temperatures, intermolecular interactions. Secondly, the self-assembly of the on-surface reaction product, bis[7]H(surf), can be compared to the self-assembly of bis[7]H(sol) obtained by C-C coupling in solution. Finally, it is interesting to determine the influence of the metal catalyst (gold or copper) on the final and intermediate products of the coupling. Au(111), Cu(111), Cu(100) facets were chosen because it was already demonstrated in numerous studies, both theoretically[162] and experimentally[160,163], that these metals trigger the dehalogenation of hydrocarbons by lowering the energy barriers of the reaction and therefore decreasing the temperature at which it usually occurs. Au and Cu are some of the most studied substrates for on-surface Ullmann coupling[164]. It is already known that the first step of the reaction, namely dehalogenation, occurs below RT on Cu, leading to the formation of organometallic intermediate states (IS)[157,165,166]. On Au, dehalogenation occurs only at higher temperatures (above 393 K[167,168]) but the covalently linked structure is, in this case, directly obtained. No IS are observed except for a few exceptions[169], e.g. [168,170]. On Cu, extra-annealing is required to transform the organometallic IS into the final covalently bonded product[157,164,166].

4.1 Diastereoselective coupling of helicenes: bromotetrahelicene on Cu(100)

The Ullmann-coupling of racemic 2-bromotetrahelicene ($BrC_{18}H_{11}$, *rac*-2-Br[4]H) on Cu(100) was investigated[xxii]. The mechanism is presented in the Figure 26. 1.5 ML of Br[4]H was deposited on the Cu(100) surface cooled at 110 K. Annealing between 183 and 228 K leads to debromination as observed with XPS[50]. Further annealing to 463 K leads to Ullmann coupling and to the formation of 2,2'-bis[4]helicene (bis[4]H) as displayed in Figure 27 (STM images from the Specs Aarhus 150 STM, acquired at RT by Dr. J. Li and Dr. C. Wäckerlin).

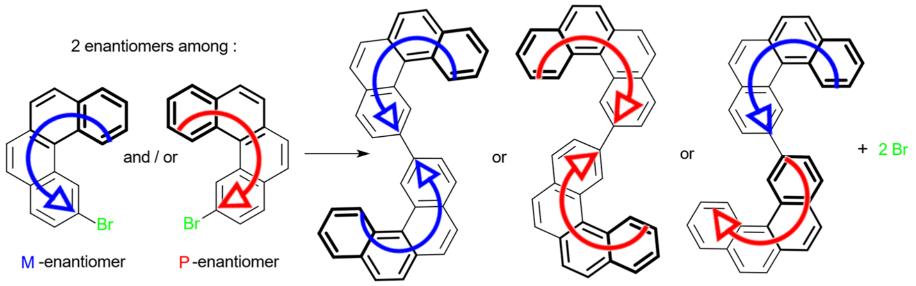

Figure 26: Scheme showing the Ullmann-coupling mechanism between two 2-Br[4]H. *P* and *M* enantiomers are depicted with a red and blue arrow respectively. The arrows go from the uppermost to the lowest rings of the helicenes. Six possible bis[7]H can be produced. Only the three trans-products of the coupling are presented here (from top to bottom: trans-*(M,M)*-2,2'-bis[4]H, trans-*(M,P)*-2,2'-bis[4]H and trans-*(P,P)*-2,2'-bis[4]H) but homochiral and heterochiral cis-configurations could perhaps be produced during the coupling.

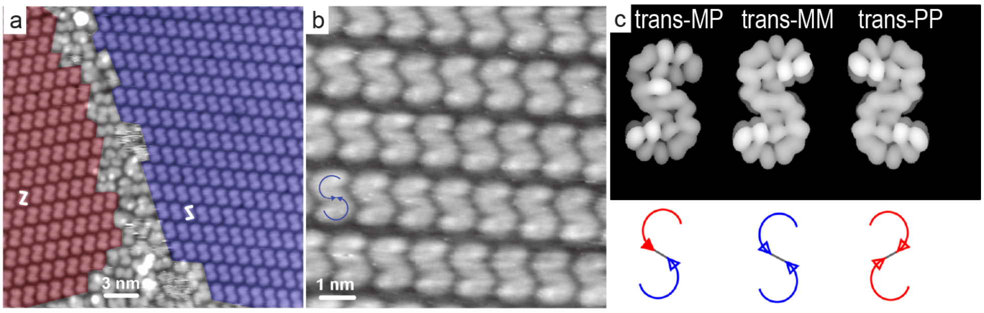

Figure 27: (a, b) STM images (a: 26.4 nm × 26.4 nm, 1.2 V, 30 pA; 8.8 nm × 8.8 nm, 1.8 V, 30 pA) obtained after annealing of Br[4]H on Cu(100) at 463 K. (a) Mirror domains made of lines of self-assembled bis[4]H : with recurrent Z motifs (red) or S motifs (blue). (b) Domains with the S motifs are made of trans-*(M,M)*-bis[4]H (see Figure 26) as confirmed by comparing the STM contrasts with the models (c). A blue arrow goes from a bright protrusion, corresponding to the uppermost part of a molecule, and follows the helix down. (c) Electron density maps of the frontier orbitals (levels 84-86 Ext. Hückel, LUMO, LUMO+3) for trans-*(M,P)*-2,2'-bis[4]H, trans-*(M,M)*-2,2'-bis[4]H and trans-*(P,P)*-2,2'-bis[4]H (from left to right) and their corresponding models.

The coupling produces two kinds of mirror domains (Figure 27a), which both have four rotational domains induced by the four-fold symmetry of Cu(100). Each domain is made exclusively of identical

---

[xxii] Most of the results presented in this paragraph were published in ref.50.

trans-building blocks with a Z- or S-motif. The absence of cis-molecules is probably due to the too strong steric repulsion that a molecule would feel between its terminal parts in a cis configuration. EHT models of the cis-bis[4]H and organometallic intermediates are given in Figure A. 12 in the appendix for comparison. Electron density maps of the three possible trans-bis[4]H products (presented in Figure 26) are displayed in the Figure 27 c. Among the three models, the trans-*(M,M)*-bis[4]H contrast corresponds perfectly to the molecular contrast of a S-motif (Figure 27b). The mirror domain with the Z-motifs, is therefore made of trans-*(P,P)*-bis[4]H (enantiomer of the trans-*(M,M)*-bis[4]H). No heterochiral dimers are formed: the surface induces diastereoselectivity.

Ullmann-coupling on Cu occurs via the formation of an organometallic intermediate bonded to a Cu adatom. Therefore, the bonding site, where the Cu is, stays close to the surface and the uppermost part of the molecule (at the opposite end of the Br atom) naturally spirals away. If the Ullmann-coupling is as random and efficient on-surface as in solution, the following ratio is expected: ¼ of *(P,P)*-bis[7]H, ¼ of *(M,M)*-bis[7]H and ½ of *(P,M)*-bis[7]H. However, when the C-C bond is finally formed, at higher temperature, the two helical parts of the molecule can easily invert due to the low inversion barrier of the [4]H (about 4 kcal/mol based on theoretical calculations[97]). Consequently, the homochiral configuration observed with the STM could eventually be formed during the cooling to room temperature. In other words, the stereoselectivity would be induced after the Ullmann coupling to form the most stable configuration on surface and avoid steric overcrowding. This will be tested in the paragraph III.4.2.3 by performing Ullmann-coupling on larger helicenes which have a higher inversion barrier such as Br[7][96].

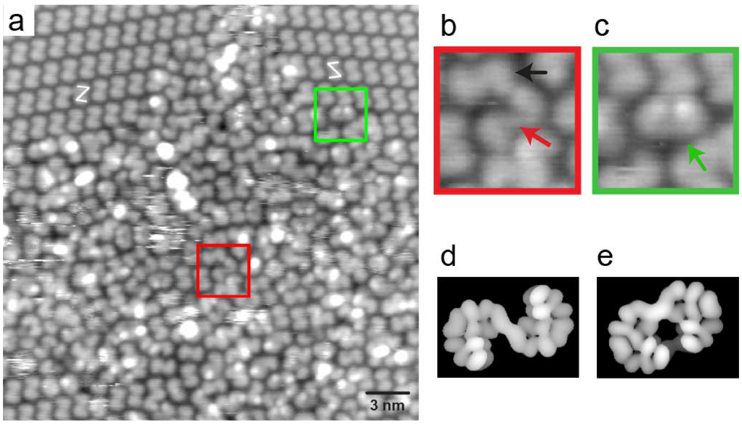

Figure 28: (a) STM image (a: 30 nm × 30nm, 1.2 V, 30 pA) obtained after annealing of Br[4]H on Cu(100) at 463 K. Ordered areas made of trans-homochiral-bis[4]H-(b, black arrow) as well as disordered areas are visible. Longer trans- (b, red arrow) and cis- (c, green arrow) species are often observed. Their corresponding organometallic models (levels 90-92 Ext. Hückel: LUMO- LUMO+3) are displayed in (d) and (e) respectively.

In addition to the ordered areas presented in Figure 27, about 40% of the surface is covered with disordered areas (Figure 28). Among the molecules that could be identified, a large fraction appears as trans-homochiral-bis[4]H. A significant portion of longer dimers in cis and trans configurations are also observed. The molecular lengths were measured at half-height intensity on images having stable and identical imaging conditions. The apparent length of trans-*(M,M)*- and trans-*(P,P)*-bis[4]H observed in the self-assembly is 14.6 ± 0.4 Å. The lengths of the longer trans (Figure 28b, red arrow) and cis molecules (Figure 28c, green arrow) are 17.0 ±0.3 Å and 16.2 ±0.4 Å respectively. These lengths were compared with the lengths of molecules optimized with AMBER force-field simulations (Table 4). The difference between the regular trans-*(M,M)*-bis[4]H (Figure 28b, black arrow) and the longer trans-species (shown in Figure 28b, c) corresponds to the difference which was calculated between trans-bis[4]H with and without Cu. In addition, the long cis species were observed with STM to be longer than the regular trans-bis[4]H whereas the calculated cis-bis[4]H is shorter than the regular trans-bis[4]H. It means that the long cis-species do not correspond to cis-bis[4]H. The long cis- and trans-species are therefore organometallic. The extended Hückel models for the cis- and trans-organometallic species are displayed in Figure 28 as a confirmation. Their contrasts correspond to the STM images.

Organic species	**Length (Å)**	**Organometallic species**	**Length (Å)**
trans-*(M,M)*	13.7	trans-*(M,M)*-Cu-dimer	15.8
trans-*(M,P)*	13.7	trans-*(M,P)*-Cu-dimer	15.7
cis-*(M,M)*	11.4	cis-*(M,M)*-Cu-dimer	13.6
cis-*(M,P)*	11.3	cis-*(M,P)*-Cu-dimer	13.7

Table 4: Comparison between the theoretical (molecular mechanics) lengths of organometallic and organic bis[4]H that could be formed during Ullmann-coupling. The length measured between the two opposite C atoms on the longest direction of a molecule.

In conclusion, bis[4]H was successfully synthetized on Cu(100) via on-surface Ullmann-reaction of *rac*-Br[4]H. The formation of disordered areas with organometallic intermediates was also observed as often reported in the literature[166]. Diastereoselectivity was observed in the coupling's products. It is not clear whether this specificity occurs during or after the coupling due to the low inversion barrier of the molecules. It will be tested with longer helicenes having larger inversion barrier.

4.2 On-surface coupling of Br-heptahelicene

4.2.1 Self-assembly of rac-bis[7]H (sol)

Bisheptahelicene (bis[7]H, $C_{60}H_{34}$) was studied with STM at 50 K on Cu(111) and Au(111). On copper, an extra annealing at 383 K was required to help the molecules to diffuse and self-assemble. The powder of bis[7]H was synthetized in solution (prior to sublimation on the surface) using a mixture of *rac*-9-bromoheptahelicene. The coupling reaction resulted in a mixture of the chiral *(P,P)*-and *(M,M)*-

9,9'-bisheptahelicene and of the meso isomer *(M,P)*-9,9'-bisheptahelicene. As the Negishi coupling between two bromoheptahelicene is random and efficient, the following ratio is expected: ¼ of *(P,P)*-bis[7]H, ¼ of *(M,M)*-bis[7]H and ½ of *(P,M)*-bis[7]H and was confirmed by NMR.

The study of *rac*-bis[7]H was performed on both Au(111) and Cu(111) to analyze the self-assembly differences on those surfaces. In addition, they serve as reference for comparison with the bis[7]H formed vis on-surface Ullmann coupling of Br[7]H which will be reported later in paragraphs III.4.2.2 and III.4.2.3. In order to determine the handedness of the bis[7]H on the STM images, the molecules were modeled using MM and EHT. The associated electron density maps of the frontiers orbitals (electron density cutoff: 0.0004 e/Å^3) for all possible bis[7]H configurations, are presented in Figure A. 4. They were chosen depending on the polarity of the bias voltage in the corresponding STM image[xxiii].

a. Self-assembly on Cu(111)

The STM images on Cu(111) were acquired by Dr. M. Parschau. The STM measurements show the presence of two distinct structures coexisting on surface (Figure 29).

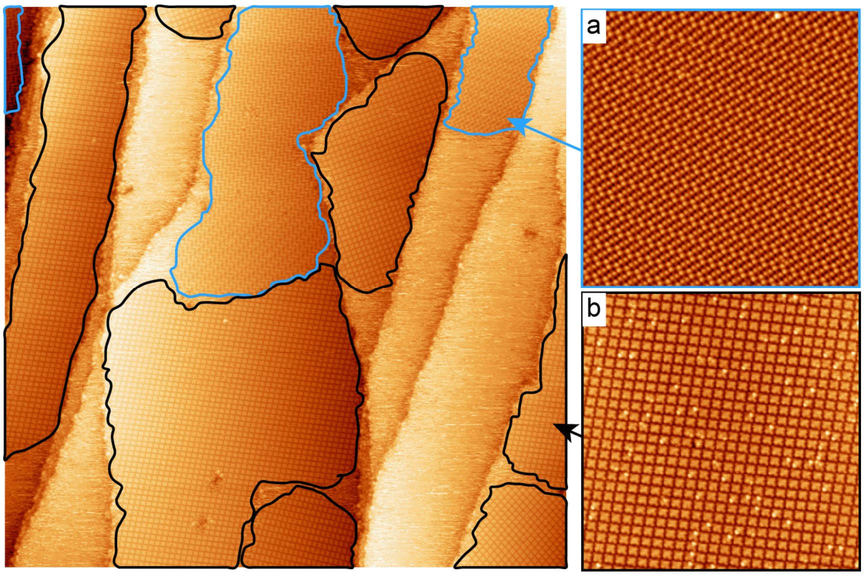

Figure 29: Large scale STM image (200 nm×200 nm, 29 pA, 1.58 V) of bis7[H]on Cu(111) below monolayer (ML) coverage. Rotational and mirror domains of two different structures are observed. One has a zigzag motif (blue domains) and the other is made of parallelograms (black domains). Large images (50nm×50nm) integrally covered with these structures are displayed in the insets: (a) zigzag structure (20 pA, 2.14 V), (b) parallelogram structure (21 pA, 2. 18 V). Non-ordered areas are also observed: the too high molecular mobility and the too small coverage prevent the formation of ordered structures.

[xxiii] For instance, applying a positive bias on the sample with respect to the tip implies that the unoccupied states of the sample close to the Fermi level (LUMO) contribute the most to the STM image's contrasts.

Zigzag structure

The first structure has a zigzag shape (Figure 30). Its unit cell (master matrix: (8,1;2,14))[xxiv], is made of two molecules which are rotated by 90° with respect to each other. The contrasts of the molecules in the Figure 30 allow to identify this structure as a racemate made of a succession of *(M,M)*-bis[7]H and *(P,P)*-bis[7]H. Both *(M,M)*-9,9'-bis[7]H[xxv] (resp. *(P,P)*-9,9'-bis[7]H) and *(M,M)*-10,10'-bis[7]H (resp. *(P,P)*-10,10'-bis[7]H) contrasts could correspond to the STM contrasts (see EHT models in the Figure A. 4 in the appendix). Molecular mechanics calculations suggest that the 9,9' configuration is the most energetically favorable. It is therefore the one used for the models. Rotational and mirror domains are presented in the Figure A. 11.

The three-lobes contrast observed for each of the two identical parts of a *(M,M)*-bis[7]H (resp. *(P,P)*-bis[7]H) corresponds to the contrast observed in the literature for the self-assembly of *(M)*-[7]H (resp. *(P)*-[7]H)[115]. A closer look at the Figure 30 reveals the presence of an additional lobe at each extremity of the *(M,M)*-bis[7]H (see the white squares). This lobe does not correspond to atoms in a bis[7]H. It can be excluded by comparing the lengths of the molecule with and without this fourth lobe with the theoretical length of a *(M,M)*-bis[7]H (Table 5). Moreover, with only three lobes, both *(P,P)*-and *(M,M)*-bishelicenes show approximately the same length on the STM pictures (about 1.7 nm). The extra lobe might therefore be due to an adatom or to electron transfer between the molecules.

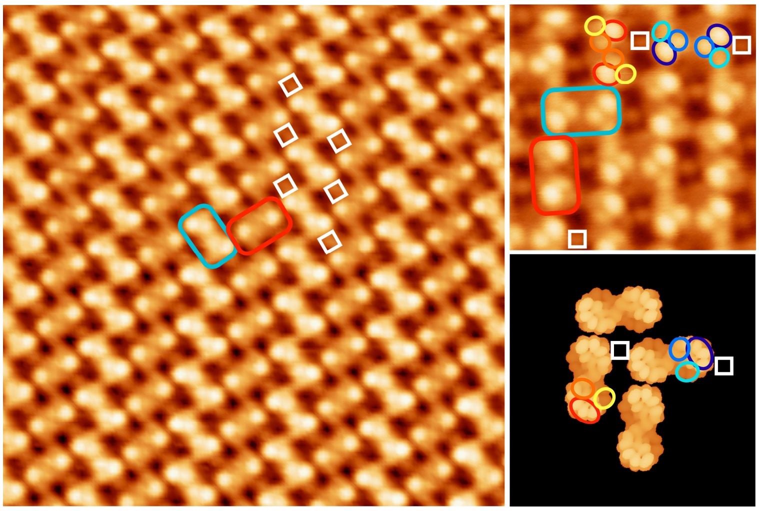

Figure 30: STM image (16.8 nm × 16.8 nm, 1.93 V, 31 pA) showing the zigzag structure made of a succession of rows built with molecules having the same orientation. One row is made of molecules which are rotated by 90° with respect to the adjacent row. On the top right corner, another STM image (6.5 nm × 6.5 nm, 2.09 V, 91 pA, rotational domain of the left image) allows to determine the handedness of the bis[7]H. Each molecule (for example in the red

---

[xxiv] Matrix notation as defined by L. Merz et al. in ref. [141].

[xxv] The notation 9,9' refers to the position of the C-C bond between the two de-brominated [7]H parts of a bis[7]H. It is defined by counting the H atoms until the C-C bond, along the helical backbone, from top to bottom. On surface, a *(M,M)*-9,10'-bis[7]H means that a C-C bond is formed between the 9th position of one [7]H and the 10th position of the other [7]H part of a bis[7]H.

or blue rectangle) is made of two identical parts with three lobes, rotated by 180°. They are therefore homochiral. By following the lobes on one side of the molecule, from the darkest to the brightest, one can see that the molecules in the red and blue rectangles have an opposite handedness (*(P,P)* and *(M,M)* respectively). This structure is therefore a racemate made of homochiral [7]H-dimers. In between each *(P,P)* and *(M,M)*-9,9′-bis[7]H, there is always a round lobe (white squares). The EHT models (states 138-142 Ext. Hückel, LUMO to LUMO+4) are displayed in the bottom right corner and their contrasts are compared to the ones in the STM images using red and blue circles for the *(P,P)* and *(M,M)*-9,9′-bis[7]H respectively. These models were arranged based on the contrasts observed in the STM images.

The substrate used in this experiment is Cu(111) which has a 2D gas of copper adatoms on its surface. These adatoms come from the kinks and their density therefore depends on their detachment-attachment rate to the kinks (influenced by the temperature), on the number of kinks on the surface, on the energy barrier of detachment and on the diffusion[171]. The molecules were evaporated on a Cu(111) surface at RT which was annealed to 383 K to help the assembly formation. Adatoms are present in the surface at these two temperatures. Nevertheless, according to the literature, the formation of organometallic compounds is very unlikely at this temperature because the dehydrogenation temperature of organic compounds is higher than 383 K on copper. The dehydrogenation of the hydrogen at the periphery of pyrphirin occurs for instance at only 523 K on Cu(111)[172]. The dehydrogenation temperature depends on the molecular conformation, i.e. the respective position of the hydrogen with respect to each other or to the surface. Note that when the conformation of the C-H bond is non-sterically favorable, partial dehydrogenation can be observed at lower temperature than expected for complete dehydrogenation. It is the case for tetraphenylporphyrin on Cu(111) where partial dehydrogenation (from two adjacent hydrogen leading to the formation of a C-C bond) occurs at 543 K and the complete dehydrogenation occurs at 693 K[173,174]. It occurs partially around 473 K for a type of cyclic polyphenylene called cyclohexa-o-p-o-p-o-p-phenylene[175] with non-sterically favorable hydrogen atoms. However, the reported temperatures for partial dehydrogenation are still higher than the 383 K used for annealing in the present study. The extra lobe might therefore be due to an electronic effect in the substrate.

	Experimental Length (Å)	**Theoretical Length (Å)**
(M,M)-bis[7]H	18.5	18.3
	28.9 (four lobes)	
(P,P)-bis[7]H	16.8	18.7

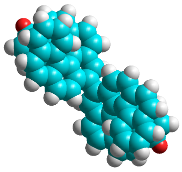

Table 5: Comparison between the experimental and theoretical (molecular mechanics) of the molecules. For the experimental values, the length is measured along the long axis of the molecule, i.e. in the parallel direction to the long axis of the blue or red rectangle in the Figure 30. For the *(M,M)*-bis[7]H, the 'four lobes' value corresponds to the length when the extra lobe (see white squares in Figure 30) is included. The theoretical lengths are measured along the longest axis of the molecules between the two most outer hydrogen (highlighted in red on the *(M,M)*-bis[7]H model on the right side of the table).

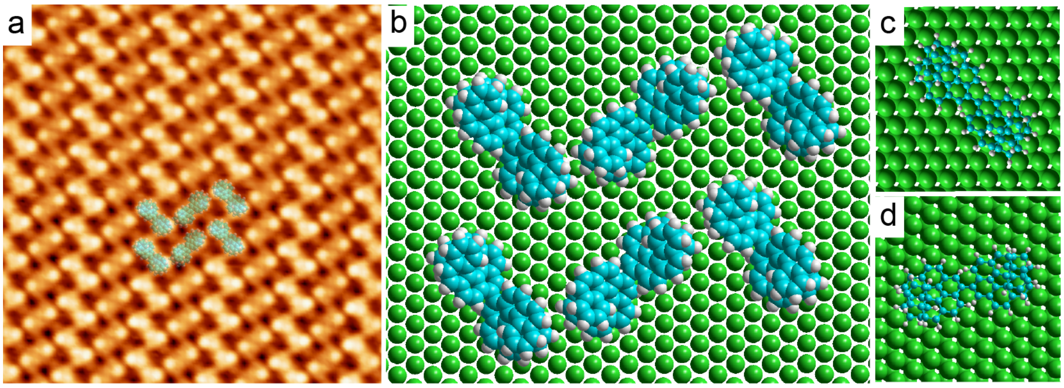

Figure 31: (a) Superposition of the molecular model (b) and an STM image (16.8 nm × 16.8 nm, 1.93 V, 31 pA) of the zigzag structure. (b) Molecular model (matrix notation: 7, –1; 5, 15), manually made based on the STM images of the surface, of the self-assembled *(M,M)*-and *(P,P)*-bis[7]H and on the best optimized configuration of a homo-bis[7]H on Cu(111). (c, d) Minimum energy configuration of a *(P,P)*-bis[7]H (c) and *(M,M)*-bis[7]H (d) calculated with molecular mechanics (AMBER-force field). The optimized configuration are in both cases computed on 9,9'-bis[7]H over 420 initial conditions (different x, y, z positions and angle of the molecule with respect to the surface). The calculations were performed under periodic boundary conditions, on a four-layers Cu(111) slab. The molecule could relax unconstrained on the surface.

A model of the structure (Figure 31) was realized based on the unit cell of the zigzag structure, the Cu(111) orientation (Figure A. 6) and the adsorption footprint of the lowest-energy homochiral bis[7]H computed with MM. The model is in good agreement with the STM images. Two features are noticeable. Firstly, there is a difference in brightness (Figure 31 a) between the lines of molecules with opposite handedness. Secondly, there is a quite large distance between two consecutive zigzag rows. The presence of an adatom discussed previously is unlikely: the self-assembly of bis[7]H on Au(111) at room temperature, without annealing, also displays the same features (

and Figure 41). A possible explanation for these two features could be a mismatch between the substrate and the assembly (Figure A. 8) or by dipole-dipole interactions which depend strongly on the orientation of the dipoles with respect to each other [176]. The dipole moment for [5]H was for example calculated with DFT to be 4.5 D for a single molecule and 7.3 D for a dimer (paragraph III.2.1). The dipole moment for a single bis[7]H might be even higher and dipolar interactions could therefore rule out CH-CH or CH-π intermolecular interactions as was already observed in ref.[177].

Mirror domains of the zigzag structure are observed in the Figure 32 and in a larger scale in Figure A. 10. Due to the C_2 symmetry of the structure associated to the C_6 symmetry of the surface, three rotational domains for each mirror domain are present on the surface.

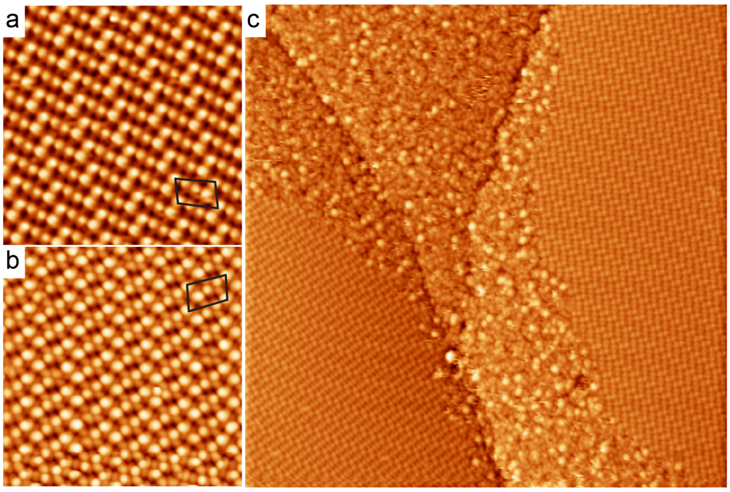

Figure 32: (a, b) Mirror domains of the zigzag structure (top: 20 nm × 20 nm, 2.14 V, 20 pA; bottom: 20 nm × 20 nm, 1.98 V, 34 pA). The unit cells are highlighted in black. (c) Rotational domains of the zigzag structure observed below monolayer coverage (100 nm × 100 nm, 2.14 V, 24 pA).

Parallelogram structure

In order to determine the composition of a parallelogram which is the building block of the second long-range ordered structure, a few molecules were evaporated on the surface at 40 K. Unfortunately, only single molecules were observed. After annealing at RT, clusters made of two molecules (parallelograms with a C_2 symmetry, Figure 33b, c) and three molecules (C_3 symmetry, Figure 33d, e) formed. Lateral manipulation[xxvi] was carried out on a parallelogram. It resulted in the separation of this structure into two molecules (Figure 34). Both molecules are identical but rotated by 180° with respect to each other in the parallelogram motif. Each molecule is made of two lobes with non-symmetric contrasts which are only observed for heterochiral bis[7]H as shown with EHT simulations (Figure A. 4).

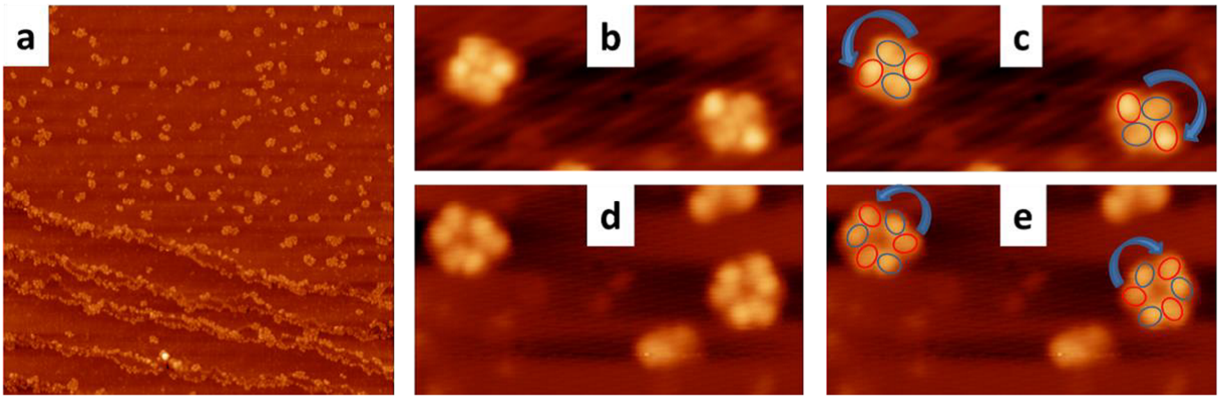

Figure 33: (a) STM image (137 nm × 137 nm, 1.29 V, 59 pA) showing a large area of Cu(111) with decorated steps and clusters of bis[7]H. (b) (12.5 nm × 5.4 nm, 1.29 V, 59 pA) and (d) (16 nm × 8.7 nm, 1.51 V, 64 pA) show respectively the clusters made of four and six lobes. In both cases, brighter and darker lobes can be distinguished: blue and red

---

[xxvi] The tip was placed on top of one of the molecules (starting point) and brought really close to the surface. Constant tunneling current and bias voltage were maintained in order to laterally move the molecule away from the other molecules.

circles are used to identify them in the images (c) and (e). Blue arrows follow the lobes of the clusters arranged in both clockwise and anticlockwise directions. Single molecules imaging and manipulation were performed by Dr. J. Seibel on a home-built, LT-STM at 10 K.

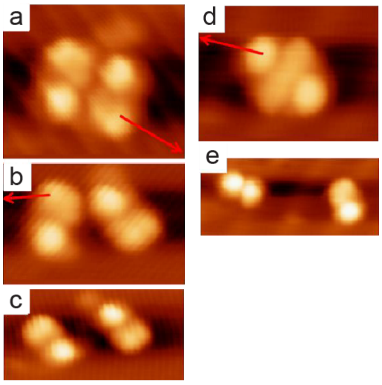

Figure 34: STM images showing the lateral manipulation of the molecules in a parallelogram (a-c and d-e). Red arrows indicate the initial position and movement direction of the tip during the manipulation. (Measuring parameters: a: 4.6 nm × 3.9 nm, b: 5.2 nm × 3.4 nm, c: 7.1 nm × 3.6 nm, d: 5.3 nm × 3.9 nm, e: 78.6 nm × 3.7 nm, 1.51 V, 220 pA. Single molecules manipulation was performed by Dr. J. Seibel on a home-built, LT-STM at 10 K.

Observation of the self-assembly and EHT simulations confirm the heterochiral identification (Figure 35). Each parallelogram in an ordered domain is composed of two *(M,P)*-bis[7]H rotated by 180° with respect to each other. *(P,M)* and *(M,P)*-bis[7]H are arranged into distinct mirror domains. Other EHT trials are presented in the appendix (Figure A. 5). The master-matrix characterizing the structure is (7,–1; 5,9).

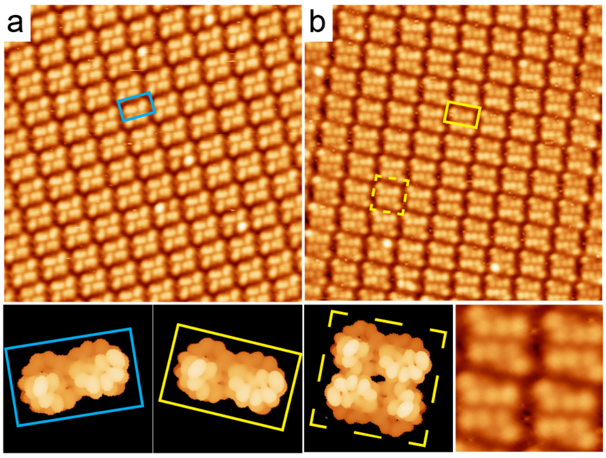

Figure 35: Top: STM images (20 nm × 20 nm) of mirror domains of the parallelogram structure: (a: 1.78 V, 29 pA; b: 1.85 V, 25 pA). Bottom-left: Electron density maps (states 138-142 Ext. Hückel, LUMO to LUMO+4) of *(P,M)*-9,9’-bis[7]H (blue rectangle) and *(M,P)*-9,9’-bis[7]H (yellow rectangle) which are the building blocks of the parallelograms in (a) and (b) respectively. Bottom-right: the STM simulations of two *(M,P)*-9,9’-bis[7]H were assembled together. The contrasts of this simulated parallelogram correspond to the contrasts of a parallelogram in the inset in the bottom right corner (4 nm × 4 nm, 1.85 V, 25 pA, zoom of b). A superposition of the models with a STM image is also presented in Figure A. 9 in the appendix.

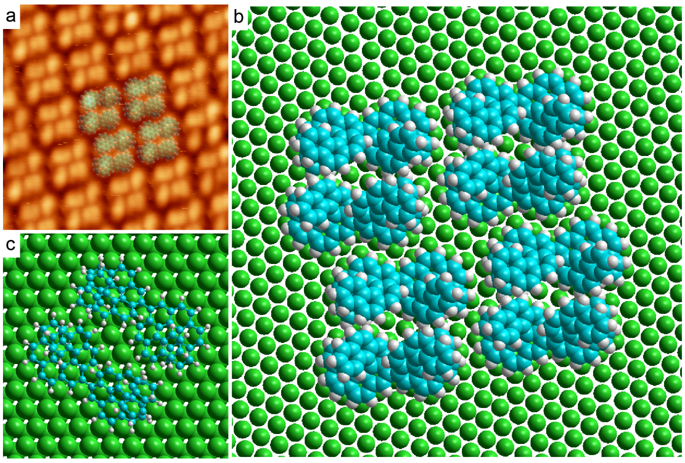

Figure 36: (a) Superposition of the molecular model (b) on a STM image (10 nm × 10 nm, 1.78 V, 29 pA) of the parallelogram structure. (b) Molecular model made based on the STM images of the surface, of the self-assembled *(P,M)*-bis[7]H and on the force-field calculations. (c) Minimum-energy heterochiral dimer obtained with Amber-force field geometry optimization calculation. The molecules could relax freely on the surface.

AMBER force-field calculations were performed on heterochiral bis[7]H. *(P,M)*-9,9'-bis[7]H (Figure A. 12) is the most favored configuration once adsorbed on the surface. The minimum-energy dimer made of two heterochiral bis[7]H is displayed in Figure 36c. A model of the parallelogram structure (Figure 36b) was realized based on the unit cell of the motif, on the Cu(111) orientation (Figure A. 6) and on the minimum energy dimer (Figure 36c). It corresponds to the STM observations (Figure 36a).

For each mirror domain, three rotational domains are observed (Figure 37). This can be explained by symmetry arguments. The top layer of the Cu(111) substrate has a C_6 symmetry which would usually lead to the presence of six rotational domains. However, the C_2 symmetry of the parallelogram structure leads to only three pairs of indistinguishable rotational domains.

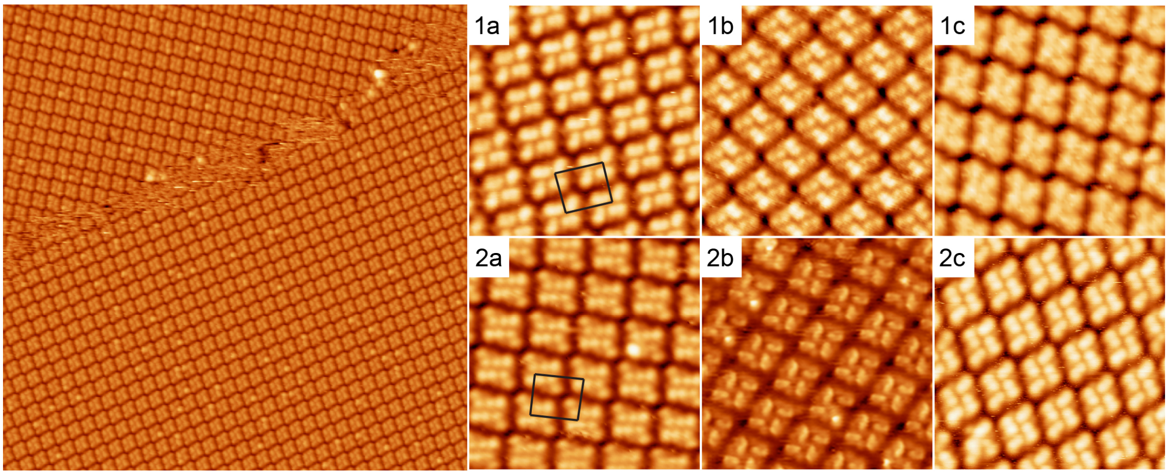

Figure 37: A large scale STM image (60 nm × 60 nm, 2.093 V, 20 nA) presents two mirror domains of the parallelogram structure. Rotational domains (10nm×10nm) of the domain on top are displayed in (1) (a: 1.779 V, 29 pA; b: 2.093 V, 23 pA; c: 1.71 V, 29 pA) and rotational domains of the domain at the bottom of the large scale STM image

are displayed in (2) (a: 1.85 V, 25 pA; b: 2.09 V, 29 pA; c: 2.18 V, 32 pA) respectively. The unit cells of the structures 1a and 2a are highlighted in black.

Additional information

The area per molecule for every structure is given in the Table 7. The zigzag structure which is a racemate made of homochiral molecules is less dense than the parallelogram structure made of heterochiral bis[7]H.

	Nbr. of molec. /unit cell	Nbr. of atoms /unit cell	Area/molec.
Parallelogram	2	68	191.5 Å^2
Zigzag	2	110	309.7 Å^2

Table 6: parameters of the motifs observed in the self-assembly of bis[7]H on Cu(111)

b. Self-assembly on Au(111)

Unlike for Cu(111), the mobility of the molecules at room temperature was high enough on gold to self-assemble without the need of any extra annealing. The *rac*-9,9’-bis[7]H adsorb and diffuse at first to the terraces' edges of the gold sample (Figure 38a). Then, the molecules sit on the herringbone pattern (Figure 38b, c). When the coverage is high enough, ordered domains appear (Figure 38d). Two distinct structures are visible (Figure 39): one with a zigzag pattern and one with a parallelogram pattern.

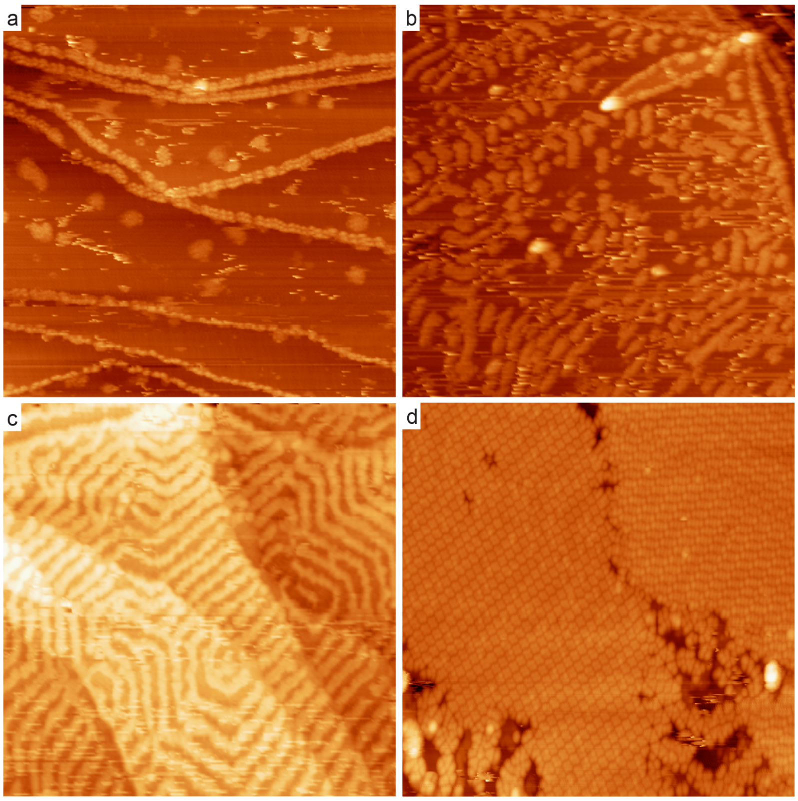

Figure 38: STM images (a: 300 nm × 300nm, 30 pA, −3.0 V, b: 199.2 nm × 199.2 nm, 31 pA, 3.4 V, c: 199.2 nm × 199.2 nm, 30 pA, −3.8 V, d: 65.5 nm × 65.5 nm, 30 pA, −3.6 V) of *rac*-bis[7]H on Au(111) as a function of the coverage θ. (a) θ = 0.04 ML : The molecules sit mainly on the edges of the gold terraces and form few clusters on the surface.

(b, c) θ = 0.13 and 0.44 of ML respectively: The molecules sit on the herringbone reconstruction of the Au(111) surface. (d) θ = 0.82 ML: Large ordered domains and a few non-ordered areas are observed.

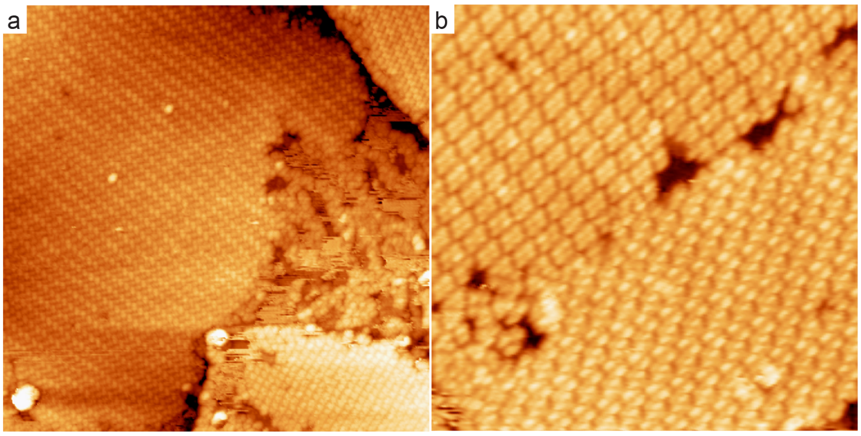

Figure 39: STM images of the two structures formed by *rac*-bis[7]H on Au(111) (a) On top, two rotational domains of the zigzag structure are observed. A domain of the parallelogram structure is in the bottom-right corner. (b) Every parallelogram has a four-lobes contrast. The zigzag structure is made of successive rows of molecules with two different orientations. Each of them has two bright protrusions. (a: 121 nm × 121 nm, 29 pA, 3.0 V, b: 65.5 nm × 65.5 nm, 30 pA, −3.5 V)

Zigzag structure

The zigzag structure is made of molecules rotated by 90° with respect to each other (Figure 40, Figure 41). Some of the molecules appear brighter (Figure 40b) and three rotational domains and their associated mirror domains are observed. The zigzag structure is a racemate made of a succession of rows of homochiral dimes with alternating handedness (Figure 41), identical to one of the two structures observed on Cu(111).

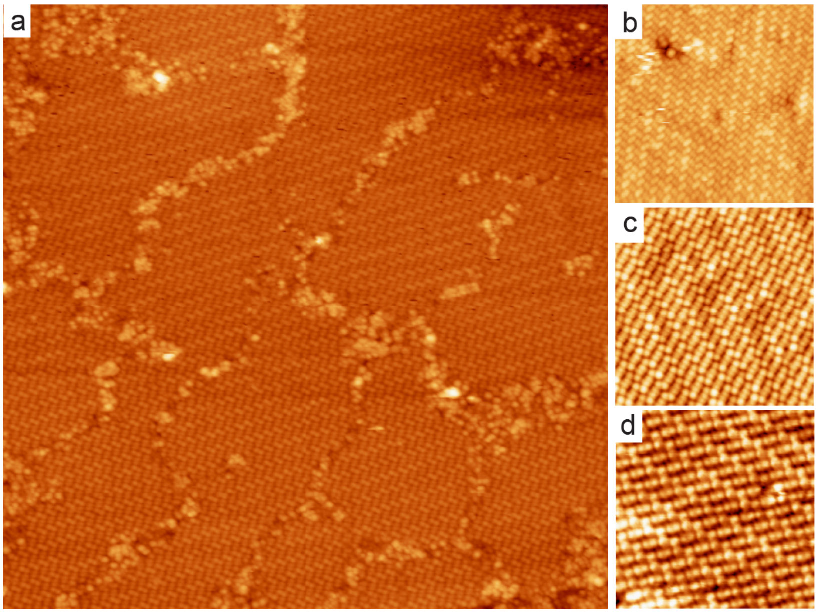

Figure 40: STM images (a: 121 nm × 121 nm, 30 pA, 3.4 V; b: 52.7 nm × 52.7 nm, 30 pA, 3.5 V; c: 35 nm × 35 nm, 30 pA, −3.9 V, d: 25.4 nm × 25.4 nm, 28 pA, 3.3 V) of the zigzag structure. (b) and (d) are rotational domains of (a) rotated by by 60° and 120° counter clockwise respectively. (b) and (c) are mirror domains.

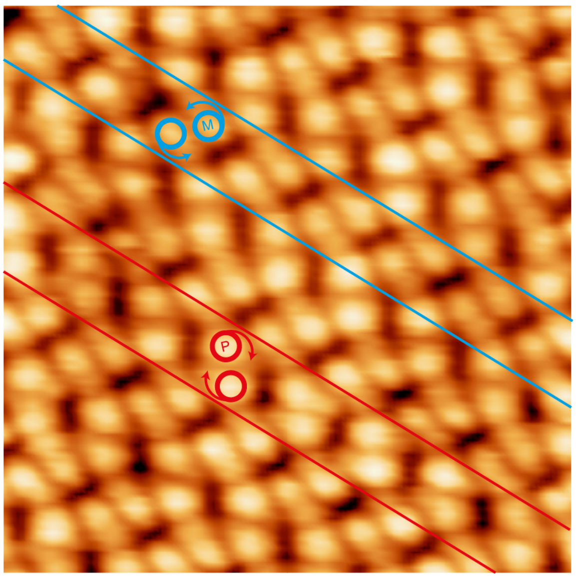

Figure 41: STM image (13.7 nm ×13.7 nm, 63 pA, 3.2 V) of the zigzag structure formed by *rac*-bis[7]H on Au(111). The structure is made of line of homochiral molecules with alternating handedness: *(P,P)* (red) and *(M,M)* (blue). The bright off-centered protrusions highlighted with colored circles correspond to the two uppermost parts of a bishelicene. The arrows follow the direction of the helices down.

Parallelogram structure

The second structure is made of parallelograms which arrange in three rotational domains. Mirror domains are also observed (Figure 42). The parallelograms (Figure 43) have identical contrasts than the ones observed on Cu(111) (Figure 35). Each of them is made of two *(P,M)*-bis[7]H rotated by 180° with respect to each other.

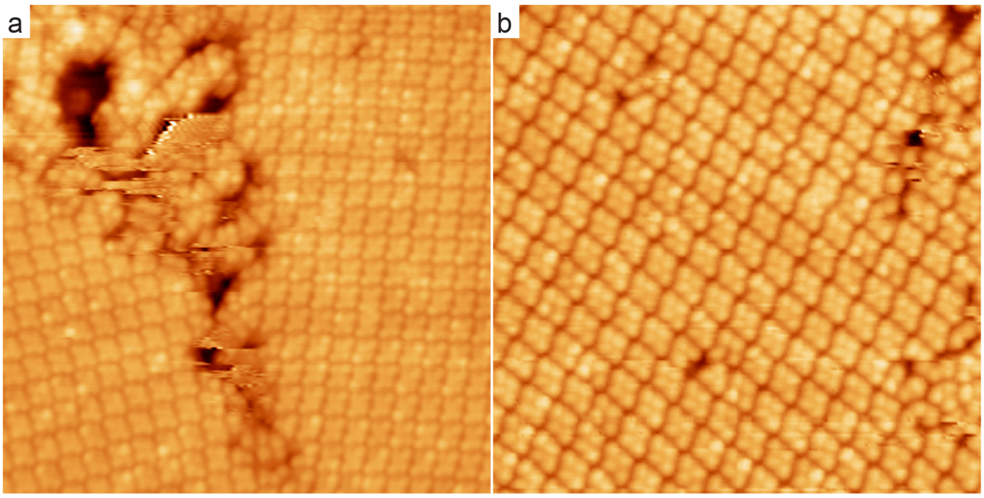

Figure 42: STM images (a: 42 nm × 42 nm, 52 pA, 3.2 V, b: 33.4 nm × 33.4 nm, 52 pA, 2.9 V) of the parallelogram structure. (a) Two mirror domains are observed. The domain on the left is a rotational domain of (b), rotated by 60° in the clockwise direction.

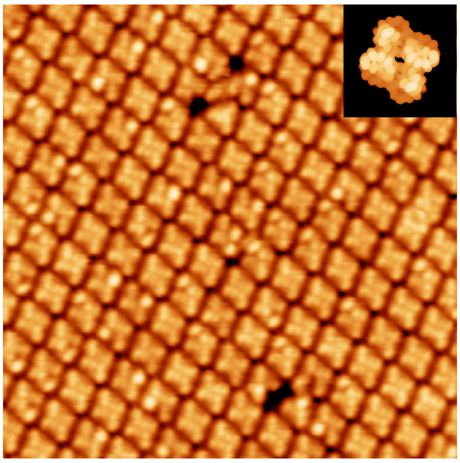

Figure 43: STM image (27 nm × 27 nm, 52 pA, 2.9 V) of the parallelogram structure formed by *rac*-bis[7]H on Au(111) made of two *(M,P)*-bis[7]H rotated by 180° with respect to each other. Inset: electron density maps (states 138-142 Ext. Hückel, LUMO to LUMO+4) of two *(M,P)*-9,9'-bis[7]H (calculated separately) corresponding to a parallelogram unit on the STM image.

Additional remarks

Note that for both structures, a pattern, the usual herringbone reconstruction of the top most Au layer is visible (Figure 38d, Figure 40, Figure 42b). It means that the standard reconstruction of the surface is unmodified by the molecules-substrate interactions, implying that the large distance observed between two consecutive zigzag rows and discussed in detail previously is probably not due to a surface reconstruction. If it would be the case, the herringbones pattern would be modified as observed in ref.170.

c. Conclusion

The self-assembled structures formed on both Cu(111) and Au(111) by *rac*-bis[7]H are identical. The first structure is patterned by zigzag rows made of homochiral bis[7]H with alternating handedness. The second is made of parallelograms, each made of two heterochiral bis[7]H. On Au (111), the typical herringbone reconstruction of the top most layer, is observed for both structures. This standard reconstruction of the surface is unmodified by the molecules-substrate interactions, which are only weak van der Waals interactions[178]. The only notable difference between the two metallic templates is the need of annealing at 383 K on copper to help the molecules diffuse and self-assemble whereas spontaneous self-assembly occurs already at RT on Au(111). The electronic structures of Au ([Xe]$4f^{14}5d^{10}6s^1$) and Cu ([Ar]$3d^{10}4s^1$) are similar. Both metals have a 4s electron outside their filled 3d shell in the ground state. Nevertheless, the 5d states are more extended than the 3d states making gold nobler than Cu[179]. In conclusion, the larger unit cell of Au(111) with respect to Cu(111), which implies a mismatch with the size of benzene rings of polycyclic aromatic hydrocarbons, has here no impact.

4.2.2 *Ullmann-coupling of rac-Br[7]H on Cu(111)*

Ullmann reaction of *rac*-9-Br[7]H was studied at 50 K on Cu(111) to understand the factors which could give rise to a surface-induced diastereoselectivity during the Ullmann coupling of *rac*-Br[4]H[50], which has indeed only produced homochiral bis[4]H and no heterochiral *(M,P)* diastereomer. The low inversion barrier of Br[4]H (calculated to be about 4 kcal/mol for [4]H [97]), allowing the molecules to racemize in order to adopt a more favorable configuration on surface, could be one reason for the diastereoselectivity. In the case of 9-Br[7]H, the inversion barrier is much higher (41.7 kcal/mol for [7]H at 300 K[96]) and the molecules are not able to invert at room temperature anymore. This study will determine if a low inversion barrier is responsible for diastereoselectivity after Ullmann coupling or if this chiral bias is already induced on surface during the formation of the intermediate state [7]H$^-$-Cu-[7]H$^-$. The self-assembly of the bis[7]H(surf) synthetized on surface and the self-assembly of the bis[7]H(sol) synthetized in solution prior to sublimation (paragraph III.4.2.1), will be compared. The self-assembly of bis[7]H(sol) on Cu(111) was made of two motifs. If those two structures are present identically in the self-assembly of bis[7]H(surf), it would prove the absence of diastereoselectivity on surface whereas the absence/modification of certain structures would prove the opposite.

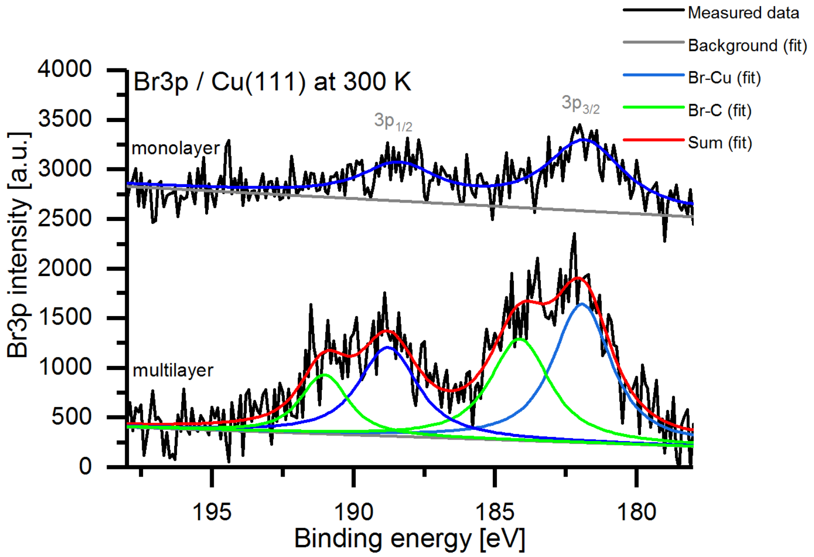

Figure 44: XP spectrum revealing the C-Br bond breaking of *rac*-Br-9-[7]H on Cu(111) at room temperature. The background of the clean sample has been subtracted. The binding energy scale was calibrated based on the Cu $2p_{3/2}$ peak (932.7eV). The spectra are offset for clarity.

The Br3p XP spectra were recorded after deposition at two distinct coverages (Figure 44). In the high coverage spectrum (multilayer), the $3p_{3/2}$ and $3p_{1/2}$ peaks can both be decomposed into two components:

- The first component, which is also observed at ML coverage, has two maxima at 189.1 eV and 182.3 eV for the $3p_{1/2}$ and $3p_{3/2}$ peaks respectively. It corresponds to the presence of Br-Cu bonds. Br-Cu bonds can only form subsequently to a scission of the Br-C bonds of the molecules[50].

- The second component is found at higher energy (maxima at 184.5 eV for $3p_{3/2}$ and 191.3 eV for $3p_{1/2}$) and corresponds to intact C-Br bonds[50,180,181]. The presence of the C-Br component suggests that the molecules from the multilayer which are not in the first layer are still intact. Only the molecules in contact with the copper surface lose their Br atoms.

The attentive reader can notice a small energy difference between the monolayer and multilayer cases for the first component's maxima. There is a slight shift of the Br-Cu (about 0.3 eV) component to lower energy with decreasing coverage. The little shift in the multilayer peaks was already reported and can be explained by core-hole screening by the substrate image charge[182].

The XPS data at room temperature proved that Br-C bonds break without desorption of the Br from the surface. This reaction is catalyzed by the copper surface because the molecules must be in contact with Cu for the scission to happen. The dehalogenation was reported to happen at about 180 K on copper with the bromine atom still present on surface[50,181].

The scission of the Br-C bond was the initial step of the Ullman coupling reaction. The Br-C bonds breaking is also known to happen already at room temperature on Cu and Ag, but requires an additional annealing at 393 K on Au[164]. This difference of mechanism depending on the metal surface is still not completely understood. Nevertheless, theoretical calculations[162] could reveal a lower energy barrier for the dehalogenation of hydrocarbons on Cu and Ag compared with Au.

The self-assembly of the dibrominated [7]H as function of the coverage is shown in Figure 45. Large domains with a zigzag pattern are observed (Figure 45a). The ordering (Figure 45a, b) is only observed for a non-saturated monolayer which allows molecular diffusion, a key factor for the self-assembly formation. Adding more molecules (Figure 45c) to the surface destroys the assembly. It does not help filling the darker pockets observed in the 1st ML. The second layer starts to form on top instead (Figure 45d). XPS (Figure 44) proved that the bromine does not desorb from the copper surface at room temperature. Bromine atoms are therefore either in the observed dark pockets (Figure 45b, c, d) and/or between the helicenes molecules. Br limits the molecular diffusion on surface and prevents the self-assembly.

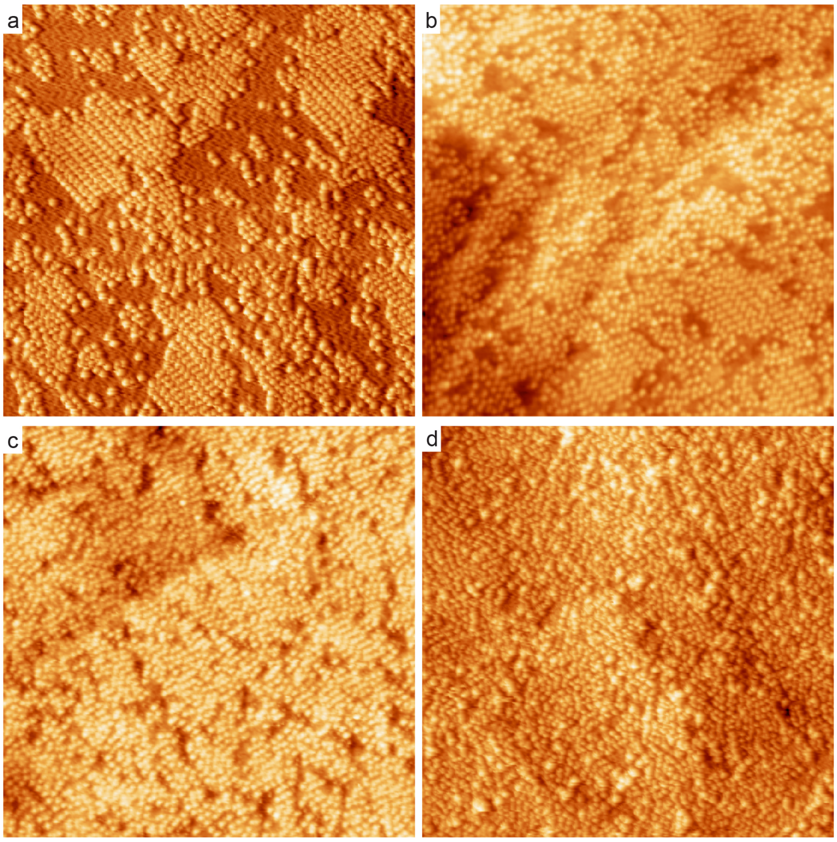

Figure 45: STM images of the self-assembly of *rac*-9-Br[7]H on Cu(111) depending on the evaporation time t_{evap}. The expected debromination of the molecule has already happened as confirmed with XPS (Figure 44). (a) At low coverage, the [7]H- radicals form domains made of zigzag motifs (t_{evap}= 4 min at 442 K, 31 pA, –3.1 V, 90 nm × 90 nm). (b-d) Increasing the coverage (d) does not lead to a better ordering but rather to a disappearance of the well-ordered domains and finally to the formation of a second layer. The dark holes visible on the surface (b, c) remain. They are probably filled with the Br atoms which do not desorb from the surface and prevent a better ordering of the molecules. (Measuring parameters: b: t_{evap}= 7 min at 440 K, 28 pA, –2.8 V, 80 nm × 80 nm; c: t_{evap}= 7 min at 441 K, 28 pA, 2.7 V, 80 nm × 80 nm; d: t_{evap}= 7 min 15 s at 441 K, 31 pA, –2.6 V, 80 nm × 80 nm)

Dimers with two different orientations are the building blocks of the zigzag pattern (Figure 46). A dimer is an intermediate state which could be made of two [7]H- attached via a Cu adatom as observed in ref.[166]. The formation of organometallic IS on Cu(111) after dehalogenation is something currently mentioned in the literature[159,166,183]. The experimental length of the IS is 20.2 Å. It is an average value obtained by measuring thirteen intermediate compounds on five different STM images. By using AMBER-force field optimization, it is possible to find the lowest-energy configuration of a bis[7]H on surface and to measure its maximal length. The results are given in the Table 7. The experimentally measured length of the IS corresponds to the theoretical length of organometallic species. Because the lengths of trans-9,10′-*(M,M)*-Cu-dimer, cis-9,9′-*(P,M)*-Cu-dimer and cis-10,10′-*(P,M)*-Cu-dimer make them all be possible candidates, it is not possible to conclude on the formation of hetero- or homo-chiral organometallic IS.

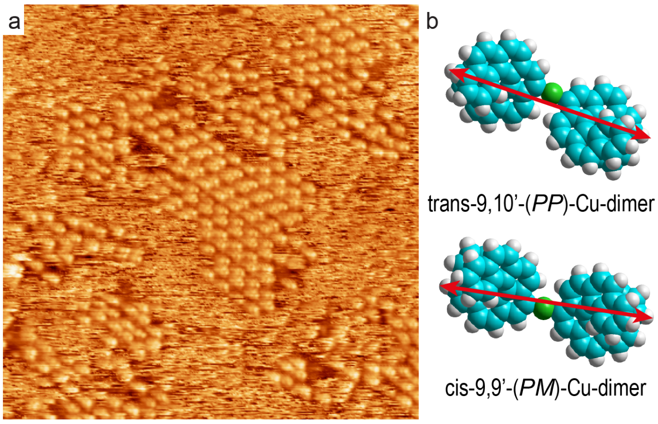

Figure 46: (a) STM image (90 nm × 90 nm, 31 pA, −3.1 V) of the self-assembly of *rac*-9-Br[7]H on Cu(111) at low coverage. The expected debromination of the molecule has already happened as confirmed with XPS (Figure 44). The [7]H- radicals form dimers which are probably intercalated by a Cu adatom ($C_{30}H_{17}$-Cu-$C_{30}H_{17}$). (b) As examples, two molecular models of possible IS are presented: a trans-9,10'-*(P,P)*-Cu-dimer and a cis-9,9'-*(P,M)*-Cu-dimer. C, H and Cu atoms are respectively displayed in blue, white and green. For each model, the red arrow indicates the maximal length, reported in the Table 7.

Organic species	**Length (Å)**	**Organometallic species**	**Length (Å)**
trans-9,10'-*(M,M)*	18.3	trans-9,10'-*(M,M)*-Cu-dimer	20.5
trans-9,9'-*(M,M)*	18.6	trans-9,9'-*(M,M)*-Cu-dimer	21.1
trans-10,10'-*(M,M)*	18.6	trans-10,10'-*(M,M)*-Cu-dimer	21.2
cis-9,10'-*(P,M)*	18.1	cis-9,10'-*(P,M)*-Cu-dimer	20.9
cis-10,10'-*(P,M)*	17.9	cis-10,10'-*(P,M)*-Cu-dimer	20.6
cis-9,9'-*(P,M)*	17.6	cis-9,9'-*(P,M)*-Cu-dimer	20.5
Average length of organic species	18.2	Average length of organometallic species	20.8

Table 7: Comparison between the theoretical (molecular mechanics) lengths of organometallic and organic molecules which could be formed during or after Ullmann coupling. The length is measured along the long axis of the molecule (see arrows on the molecular models in Figure 46).

The dehalogenation is only the first step in the Ullmann coupling. To form the bis[7]H(surf), C-C linking requires an extra annealing on Cu [157,165,166]. To determine the coupling temperature, the surface was annealed to a temperature which was increased step by step. Each step was maintained for 10 min. Between 449 and 458 K, a change in the assembly was observed (Figure 47a): the previous IS's zigzag assembly is not observed anymore and lines are formed. Between 469 K and 482 K, coupling occurs (Figure 47b, inset), giving rise to the formation of bis[7]H(surf). This range of temperatures is coherent with what is reported in the literature[50,181,184]. Unfortunately, no self-assembly could be observed. Br atoms are still intercalated between the molecules as shown in the Figure 47b. Self-assembly is prevented by the presence of too many Br- atoms on the surface, limiting the diffusion of the molecules and the recombination rate[162].

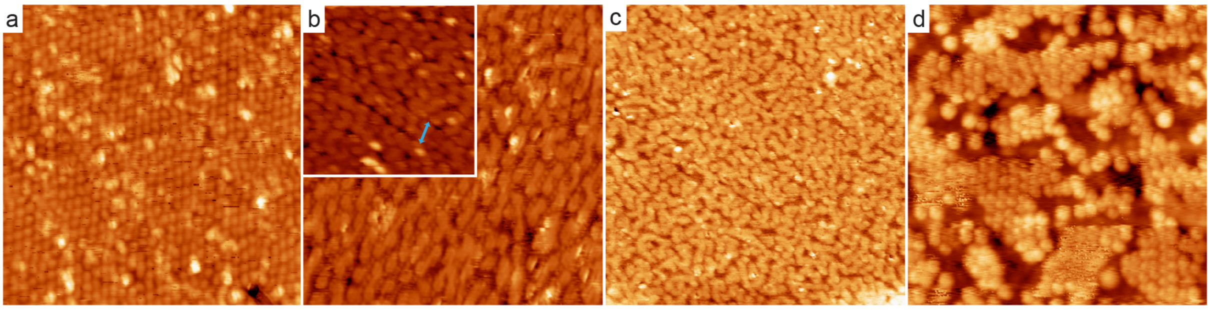

Figure 47: STM images presenting different steps of the 9-Br[7]H Ullmann coupling on Cu(111) at various temperatures. (a) Well-ordered rows are observed (46 nm × 46 nm, 38 pA, 2.3 V, 449 K). (b) Bonded dimers are visible and Br atoms are intercalated between them: the last step of Ullmann-coupling was completed but no self-assembly is observed. The blue arrow in the inset indicate the length of a typical dimer (large image: 28.9 nm × 28.9 nm, 100 pA, –1.0 V, 473 K; inset: 16.8 nm × 16.8 nm, 100 pA, 1.0 V, 482 K). (c) Chains of molecules are observed: polymerization of the molecules are due to excessive annealing (46 nm × 46 nm, 38 pA, 2.3 V, 494 K). (d) Above 573 K, self-assembly between fragments of bis[7]H is observed (37 nm × 37 nm, 30 pA, 1.9 V, 576 K).

Further annealing (T > 493 K) only gives rise to polymerization due at least to dehydrogenation. Only high enough annealing (576 K), leads to the formation of ordered areas which might be a consequence of the higher mobility of the Br atoms or of their desorption. At this range of temperatures, the molecules are already dehydrogenated and are probably further decomposed: the ordered components are made of fragments or recombination of the bis[7]H molecules.

The post-Ullman-coupling self-assembly of bis[7]H(surf) is prevented by the presence of the Br adatoms on surface and/or by the limited molecular diffusivity on Cu. It makes it impossible to state on the species formed during the coupling reaction on surface. The comparison with the self-assembly of bis[7]H(sol) on Cu(111) is not possible. Consequently, the presence or absence of enantioselectivity on surface could not be demonstrated. To solve this question, molecules should have a sufficient mobility which depends on the metal surface and on the diffusion process (sliding, flipping, rotational motion…). A theoretical comparison of the diffusion mechanisms of a phenyl on the (111) facet of Ag, Cu and Au is presented in ref.[162]. The sliding diffusion barrier on Cu(111) is in this case twice higher than the one on Au and about 1.3 times higher than on Ag. The sliding mechanism (together with a rotational motion) seems to be the one preferred for larger organic molecules due to their stronger physisorption. Au is therefore a better candidate than Cu for the successful recombination step of the Ullmann coupling[185]. In addition, the presence of copper adatom on the flat surface can impact even more the self-assembly[186]. These adatoms were already shown to form covalent bonds with the de-halogenated molecules and prevent the formation of a well ordered covalent network with only C-C bonds. Finally, the halogen species are more strongly bonded on Cu than on Au. Often, molecular desorption and/or decomposition occurs before reaching the elevated temperatures needed for halogen desorption on Cu[164]. For all these reasons, the formation of well-ordered self-assembled is more probable on gold.

4.2.3 Self-assembly and Ullmann-coupling of rac-Br[7]H on Au(111)

Because the Ullmann reaction of *rac*-9-Br[7]H on Cu(111) did not lead to a successful self-assembly and did not allow any conclusion on the presence or absence of diastereomeric selectivity of the Ullmann coupling on surface, this reaction was investigated on Au(111).

a) Self-assembly of *rac*-9-Br[7]H on Au(111)

Racemic 9-bromoheptahelicene ($BrC_{30}H_{17}$, *rac*-Br-9-[7]H) was measured at 50 K. The molecules form self-assembled domains made of zigzag rows (Figure 48). These rows are oriented along the high-symmetry directions of the gold sample. An additional pattern with lines of larger spacing than the molecular rows is also shown (Figure 48a).

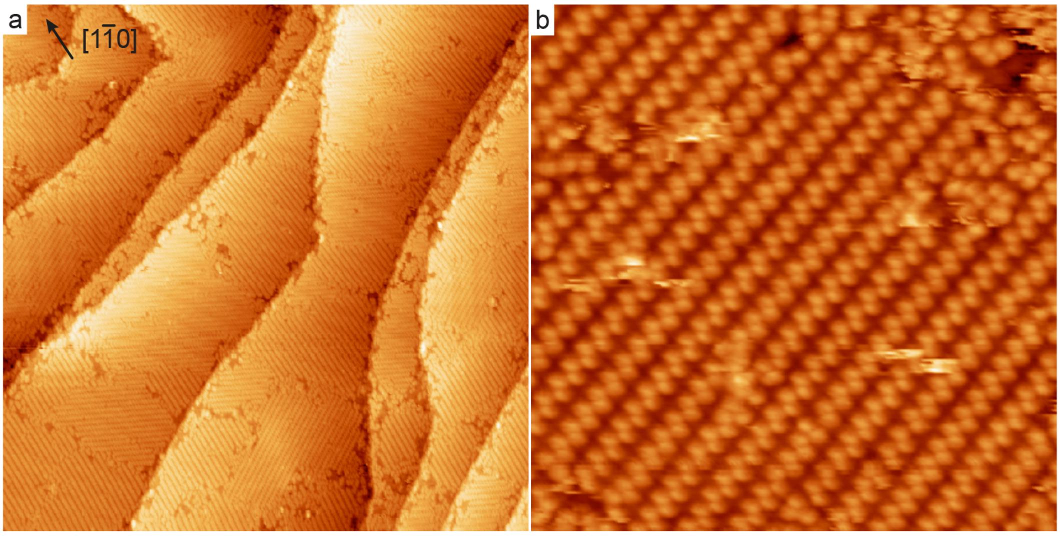

Figure 48: (a) Large scale STM image (219.2 nm × 219.2 nm, 28 pA, −2.8 V) of a ML of Br-9-[7]H on Au(111). The molecules form lines oriented along the high-symmetry axes of the substrate and arranged in rotational domains. The [1$\bar{1}$0] direction of the Au substrate is indicated by the black arrow in the top left corner. (b) STM image (26.2 nm × 26.2 nm, 23 pA, −2.8 V) of a domain showing that the lines are in fact zigzag rows.

A closer look (Figure 49a) to the structures indicates that heterochiral dimers are the building blocks of these rows. On Au(111) at room temperature, the Br is expected[xxvii] to still be attached to the

---

[xxvii] It is verified here by XPS (Figure 53).

molecules[157,166]. The Figure 49b presents on top, the most favorable configuration of a single Br[7]H. It was calculated from 216 different initial configurations with MM (AMBER force field). It allows to conclude that each molecule adsorbs with a Br atom in a bridge position in between two Au surface atoms. The most-favorable configuration calculated for a heterochiral dimer is given in the Figure A. 13 in the appendix. It was used, together with the STM images, the Au(111) orientation and the Extended Hückel simulation of a 9-Br[7]H (Figure 49a), to model the self-assembled structure (Figure 49b).

The geometry of the structure is similar to the one observed by Fasel *et al.* for [7]H[7] on Cu(111) and by Seibel *et al.* [187] for [7]H on Ag(111) and Au(111). The rows are built by both enantiomers as observed on Cu(111) and Au(111), interacting via vdW interactions. It means that the replacement of the 9th H atom by a Br atom on the heptahelicene backbone does not have an impact on the heterochiral interaction between helicenes. This makes sense because the Br atom is positioned on each molecule in a way which does not influence the intermolecular interaction observed previously [7]. The matrix notation[141] of this structure is (5,0; 2,8). The area per molecule is therefore 1.45 nm^2/mol which is higher than the 1.04 nm^2/mol found on Cu(111) and Ag(111)[187]. The length of a Br···Br non-bonded interaction is longer than Br···H interaction[188,189]. The distance between two Br[7]H is therefore expected to be larger than between two [7]H, increasing the areal density. It might explain why a long range ordering is observed for Br-9-[7]H on Au(111) whereas [7]H on Au(111)[187] forms somewhat less ordered domains of zigzag rows.

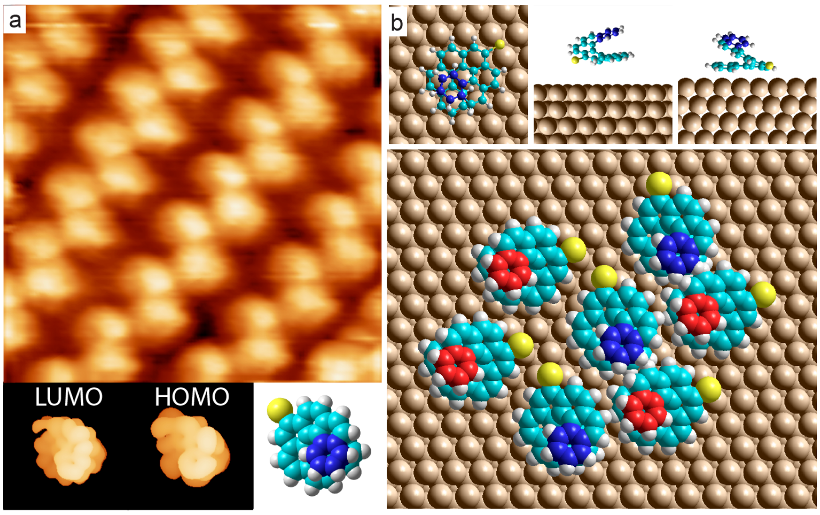

Figure 49: (a) Top: STM image (9.3 nm × 9.3 nm, 23 pA, −2.8 V) of the zigzag rows formed by Br-9-[7]H on Au(111). Bottom, from left to right: EHT models of the LUMO (levels 73 to 76) and HOMO (levels 69 to 72) and ball model (H in white, C in blue, Br in yellow) of a single *(M)*-Br-9-[7]H. (b) Molecular model (bottom) of a zigzag domain based on the STM images and on the AMBER force field calculation of a single molecule (top). The uppermost terminal ring of each molecule is highlighted in dark blue or red for a *(M)*- or *(P)*-enantiomer respectively.

b) Ullmann coupling of Br[7]H and self-assembly of bis[7]H(surf) on Au(111)

Coupling and subsequent self-assembly: observations

The Ullmann coupling on gold is reported to happen around 473 K[183,190,191]. Although the increase of the annealing temperature was progressive, no intermediate compound was ever observed with the STM. It suggests that the lifetime of the IS is really short on Au[166]. After annealing the sample between 469 K and 486 K during 15 min, enough thermal energy was provided for Ullmann coupling to happen, creating bisheptahelicene (bis[7]H(surf)).

Two different structures were observed (Figure 50): one with the same zigzag pattern as observed for bis[7]H(sol) and one appearing in lines. The first one is made of homochiral molecules (*(M,M)* and *(P,P)*) with alternating handedness as described in the paragraph III.4.2.1. The structure with lines (Figure 51) is however different than the second structure with parallelogram motifs observed for bis[7]H(sol). A parallelogram unit was composed of two *(M,P)*-9,9'-bis[7]H rotated by 180°. In the structure with lines presented in Figure 51, a building block (black rectangle) appears to have, in both STM data and EHT simulation (inset), two bright protrusions exclusively on one half of the molecules. This non-symmetric contrast could also correspond to a *(M,P)*-9,9'-bis[7]H because the overall contrasts in model and experiment correspond quite well. Yet, a noticeable difference in the assembly with respect to the parallelogram structure is observed.

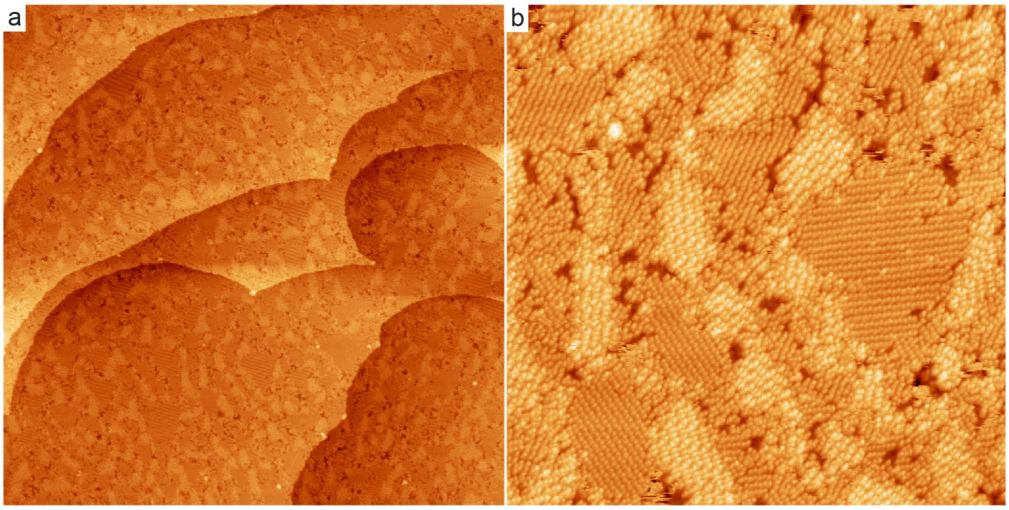

Figure 50: STM images (a: 500 nm × 500 nm, 30 pA, 1.4 V, b: 99 × 99 nm, 30 pA, 1.4 V) of the two structures formed after Ullmann coupling of Br[7]H on Au(111), between 469 K and 486 K. (a) The surface is completely covered with two types of small domains appearing in different brightness. (b) The bright domains have a zigzag pattern and the darker ones are made of lines of molecules.

The first hypothesis to explain the difference in assembly is that the dissociated Br atoms are intercalated between the molecules. To verify this hypothesis, the sample was annealed to a higher temperature. Annealing at 581 K (Figure 52) led to a pronounced reduction of the coverage (naked surface patches are observed) and only a few ordered domains are still observed. In Figure 52, domains with lines and zigzags are distinguishable. A few parallelograms appear on the sides of the domains with the lines. It suggests once more that the lines have a similar composition as the parallelograms as already expected from the EHT simulation contrasts. They are both made of *(P,M)*-9,9′-bis[7]H. Therefore, the Ullmann coupling of heptahelicenes is not diastereoselective as both homochiral and heterochiral bis[7]H are formed on surface. We recall that in the case of Br[4]H (paragraph III.4.1), the diastereoselectivity observed after the reaction was due to the low inversion barrier of the molecule.

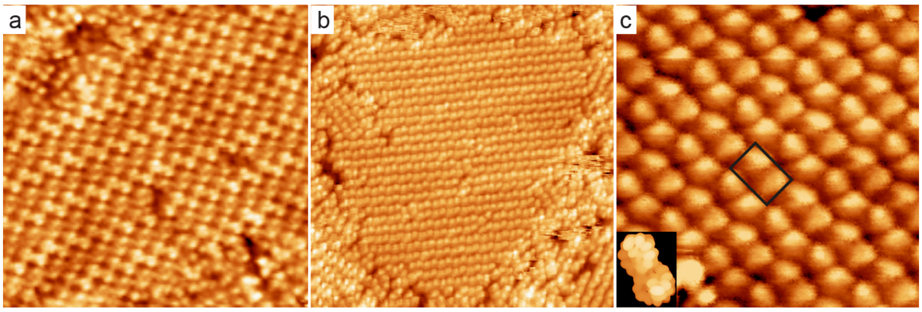

Figure 51: STM images (a: 27.3 nm × 27.3 nm, 35 pA, −2.9 V; b: 38.9 nm × 38.9 nm, 30 pA, 1.5 V, c: 9.7 nm × 9.7 nm, 30 pA, 1.5 V) of the two structures formed after the Ullmann coupling of Br[7]H on Au(111) at 499K. (a) Zigzag motif made of homochiral bis[7]H with alternating handedness. (b, c) Second structure observed after the coupling of Br[7]H. An electron density map (states 138-142 Ext. Hückel, LUMO to LUMO+4) of a *(M,P)*-9,9′-bis[7]H is presented in the inset of (c) and serves as a comparison with the molecules observed in this structure, e.g. in the black rectangle.

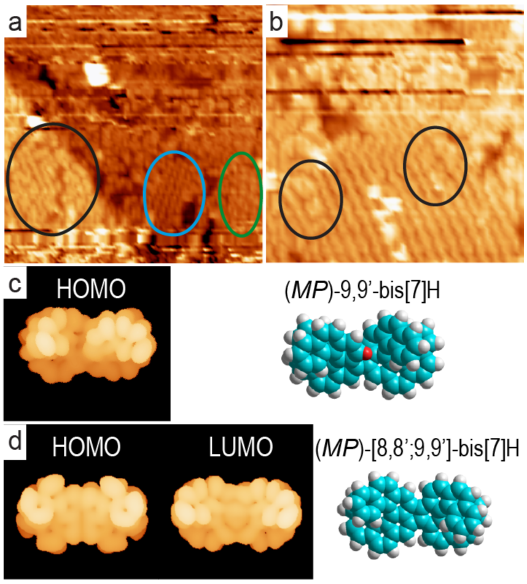

Figure 52: (a, b) STM images (a: 15.5 nm × 15.5 nm, b: 10.4 nm × 10.4 nm; 30 pA, 3.0 V) of the Au(111) surface after post-Ullmann-coupling annealing at 581K. (a) The image displays the structure with the zigzag motif (circled in green), the lines structure (blue) and an area which is composed by both lines and parallelograms (black). (b) The image shows the structure with lines. On its sides, a few parallelograms appear (black circles). The rest of the surface is mostly covered with disordered areas. The horizontal lines observed in the upper parts of the images (a) and (b) are due to the reduced coverage: the tip was constantly catching and dragging molecules. (c, d) Molecular models and associated electron density maps of the frontiers orbitals of (c) a *(M,P)*-9,9′-bis[7]H (states 138-142 Ext. Hückel, LUMO to LUMO+4) and of (d) a *(M,P)*-[8,8′-9,9′]bis[7]H (states 137- 141 Ext. Hückel, LUMO to LUMO+4 and states 132-136 Ext. Hückel, HOMO to HOMO-4). In the *(M,P)*-9,9′-bis[7]H, the strong steric repulsion between the red-marked H atom and the one which is hidden at the 8th position on the other part of the molecule, could favor a cyclodehydrogenation such as observed in refs.174,192, giving rise to the formation of *(M,P)*-[8,8′-9,9′]bis[7]H.

Diastereoselectivity is not observed during Ullmann-coupling of Br-helicenes which have a high inversion barrier (41.7 kcal/mol for [7]H at 300 K[3]). However, the question about the structural difference between the parallelogram and line structures is still not solved. Annealing to higher temperature (581 K) triggers the appearance of the parallelogram structure but not everywhere. Unfortunately, due to the messy surface, it was difficult to get good resolution images with STM for a longer or warmer annealing. From the literature, Br are expected to be desorbed above 523 K[192,193]. Are some Br atoms still intercalated between the molecules despite the high annealing temperature? To verify it, XPS measurements were performed on a different system (Figure 53).

Both the Br3p and the C1s decrease in intensity after annealing at 373 K because molecules from the multilayer have desorbed. From that, we estimate that the initial coverage was 1.9 ML. Between 373 K and 413 K, the Br3p peaks shift to lower energy due to the breaking of the C-Br bonds and the formation of Br-Au as observed in refs.[164,192,194] for the Br3d doublet. After annealing at 493 K, no Br3p signal is observed. XPS confirmed that Br atoms have desorbed from the surface between 463 K and 493 K. The C1s peak at 284.5 eV also shifts to lower energy due to the breaking of the C-Br bonds and the formation of new C-C bonds, as observed in refs.[164,192,194].

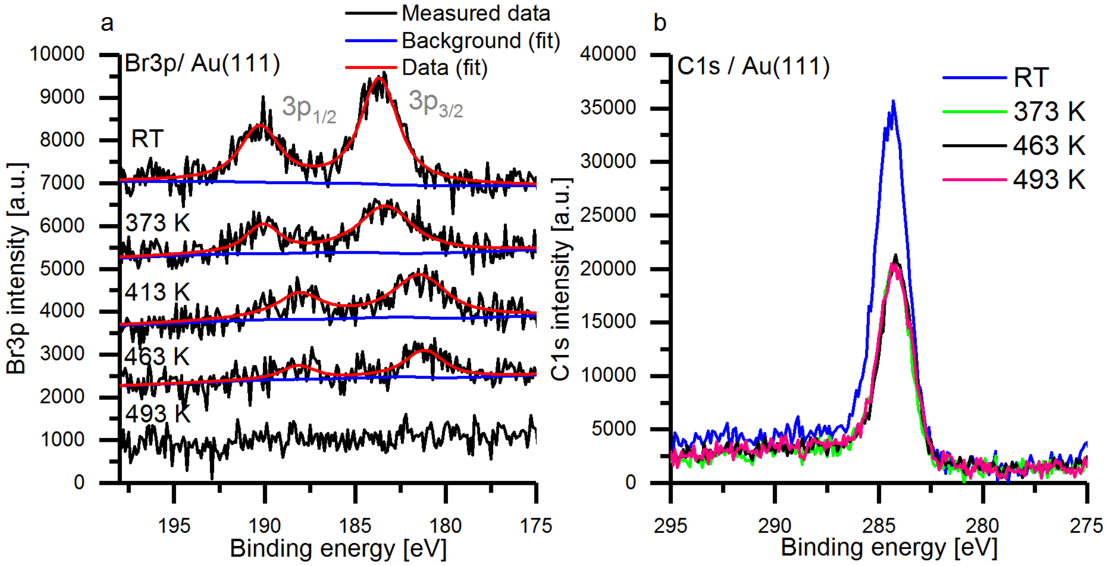

Figure 53: Br3p (a) and C1s (b) XP spectra of 1.9 ML of Br[7]H on Au(111) at different temperatures: at RT (300 K) and after annealing 10 min at 373 K, 413 K, 463 K and 493 K. For both C1s and Br3p, a decrease in intensity is observed between RT and 373 K due to the desorption of the multilayer (from 1.9 to 1.0 ML). Above 413 K, Br3p and C1s peaks shift toward lower binding energy due to the breaking of the Br-C bond. The Br desorbed during annealing at 493 K but the same quantity of carbon was still present on the surface. The Br3p spectra are offset for clarity.

The structure with the lines was still observed above 493 K when the Br atoms are not supposed to be on the surface anymore. However, the poor quality of the STM images after annealing at high temperatures and the non-negligible error in the temperature comparison due to the use of two separated systems (with different devices to measure the temperature), we cannot exclude that Bromine is responsible for the formation of the different structures. Several other hypotheses could also explain the difference. Firstly, there could be a reconstruction of the Au(111) surface during the Ullmann coupling. It was observed for the system perylene / iron-phthalocyanine (FePc)[195] and for Gd[196] on Au(111). Both cases were explained by surface stress anisotropy induced by large charge transfer differences due to the coupling between the gold and the metal atoms from the molecule (Gd or the central Fe atom of FePc). It is possible that such charge transfer differences are observed in the Br[7]H case because it was demonstrated that electronegative halogen atoms (Cl, I) can lift some of the Au atoms from the top most gold layer to release the surface stress[168,197]. Pham *et al.*[170] also reported a distortion of the herringbone reconstruction during the annealing step of Ullmann coupling of Br_4-pyrene on Au(111). They showed that the lifting of these Au adatoms can even lead to the uncommon formation of an organometallic compound on Au(111). The formation of organometallic IS on Au was also observed by A. Saywell *et al.*[168] The presence/absence of Au reconstruction in the present work could be investigated further via LEED measurements. Secondly, the difference in assembly can be due to steric repulsion between the H atoms which are situated in the neighboring of the C-C bond linking the two parts (individual [7]H) of a bis[7]H (Figure 52c). Under steric overcrowding, partial cyclodehydrogenation of a molecule can occur as observed in the literature[174,184,192,198,199]. In the present case, this could for example lead to the formation of a *(M,P)*-[8,8'-9,9']-bis[7]H (Figure 52d). If this reaction occurs here, it would anyway hardly explain the change in assembly observed with STM because the structure with parallelograms is formed after annealing of the structure with lines and not the other way around. Finally, other stereomers (9,9'-; 9,10'- or 10,10'-*(P,M)*-bis[7]H) than the ones observed after adsorption of the evaporated bis[7]H(sol) could be formed on surface. It would induce different intermolecular interactions and self-assembly. The annealing at high temperature can provide sufficient energy for the inversion, leading to the formation of the stereomers observed after adsorption of the evaporated bis[7]H(sol), i.e. to the parallelogram structure.

Bromine desorption induced by dehydrogenation

Ullmann coupling is well documented on Ag, Au and Cu[xxviii]. In particular, dehalogenation is known to happen before RT on Cu, at RT or after a mild annealing on Ag and at more than 393 K on Au. Nevertheless, post-coupling Br desorption is reported to happen at very different temperatures depending on the references in the literature. On Au(111), it occurs at 523 K for dibromobianthryl

---

[xxviii] See for example refs. 10,11,168–170,183,184,190–193,200,50,201,265,156,160–164,166.

(DBBA)[192,193,200], between 473 K and 573 K for tetrabromopyrene[170] or above 573 K for copper-octabromotetraphenylporphyrin[201]. Br desorption was found in this work to happen between 463 K and 493 K on Au(111). So, what triggers this desorption at different temperatures for different molecules?

TDS measurements of H_2 (2 amu), HBr (80 and 82 amu) and Br (79 and 81 amu) presented in Figure 54 reveal that the Br and HBr desorption peaks evolve at the same temperature: Br desorbs as HBr. Because both isotopes of Br (79, 81 amu) and both isotopes of HBr (80, 82 amu) show the same desorption features, the measured signals for the masses 79-82 amu cannot be due to molecular fragments[191]. The Br and HBr peaks then vanish before the appearance of the first peak in the H_2 spectrum. Bronner *et al.*[191] performed a similar study where they monitored the desorption of Br during the cyclodehydrogenation of DBBA on Au(111). They observed the same behavior for H_2, HBr and Br as observed in this work. They also observed no Br_2 signal at all, proving that Br desorbs only as HBr and not as Br_2.

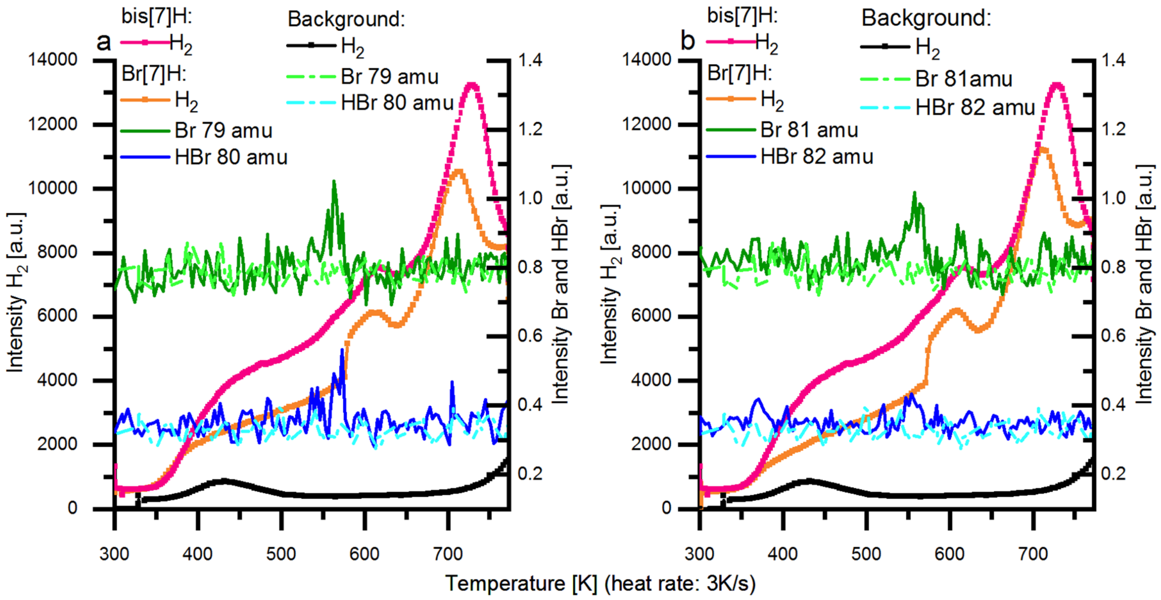

Figure 54: Two TDS measurements of H_2, HBr and Br for 1.5 ML of Br[7]H and of H_2 for Bis[7]H on Au(111) at a heating rate of 3 K/s. Isotopes 79 amu of Br and 80 amu of HBr are displayed in (a). Isotopes 81 amu of Br and 82 amu of HBr are presented in (b). The spectra are offset for clarity.

Br can only desorb as HBr if atomic H is available. In the case of bis[7]H(surf) produced by on-surface Ullmann coupling, H can only be produced by partial (Figure 52) or total dehydrogenation and can leave the surface in two possible ways[191]:

$$\mathrm{H} + \mathrm{H} \rightarrow \mathrm{H_2\,(g)} \tag{20}$$

$$\mathrm{H} + \mathrm{Br} \rightarrow \mathrm{HBr\,(g)} \tag{21}$$

However, HBr and H_2 desorption are not simultaneous (Figure 54: as soon as HBr decreases, H_2 increases) and the transition between them is abrupt. It means that the hydrogen produced during dehydrogenation of the molecule is directly consumed to form HBr (equation (21)) and the H_2 production is not favored. Only after complete desorption of Br as HBr, H_2 is finally produced according to equation (20). The fact that the atomic hydrogen produced during dehydrogenation is consumed first to produce HBr and only then to produce H_2 is confirmed by studying the TDS of bis[7]H(sol) obtained by C-C coupling in solution prior to adsorption. On Au(111), H_2 desorption starts at the same temperature at which HBr is produced for Br[7]H but no sharp transition is observed because there is no Br to desorb. The second peak of the H_2 signal at higher temperature is almost at the same temperature for both molecules (between 703 and 713 K). A similar observation was made for DBBA[191] by measuring the continuous atomic hydrogen (1 amu) emission during both HBr and H_2 production. In Figure 54, the first peak observed in the TD spectra of H_2 is probably induced by partial dehydrogenation due to the steric repulsion between certain atoms (Figure 52c, d). In the case of bis[7]H, this could lead to the formation of a *(M,P)*-[8,8'-9,9']-bis[7]H (Figure 52d). Note that the H could also come from the dehydrogenation of certain of the bis[7]H which are in a non-favorable configuration, e.g. on the step edges. However, because the dehydrogenation and debromination temperatures (i.e. TD signals) are molecules-dependent (as confirmed by performing the same experiment with Br[4]H and di-Br[4]H: Figure 55), it is very unlikely. It is more likely due to the specific partial dehydrogenation of each molecule which depends on the steric overcrowding intrinsically built within the molecule. The second peak in the H_2 signal corresponds to the complete dehydrogenation of the molecule. Note that Br atoms are still on the surface during the cyclodehydrogenation of the molecule similarly as what found for the DBBA molecules of Bronner *et al.*[191]. The cyclodehydrogenation and the products of this reaction will be investigated in a future project with TOF-SIMS.

The same experiment with Br[4]H and di-Br[4]H[xxix] (Figure 55) shows that Br desorption occurs at a higher temperature than in the Br[7]H case. The HBr desorption peak occurs when the H_2 production start to increase and there is no clear step in the H_2 curve. Because the dehydrogenation occurs for these molecules at a more elevated temperature, it seems that HBr production (equation (21)) is not favored anymore over H_2 production (equation (20)). The two dehydrogenation peaks for Br[7]H are observed at 608 K and 711 K respectively whereas for Br[4]H and diBr[4]H, they are observable at 705 K and 768 K respectively.

[xxix] Note that for all molecules used in this study, the saturation to 1 ML was determined by different techniques. For Br[7]H and Br[4]H, it was defined by desorption of the multilayer by annealing to 373 K and 413 K respectively. The coverage of bis[7]H and diBr[4]H was assigned by comparing the amount of carbon measured for this molecule with 1 ML of Br[7]H and Br[4]H respectively.

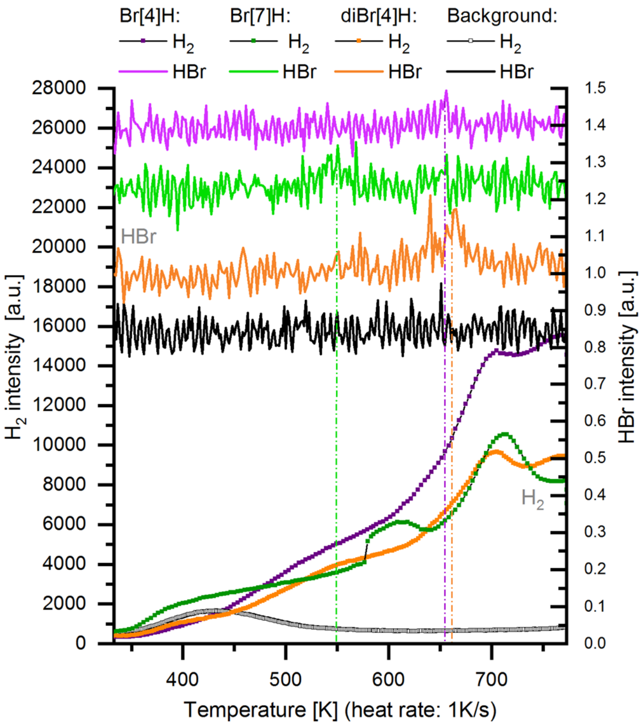

Figure 55: TD spectra of H_2 (2 amu) and HBr (amu) for coverages above monolayer of Br[7]H (1.5 ML), Br[4]H (1 ML) and diBr[4]H (1.2 ML) on Au(111) at a heating rate of 1K/s. The background signals, recorded on clean Au(111) are also displayed. The spectra are offset for clarity.

Based on the experimental observations on various molecules, the Br desorption process can be explained. Two competing reaction paths occur, namely HBr and H_2 desorption. Their reaction rates are respectively first order and second order with respect to the concentration of atomic hydrogen. They are both limited by the slow release of hydrogen atoms during partial dehydrogenation of the molecule. The barrier for this first step is indeed much higher than the barriers for HBr and H_2 desorption[191]. However, for Br[7]H, HBr production is favored over H_2 production (large step in the H_2 TD signal as soon as HBr production is over). One may argue that HBr formation could be more thermodynamically favored. However, Bronner *et al.* [191] performed DFT calculations on the desorption of H_2 and HBr and they found that similar energies are needed in both cases. It seems more probable that this effect is simply due to kinetics: because of the dependency of the two competing processes with respect to the concentration of atomic hydrogen and considering a similar barrier of desorption for both H_2 and HBr, the desorption rate will be larger for HBr. For molecules with a much higher dehydrogenation temperature such as Br[4]H and diBr[4]H, no steps are observed in the TD signals of H_2 and HBr and the desorption of both processes occur in parallel. At higher temperature, both processes are thermodynamically favored and it seems that kinetics does not dominate anymore.

In summary, although all molecules experience two dehydrogenation steps, they appear at various temperatures. Consequently, different Br desorption temperatures, dictated by the specific partial dehydrogenation process, are observed for different molecules. Because Br requires H to desorb, some of the molecules must dehydrogenate at least partially. In other words, after Ullmann coupling, when the Br atoms are finally desorbed, the molecules have already undergone structural modifications. This could be avoided by removing the Br atoms with atomic hydrogen gas[191].

4.3 Conclusion

Successful Ullmann coupling of Br[4]H on Cu(100) leads to diastereoselectivity. It is induced by the low inversion barrier of the two parts of a bis[4]H, allowing the molecules to choose the best steric configuration on surface. Diastereoselectivity was not observed after coupling of Br[7]H because bis[7]H has a higher inversion barrier. Bis-[7]H(sol), synthetized in solution prior sublimation, formed identical structures on Au(111) and Cu(111). The first structure was made of rows of bis[7]H enantiomers with alternating handedness. The second was made of parallelograms built with two *meso*-bis[7]H. Adsorption of Br[7]H at ML coverage induces the formation different structures on Au(111) and Cu(111) but leads to successful coupling on both surfaces. The presence of Br prevented the self-assembly of the coupling products (bis[7]H (surf)) on Cu(111). On Au(111), self-assembly was observed, but one of the ordered-structure formed by bis[7]H (surf) was different with respect to the assembly observed for bis[7]H (sol). The presence of Br atoms on surface could be responsible for this modification. It could also be due to a reconstruction of the Au(111) surface during the coupling, to cyclodehydrogenation of the molecules after annealing or to the formation of different stereomers on surface compared to those observed after adsorption of the sublimated bis[7]H(sol). The different hypothesis will be analyzed by using TOF-SIMS.

In the case of on-surface synthetized bishelicenes, it was shown that, as observed previously for DBBA[191], cyclodehydrogenation allows the desorption of Br in the form of HBr. The cyclodehydrogenation also occurs for bis[7]H(sol). The different values reported for the desorption temperatures of Br are explained by the different dehydrogenation temperature of the helicenes which depends on the presence of steric overcrowding in their backbone.

Ullmann reactions on metal surfaces are widely studied and awareness should be raised on the fact that Br desorption, at least on Au(111), implies small structural modifications of the studied molecules. These modifications cannot always be easily observed with STM and XPS.

III.5. Autocatalytic decomposition of helicenes

Autocatalytic reactions are observed in many area of physics, chemistry and biology such as catalysis, radical polymerization, nuclear chain reactions or protein mediated-biosynthesis[202]. The common aspect in all those reactions is the fact that a product/radical produced during the reaction is used as a catalyst and therefore enhances the process rate exponentially with time. An example from surface chemistry is "surface explosion"[12]. During the last 45 years[203–205], surface explosion on metal surfaces in UHV was observed for many oxygen-containing molecules, such as carboxylic acids[12,147,203–208], H_2O[209], NO/CO[210,211] and NO/H_2[212–214]. Other templates such as oxygen-covered Pd[215] or Rh-based catalysts (at atmospheric pressure)[216–218] have also been studied. The reaction was explained by the formation of vacancies (denoted here with an asterisk $*$) in the close packed layer of oxygen-containing molecules (*A*). These vacancies are in fact surface sites, which act as catalyst for the decomposition and then create new vacancies. It is well described by the equation (22)[12].

$$A + n * \rightarrow B(g) + (n+m) * \tag{22}$$

where *n* and *m* are positive integer numbers and *B* is a product of the reaction which desorbs in the gas phase (*g*). At the beginning of such autocatalytic reactions, the decomposition of adsorbed molecules at saturation coverage is inhibited by the presence of the neighboring molecules which stabilize each other. Upon annealing to a certain temperature, which is higher than the regular decomposition temperature of the isolated molecule[147,206], a reaction site on the surface becomes available to start the decomposition. This initiation step produces more active sites which leads to an exponential increase of the decomposition rate. The difference with standard decomposition is that the active sites are needed for the decomposition are also produced by the reaction.

This work presents the first autocatalytic decomposition of oxygen-free molecules for which the reaction path is even more complex. Br-helicene, a type of helical polycyclic aromatic hydrocarbons containing only C, H and Br but no O, are used. These molecules are deposited on an oxygen reconstructed copper surface: (2√2×√2)R45°-O-Cu(100) [219,220]. In this case, the oxygen coverage, molecular coverage and vacancies in both the oxygen and molecular layers are potentially involved in the mechanism. By comparing different oxygen-free molecules on a well characterized O/Cu(100) surface, the present study highlights new key parameters to obtain surface explosion. This reaction is often studied for the formation of certain reactions' products[203] or for its enantiospecificity[206,207], etc. In addition, this reaction is fast and complex and getting insight into the kinetics and thermodynamics of this process is important for the understanding of autocatalytic reactions and heterogeneous catalysis. Finally, this study aims to obtain new information about chemical reactions on oxygen-covered metal surface. Nowadays, new electronic devices and industrial process call for surface functionalization obtained via on-surface chemistry. The decomposition of polycyclic aromatic hydrocarbons on O/Cu(100) presented here should raise the awareness to the fact that many metal oxides, in particular the oxide of the noble metal copper can be relatively easily reduced by carbon, a phenomenon which was employed already in the Bronze age (about 3000 B.C.) to produce pure metallic copper.

5.1 Autocatalytic decomposition of bromoheptahelicene on O/Cu(100)

The oxygen layer was created using O_2 (gas) at 573 K followed by a 5-minutes post-annealing at 573 K. The coverages of molecules and oxygen were determined from the integrated C1s and O1s XPS intensities. A coverage of one monolayer (1 ML) corresponds to a saturated layer. For all molecules used in this study the saturation to 1 ML was determined by either i) confirming that further sublimation does not lead to an increased amount of carbon (Br-pyrene, Br-tetraphenylene, diBrbianthracene, diBranthracene), or by ii) desorption of the multilayer by annealing to 348 K for Br[7]H and to 413 K for Br[4]H. The coverage of [7]H, bis[7]H and diBr[4]H was assigned by comparing the amount of carbon measured for this molecule with 1 ML of Br[7]H and Br[4]H respectively because they have the same number of C atoms. As mentioned previously, for more than 1ML of Br[7]H, the excess easily desorbs with annealing at low temperature (348 K), much before the explosion process and does not affect the surface explosion process (Figure A. 14). Therefore, a nominal 1.0 ML was assigned for Br[7]H to all coverages above saturated ML. It avoids confusions in the simulation. The same was done for [7]H above ML coverage.

5.1.1 *General observations*

Figure 56 presents STM data (Specs Aarhus 150, at 150 K) of Br[7]H (bromoheptahelicene, $C_{30}H_{17}$) which were sublimated at 453 K on a reconstructed (2√2×√2)R45° O-Cu(100) surface kept at room temperature. Models of this reconstruction were described in detail in refs. [219,220].

The TD spectra[xxx] of 1 ML Br[7]H on 1 ML O/Cu(100) are displayed in Figure 57. Both CO_2 and H_2O are produced at T_{exp}=520 K. The peaks are extremely narrow (about 5 K full width half maximum,

---

[xxx] CO was also measured: it follows the same trend as CO_2. It does not bring any information because mass 28 amu (CO) is a fragment of 44 amu (CO_2) and the detected signal was in the limit of the measured ratio between the CO_2 and CO detected by the mass spectrometer. This ratio was measured by injecting CO_2 in the chamber.

FWHM) and the produced quantity of both species is large. This is one of the signature features of a surface explosion[12] which cannot be associated with the kinetics of a zero, first or second order reaction. Note that H_2 also has a small peak at T_{exp}. It increases considerably only after the explosion: a peak is observed at 741 K. The only sources of hydrogen in the chamber are the helicenes themselves: this last peak corresponds to the complete dehydrogenation of the molecules.

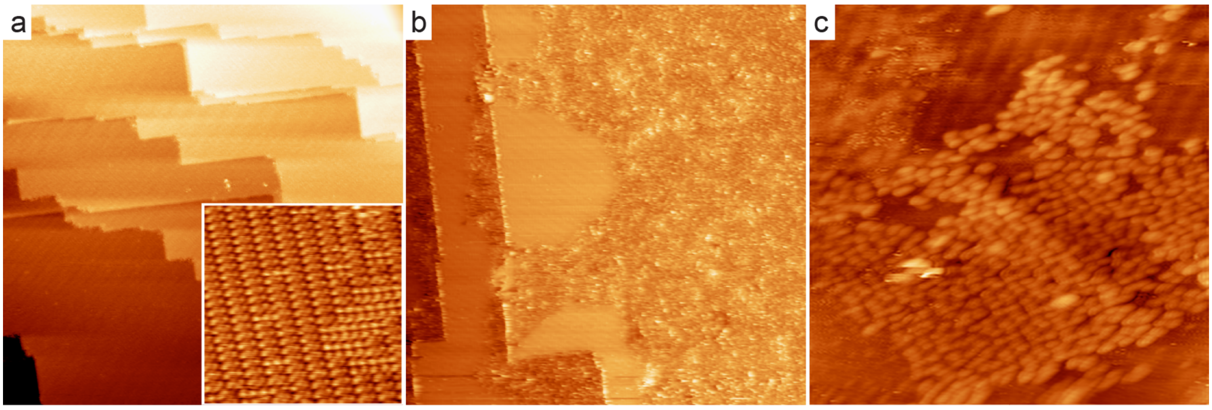

Figure 56: STM images of the (2√2×√2)R45° O-Cu(100) reconstructed surface for a (a) full ML of oxygen (large image: 150 nm × 150 nm, –0.9 V,–1.0 nA, RT; inset: 7 nm × 7 nm, –0.05 V,–3.0 nA, RT), (b) 0.56 ML of oxygen (94 nm × 94 nm, –0.07 V,–1.0 nA) having both the same structure in the ordered area. (c) STM image of 0.27 ML of Br[7]H on 1 ML of O (30 nm × 30 nm, –3.1 V, –0.16 nA, 130 K) annealed at 348K. Dimers of molecules are observed.

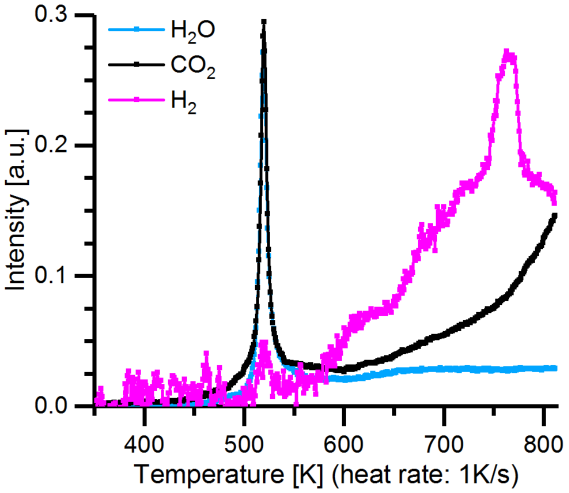

Figure 57: TDS graph of 1 ML of Br[7]H on 1 ML of O on Cu(100), presenting the evolution of the masses 44 (CO_2),18 (H_2O) and 2(H_2) amu as a function of the temperature (heating rate 1 K/s).

5.1.2 Influence of the oxygen and molecular coverage

The importance of vacancies in the autocatalytic decomposition process was discussed above. In this study, two types of vacancies are present: V_{ox} in the oxygen layer and V_{mol} in the molecular layer. This brings us to the following question: does the explosion depend on the molecular and/or on oxygen coverage? To answer this important question, the coverage of both oxygen and molecules are varied separately. One expects to observe the second characteristic aspect of a surface explosion[12,147]: a peak shift to higher temperatures as the coverage increases.

Figure 58 displays series of TD spectra where the coverage of molecules and oxygen is varied. The explosion temperature T_{exp} of both H_2O (18 amu) and CO_2 (44 amu) increases with the coverage of oxygen. With increasing oxygen coverage, the TD signal becomes narrower. Note that T_{exp} is always a bit smaller for H_2O than for CO_2: for 0.76 ML O, $T_{exp}^{H_2O}$ is 499 K and $T_{exp}^{CO_2}$ is 503 K and for 0.82 ML O, $T_{exp}^{H_2O}$ is 508 K and $T_{exp}^{CO_2}$ is 512 K (Figure 64). Therefore, water starts to be produced before carbon dioxide. H_2 (2 amu) has a small peak at T_{exp} only when the coverage of oxygen is 1 ML but does not indicates any explosion behavior. These behaviors for the different masses were observed for all measurements presented in this work: therefore, only CO_2 will be discussed in the rest of this work.

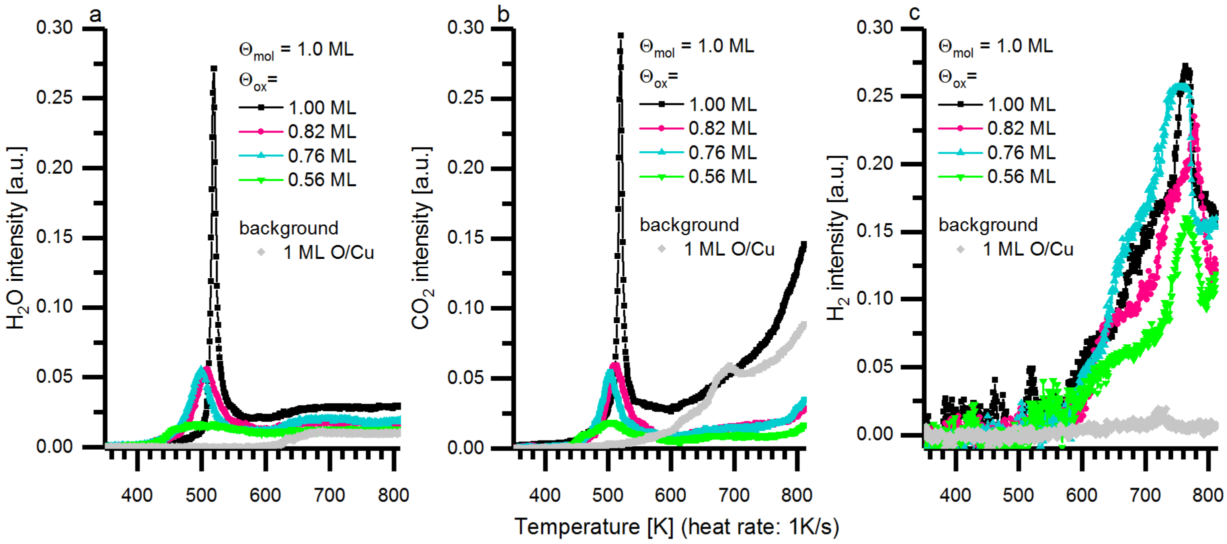

Figure 58: TD spectra (heating rate 1 K/s) of Br[7]H/O/Cu(100) of the masses 18 (a), 44 (b) and 2 amu (c) for a saturated ML of Br[7]H (θ_{mol} = 1) and various O coverage (θ_{ox}). (a, b) The autocatalytic decomposition of Br[7]H/O produces both H_2O (a) and CO_2 (b). In both cases, the explosion peak gets sharper, more intense and occurs at a higher temperature when the coverage of oxygen increases. (c) For H_2, a small peak is observed for 1 ML of oxygen (black curve).

Moreover, the explosion temperature does not change significantly with the coverage of molecules (Figure 59). The intensity of the TD signal just becomes lower as the coverage of Br[7]H is reduced. The smaller the molecular coverage is and the broader is the tail after the explosion temperature. This corresponds to a normal combustion of helicenes as will be discussed in the Figure 62. The autocatalytic decomposition is indeed limited because only a few islands of ordered molecules are present on the surface (Figure 56c). This quenches the reaction. The explosion temperature is not significantly affected by the coverage of molecules (Figure 59). It means that the limiting factor for the autocatalytic production of CO_2 and H_2O is the quantity of oxygen vacancies. A full ML of oxygen corresponds to about 7 oxygen atoms and 10 Cu atoms from the 1st layer per nm^2. The footprint of a molecule on the surface is about 2.1 nm^2. At molecular coverages above one ML (Figure A. 14 in the appendix), the TDS signal does not change. This is due to the desorption of the multilayer before explosion during annealing as shown with XPS (Figure 60). After TDS, some carbon is still present on the surface but no oxygen anymore.

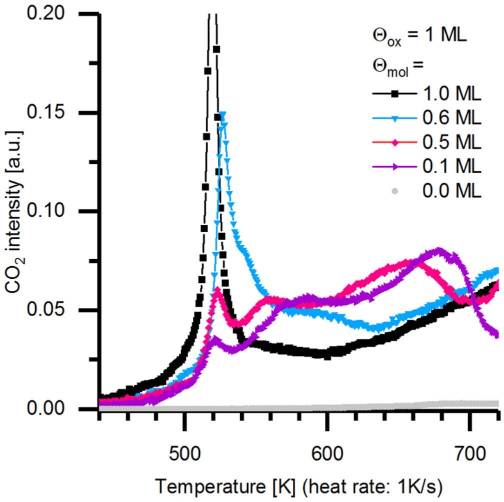

Figure 59: TD spectra at different coverages of Br[7]H (θ_{mol}) on 1ML of O on Cu(100). The explosion intensity decreases and the range of CO_2 production increases with the coverage, e.g. CO_2 is produced between 500 K to 700 K for 0.1 ML of Br[7]H. At all coverages, the explosion occurs around the same temperature. The case with 1 full ML of molecules is the one with the minimum T_{exp}=520 K.

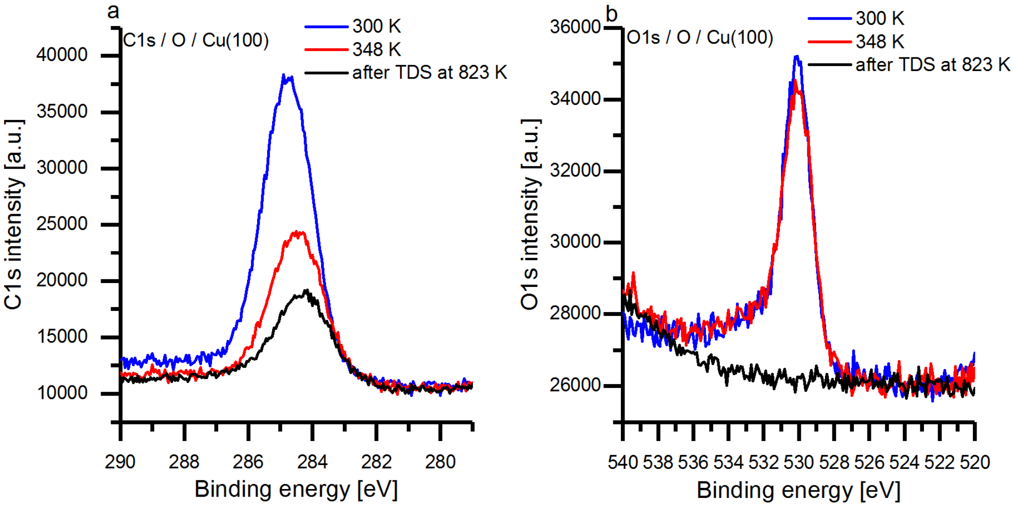

Figure 60: C1s (a) and O1s (b) XP spectra of 1.9 ML of Br[7]H on 1 ML of O on Cu(100) at different temperatures: RT (300 K), after annealing 10 min at 348 K and after the TDS (until 823 K). After annealing at 348 K, both the C1s and O1s peak intensities decrease, due to desorption of the molecules in the second layer. After the TDS, no oxygen is left but a peak of C1s is still observed.

5.1.3 Heating rate

Desorption rates are described by the Polanyi-Wigner equation which is an Arrhenius-type law. In principle the autocatalytic decomposition process also follows this law. The desorption rate was discussed in detail by P.A. Redhead[45] and G. Carter[46]. The desorption temperature and intensity are expected to increase with the heating rate. It is also the case for the catalytic decomposition of Br[7]H on O/Cu(100) (Figure 61). The higher the heating rate is, the higher T_{exp}. The increase of the CO_2 and H_2O intensities with increasing heating rate is simply because the TD signal is proportional to the amount of desorbing material per unit time $-d\theta/dt$.

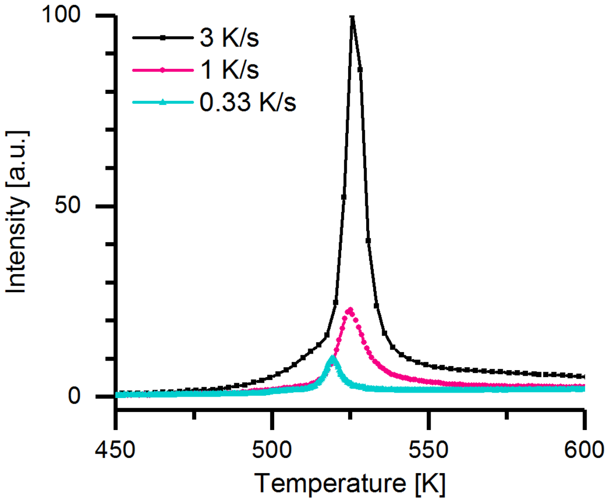

Figure 61: TD spectra at 44 amu for 1 ML of Br[7]H on 1 ML of O on Cu(100) for different heating rates. T_{exp} increases from 519 K for 0.33 K/s to 525 K for 1 K/s to 527 K for 3 K/s. At higher heating rates, the same amount of material desorbs in a shorter time, leading to a more intense signal. This trend was also observed for 18 amu.

5.2 Comparison with heptahelicene on O/Cu(100)

As comparison (Figure 62), TDS of [7]H (heptahelicene, $C_{30}H_{18}$) on the oxygen reconstructed Cu(100) surface was measured. CO_2 is produced between 473 K and 728 K with a maximum at 678 K. H_2O also starts to be produced around the same initial temperature. H_2 follows the same trend as water. No surface-explosion is observed in this case.

The coverages of [7]H and of oxygen were then varied independently (Figure 63). The desorption of H_2O and CO_2 are in the case of [7]H different from one another. They are also much wider and starts at lower temperature than observed for Br[7]H. This might be due to the need of an initiation step, the presence of the first vacancy, for the autocatalytic decomposition of Br[7]H. Autocatalytic behavior is not observed for the combustion of heptahelicene.

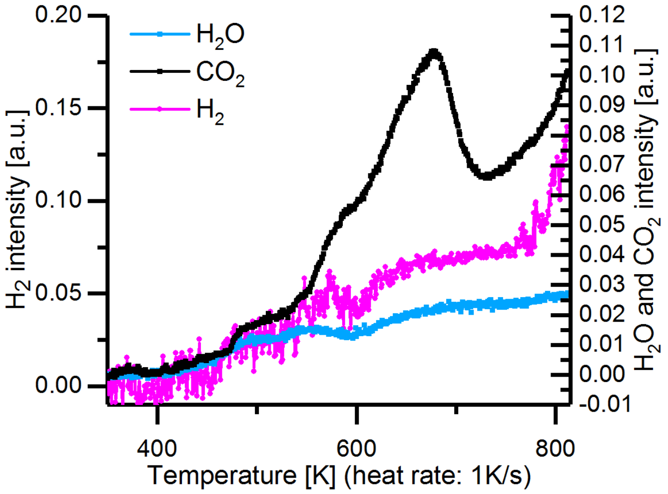

Figure 62: TDS graph of 1 ML of [7]H on 1 ML of O on Cu(100), showing the evolution of the masses 44 (CO_2),18 (H_2O) and 2 (H_2) amu as a function of the temperature (heating rate 1 K/s).

When more molecules are on the surface, more CO_2 and water are produced. The CO_2 is also produced at a lower temperature and more constantly over a broad range of temperatures. This might be due to the presence of more carbon and hydrogen (from the molecules) on the surface which are easier to use by the oxygen for desorption as water or carbon dioxide. The attentive reader can notice that the shape of the curve observed for CO_2 in the case of the normal combustion of [7]H is the same as the one observed for Br[7]H when a low quantity of Br[7]H is on the surface. In this case, the auto-catalytic decomposition is replaced by a normal combustion. At low coverage, the molecules are not stabilized anymore above their usual decomposition temperature by the presence of neighboring molecules. When less oxygen is on the surface, less CO_2 is produced but more H_2O. Since water needs only one oxygen for its formation and carbon dioxide needs two, the probability is higher for water to form. The absence of Br prevented the autocatalytic decomposition to occur. This was confirmed by studying pentaindenocorannulene (PiC) on O/Cu(100): the molecule, containing only C and O, did not autocatalytically decompose.

Note that for [7]H, as observed for Br[7]H, the H_2O TDS signal starts at lower temperature than the CO_2 signal (Figure 64). It is particularly significant (between 3 and 15 K of difference) for 1 ML of molecules on sub-monolayer coverages of oxygen. Due to the faster reaction kinetics for molecules on a full ML of oxygen, the effect is much smaller, e.g. the difference in temperature is about 0.5 K for 1 ML of Br[7]H on 1 ML of O. The fact that H_2O is produced before CO_2 is an indication towards the reaction mechanism. It is known that dehydrogenation and cyclodehydrogenation of sterically overcrowded polycyclic aromatic hydrocarbons leads to the formation of C−C bonds and the production of atomic hydrogen.[184,191,198] Such transiently produced atomic hydrogen has been reported to desorb from O/Cu as

H_2O,[221] from Br/Au as HBr,[191] and as HCN from cyano-groups containing species.[222] In the present case, the leading H_2O peak strongly suggests that the atomic hydrogen produced during partial dehydrogenation of sterically overcrowded Br[7]H leads to the desorption of H_2O thereby creating initial vacancies in the oxygen layer.

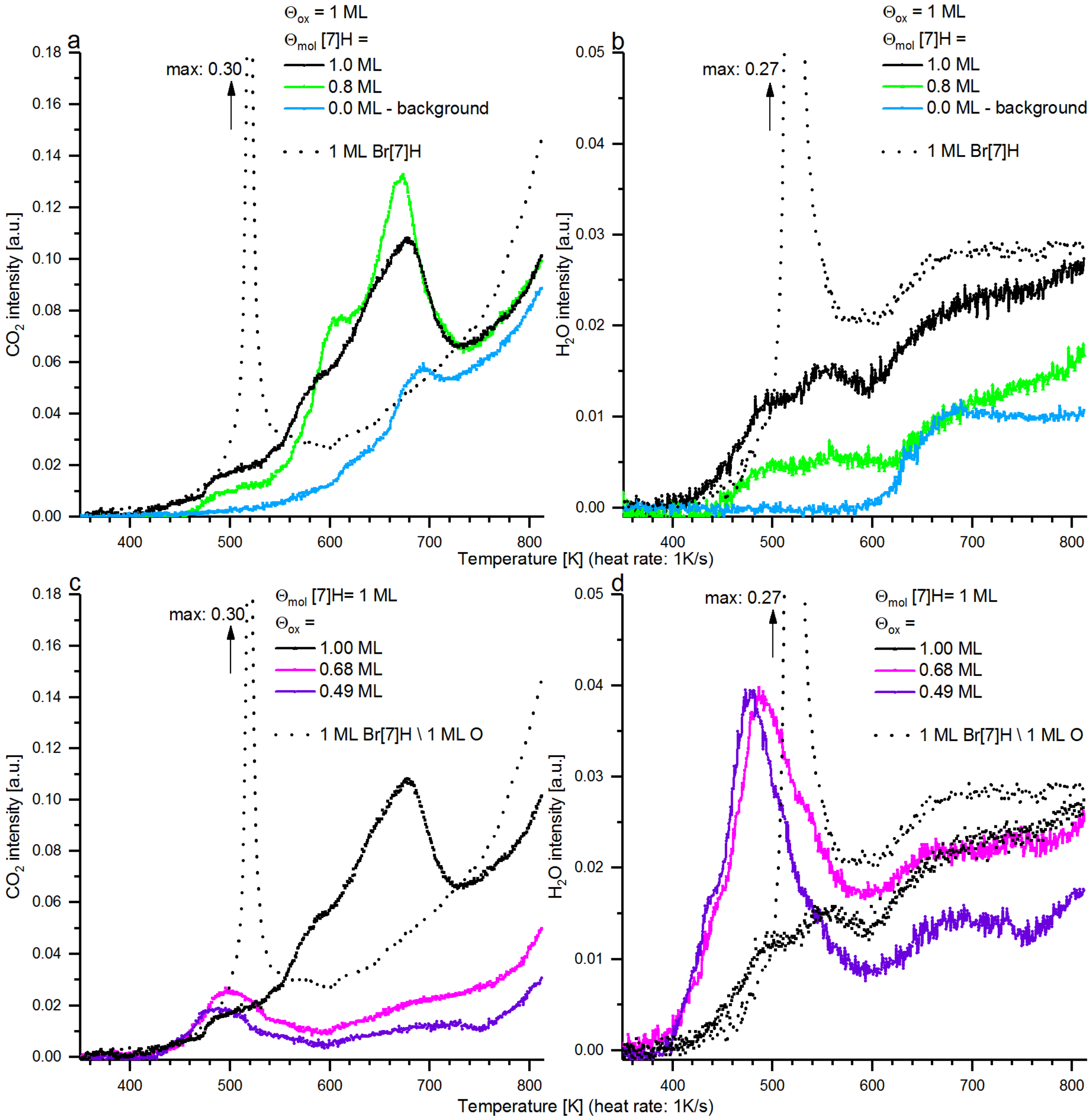

Figure 63: CO_2 and H_2O TDS graphs of [7]H on O/Cu(100) for different molecular coverages θ_{mol} and 1 ML of oxygen (a, b), and for different oxygen coverages θ_{ox} and 1 ML of molecules (c, d). (a, b) As the coverage of molecules increases, the production of CO_2 is reduced and starts at a lower temperature. Nevertheless, more water is produced. (c, d) When the coverage of oxygen increases, CO_2 emission gets wider and increases but the H_2O emission decreases. It also reduces as soon as the CO_2 production starts. The explosion curve for 1 ML of Br[7]H on 1 ML of O/Cu(100) is displayed as a dot line for comparison. Both CO_2 and H_2O desorption happen at a lower temperature for heptahelicene compared to Br-heptahelicene.

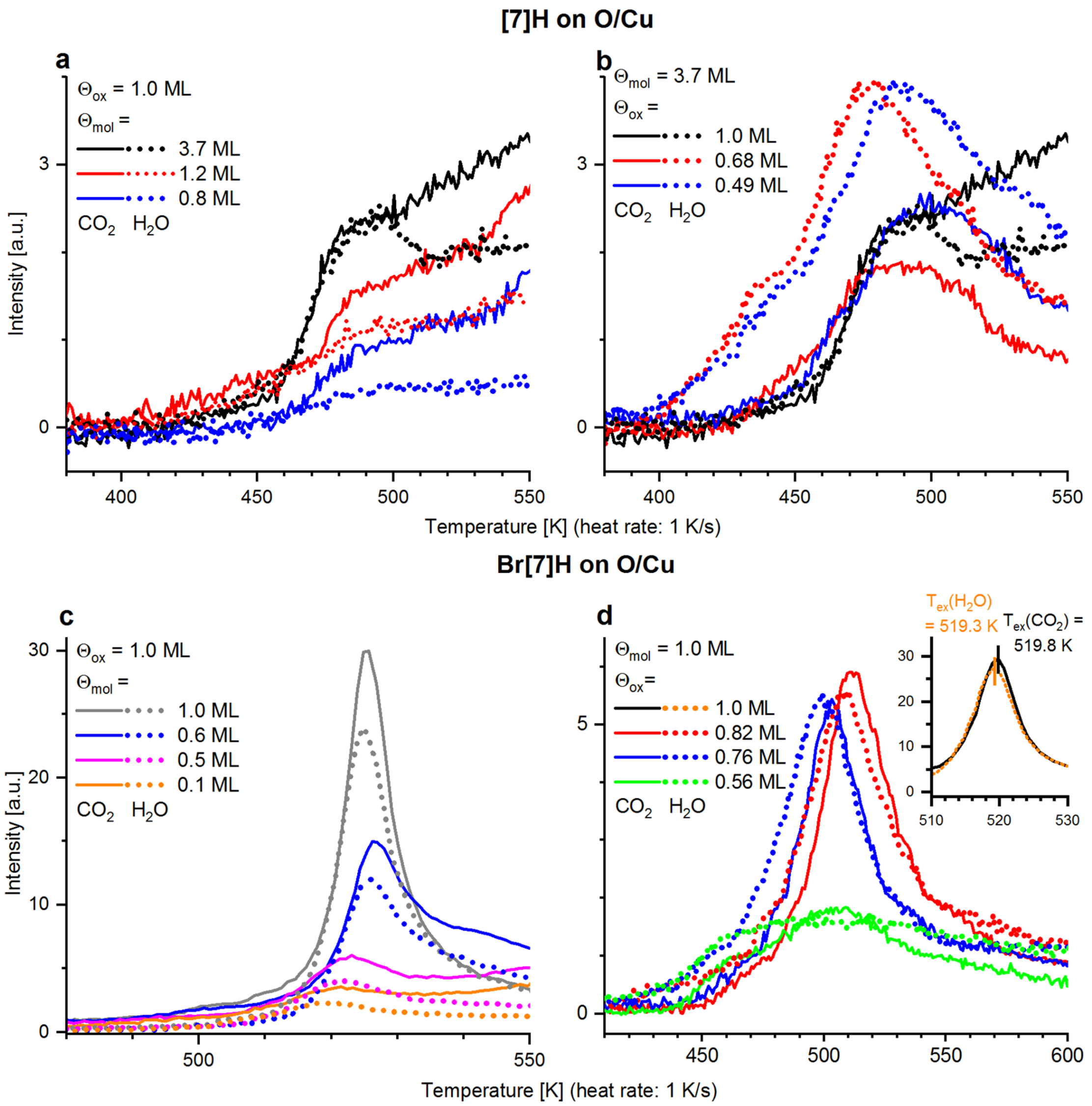

Figure 64: Comparison of simultaneously recorded CO_2 and H_2O TD spectra for [7]H (a, b) and Br[7]H (c, d) as a function of molecular coverage θ_{mol} (a, c) and oxygen coverage θ_{ox} (b, d). H_2O desorption always starts before CO_2, i.e. at lower temperature.

5.3 Influence of bromine on the surface explosion

The Br3p XP spectrum presented in the Figure 65 reveals that the Br atoms start to dissociate from the molecules at 348 K on the (2√2×√2)R45° O-Cu(100) surface, i.e. much before the explosion occurs. In addition, STM shows (Figure 56c) that the molecules form dimers at this temperature. This means that the molecules probably bind to the copper and form an intermediate state. It was already observed for Ullmann coupling on copper without any oxygen layer[50] (paragraph III.4.2.2). After the TDS (up to 823 K), all Br atoms have desorbed.

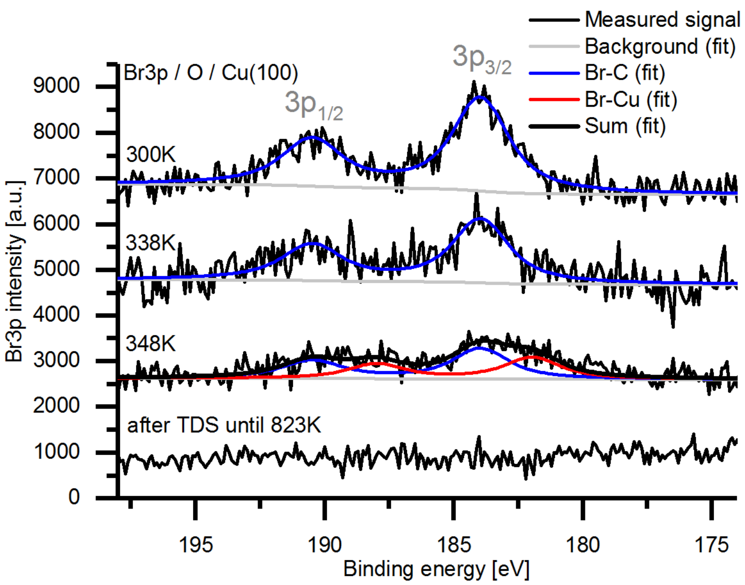

Figure 65: Br3p XP spectrum of 1.9 ML of Br[7]H on 1 ML of O on Cu(100) at different temperatures: at RT (300 K), after 10 min annealing at 338 K and at 348 K and after TDS (up to 823 K). From 300 K to 338 K, the Br3p$_{3/2}$ peak is at 184 eV which corresponds to the presence of C-Br bonds[50]. This means that the Br is still on the molecules. After the annealing at 348 K, a new signal at about 182 eV appears corresponding to the formation of Br-Cu bonds[50]. It means that some of the Br atoms are already detached from the molecules at this temperature. After TDS, no Br is left.

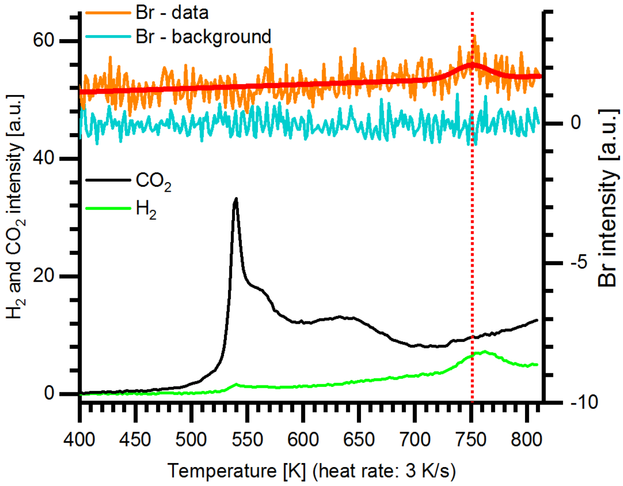

Figure 66: TDS trace of Br[7]H on 1 ML of O on Cu(100), showing the evolution of the masses 44 (CO_2), 2 (H_2) and 79 (Br) amu as a function of the temperature (heating rate: 3 K/s). The Br signal (79 amu) of the background was also measured as a comparison with the data. At 538 K, the explosion is observed. Between 725 and 785 K, an increase of both H_2 and Br (with respect to the background) is observed.

In order to determine if the Br is leaving the surface before, during or after the explosion, Br (79 amu) desorption was measured (Figure 66) together with H_2 and CO_2 with TDS. The Br desorbs from the surface at around 750 K. A peak is also observed in the H_2 at the same temperature. The Br and H desorption are therefore happening at the same time: during dehydrogenation of the molecules, some of the hydrogen are liberated as H_2 whereas some are probably liberated as HBr as observed in[191] and in the study of Br[7]H on Au(111) in the paragraph III.4.2.3. Note that on bare copper surfaces, the C-Br bond in organohalides is dissociated significantly below room temperature and organometallic C-Cu bonds are formed.[11,50,166] On oxygen covered copper surfaces this reaction occurs slightly above room temperature[50,223], *e.g.* at 338 K for Br[4]H/O/Cu(100).[50] For Br[7]H on O/Cu(100), the onset of C−Br bond scission occurs at 348 K, as evidenced by the appearance of a Br3$p_{3/2}$ at lower binding energy (Figure 65). Moreover, it has been reported that the C−C coupling (Ullmann reaction) does not occur on O/Cu.[50,159,223] The fact that the molecules appear as dimers (Figure 56c) strongly suggests the formation of organometallic copper complexes[50,159]. This is confirmed by the C1s XP spectra of diBr[4]H/O/Cu[xxxi] annealed at 348 K (Figure A. 15 in the appendix) exhibiting a signal at 283.2 eV characteristic for organometallic carbon,[224,225] *i.e.* molecules forming C-Cu bonds with the substrate or with Cu ad-atoms, thereby 'anchoring' the molecules after C-Br bond scission.

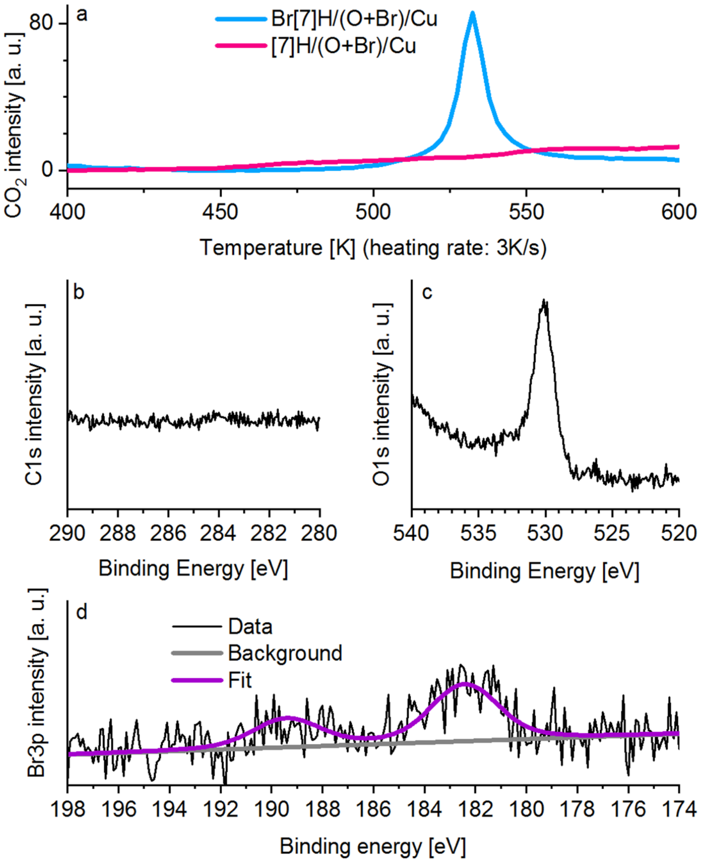

Figure 67: (a) TD spectra showing the CO_2 evolution for 1 ML [7]H and Br[7]H on 1 ML of Br doped O/Cu. Like on normal O/Cu, Br[7]H undergoes surface explosion and [7]H does not. (b, c, d) XP spectra of a carbon free Br-doped O/Cu layer. The Br-doped O/Cu is prepared by deposing 1 ML of Br[7]H on 1ML O on Cu(100) and then annealing 20 min at 633 K in 3×10^{-5} mbar O_2, followed by 5 min post-annealing (633 K). Under these conditions the carbon burns completely but the bromine remains.

[xxxi] diBr[4]H was studied because the ratio of Br/C atoms is larger for diBr[4]H than for Br[7]H and the C1s shift is more pronounced.

The previous experiments showed that the explosion occurs when the Br atoms are dissociated from the molecules (Figure 65), however the atoms are still present on the surface during the explosion. To determine whether the explosion is triggered by the presence of Br or by the "anchoring" of the dehalogenated Br[7]H to the surface, [7]H and Br[7]H decompositions were studied on Br-doped O/Cu. The sample is prepared by depositing 1 ML of Br[7]H on O/Cu(100) and annealing 20 min at 633 K in 3 × 10^{-5} mbar O_2, followed by 5 min post-annealing (633 K). Under these conditions (Figure 67b-d), the carbon burns completely but the bromine remains. As seen in Figure 67a, in presence of Br atoms on the surface, [7]H does not undergo an autocatalytic decomposition whereas Br[7]H does. Br has therefore no catalytic role in this process, it is the anchoring of the molecule which is required for a surface explosion.

5.4 Computational modelling: insights into the autocatalytic decomposition

The explosion of oxygen-based molecules on surfaces, described by the equation (22)[12] depends on vacancies, i.e. surface sites, formation.

The reaction rate r_A therefore depends on the coverage of molecules θ and the number of vacancies (1 - θ) as follow[147,206]:

$$r_A = -\frac{d\theta}{dt} = \nu\, \theta(1-\theta)^n e^{-E/RT} \tag{23}$$

where ν is the attempt frequency and E is the activation energy for desorption, T is the temperature and R the gas constant. *n* is a positive integer number corresponding to the reaction order of vacancies in the decomposition reaction of A. Note that, in order to observe the autocatalytic process, it is important that the molecules are stabilized above the temperature at which a single molecule would usually decompose[147,206]. This can occur if single molecules are less stable than those in a closed-packed layer. In that case, the surface concentration of vacancies (1–θ) would enter the rate equation. For a close-packed layer, this term is zero. Since desorption produces vacancies, the reaction rate is amplified exponentially and leads to the autocatalytic behavior.

In the case of oxygen-free molecules on O/Cu(100), the reaction path and rate are a bit more complex. The oxygen coverage θ_{ox}, molecular coverage θ_{mol} and vacancies both in the oxygen ($1-\theta_{ox}$) and molecular ($1-\theta_{mol}$) layers might be involved. A generalized form of the reaction rate is given in equation (24):

$$-\frac{d\theta}{dt} = \nu\, {\theta_{Ox}}^{l}(1-\theta_{Ox})^{m}{\theta_{mol}}^{n}(1-\theta_{mol})^{p}e^{-E/RT} \tag{24}$$

where l, m, n and p are exponents which determine the order of the reaction, i.e. the influence of the oxygen, molecular coverage and vacancies on the explosion process, respectively.

Equation (24) was applied to both [7]H and Br[7]H (Figure 68). [7]H does not decompose autocatalytically: m = p = 0 because the rate does not depend on the vacancies formation. The model reproduces properly the initial temperature burst around 470 K which is consistent with the obvious assumption that the TDS signals at high temperature correspond to later decomposition processes. For the modelling of the Br[7]H, m>0 and p=0, because the autocatalytic decomposition depends only on the vacancies in the oxygen layer but not in the molecular layer. It is not possible to know how many oxygen vacancies are needed for the Br[7]H dissociation. To keep the model as simple as possible we assumed that, the reaction was first order with respect to the oxygen coverage: l = m = 1. This simple model of the explosion as a function of the oxygen coverage reproduces quite well what was experimentally observed (Figure 68). It could be that m is higher in reality, i.e. more than one oxygen vacancy is needed for a Br[7]H to explode (as was observed for tartaric acid (TA) which needs two vacancies[12]). The behavior of both [7]H and Br[7]H could be reproduced using the same energy barrier (150 kJ/mol) and attempt frequency (10^{15} Hz). The attempt frequency[12] value for the explosion modelling is in the range of what is usually used in the literature. 10^{13} Hz and an energy barrier of 131 kJ/mol also reproduce correctly the overall experimental behavior. However, the present choice of 10^{15} Hz reproduces slightly better the oxygen coverage dependency.

In the experimental data, T_{exp} is constant or slightly increasing with a decreasing coverage of molecules, i.e. almost independent of the molecular coverage. Thus, the exponent of the molecular coverage n must be a fractional order rate in the model. Therefore, n=1/3 was chosen because it fits best the experimental data. When using the model to simulate the explosion as a function of the molecular coverage, the temperatures of the initial peaks are almost the same as observed in the experiment. Nevertheless, the model does not grasp the correct variation of the peak intensities. The model is also exclusively made to simulate the first step/peak. The later steps observed at low molecular coverages correspond to later decomposition processes, which are not of interest here. They could be caused by the formation of molecular islands. Depending on their size, the islands would give rise to several independent explosion processes which would stop as soon as all educts in one island are depleted from the surface. It is not clear weather molecular islands really form or if a 2D gas of molecules, acting differently as a full layer of molecules, is present on the surface.

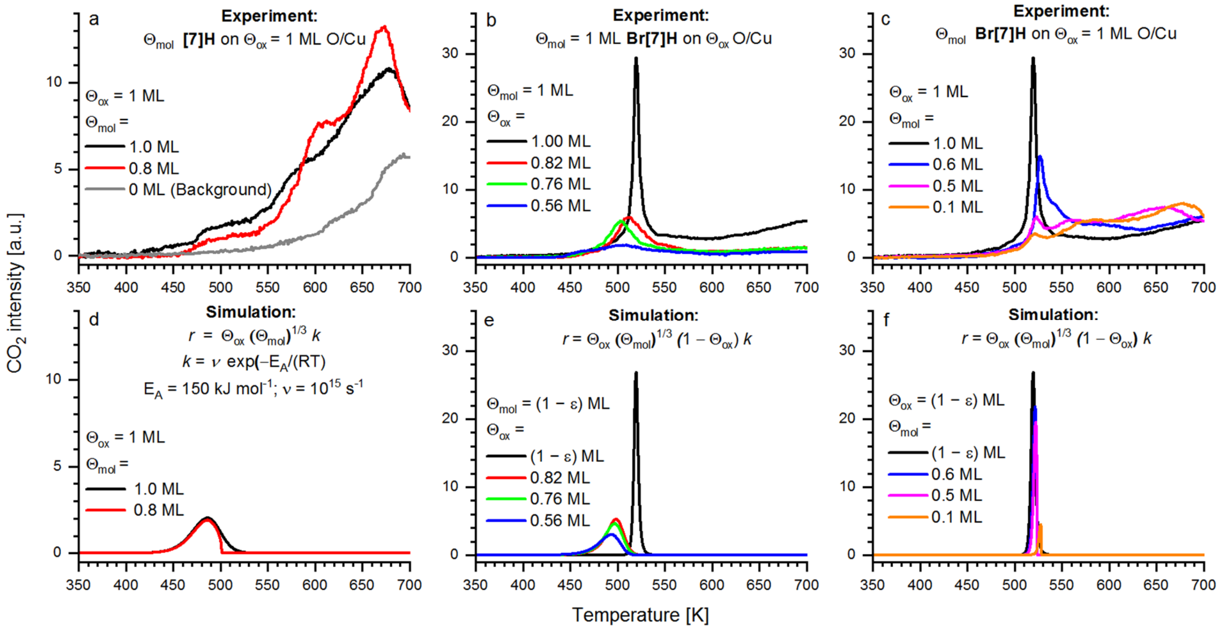

Figure 68: Measured data (a-c) and corresponding models (d-f) for several coverages of [7]H on 1 ML of oxygen (a, d), for 1 ML of Br[7]H (b, e) on different coverages of oxygen and different coverages of Br[7]H on 1 ML of oxygen (c, f).

Note that with this model, when the coverages of molecules and/or oxygen are equal to 1, the (1–θ) terms becomes zero: the adsorbate stays stable and rate is zero. To overcome this problem, the full layer was approximated as (1–ε), with $\varepsilon = 10^{-5}$, which corresponds to the initial defects which are always present in the layers. Mhatre *et al.*[12] included in their model an initiation term allowing to model the creation of a vacancy. They demonstrated that this step was slow, irreversible and independent of surface defects. In order to keep it as simple as possible, the model presented here does not include an initiation process. However, the same behavior can also be obtained by including a second process leading to initiation as in ref.[12]. To reproduce the experimental behavior, the initial term must lead to a reduction of the oxygen coverage by $\varepsilon = 10^{-5}$ at the temperature of autocatalytic decomposition.

5.6 Decomposition of other polycyclic aromatic hydrocarbons

To better understand the explosion mechanism, other PAH were tested to determine which factors lead to an autocatalytic decomposition (Figure 69). The explosion of Br[7]H as well as the normal decomposition of [7]H were extensively discussed above. The anchoring to the copper surface due to the rupture of the C-Br bond was found to be important for the explosion mechanism to happen. Br[4]H and diBr[4]H, whose helicity is due to the repulsion between the H atoms indicated in blue in the Figure 69, also decompose autocatalytically (Figure 70 and Figure A. 16 in the appendix). The presence of two Br instead of one at different position on the helicene decreases T_{exp} from 551 K to 538 K. The explosion of 9-Br[7]H which has a Br atom at a different position than 2-Br[4]H occurs only at 527 K. It means that the number and presence of Br has an influence on the kinetics of the phenomenon. It could be due to a different distance between the Br-atom and the copper surface depending on where Br is situated on the helicene backbone. This has an impact on the C-Cu bond formation and probably also on the formation of intermediate organometallic states (e.g. dimers for Br[7]H).

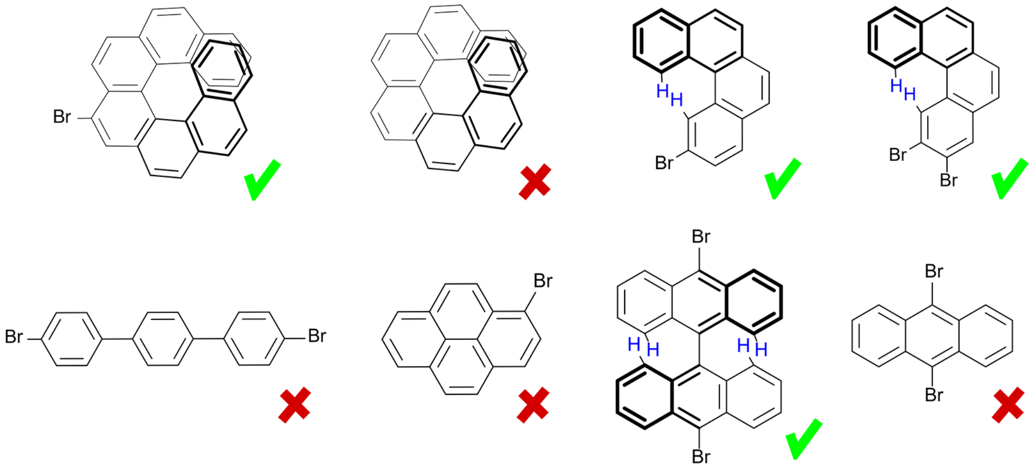

Figure 69: Molecular structures of the molecules for which the decomposition was studied. From left to right: 9-Br[7]H, [7]H, 2-Br[4]H, 2,3′-diBr[4]H, 4,4'-diBrterphenyl, 1-Br-pyrene, 10,10′-diBr-9,9'bianthracene, 9,10′-diBranthracene. A green check means that an autocatalytic decomposition was observed whereas a red cross indicates the absence of explosion, that is, standard combustion. For the sake of clarity, hydrogen atoms at the rim of the molecules were not drawn, only those which are encountering a stronger steric repulsion and are candidate for cyclodehydrogenation are highlighted in blue. Note that PiC decomposition was also studied and did not lead to an explosion.

As a comparison, other PAH with Br and selected characteristic were analyzed. Unfortunately, Br-benzene, the simplest of all PAH, could not be successfully adsorbed at room temperature on O/Cu(100). Dibromoterphenyl was therefore analyzed: the observed decomposition was not autocatalytic[xxxii] (Figure 70). It was therefore clear that the anchoring was a necessary but not sufficient condition for the surface-explosion. Many differences between dibromoterphenyl and helicenes exist. Firstly, it is not made of ortho-fused benzene rings. In addition, it is more or less planar (absence of strain). In the case of tetrahelicene, the strain and the helicity are induced by the presence of hydrogens atoms at carbons No. 1 and 12. The steric repulsion between them would be too strong if the molecule would be planar. This applies also to larger helicenes. The strain energy can be quite important: According to

---

[xxxii] Another example came from the literature: Lin et al.[266] performed TDS on CH_2CHBr and CH_3CHBr_2 on O/Cu(100), in order to study their reaction products. In both cases, no autocatalytic behavior is visible in their results. However, these results cannot really be considered in our work because the quantity of oxygen deposited on surface was in this case between 15 and 30 L (about 0.1 ML). It is far too low to observe the presence of an autocatalytic decomposition.

theoretical calculations, [7]H is less stable than [7]phenacene (1,2;9,10-dibenzopicene) by about 23 kcal/mol[226].

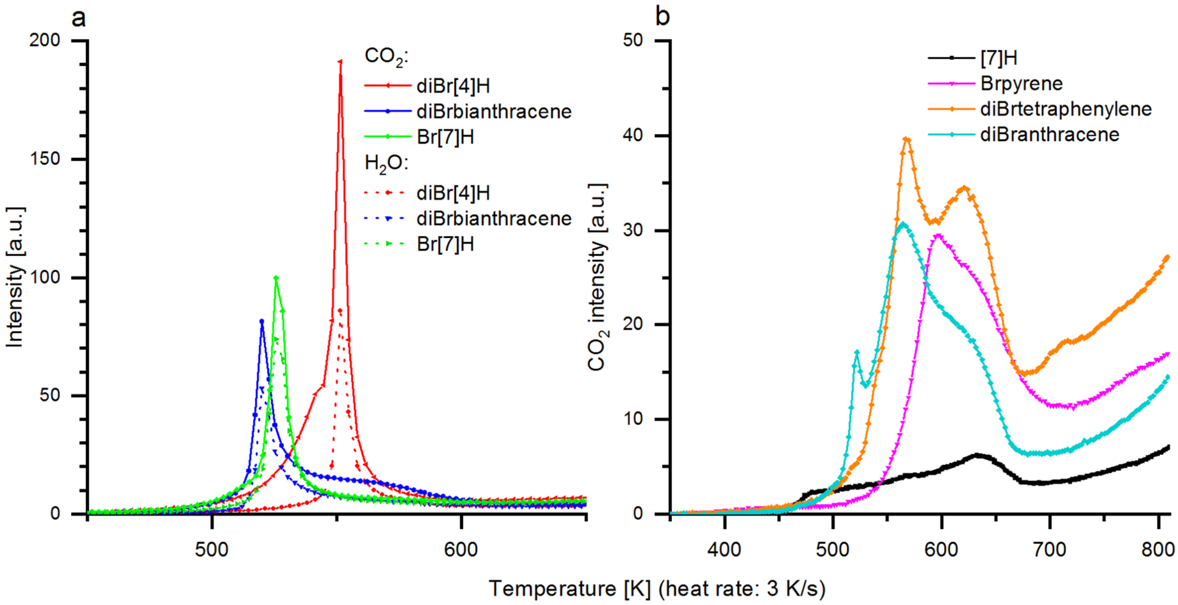

Figure 70: TDS traces showing the autocatalytic decomposition of Br[7]H, diBr[4]H and dibromobianthracene (a) and the non-autocatalytic decomposition of [7]H, Br-pyrene, diBrtetraphenylene and diBranthracene (b). H_2O (dash line) and CO_2 (solid line) were measured for a heating rate of 3 K/s.

In order to test the importance of the steric overcrowding (giving rise to the helical strain in helicenes), a planar PAH Br-pyrene, was tested. Br[4]H explodes but Br-pyrene which also possess four benzene rings and one Br atom does not (Figure 70 and Figure A. 16 in the appendix). Nevertheless, DBBA, which is not planar[227,228], decomposes autocatalytically (Figure 70 and Figure A. 16 in the appendix) on the oxygen reconstructed Cu(100) surface. As in helicenes, the proximity of the hydrogen atoms at the inner rim of both anthracene parts induces steric overcrowding. New C−C bonds between the anthracene units could be easily formed during cyclodehydrogenation.[184] As a comparison, 9,10′-dibromoanthracene (DBA) with two Br atoms but only one anthracene unit, i.e. without strain, was tested. It did not decompose autocatalytically. Consequently, we identify the strain as a necessary condition for the explosion. Note that C-C coupling of diBrA would lead to steric overcrowding like in diBrbiA.[184] Therefore the absence of autocatalytic decomposition of diBrA is further evidence against Ullmann or C-C coupling on the O/Cu substrate.

For both helicenes and DBBA, a way to reduce the strain energy on surface, using the thermal energy provided by the annealing is to form planar molecules by cyclodehydrogenation, i.e. formation of an aromatic ring accompanied by hydrogen removal. This occurs on metal surfaces for both molecules[xxxiii]. It was indeed observed for a helicene derivative *(P)*-benzo[2,1-g:3,4-g']dichrysene on Ag(111) [198] that, upon annealing to 520 K, the molecules can undergo a Diels-Alder cycloaddition and dehydrogenation, followed by C-C bond rupture and hydrogen shift leading to the formation of a flat 6-phenyldibenzo[a,g]coronene. Further annealing up to 670 K leads to cyclodehydrogenation and the formation of flat dibenzo[a,m]indeno[1,2,3-ef]coronene. It is even simpler for smaller helicenes such as pentahelicene: the molecule becomes flat when enough energy is provided by flash vacuum pyrolysis for the detachment of the two hydrogen atoms (1,14) which are strongly repulsing each other. A C-C bond is formed instead, making the molecule flat (benzo[ghi]perylene)[199]. DBBA undergo cyclodehydrogenation on both Au(111) and Cu(111) [184,192] (at 523 K[192] on copper) forming planar molecules that serve as precursor for carbon nanotubes (CNT) formation. If the same reaction occurs on an oxygen-reconstructed surface, the hydrogen atoms produced during dehydrogenation would react with the oxygen atoms to form H_2O. This would create vacancies in the oxygen layer and provide an initiation step for the explosion process. This can explain why cyclo-dehydrogenation in sterically overcrowded PAHs is required for the explosion. Such explanation is strongly motivated by the observation of earlier H_2O desorption compared to CO_2 (Figure 64).

In summary, two factors are necessary for the surface explosion phenomenon. Firstly, the presence of sterically overcrowded regions in the PAH plays a crucial role as shown by comparing similar molecules with and without strain such as Br[4]H vs bromopyrene or DBBA vs DBA. Interestingly, the literature[184,192,198,199] reports that strained molecules adsorbed on annealed single-crystal metallic surfaces (Au, Cu…), undergo cyclodehydrogenation giving rise to the formation of planar molecules and the production of hydrogen. The same dehydrogenation reaction can probably occur on O/Cu. Gottardi *et al.*[229] demonstrated for instance, that it is possible to grow graphene on an annealed copper oxide layer (1200 K). Our results strongly suggest that the hydrogen atoms produced during cyclo-dehydrogenation of sterically overcrowded molecules react with the oxygen to form H_2O. The desorption of H_2O generates vacancies in the oxygen layer: this is the initiation process. Without this step, the explosion does not happen. Secondly, the presence of an organometallic bond with the copper surface created by the breaking of the Br-C bond is required for the explosion to happen. It could be due to the fact that without this bond, the molecules are more prompt to desorb at high temperature. On the other end, a study of chemisorbed acetylene on Cu(100) [230], with high-resolution electron energy loss scattering (HREELS) and surface-extended X-ray absorption fine structure (SEXAFS) indicated a strong perturbation of the adsorbate with a C-C bond length of 1.41 Å instead of the usual 1.20 Å [231]. The binding of the

---

[xxxiii] On Au(111), the molecules of interest, namely Br[4]H, Br[7]H and diBr[4]H undergo partial dehydrogenation as observed with TDS in the paragraph III.4.2.3.

molecule to the copper in our study is expected to similarly weaken the neighboring C-C bonds in the adjacent benzene ring, which are then easier to dissociate to form CO_2 and to create an autocatalytic reaction. To confirm this mechanism, it would be interesting to know which carbon and hydrogen atoms are used to produce CO_2 and H_2O in the first stage of the reaction. The molecules provide indeed much more C and H than necessary to desorb all the O. An experiment with modified Br-helicenes, replacing the C^{12} atom in the C-Br bond by a C^{13} isotope and replacing the hydrogen atoms supposed to leave during cyclodehydrogenation by deuterium atoms, could shed new light on this question. However, the production of such molecules is most likely synthetically very challenging.

Required property	**Mode of action**
Br-R bond in PAH	Organometallic C-Cu bond → 'Anchoring' of PAH
Sterically overcrowded PAH	Atomic hydrogen produced at lower temperature while C-Cu still intact → Initiation (first vacancies) by desorption of H_2O
Saturated ML of oxygen	Low density of vacancies (active sites) → Increasing rate of combustion after initiation

Table 8: Requirements for an autocatalytic decomposition of organic molecules

In other words, if the molecule is bromo-terminated but has no strain, there is no explosion because there is no partial dehydrogenation and no initiation. Full dehydrogenation of the molecule at higher temperature does not lead to an explosion, probably because different reaction pathways are favored at higher temperature. This explanation is supported by our work on the desorption of Br during Ullmann coupling of brominated helicenes (paragraph III.4.2.3): the production of HBr was differently favored over H_2 production depending on the partial dehydrogenation temperatures of Br[4]H, Br[7]H and diBr[4]H (different kinetics). These molecules show different partial dehydrogenation temperatures and therefore involve different initiation temperatures for surface explosion as verified experimentally (Figure A. 16 in the appendix). If the molecule is not brominated but has strain, surface sites are available for reaction but because the decomposition is independent of the presence of vacancies (as tested in the theoretical model in paragraph III.5.4), the explosion do not occur. A summary of the main findings is given in the Table 8.

5.7 Conclusion

In this experiment, the first surface explosion of oxygen-free molecules was presented. Br[7]H, Br[4]H diBr[4]H and DBBA decompose autocatalytically whereas [7]H, PiC, Br-pyrene, tetraphenylene and DBA do not. All molecules produced H_2O and CO_2 during their decomposition. The explosion depends on the vacancies in the oxygen layer and not on the vacancies in the molecular layer. In addition, to undergo a flash autocatalytic decomposition, oxygen-free molecules need two specificities. Steric overcrowding in the molecular backbone is required because it leads to easier dehydrogenation of the molecules and initiates surface explosion by creating vacancies in the oxygen layer by water formation. The molecules also must be anchored to the surface in order to avoid the desorption of the molecules from the surface upon annealing. Moreover, it could even weaken some of the C-C bonds in the benzene rings of the molecules allowing easier CO_2 production.

Many questions about the presented autocatalytic decomposition still need to be investigated. The first one is about the nature of the decomposition products: what is left from the molecules after explosion? Is it different on O/Cu than on normal Cu? Replacing certain C or H by their isotopes could answer this question and could even tell which H atoms leave during cyclodehydrogenation.

In addition, not so much is known about adsorption footprint of organic molecules on oxygen/metal surfaces. From the literature, adsorption footprints of some of the analyzed molecules[107,178,184] are only known on single crystals surfaces. However, this might have an impact on the autocatalytic decomposition. Then, the autocatalytic decomposition worked with Br but it should work with other halogens or any other functional groups which could easily dissociate and provide an anchor for the molecule on the surface, e.g. a C-N bond. This must be tested, together with the influence of the number of Br atoms and their positions should also be methodically investigated. Another question would be on the influence of the surface. The geometry of the oxygen layer will be different on Cu(110)[232] or Cu(111)[233,234]. Does it have an impact on the explosion? Is the absence of an intermediate organo-metallic compound decisive for the observation of the explosion? The purity of the molecules might also influence the explosion. Would a few percent of Br[7]H in a layer of [7]H on a O/Cu(100) surface be enough to create an explosion? Finally, superenantiospecificity in autocatalytic surface explosion has been demonstrated for tartaric acid on a naturally chiral Cu(643) surface[207]. It would be interesting to see if the enantiospecificity is observed for Br-helicenes on a O/Cu(643), knowing that the vacancies in the oxygen are the limiting factor for the explosion.

Even though many questions are still open, the impacts of this study can be manifold. At first, it should raise the awareness on the easy reduction capability of certain metal-oxides such as copper: in the race for surface functionalization for new devices, many chemical and coupling reactions are now studied on surfaces but this aspect is often neglected. Graphene was for instance produced on oxygen-induced reconstructed Cu(111) by CVD of methane on a hot surface (1200 K)[229]. However, on O/Cu(100), it seems that part of the CuO, at least at the surface, is reduced to Cu by forming H_2O. Furthermore, the present work on the autocatalytic combustion of PAHs on oxygen-covered surfaces is a new type of surface chemistry which include the surface coverage of oxygen in the mechanism. Oxygen is a common participant in numerous heterogeneously catalyzed reactions. This work could help improving our current understanding of autocatalytic surface reactions as well a heterogeneous catalysis.

IV. Curved polycyclic aromatic hydrocarbons

IV.1. Introduction

1.1 Geodesic polyarenes

Buckybowls are curved polycyclic aromatic hydrocarbons made of an ensemble of pentagonal or hexagonal carbon rings. The curvature is based on the impossibility to contiguously place pentagons and hexagons in a plane[235]. A few examples are shown in Figure 71.

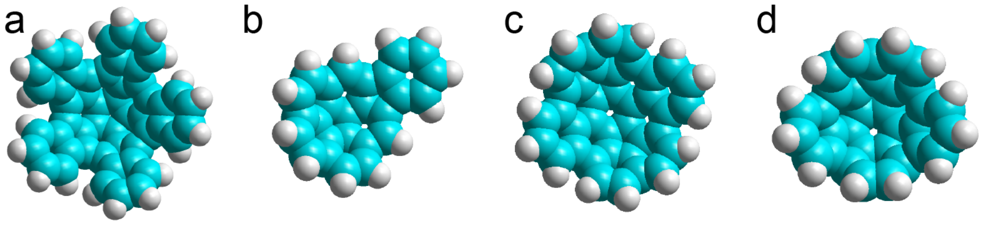

Figure 71: Ball representations of a pentaindenocorannulene (a), monoindenocorannulene (b), $C_{38}H_{14}$ (c) and terphenylcorannulene (d). C atoms are displayed in blue and H atoms in white.

The first buckybowls, corannulene ($C_{20}H_{10}$), was synthetized in 1965[236]. Most of the bowl-shaped fullerene fragments encountered today have a basic core made of corannulene (having a pentagonal central ring) or sumanene, $C_{21}H_{12}$, (having a hexagonal central carbon ring). 20 years after the synthesis of corannulene, the buckminsterfullerene (C_{60}) was discovered by Kroto, Curl and Smalley[237], a finding for which they received the Nobel Prize in 1996.

Understanding the self-assembly of buckybowls would be beneficial for various applications, especially in organic electronics: organic semiconductors[13], photovoltaics[14,15], light-emitting diodes[16,17] and thin film transistors[18]. All these devices require using the proper organic molecules which must provide an adapted work function to allow good charge carrier injection of the charge carriers between the electrodes and the device. This property strongly depends on metallic substrate-molecules interactions[19–22]. Some of the buckybowls can also be useful for medical applications (toxin inhibitors[25], drugs-encapsulation[26,27], nano-membranes fabrications[28]) or as precursors for carbon-nanotubes growth[29,30]. Some buckybowls such as pentaindenocorannulene are possible candidates for hydrogen storage[23] or to act as fullerene receptors[24].

1.2 Previous work

As shown in the literature, buckybowls are expected[8,128,238–240] to adsorb on metal single crystals with a bowl opening-up configuration (tilted or not) because the higher electron density at the convex site causes strong electrostatic interactions with the metal surface. On the contrary, the interaction between the hydrogen atoms at the rim of the buckybowls and the surface is usually weak.

In the case of five-fold symmetric molecules, at densely packed coverage, a tilt of the molecules is often observed. Self-assembly of five-fold symmetric objects is usually less favorable than with other symmetries because of their incompatibility with all 17 crystallographic plane groups. Therefore, if no steric hindrance forces the molecule to express its five-fold symmetry[241], it is usually avoided, for example by inter-digitation[240] or by a substantial tilt of the molecule[242]. For instance, on Cu(110)[8,128] and Cu(111)[128], corannulene adsorbs with a slightly tilted configuration in order to maximize the vdW interaction and reduce the Pauli repulsion with the surface (which would not be the case if the molecule would adsorb bowl opening-up with its central five-fold axis perpendicular to the surface). This tilt gives to the molecule a way to reduce the mismatch between its five-fold symmetry and the symmetry of the surface.

Tilting of buckybowls might be induced by vdW interactions between the convex side of a buckybowl and the metal surface. For instance, on Cu(100), Q. Stöckl at al.[241] showed that monoindenocorannulene (MiC, $C_{26}H_{12}$) form rotational domains made of rows of tilted molecules with a (4,0;–1,4) unit cell. The adsorption footprint of MiC was determined via MM+ force field computation but could not be verified via STM measurements. According to computations[241], the C_{1v} symmetry of MiC is compatible with the symmetry of the surface lattice so the molecule aligns along one of the symmetry axes of the surface.

1.3 Goals and outline

The goals of this chapter on curved polycyclic aromatic hydrocarbons are multiple. The paragraph IV.2 reports on pentaindenocorannulene (PiC) on Cu(100). The self-assembly of this molecule is interesting because it can allow a better understanding of the fundamental principles of intermolecular interactions between five-fold symmetric corannulene derivatives. In this case, the incompatibility between the five-fold symmetry of PiC and the four-fold symmetry of Cu(100) might create an additional “stress” on the assembly. This study also aims to determine the influence of additional indeno-groups on the self-assembly by comparing the results on this molecule with those obtained for MiC. Thermally induced chemical modification of PiC will also be presented: the possible use of these molecules as precursors for carbon nanotube[29] or graphene growth or even for the formation of endofullerenes[243] is appealing.

In a second part (paragraph IV.3), the self-assembly of other curved polycyclic aromatic hydrocarbons will be presented to explore aspects of molecular recognition such as the influence of concave and convex sides in intermolecular interactions between buckybowls. Monoindenocorannulene, terphenylcorannulene (both with C_s symmetry) and $C_{38}H_{14}$ (C_{2v} symmetry) will be studied. In these three cases, MM and EHT studies will be used to improve the understanding of adsorption and intermolecular interactions, needed to adjust the physical properties of organo/metallic systems for organic electronics.

IV.2. From curved to flat PAH via on-surface chemistry: pentaindenocorannulene on Cu(100)

Pentaindenocorannulene[xxxiv] (PiC, $C_{50}H_{20}$, Figure 71) is the largest open geodesic PAH discovered so far and its curvature is larger than C_{60}[244]. It is made of a corannulene core and five indeno-groups and belongs to the C_{5v} point group (symmetry operations: vertical reflection plane and rotation by $\frac{2\pi}{5}$). Molecular packing[xxxv] of PiC in the bulk (3D crystallization) was studied[5] : it forms infinite columns made of dimers based on convex to concave π-π interactions.

2.1 Saturated ML coverage

The mobility of PiC at room temperature on Cu(100) is low. However, self-assembly of these molecules close to monolayer (ML) coverage was already observed at room temperature (Figure 72) without the need of any annealing. No change in the self-assembled structure was observed after annealing up to 473 K. However, slight annealing yielded larger domains. All STM images presented in this paragraph were measured at RT. Note that the tip drift at this temperature is larger than at 50K and the

---

[xxxiv] Information concerning bowl-to-bowl inversion barrier, bonds length and various parameters on this molecule can be found in[267].

[xxxv] Solid state molecular packing of curved aromatic compounds could be classified into three different categories (bowl-in-bowl stacking with all columns oriented toward the same direction or opposite directions or no columnar arrangements at all). The packing mode depends on the length and depth of the bowls. The interested reader can find information in ref.[268].

resolution can also be affected by the relatively high temperature (molecular vibrations, higher mobility of the molecules or lower stability of the assembled structures).

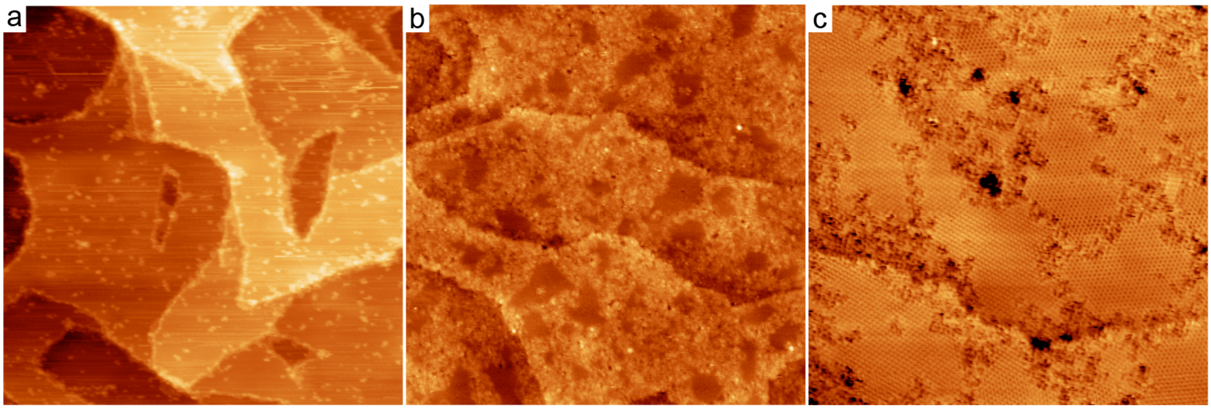

Figure 72: Large scale STM images of different coverage of PiC deposited on Cu(100) kept at RT. (a) θ = 0.02 ML (165.3 nm × 165.3 nm, 25 pA, 3.08 V): a few molecules are observed on the surface and steps edges. (b) θ = 0.70 ML (179.8 nm × 179.8 nm, 25 pA, 2. 839 V): A few ordered domains surrounded by disordered area are observed. (c) θ = 1.30 ML (100.2 nm × 100.2 nm, 2.62 V, 25 pA): ordered domains cover all the surface.

The assembly is made of rows of molecules (Figure 73). Perpendicular rotational domains are observed (Figure 73b): it corresponds to the C_4 symmetry of the Cu(100) surface. This large-range ordered structure is observed already at room temperature (Figure 73 and Figure A. 18 in the appendix) and persists after annealing to 473 K (Figure A. 17 and Figure A. 18).

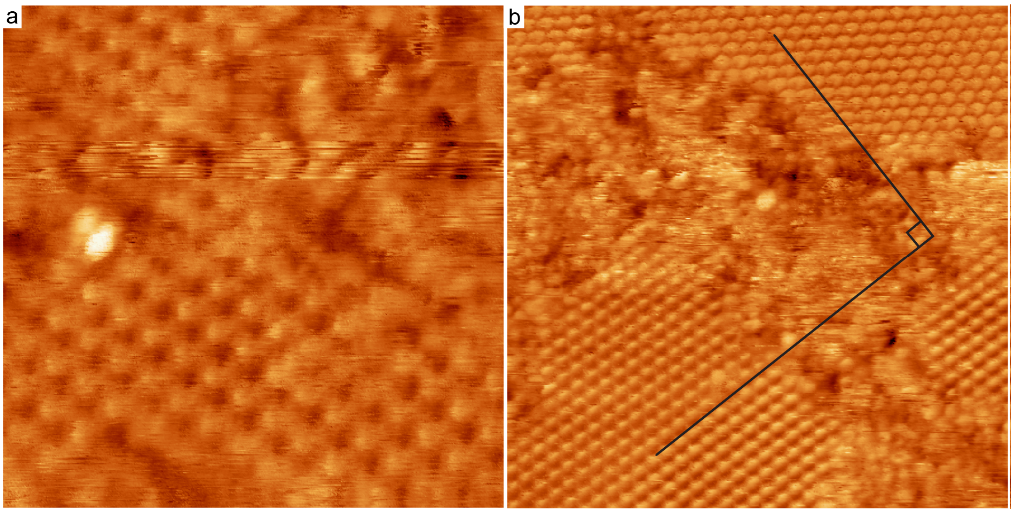

Figure 73: STM images of PiC deposited on Cu(100) kept at RT, showing ordered structures at ML coverage. (a) In each domain, single molecules arrange in rows. Each building block of the row has a non-symmetric contrast with a brighter protrusion on one side (13.3 nm × 13.3 nm, 2.3 V, 24 pA). (b) The molecules arrange in rotational domains which are perpendicular to each other (29.7 nm × 29.7 nm, 2.6 V, 25 pA). The asymmetric contrast of each molecule is also visible in this case.

In each rotational domain, the single molecules are oriented in the same direction and have a non-uniform contrast: a round lobe with a bright protrusion on one side (Figure 73a). A comparison with

EHT simulations (Figure 74) of four possible adsorption configurations allows to exclude the bowl opening-up and bowl opening-down configurations. On the electron density maps of the frontier orbitals, the bright off-centered protrusion is only observed if the molecule adsorbs in a tilted configuration. Five-fold symmetric objects usually try to avoid keeping their five-fold symmetry in their self-assembly by inter-digitation or by a tilt of the molecule[242] for example. PiC tilt on Cu(100) at saturated ML coverage.

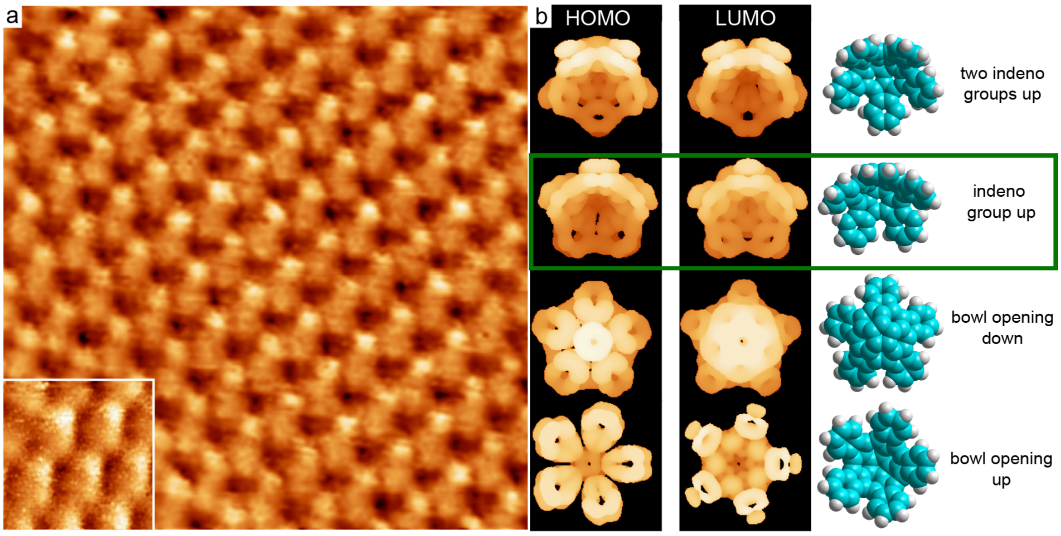

Figure 74: (a) Small scale STM image of the self-assembly of PiC deposited on Cu(100) kept at RT (9.3 nm × 9.3 nm, –2.18 V, 25 pA). Inset: high-resolution STM image of a few PiC molecules arranged in ordered row (4.8 nm × 4.8 nm, –3.08 V, 26 pA, no annealing). (b) Molecular drawings of the four possible adsorption footprints of PIC and their corresponding electron density maps (cutoff: 0.001 e/Å^3) of the frontiers orbitals (Left: states 107-110 Ext. Hückel, HOMO to HOMO-4; Middle: states 111-114 Ext. Hückel, LUMO to LUMO+4). The green rectangle highlights the electron density map which has a similar contrast as a single molecule contrast in the STM images.

In addition, the STM image with sub-molecular resolution show that the bright off-centered protrusion is made of only one lobe and not of two (Figure 74). Therefore, the overall contrast of a molecule corresponds better to the electron density maps of a molecule adsorbed with two indeno-groups on the surface and one indeno-group pointing up.

This adsorption configuration observed experimentally is confirmed by theoretical calculations. MM and DFT simulations both reveal (Figure 75) that the relaxed molecule adsorbs with two indeno-groups on the surface (independently of the initial configuration of the molecule on the surface). However, the hexagonal rings labeled 1, 2 and 3 in the Figure 75 are situated on top of hollow sites in DFT and on on-top sites in MM. Many aromatic hydrocarbons were found to adsorb above hollow sites on copper[129,130]. It was already demonstrated in ref.67 (paragraph III.2) that such simple MM calculation was not reliable enough to determine precisely the adsorption site of the molecule on the surface. The MM calculations were performed on 216 randomly chosen initial configurations. In the lowest energy configuration, two indeno-groups are parallel to the surface with a minimum surface-molecule distance of

3.6 Å, substantially larger than the 2.2 Å calculated with DFT. In the DFT configuration, the two indeno groups are also almost parallel to the surface, but their terminal ends are slightly lifted upward. A similar difference in the surface-molecule distance was observed by comparing MM and DFT results for MiC[69]. It is justified by the classical nature of MM which cannot account for electronic polarization effects, proven to be important for the adsorption mechanism of buckybowls on metal surfaces[69].

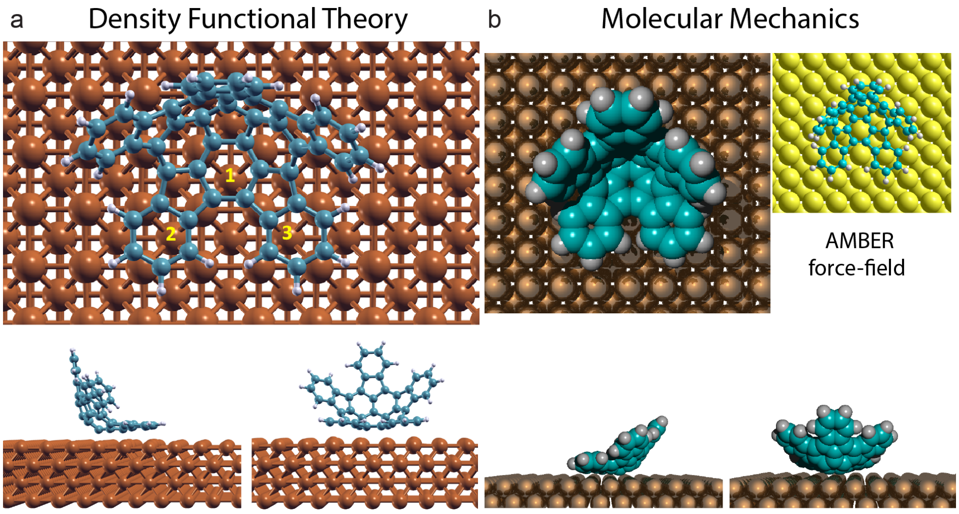

Figure 75: Most favorable configuration of a single PiC on 4 layers of Cu(100) obtained with DFT calculations (a) and molecular mechanics (b). With DFT (calculations performed by Dr. L. Zoppi), the hexagonal rings 1, 2 and 3 of the relaxed molecule adsorb on top of hollow sites at about 2.2 Å distance from the top copper layer (The atoms under these C_6 rings are 2nd layer atoms below the top layer). With MM, the molecule adsorbs with the rings on on-top sites, at about 3.6 Å above the copper atoms.

Similarly to what was calculated with DFT for monoindenocorannulene[69] (paragraph IV.3.1), the planar projection of the density of states (Figure A. 19b in the appendix) indicates no charge transfer between the molecule and the copper surface. However, the charge density plot perpendicular to the surface (Figure A. 19c in the appendix) shows strong charge reorganization: charge depletion in the molecular region and accumulation of charge underneath the molecule. This is also shown in the DFT model (Figure A. 19a in the appendix). This charge-redistribution, also called cushion effect[132–137], is responsible for the creation of a large interface dipole (7.4 D) which is similar to what was found for MiC[69] (7.5D). Thus, the adsorption with one or two indeno groups on the surface does not influence much the strength of the observed electronic polarization effect. In both cases, the Pauli repulsion lifts the terminal ends of the indeno groups away from the metal surface. The interface dipole is the same for MiC and PiC, but the binding energy, calculated with DFT[xxxvi], is much larger for PiC (5.7 eV) compared to MiC (3.4

[xxxvi] Unfortunately, this energy cannot be calculated using MM, which is powerful to compare molecular configurations on surfaces[67–69] with different initial parameters but these results cannot be compared with the energies of the individual components (surface and molecule separately) due to their different potential energy surfaces[269,270].

eV). The comparison with two naphthalene molecules reveals, as will be shown for MiC[69] in paragraph IV.3.1, that the adsorption footprint of PiC on Cu(100) is mainly defined by Pauli repulsion. Naphthalene also experiences Pauli repulsion and has an adsorption energy of 0.9 eV. It implies that the vdW contribution for two naphthalene molecules is lower than 1.8 eV. Comparing the total adsorption energy of PiC (5.7 eV) to this value suggests that Pauli repulsion dominates. PiC is another example of strong non-bonding interaction with pronounced Pauli repulsion between buckybowls and metal surfaces[245].

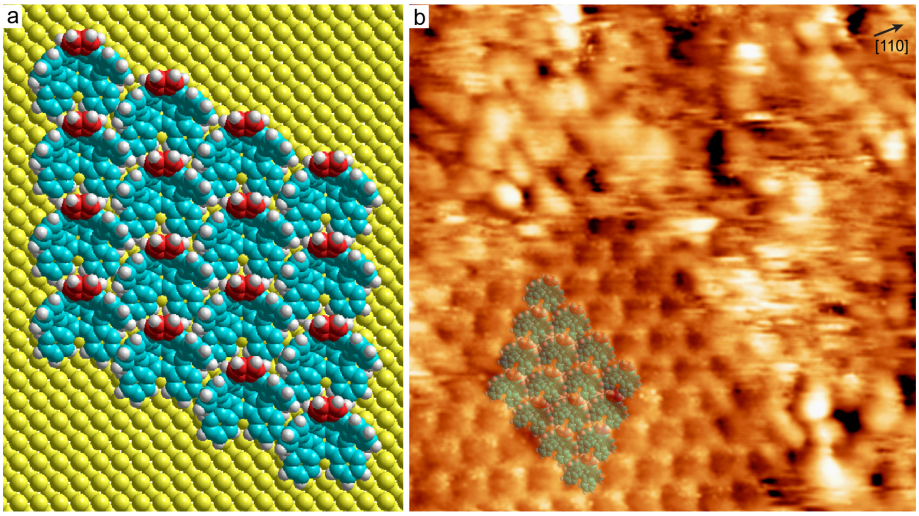

Figure 76: (a) Molecular model of one of the rotational domains based on the experimental observations and the adsorption footprint calculated theoretically. The red C_6 ring is used in each molecule to highlight the indeno-group pointing up, corresponding to the bright protrusion in the STM images. (b) Superposition of the model on a STM image (15nm × 15nm, –3.08 V, 26 pA, no annealing).

Molecule	**Monoindenocorannulene**[241]	**Pentaindenocorannulene**
Indeno-groups	1	5
Symmetry	C_{1v}	C_{5v}
Self-assembly	rows of single molecules $\begin{pmatrix} 4 & 0 \\ -1 & 4 \end{pmatrix}$	rows of single molecules $\begin{pmatrix} 4 & 0 \\ -2 & 4 \end{pmatrix}$
Area/ molecule [Å^2/molecule]	104	104
Adsorption footprint	Tilted adsorption: bowl up with the indeno-group parallel to the surface	Tilted adsorption: bowl up with two indeno-groups parallel to the surface

Table 9: Comparison of the structural parameters of the MiC and PiC self-assembly on Cu(100)

The matrix notation of the adsorbate structure on Cu(100) is (4, 0; –2, 4). The model is displayed in the Figure 76a and fits well with the STM measurements (Figure 76b). Although the symmetry and consequently the adsorption footprint of PiC and MiC on Cu(100) are different, the structure formed by PiC is similar (Table 9) to the one adopted by MiC on Cu(100)[241], discussed in the paragraph IV.1.2. This work also reveals that MM computations give similar results as DFT for PiC, a curved PAH for which molecule-metal interactions are more complex to model than for planar PAH. As already shown for [5]H[67], the determination of the precise adsorption site requires computationally expensive DFT calculations. Note that, even with DFT, the binding energy with the surface seems to be overestimated: 5.7 eV for a non-covalent interaction is large, even considering the large size of the molecule.

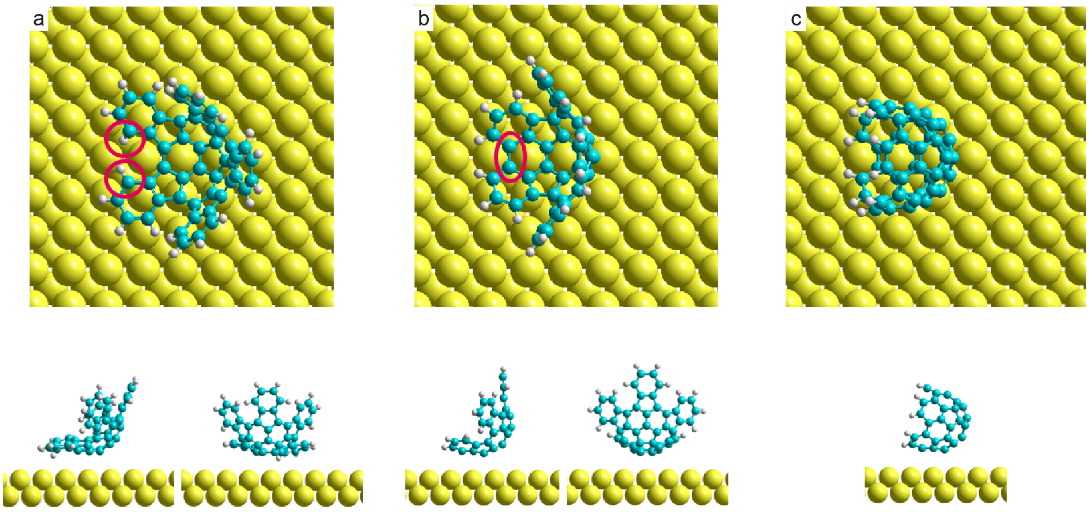

Figure 77: (a-c) hypothetical steps in the PiC post-annealing dehydrogenation which could lead to the creation of a CNT end

On copper surfaces, post-annealing dehydrogenation[246,247] or even cyclodehydrogenation of hydrocarbons has been reported, e.g. for 10,10'-dibromo-9,9'bianthracene[192] or tetraphenylporphyrin[174]. This occurs preferably at sites where several hydrogen atoms are close to each other and strongly repulse each other. A closer look at the configuration of PiC at saturation coverage, indicates that the two hydrogen atoms highlighted in red in the Figure 77 are close and are possible candidates for cyclodehydrogenation. By removing the two hydrogens atoms (red encircled), a bond between the two carbon atoms of the two adjacent indeno-groups might be formed (Figure 77b). Subsequent steps could even lead to the formation of a carbon nanotube end of controlled structure (Figure 77c). Unfortunately, annealing at higher temperatures (623 – 673 K) destroyed the well-ordered self-assembly. Further annealing to 773 K led to the formation of a non-uniform structure (Figure 78) made of areas with mobile molecules, graphene (green arrows) and defects (structures resembling to the appearance of C_{60} in STM [248]: blue arrows). This non-uniform structure is not ideal for carbon nanotubes growth and could maybe be avoided by reducing the coverage.

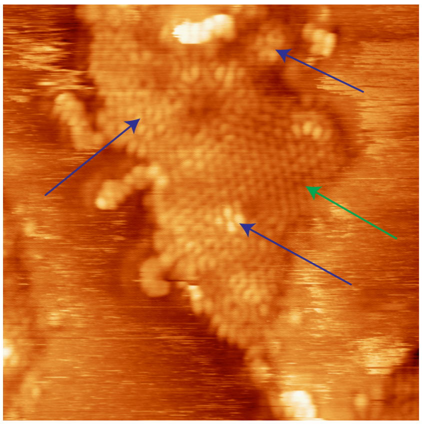

Figure 78: STM image (9.3 nm × 9.3 nm, 25 mV, 70 pA) obtained after deposition of PiC on Cu(100) and annealing to 773 K. The green arrow indicates normal graphene and blue arrows point to graphene defects. These structures are surrounded by disordered areas. This image was acquired at 295 K.

2.2 Non-saturated coverage: from curved to flat molecules

Because annealing at high coverage did not give successful results for on-surface chemistry, lower coverage was investigated. Single molecules can already be measured at RT due to their low mobility at this temperature. However, low-temperature allows for more stable imaging conditions and many of the images presented in this paragraph were acquired at 50 K. The single molecules were evaporated on a sample kept at room temperature and then cooled down for measurements.

2.2.1 Adsorption footprint of single molecules at very low coverage (θ << 0.3 ML coverage)

At low coverage, the molecules populate the steps boundaries and adopt different adsorption footprints (Figure 79). On the flat terraces, most of the molecules have a flower-like contrast: a dark central core surrounded by five lobes with a homogeneous brightness (Figure 79 and Figure 80). Based on the electron density maps of the frontier orbitals calculated with EHT and presented in Figure 74, they can be identified as bowls opening-up. Note that a close-up of these bowl-up molecules (Figure 80b) shows that all lobes do not have exactly the same brightness: for some molecules, two lobes appear brighter whereas for the other molecules, four lobes appear brighter. This difference might be explained by the mismatch between the five-fold symmetry of the PiC and the four-fold symmetry of Cu(100). This most-observed bowl-up adsorption footprint is not compatible with the configuration which was observed for a closed-pack layer.

Some of the PiC also adsorb with a tilted configuration at low coverage (Figure 80a, c, d, e). They have, in this case, one lobe which is much brighter and their contrast corresponds to the adsorption footprint with two indeno groups on the surface, as observed at ML coverage (Figure 74). This tilted configuration is encountered when the molecule adsorbs close to contamination or defects (Figure 80c) or close to another molecule, e.g. bowl-up (Figure 80d) or bowl-down (Figure 80e). Furthermore, a few molecules appear as large bright protrusions (Figure 80e, Figure 80f). Sometimes, five darker legs are observed around the central protrusion. These molecules seem to correspond (Figure 74) to bowls opening-down. They are rarely observed on the flat terraces but more often observed at the steps.

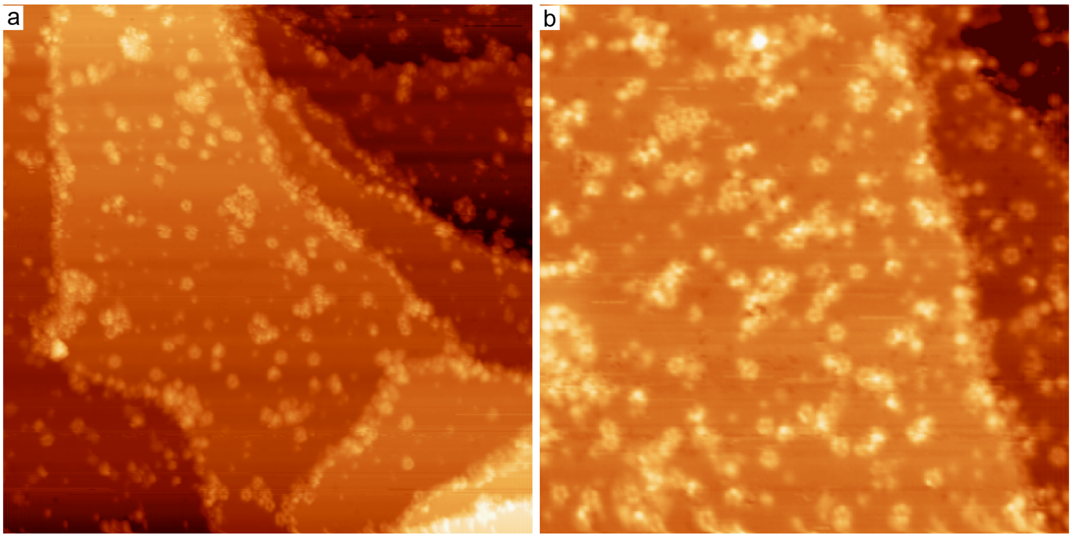

Figure 79: STM images (measured at 50 K, a: 100 nm × 100 nm, –2.6 V, 30 pA, b: 60.9 nm × 60.9 nm, 3.0 V, 30 pA) obtained after low coverage deposition of PIC on Cu(100). The steps are occupied with molecules having different adsorption footprints. On the flat terraces, most of the molecules look like flowers with five lobes of the same brightness.

In conclusion, the tilted configuration observed for a closed-pack layer was induced by intermolecular interactions. Single molecules adsorb preferentially with the bowl opening-up despite the mismatch between their five-fold symmetry and the C_4 symmetry of the substrate. This mismatch leads to the redistribution of the electrons among the five legs of the molecules as observed with STM (different brightness in the lobes, i.e. a non-symmetric DOS). As mentioned previously, five-fold-symmetric objects usually avoid keeping their symmetry on surface, except if steric hindrance is involved due to the molecular structure[242]. It is not the case for PiC because they tilt as soon as they find another defect or molecule on the surface. The reason for this absence of tilt at low coverage is not clear. Without external interaction, the strong Pauli repulsion between the metal surface and each indeno-group (so called-cushion effect, Figure A. 19 in the appendix) might stabilize the PiC in the bowl opening-up configuration. It could also be that the molecules are stabilized by copper adatoms. In addition, the higher electron density at the convex site of a PiC can cause strong electrostatic interactions with the metal surface which could stabilize a single molecule. The bowl opening-up adsorption contrasts with the results (Figure 75) obtained by both DFT and MM on Cu(100) which predicted a tilted configuration for a single molecule. Even DFT encounters difficulties to model the non-bonding interactions between metals and organic aromatic molecules with curved π-conjugation. It also reflects in the really high value of the vdW interaction between PiC and surface, calculated to be 5.7 eV.

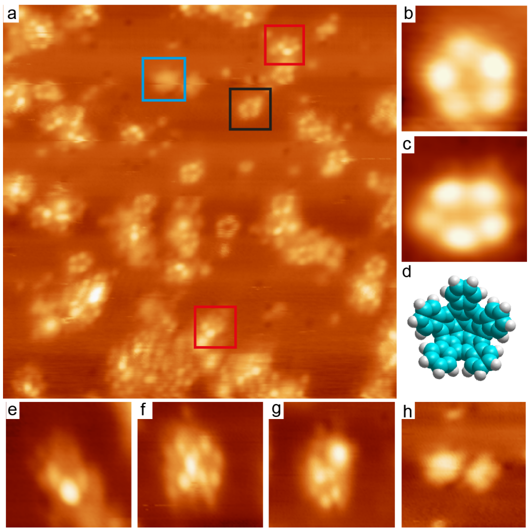

Figure 80: (a) Large scale STM image with PiC molecules adsorbed in three different configurations highlighted with blue, red and black rectangles. By comparing with the EHT electron density maps presented in Figure 74, the adsorption configurations can be determined. (b-d) Most of the molecules adsorb with five lobes pointing up (black rectangle in (a)) as presented in the molecular model of the bowl opening-up. Two contrasts are observed: molecules have either two or four brighter lobes. (e-g) A certain number of molecules adsorb with a tilted configuration (red rectangles in (a)), corresponding to the adsorption footprint with two indeno-groups parallel to the surface, as observed at saturated ML coverage. This tilted footprint is observed when the molecule adsorbs close to contamination or defects (e), another molecule bowl-up (f) or another molecule bowl opening-down (g). (f) A few molecules like the two presented here or in the blue rectangle in (a), adsorb with the bowl opening-down configuration (bright protrusion in the center). (Measuring parameters, at 50 K: a: 31.9 nm × 31.9 nm, 3.0 V, 30 pA; b: 2.5 nm × 2.5 nm (top) and 2.6 nm × 2.6 nm (bottom), 3.0 V, 30 pA; c: 5.9 nm × 5.9 nm, 3.0 V, 30 pA; d: 7.5 nm × 7.5 nm, 3.0 V, 30 pA; e: 7.6 nm × 7.6 nm, 3.0 V, 30 pA; f: 6.9 nm × 6.9 nm, 3.0 V, 30 pA).

2.2.2. On-surface chemistry at low coverage (θ << 0.3 ML coverage): from curved to flat PAH

Thermally induced on-surface chemistry was performed at low coverage. At 503 K, conformational changes are observed for a small number of PiC (Figure 81a). The modified molecules are flat and have a star-like shape, with five or six lobes, sometimes forming dimers (Figure 82a, b, c). Annealing to 513 K leads to a larger number of flat stars but a few of them are still intact. At 530 K, all molecules are transformed. Regardless of the annealing temperature, one can also observe the presence of a few molecules with a large bright central protrusion which might correspond to bowl opening-down molecules. The abundance of the three kinds of molecules was evaluated (Figure 81). The proportion of large bright molecules is constant (in the limit of the error bars) and all the normal PiC are converted into flat starts by annealing.

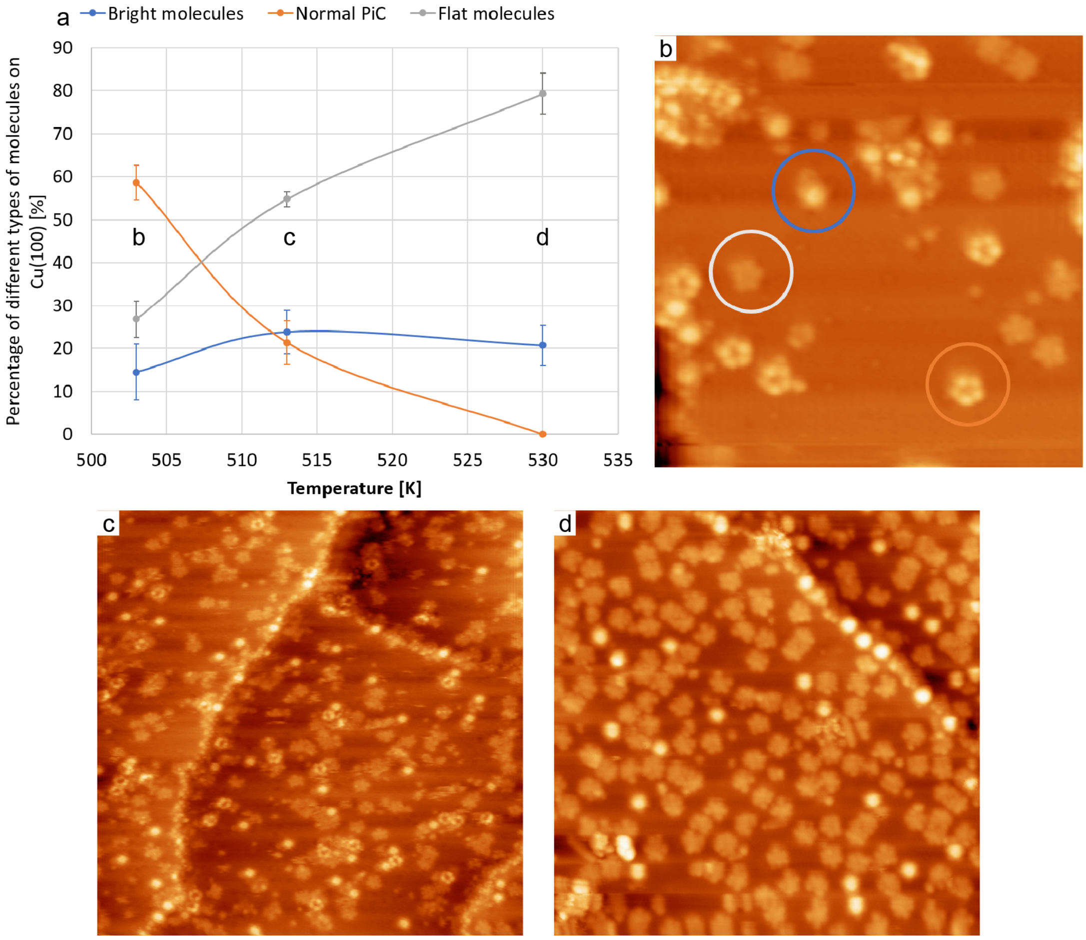

Figure 81: STM images (b-d) of PiC at low coverage on Cu(100) after annealing at different temperatures and their corresponding graph (a) showing the evolution of the three observed species as a function of the temperature. The statistic was done on 1352 molecules on 9 different images (3 per annealing temperature). (b) After annealing at 503 K: PiC with bowl opening-up (or tilted) configuration (orange) are dominating and a few bowls opening-down are observed. Due to annealing, a few flat star-like molecules with five or six lobes are observed (white). (c) After annealing at 513 K: flat molecules are the majority. A few bowls opening-up and opening-down are still observed. (d) After annealing at 530 K: a few bright molecules (probably opening-down) are still observed and all the other molecules transformed into flat stars. (Measuring parameters, at 50 K: b: 26 nm × 26 nm, –3.1 V, 28 pA; c: 51.4 nm × 51.4 nm, –0.3 V, 30 pA; d: 39.8 nm × 39.8 nm, –1.8 V, 24 pA). The letters (b), (c) and (d) in the graph (a) correspond to the STM images.

The formation of C-C bonds[174,192] between indeno groups, the formation of organometallic compounds[249] and the breaking of a covalent bonds[250] are reactions which can all be induced, by thermal energy, on a copper surface. EHT density maps of the HOMO and LUMO of molecules which could possibly be created by annealing were modelled (Figure 82d). On the STM images, the modified star-shaped molecules are quite flat and no prominent bright protrusion is observed which rules out the models with newly created C-C bonds between the indeno groups. In addition, the overall shape of a molecule suggests that the flattening occurs via the rupture of 1 or 2 C-C bonds mediated by an eventual organometallic bond. In the Ext. Hückel models (Figure 82d), the compounds with two broken C-C bonds (green rectangle), leading to flat molecules, seem to have the most similarities with the STM contrasts of the flat star (angle between the two legs with the largest separation, presence of an extra lobe in the HOMO but not in the LUMO). The presence or absence of Cu adatoms cannot be confirmed due to the similarities of the electrons density maps with or without a Cu metal atom. The breaking of 1 or 2 C-C bonds will be confirmed by TOF-SIMS in later experiments.

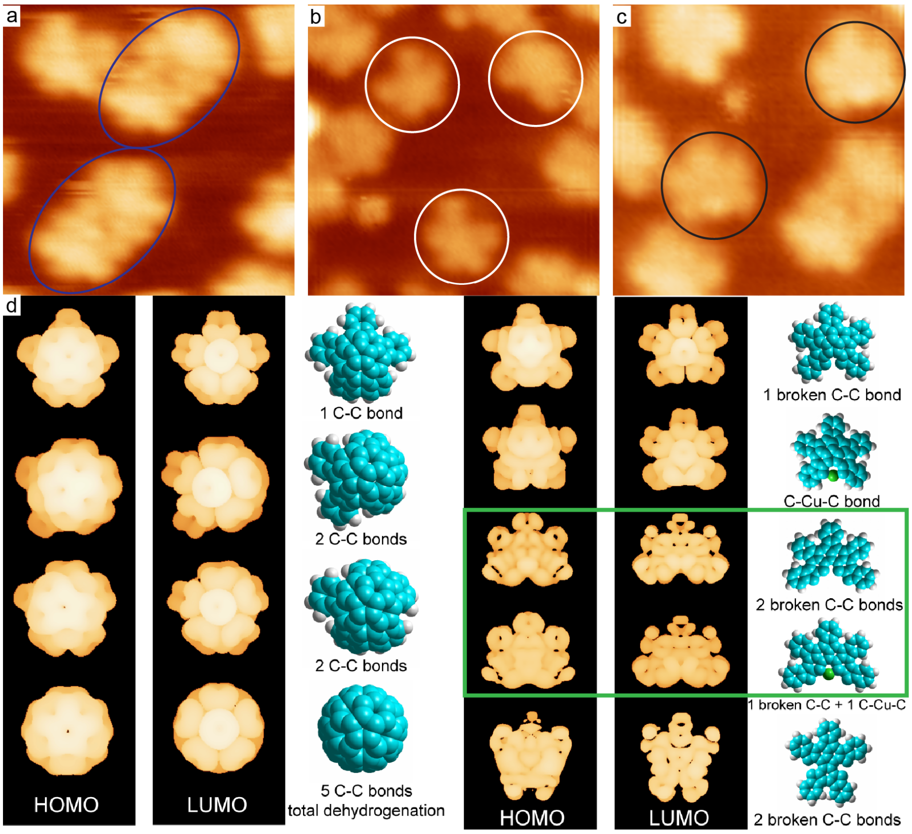

Figure 82: STM images showing the most frequent species of flat molecules: flat molecules with five (b) and 6 lobes (c) are the most encountered. Some molecules form dimers made of two flat molecules (a). (d) EHT electrons density maps of the frontiers orbitals (HOMO to HOMO-3 or LUMO to LUMO+3) of different possible species formed after annealing and corresponding to the STM contrasts. A flat molecule seems to correspond to the EHT contrasts of a molecule with two broken C-C bonds (green rectangle). It is not clear whether it is an organometallic compound or not. (Measuring parameters, at 50 K: a: 6.5 nm × 6.5 nm, –1.7 V, 24 pA; b: 8.4 nm × 8.4 nm, –1.8 V, 24 pA, c: 6.5 nm × 6.5 nm, –1.8 V, 24 pA). For the EHT maps, the electron density cutoff is 0.001 e/Å^3 and 0.0004 e/Å^3 for organic and organometallic compounds respectively.

Further annealing between 530 K and 624 K did not lead to further apparent changes in the flat molecules (see for example the Figure 83a at 617 K). Annealing above 643 K (see Figure 83b at 643 K) led to the polymerization of the molecules and to the formation of chains made of molecular fragments (see Figure 83c at 678 K).

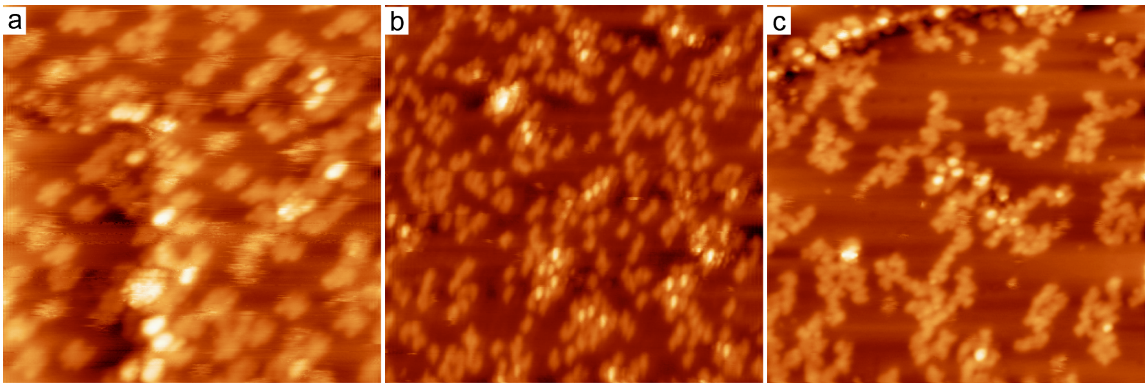

Figure 83: STM images of PiC on Cu(100) at low coverage, after annealing at high temperature. (a) After annealing at 617 K: the molecules still have the flat star shape except a few which appear as bright protuberances. (b) After annealing at 643 K: The molecules start to polymerize. (c) After annealing at 678K: Long chains of polymerized molecular fragments are observed. They are at least dehydrogenated as will be shown with TDS in the paragraph 2.2.4. (Measuring parameters: a: 25.2 nm × 25.2 nm, –2.7 V, 29 pA; b: 67.2 nm × 67.2 nm, –1.8 V, 30 pA; c: 46.3 nm × 46.3 nm, –2.6 V, 30 pA).

2.2.3. *Adsorption footprint and on-surface chemistry of single molecules at higher coverage (0.3 ML < θ < 0.7 ML coverage)*

At larger coverage (Figure 84a), many molecules in a bowl-up configuration are observed (flower-like appearance), but a few molecules have the opening-down configuration (round with bright appearance). After annealing at 530 K (Figure 84b), many molecules tilt. After heating up to 543 K (Figure 84c), almost all molecules are tilted and start to form lines of molecules in the same direction. Ordered domains made of lines of tilted molecules fitting into each other are visible after annealing at 597 K (Figure 84d). However, it is not clear until which temperature the molecules stay intact.

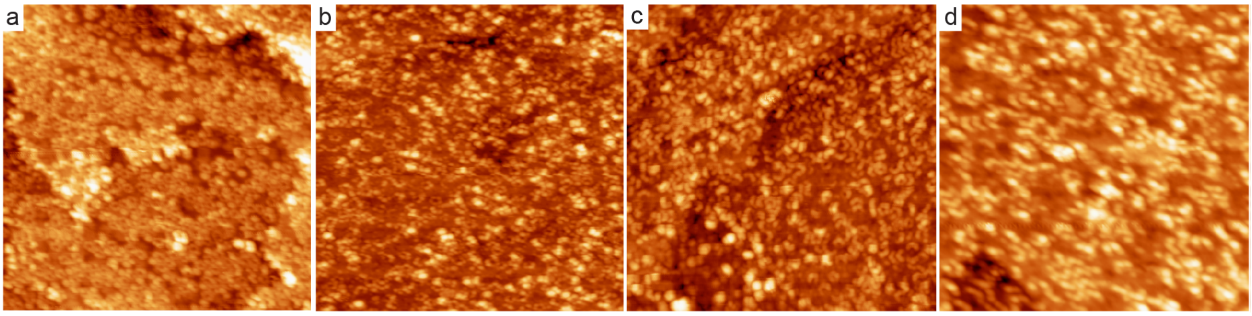

Figure 84: STM images of PiC on Cu(100) at a moderate coverage 0.3 ML < θ < 0.7 ML. (a) Without annealing, most of the molecules are bowl-up. (b) After mild annealing to 530 K, most of the molecules are tilted. (c) Annealing to 543 K lead certain molecules to form lines. (d) Higher annealing at 597K drives the formation of ordered structures made of molecules fitting into one another. (Measuring parameters, at room temperature: a: 50.1 nm × 50.1 nm, –2.8 V, 30 pA; b: 40.8 nm × 40.8 nm, –3.0 V, 27 pA; c: 47.3 nm × 47.3 nm, –2.6 V, 30 pA; d: 29.0 nm × 29.0 nm, –2.3 V, 30 pA). This was measured at room temperature.

2.2.4. XPS and TDS measurements

Dehydrogenation was measured by acquiring a H_2 TD spectrum (mass 2 amu). To do so, a flash annealing (3 sec) of the sample, initially at RT, was done just before the experiment to avoid a burst in the measured signals due to the hot filament of the heater. This led to a temperature increase of about 20 K on the sample. The temperature was then set and maintained for 2 minutes to an initial temperature (373 K for 1 ML and 423 K for the other coverages) which was then ramped up to 873 K at a constant heating rate.

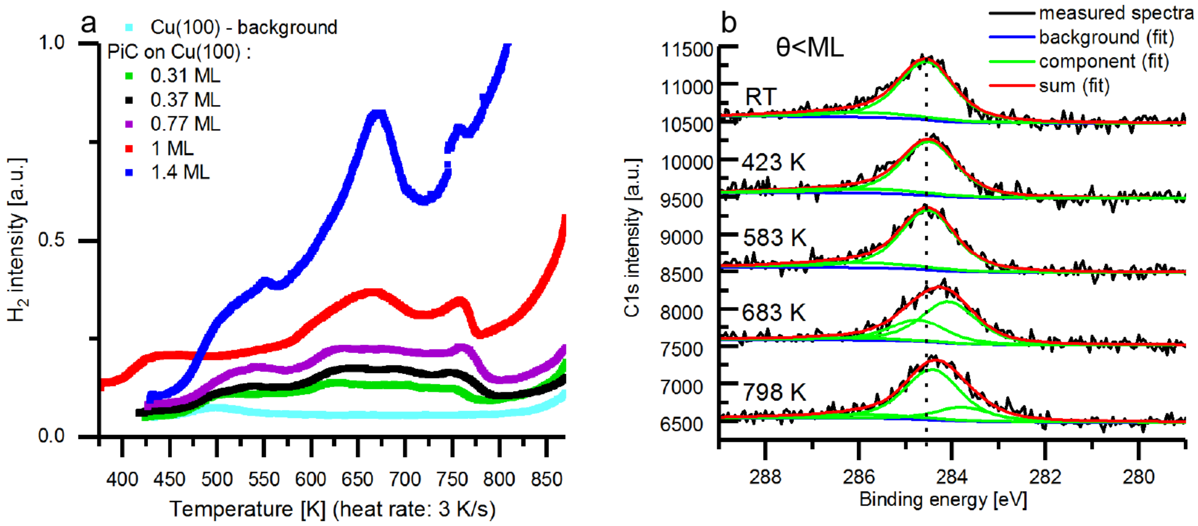

Figure 85: (a) TD spectrum of PiC on Cu(100) for different molecular coverages at a heating rate of 180 K/min. The temperature was set to 423 K and then ramped up to 873 K, except for 1 ML where the initial temperature was 373 K. (b) XP spectrum of 0.39 ML of PiC on Cu(100) after annealing for 15 min at different temperatures. The C1s peak observed at 284.6 eV after molecular adsorption shifts to lower energies due to the C-H bond breaking and the stronger binding of the molecules with the surface or with copper adatoms (formation of organometallic species) [224,225]. At 798 K, the peak switches back to higher energy due to the formation of graphene[251].

Three peaks are observed in the TD spectra at all coverages. Their intensities decrease with the coverage. Note that a raise of the signal is always visible shortly after the beginning of the TDS, independently of the initial annealing temperature (see signal for 1 ML with respect to the others in Figure 85a). This increase is also found on a clean sample (Figure A. 20, appendix) and therefore comes from the annealing of the sample holder, i.e. the background. The raise of the signal around 873 K is also coming from the holder, i.e. it becomes so hot that everything degases. The first peak is small and happens around 551 K at 1.4 ML coverage and a bit below for the smaller coverages. It corresponds approximately to the annealing temperature to obtain flat molecules (between 503 K and 530 K, as observed with STM). This dehydrogenation occurs, as expected, at lower temperature and with a smaller intensity for a lower heating rate (Figure A. 20, appendix) because the desorption is modeled by an Arrhenius law called Polanyi-Wigner equation[45,46]. It means that during the long annealing before the STM measurements (at least 15 min), the first dehydrogenation occurs before 551 K: probably during the formation of the flat stars. The second peak transforms from a well-defined peak around 673 K at high coverage into a large step with two bumps a low coverage. This second peak corresponds to the dehydrogenation steps which are involved during the polymerization of the molecules into chains (Figure 85a, Figure 86). The third peak, observed at around 773 K, is the last dehydrogenation step of the molecules, which occurs during the formation of graphene (Figure 85a, Figure 86).

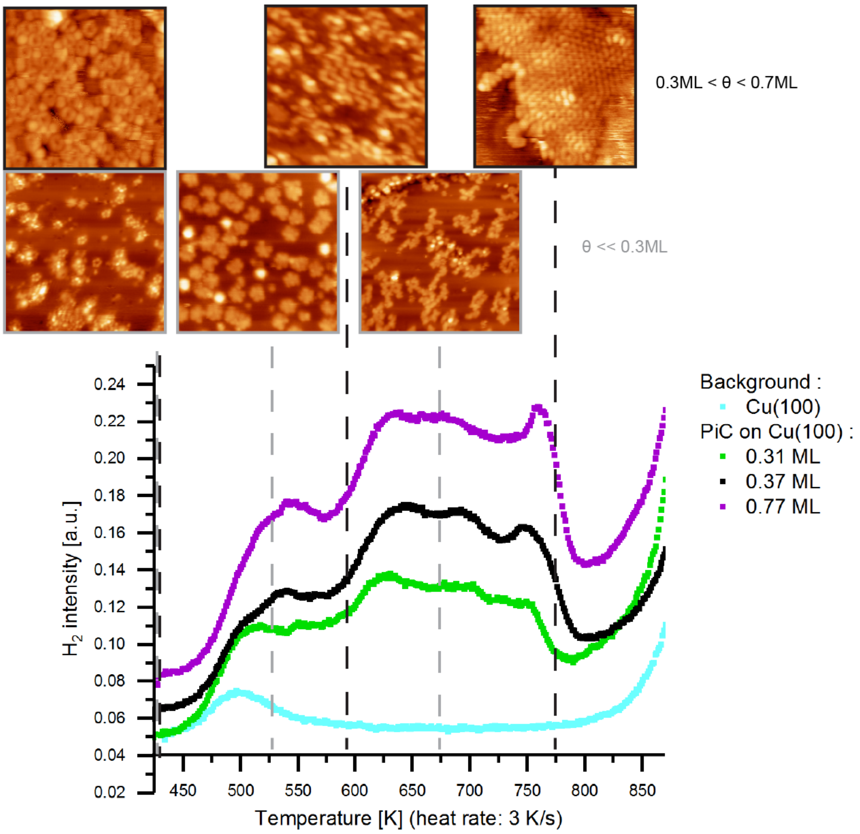

Figure 86: TD spectrum of PiC on Cu(100) for different sub-molecular coverages at a heating rate of 3 K/s. The temperature was set to 423 K and then ramped up to 873 K. On top, six STM images of the various structures obtained after a fifteen-minutes annealing at different temperatures (indicated with a dashed line on the graph) are displayed. The structures observed for a coverage smaller than 0.31 ML are framed in gray area whereas the structures obtained at larger coverage (0.31 < θ < 0.77 ML) are framed in black. (From left to right: Top: 20.3 nm × 20.3 nm, −2.3 V, 20 pA, no annealing, measured at RT; 14.7 nm × 14.7 nm, −2.3 V, 30 pA annealing at 597 K, measured at RT; 5.6 nm × 5.6 nm, 25 mV, 70 pA, annealing at 773 K, STM Specs Aarhus 150 measured at 295 K; Bottom: 31.9 nm × 31.9 nm, 3.0 V, 30 pA, no annealing, measured at 50 K; 20.7 nm × 20.7 nm, −1.8 V, 24 pA, annealing at 530 K, measured at 50 K ; 46.3 nm × 46.3 nm, −2.6 V, 30 pA, annealing at 678 K, measured at 50 K).

XPS measurements after annealing at different temperatures are presented in the Figure 85b. At room temperature, a broad C1s peak at 284.6 eV is observed, consistent with the adsorbed PiC molecules. The transformation of the molecules below 643 K is not observed with XPS. Starting from 683 K, a shift to lower energy is observed. A shift to lower energy can correspond to the formation of Cu-C bonds[224,225] because Cu is less electronegative than C[41]. The peak shifts back to higher energy at 798 K for θ << ML and only at 873 K above ML coverage (Figure 85b and Figure A. 21) due to the formation of graphene[251]. No explanation for this difference in temperatures depending on the coverage was found for the last dehydrogenation. In TDS, the dehydrogenation temperatures for the different observed steps also decrease with the coverage.

2.3 Conclusion

PiC on Cu(100) shows different adsorption footprints depending on the coverage. At extremely low coverage, the molecules have enough space to adsorb on the surface far away from each other and intermolecular interactions are negligible. In this case, PiC adsorbs bowl opening-up with its C_5 rotational axis perpendicular to the surface. However, at saturated monolayer coverage, intermolecular interactions are at play. It results in the adsorption of PiC with two indeno-groups parallel to the surface. Their assembly looks like the one observed for MiC which has only one indeno group instead of five.

Thermally induced on-surface chemistry (at 503 K) provides, at low coverage (θ < 0.3 ML), enough energy to break C-C bonds. It leads to the on-surface formation of flat star-shape molecules. Unfortunately, PiC are not the right precursor for CNT growth as in ref.29. The stars could however be used as a precursor for growing 2D materials such as graphene[198]. The dimers are oriented toward the same direction but they are tilted with respect to each other due to CH-π inter-dimers interactions between the different columns. It would be interesting to form functional layers on surface by trying to intercalate compounds between two PiC or as a precursor for endofullerene formation. PiC were already studied for possible applications in hydrogen storage[23] or to act as fullerene receptors[24]. At higher coverage (0.3 ML < Θ < 0.7 ML), annealing leads to the formation of rows of molecules fitting into one another. Dehydrogenation and C-C bonds breaking are also observed in this case.

It would be interesting to anneal PiC on other metal surfaces such as Ag and Au to determine the catalytic influence of the surface on the reaction products of the thermally-induced reaction.

IV.3. Modelling of other curved polycyclic aromatic hydrocarbons

The STM images presented in this paragraph were recorded by Q. Stöckl at Empa. Only the modelling was part of this thesis.

3.1 Monoindenocorannulene on Cu(111)

MiC ($C_{26}H_{12}$, Figure 71) self-assembly and adsorption footprint were studied on Cu(111)[xxxvii] to be compared with the results obtained previously for corannulene on Cu(111)[128]. MiC adsorbs with a slightly tilted configuration to maximize the vdW interaction and to reduce the Pauli repulsion with the surface. For MiC, the addition of an indeno group to the corannulene core breaks the five-fold symmetry (only one mirror plane is remaining) and reduces the bowl depth.

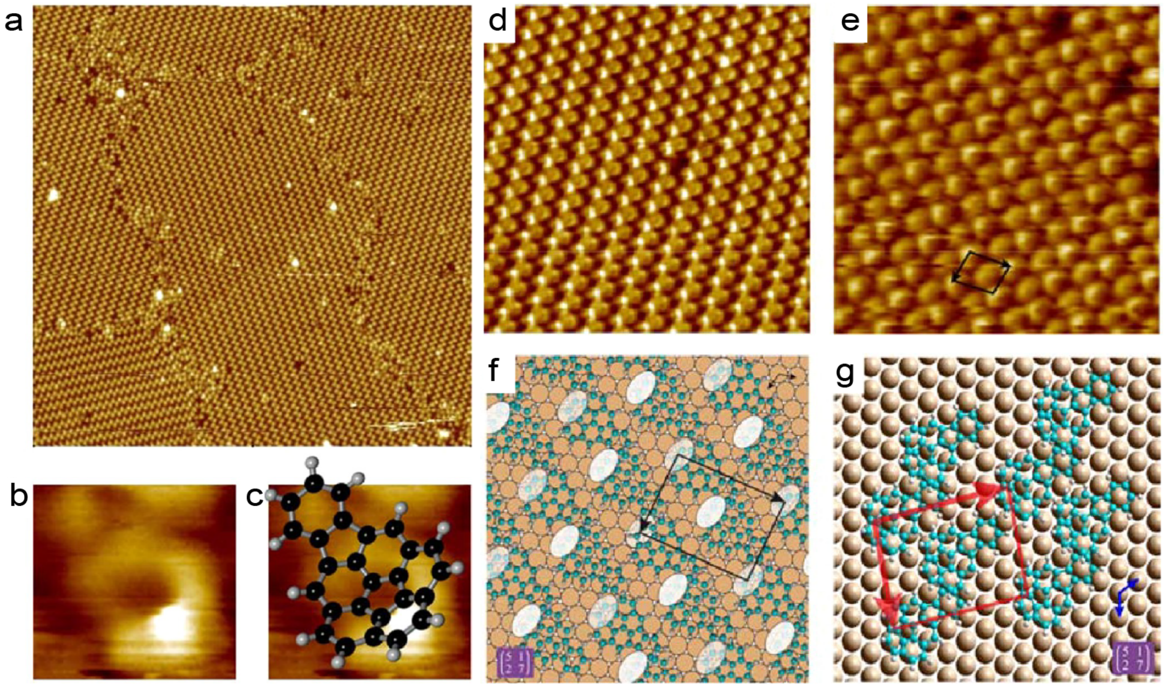

Figure 87: STM images (a-e) of the self-assembly of MiC on Cu(111) and corresponding models (f-g). (a) Rotational and mirror domains made of a zigzag structure (80 nm × 80 nm, –1.2 V, 129 pA, 63 K). (b, c) STM image (1.36 nm × 1.26 nm, –1.1 V, 179 pA, 85 K) of a single molecule with the superimposed molecular model (c). (d, e) STM images (d: 20 nm × 20 nm, –1.2 V, 129 pA, 63 K; e: 12 nm × 12 nm, –1.1 V, 238 pA, 65 K) of a zigzag domain with different measuring parameters. (f, g) Possible models of the (5, 1; 2 7) domain according to the STM images and the adsorption footprint computed via DFT calculations. The first model has molecules sitting on different adsites (f) and the other model has molecules adsorbing on the same sites but non-homogeneously distributed in a unit cell (g). A unit cell is indicated with the rectangle with arrows.[69]

The self-assembly of MiC on Cu(111) consists of domains made of parallel zigzag rows of tilted molecules (Figure 87a-e). The matrix notation of the ordered structure is (5, 1; 2, 7). Adjacent molecules in a zigzag row have a different contrast which might be due to different tilt angles of the molecules with respect to the surface or to a different adsorption sites for each of the two molecules in a unit cell. This information can unfortunately not be obtained by STM imaging. However, the STM allows to distinguish a benzo moiety from the rest of a MIC molecule and to observe that this indeno group lies more or less parallel to the surface.

[xxxvii] Most of the results presented in this paragraph were published in ref.271.

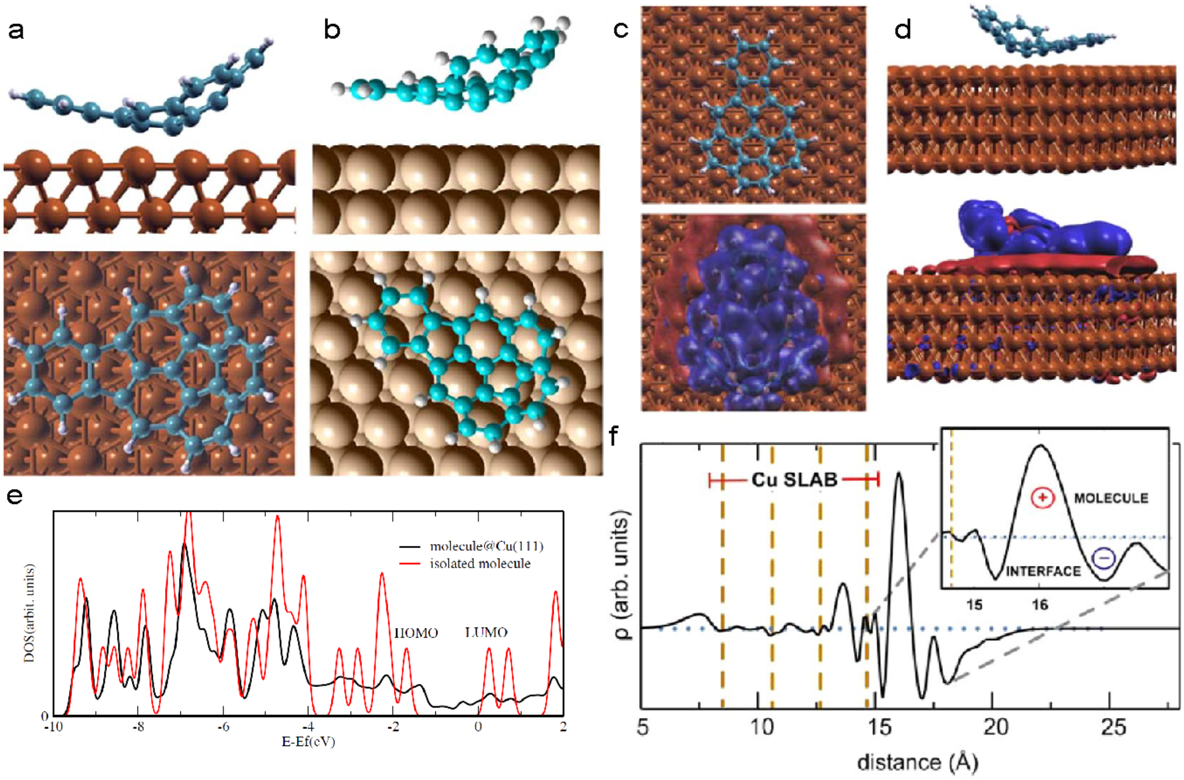

Figure 88: (a, b) Top and side view of the DFT(calculations performed by Dr. L. Zoppi.) and AMBER-force field models of a MiC on Cu(111). The DFT model was done with a optB86-vdW functional which account for the dispersion effects (a). The MM optimized configuration presented in (b) was the minimum-energy obtained after optimization of 216 initial configurations. (c, d) Charge redistribution calculated with DFT. (e) DOS of a single MiC compared with the DOS of an MiC on Cu(111) : the electronic states of the adsorbate all match with an electronic state of the single molecule. (f) Linear electron density perpendicular to the surface, revealing an accumulation of charges at the surface-molecule interface and a depletion in the molecule.[69]

The tilted adsorption footprint was also obtained with both AMBER and DFT calculations. DFT calculations yielded a minimum energy configuration, shown in Figure 88a, with an adsorption energy of 3.4 eV and a minimal distance to the surface of about 2.0 ± 0.2 Å. AMBER-force field calculation led to a similar tilted adsorption configuration with the indeno-group on top of a 3-fold hcp hollow site (Figure 88b). In addition, the minimum molecular-surface distance is calculated to be 3.48 Å with MM which is higher than what was found with DFT. Note that the indeno group is parallel to the surface with MM whereas it is slightly lifted-up with DFT. In order to explain this difference, the charge redistribution around a single molecule on copper was investigated with DFT. Both the DFT models and the electron density plot perpendicular to the surface (Figure 88c, d, f) show a strong charge redistribution due to Pauli repulsion with an accumulation of the charges on the sides and below the molecule. A depletion of the charge is also observed in the top most layer of the copper substrate. Consequently, a depletion of charge is observed in the molecule. This effect is known as cushion effect[132–137]. Note that the charge rearrangement is much more pronounced around the indeno group and explains the final distance between the indeno group and the surface computed with DFT. The charge redistribution also creates a large interface dipole moment of 7.5 D (the intrinsic dipole of MiC being 2.9 D). This large dipole is not induced by charge transfer as can be seen in the projected density of states in Figure 88e. In the case of corannulene on Cu(111), the interface dipole moment was 6.8 D with an intrinsic dipole moment of 2.2 D. It means that the difference of the intrinsic dipole moments between MiC and corannulene is the same as in between their interface dipoles.

Interface dipoles induced by charge rearrangement have already been observed for corannulene-derivatives[245]. It means that upon adsorption of a curved PAH on surface due to vdW interactions, the surface metal charge is pushed away: Pauli repulsion is at play. A balance between both interactions is responsible for the final adsorption footprint on surface. To know which of the two contribute the most, a comparison of the indeno group with naphthalene can be done. The adsorption energy of this molecule on Cu(111) was found to be 0.9 eV. Knowing that this system also shows Pauli repulsion, the upper limit of the vdW force is 0.9 eV. Compared with the binding energy of 3.4 eV obtained for MiC, adsorbing with its indeno group on the surface, it means that the Pauli repulsion contributes the most in this case.

The adsorption footprint obtained with DFT was then used in parallel with the STM images to model the self-assembled structure. Two models with the correct periodicity are presented in the Figure 87f, g. One (Figure 87f) is made using different adsorption sites for the two molecules in a unit cell while the second one (Figure 87g) has identical adsites for all molecules but a non-uniform distribution in the unit cell. It is not clear whether this non-uniformity would be induced by a constraint coming from the substrate or by intermolecular interactions, e.g. a dimer modeled with MM suggests the presence of CH-π interactions (Figure A. 22 in the appendix). STM does not allow to say which of the two models is correct but RAIRS could give more information about the orientation of the molecules on the surface.

In conclusion, MiC adsorbs on the surface with a tilted configuration, assembled into zigzag lines with different brightness. Their spontaneous ordering is induced by a complex balance between vdW and Pauli interactions with the metal surfaces as well as intermolecular interactions. The Pauli repulsion is responsible for a charge redistribution in the surface, as observed for PiC on Cu(100), and this influences the tilt angle of the molecule on the metal surface. The induced interface dipole, which does not involve charge-transfer, is large. It is on the order of what is found for adsorption of alkali metal on metal surfaces[138–140]. Such large charge redistribution was only reported for curved PAH so far. For planar PAH[132–137], the effect is much smaller. This work allowed to demonstrate how important the charge-induced polarization effects in the modelling of such curved PAH are. The motivation to compare both DFT and MM modelling techniques came from the pentahelicene case (paragraph III.2) where both gave a pretty similar final molecular configuration on Cu(111)[67]. Unfortunately, MM is based on classical mechanics which is not able to account for polarization and charge redistribution explaining the different adsorption footprint and the larger molecular to surface distance. MM predicted the correct tilted configuration, but many differences were obtained compared to DFT (footprint, surface to molecule distance…).

3.2 $C_{38}H_{14}$: a C_{70} fragment molecule on Cu(111)

$C_{38}H_{14}$ (Figure 71) is a quasi-fragment of a C_{70} fullerene and has C_{2v} symmetry. As already mentioned, buckybowls are expected[8,68,128,238–240] to adsorb on metal single crystals with a bowl opening-up configuration. Nevertheless, below ML coverage, $C_{38}H_{14}$ on Cu(111)[xxxviii] arrange in large ordered motifs, containing a few molecules with an opening-down configuration (Figure 90). MM modelling aims to explain the reason for this behavior. The STM images were acquired at 60 K.

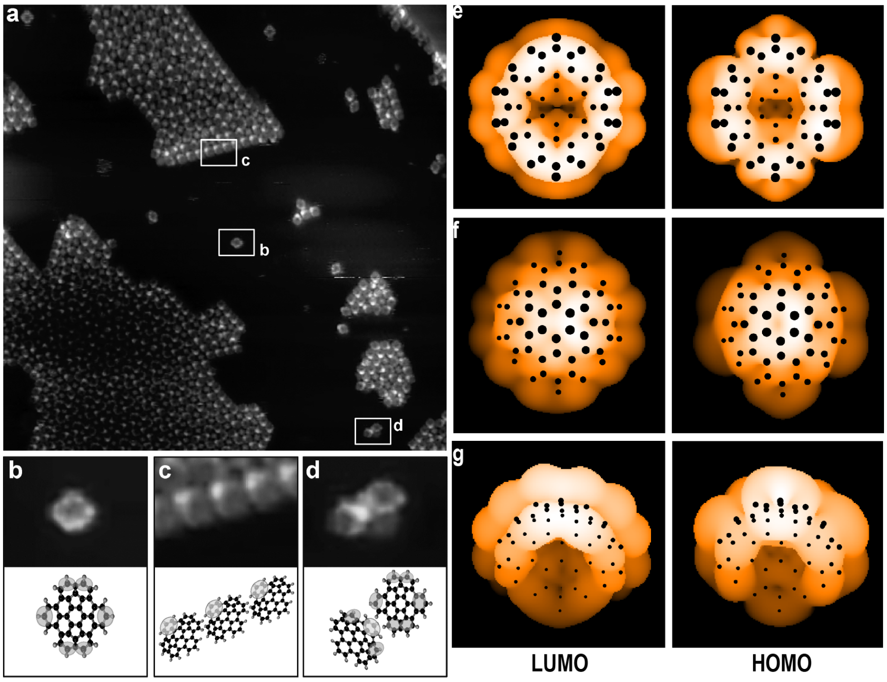

Figure 89: (a) STM image of $C_{38}H_{14}$ on Cu(111) at low coverage (60 nm × 60 nm, 0.7 V, 168 pA). In the islands, the molecules are self-assembled. Close-up 'STM views' onto a single molecule (b), of a line at the boundaries of large islands (c) and of a dimer (d) are displayed in the insets with their corresponding molecular ball and stick models (b-d: 5.2 nm × 4.0 nm). A single molecule shows a rim dominated contrast which corresponds to the EHT model of a molecule opening-up (e). The islands' edges are occupied with tilted molecules with a phenylene group up (g). An electron density map of the HOMO and LUMO for a bowl opening down is also displayed in f. (e-g: Ext. Hückel levels considered: 79-83 (HOMO to HOMO-4) and 84-88 (LUMO to LUMO+4). The positions of the atoms are indicated as black dots.)

[xxxviii] Most of the results presented in this paragraph were published in ref.68.

At low coverage (Figure 89), self-assembled domains with lines of ordered molecules at their edges are observed. In addition, single molecules and pairs are observed. EHT electron density maps of a molecule opening-up, a tilted molecule with one phenylyne (C_6H_3) ring pointing up and a molecule opening-down are presented in Figure 89. A single molecule can therefore be identified as a bowl-opening up, corresponding to the footprint which is usually expected for buckybowls. However, a dimer is made of one tilted and one opening-up molecules. Rows of molecules contain only tilted molecules with one phenylyne group pointing up and the opposite phenylyne group aligned parallel to the surface. Thus, intermolecular interactions are responsible for the tilting of the molecules as observed for PiC on Cu(100) in paragraph IV.2. In a dimer, the arrangement of the molecules with respect to each other implies that the tilt of the dimer could be induced by a π-H bonding between the top phenylyne ring of the tilted molecule and the hydrogen atoms on the rim of the non-tilted molecule.

The optimized configuration of a single molecule calculated with AMBER is tilted (Figure A. 23 in the appendix). It is probably due to the non-consideration of polarization and electronic effects, as observed for monoindenocorannulene[69] and pentaindenocorannulene (paragraphs IV.2 and IV.3.1). However, the vdW interactions between PAH is usually well taken into account by MM as observed for [5]H[67] (paragraph III.2). In order to estimate the interaction strength and site between two $C_{38}H_{14}$, the central C_6 ring of one bowl was fixed to the substrate in an opening-up configuration. All the other carbon atoms, including the other bowl could relax freely. The minimum-energy configuration is presented in the Figure 91a, b. The intermolecular binding energy of this configuration, which is in good agreement with what is observed on the STM images, is 4.3 kcal/mol. It is in the typical range for CH-π interactions[252,253]. The initial constraint on the first molecule does not have much influence on the final results: a few molecules with a constrained C_6 were compared but their difference in energy after optimization was only 0.04 kcal/mol higher.

A close-up within the ordered islands (Figure 90) reveals the presence of a complex long range ordered structure with a (27, 0; 0, 27) unit cell. In this motif, some of the molecules do not show a rim dominated contrast anymore but rather a bright protrusion in the center such as the one observed in the Figure 89f. In total, 9 out of 27 molecules in the unit cell have their concave side pointing down. Two motifs are observed within the structure (Figure 90). In both cases, only three of the six molecules surrounding the opening-down bowl have their convex sides pointing towards this bowl, establishing a π-π interaction. The three other molecules point away from it, probably because they establish attractive π–π interactions with the convex sides of other opening-down bowls nearby.

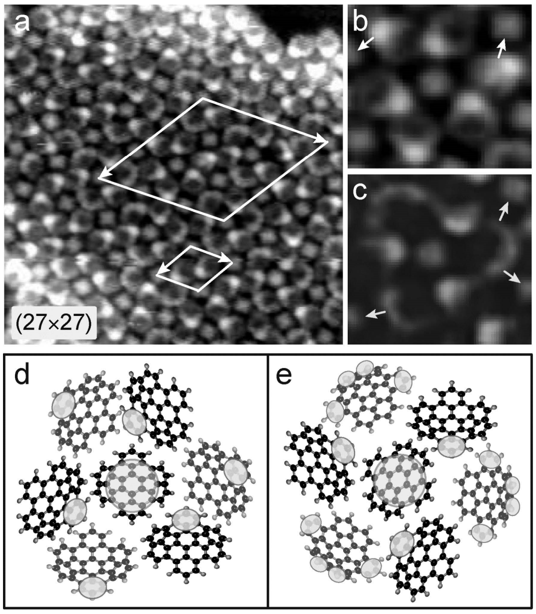

Figure 90: (a) STM image of an ordered domain formed by $C_{38}H_{14}$ on Cu(111) at low coverage (17 nm × 17 nm, 699 mV, 168 pA). Close-ups on the two motifs encountered are shown in (b) and (c) with their corresponding models in (d) and (e). White arrows point at molecules with a bowl opening down contrast, from an adjacent tilted molecule which faces it with its convex side.

MM was used to model the interaction between a bowl opening-down and a bowl opening-up (Figure 91c, d). No constraint on the molecules was needed in this case. However, one bowl was initially placed with a bowl-opening down configuration on the surface before optimization. The lowest energy configuration has a binding energy of 8.0 kcal/mol. This is larger than π-π interactions between two parallel benzene molecules[126] (2-3 kcal/mol and a distance of 4.96 Å) but much smaller than corannulene bowl-in-bowl π-π interactions[254] (15.6 kcal/mol and a distance of 3.54 Å). Exactly as observed with STM, the other molecule is tilted such that the phenylyne ring is pointing up. The smallest intermolecular distance is between two C_6 rings: one at the rim of the bowl opening-down and one close to the center of the tilted opening-up molecule. The molecules' alignment is probably supported by a favored adsorption site for the low-lying phenylyne ring of the opening-up bowl (Figure 90). An example of local-minimum configuration with the naphthalene group of the opening-up bowl interacting with the opening-down bowl (Figure A. 23 in the appendix) results in higher energy (by +1.45 kcal/mol).

So far, an opening-down adsorption geometry has only been reported for sumanene on Ag(111)[255]. This orientation has been explained by an inversion of the molecule during the process of adsorption in order to optimize intermolecular interactions. The inversion barrier of sumanene is 19.6 kcal/mol in solution[256] but it is more than 4 times higher for $C_{38}H_{14}$ (79.8 kcal/mol)[49]. It is therefore more likely that the $C_{38}H_{14}$ bowl turns during nucleation of the islands assembly such that it shows the best π–π overlap with convex sides of other molecules.

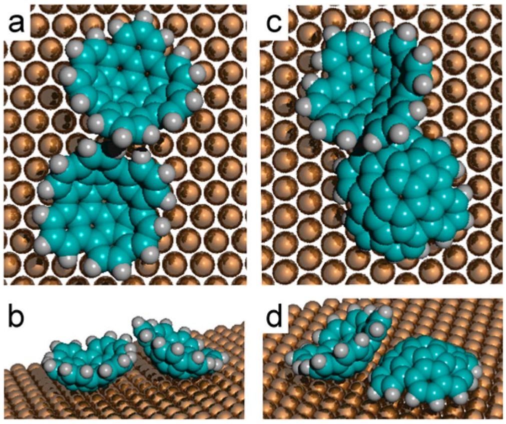

Figure 91: Top and side view of the minimum-energy models of dimers of $C_{38}H_{14}$ on Cu(111) obtained by AMBER-force field calculation. (a, b) The central C_6 ring of the bowl opening-up was constrained on the surface. (c, d) No constraint was applied but one of the bowl was initially turned in an opening-down configuration before optimization. The best configurations presented here were obtained after optimization of 216 initial configurations. They correspond well with what was observed with STM.

In conclusion, the study of $C_{38}H_{14}$ revealed that even though buckybowls are expected to preferentially adsorb in an opening-up configuration too optimize their interactions with the surface, strong lateral interactions such as π-π or CH-π bonding between the molecules can favor a tilted or an opening-down configuration, as confirmed using MM modeling. Note that this happens only at sub-molecular coverage, when intermolecular interactions are dominated by attractions. Often, short distances between molecules are assigned wrongly to attractive binding between various functional groups whereas they are often induced by packing constraints from the surface or from the surrounding molecules[257,258]. This is not the case in this work: the coverage is low and if not attracted to each other, the molecules would have enough space to stay far away from each other.

3.3 Terphenylcorannulene on Cu(111)

This study of terphenylcorannulene (TpC, $C_{32}H_{12}$, Figure 71)[xxxix] aims to show what is the influence of three additional annulated benzo groups on the self-assembly and on the adsorption footprint. At low coverage ($\theta << 0.1$ ML), single molecules and small aggregates of TpC are observed (Figure 92a-d). In all cases, the molecules appear with a bright protrusion on one side and have a C-shape with a C_s symmetry. It corresponds to the contrast of the EHT electron density map of a molecule with the naphthalene group pointing up (Figure 92d) and the middle annulated benzo group adsorbed on the surface.

[xxxix] Most of the results presented in this paragraph were published in ref.[272].

Note that these STM images were recorded at sub-molecular coverage. When dimers or other aggregates form, they must be dominated by attractions. In Figure 92b and d, the molecules seem to interact either via π-π (convex to convex) or via CH-π (convex to rim) interactions.

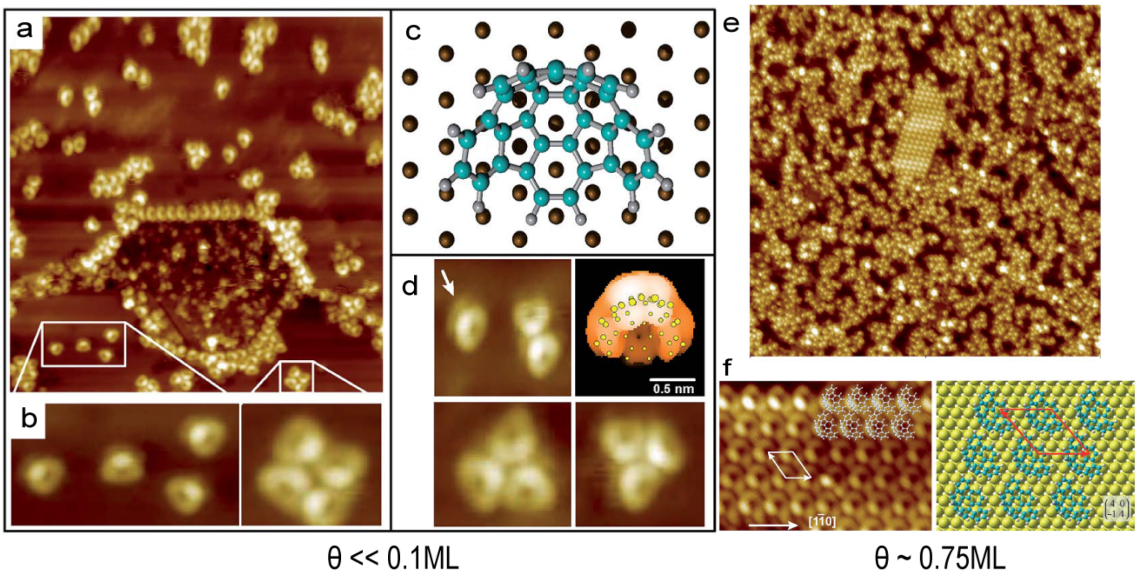

Figure 92: (a-d) Large scale STM image (40 nm × 40 nm, –2.4 V, 61 pA), close-ups and models of TpC on Cu(111) at very low coverage (θ << 0.1 ML). In the large scale STM image, all molecules are tilted as displayed in the model (c). This observation is valid for single molecules (b) and small aggregates (d). Ext. Hückel electron density map of the HOMO[xl] (levels 66-70) of a molecule with the middle benzo group of the terphenyl group parallel to the surface is presented in (d). It corresponds with a single molecule contrast in STM (e.g. white arrow). (e, f) STM images and models of TpC on Cu(111) at higher coverage (θ ~ 0.75 ML), when self-assembled domains start to form. (e) STM image showing the formation of an ordered domain with rows of molecules (80 nm × 80 nm, 857 mV, 135 pA). A zoom on this structure (f) reveals that it is made of aligned tilted molecules as modeled on the side of the STM image.

AMBER force-field optimization calculation was performed on a single TpC molecule, over 108 initial configurations. The result is given in the Figure 92c and Figure 93a. The molecule adsorbs in a tilted configuration with the central benzo group of the terphenyl moiety parallel to the surface. It was obtained without any constraint on the molecules. This configuration is in agreement with the STM images. The best dimer configuration of 216 initial configurations tested, with both molecules free to relax on the surface, is made of two bowls opening-up. It does not correspond to the STM images showing once again that the interaction between surface and curved PAH is not properly addressed by MM. To gain information on the dimer binding energy, the central terphenyl C_6 ring of both molecules was constrained on the surface. At least 16 initial configurations with various distances and angles between the molecules were tested. The best configuration is presented in the Figure 93b. The binding energy is 7.6 kcal/mol. The convex-convex interaction site suggests a π-π non-covalent binding motif. 7.6 kcal/mol is

---

[xl] Only the HOMO is displayed based on the bias voltage used in the image (a).

larger than π-π interactions between two parallel benzene molecules[126] (2-3 kcal/mol) but about two times smaller than corannulenes bowl-in-bowl π-π interactions[254] (15.6 kcal/mol).

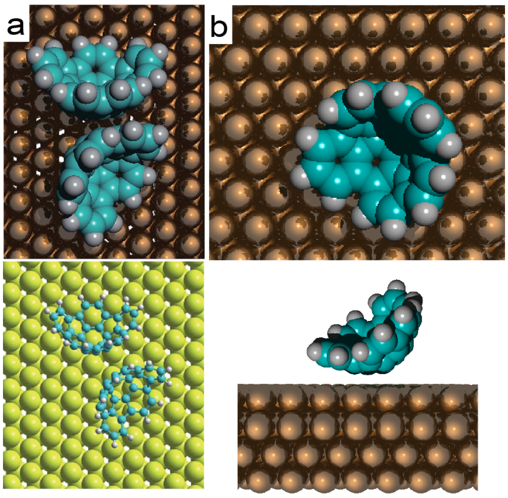

Figure 93: MM models of TpC on Cu(111). (a) Minimum-energy configuration of a dimer, with a binding energy of 7.6 kcal/mol. The central therphenyl C_6 rings of both molecules were fixed. (b) Minimum-energy configuration of a single molecule which could relax freely on the surface.

At higher coverage (θ ~ 0.75 ML), long-range ordered structures made of tilted molecules form (Figure 92 e-f). The unit cell has a (4, 0; –1, 4) periodicity on surface. Because they are fitting into each other, the assembly is probably induced by CH-π interactions, even though at high coverages, the assembly can always be induced by constraints from the substrate or from the others surrounding molecules which can be repulsive and force the molecules into a specific assembly[257,258]. This should be kept in mind, especially for saturated coverage. In this case (θ ~1 ML), two structures are observed, both made of tilted molecules and with the same areal density (1 molecule per 14 Cu atoms). The first one (see images and model in Figure 94 a-c) has a stripes motif with tilted molecules aligned in the same direction in every second row. From one row to the neighboring one, the tilted molecules rotate by 60° in accordance with the symmetry of the Cu(111) substrate. In the second structure (Figure 94 d-f), double rows of molecules are observed. Note that this motif was sometimes also observed at lower coverage. In each row, the molecules are sitting side by side (convex side against convex side). The coexistence of two structure was also observed for corannulene[128].

In summary, TpC adopts at all coverages a tilted adsorption footprint with its middle annulated benzo group parallel to the surface. It means that the addition of three annulated benzo groups to corannulene caused the molecules to change its adsorption footprint from a position with the bowl axis almost perpendicular to the surface[128] to a position where the axis is almost parallel to the surface. In addition, single-molecules can be already imaged at 60 K, whereas compounds with similar sizes, such as pentahelicenes[67] or heptahelicenes[111] are diffusing too fast on the surface to be seen. Both observations imply that the molecules strongly interact with the surface. However, the contact between the surface and a TpC is really limited and it indicates the presence of a strong electrostatic interaction (elevated interface dipole) with the copper template in addition to the vdW forces. It was already observed for corannulene[245], MiC[69] (paragraph IV.3.1) and PiC (paragraph IV.2), This strong electrostatic interaction with the Cu(111) surface stabilizes this footprint at all coverages. Based on low coverages observation, intermolecular interactions seem to be dominated by π-π and CH-π non-covalent bonding.

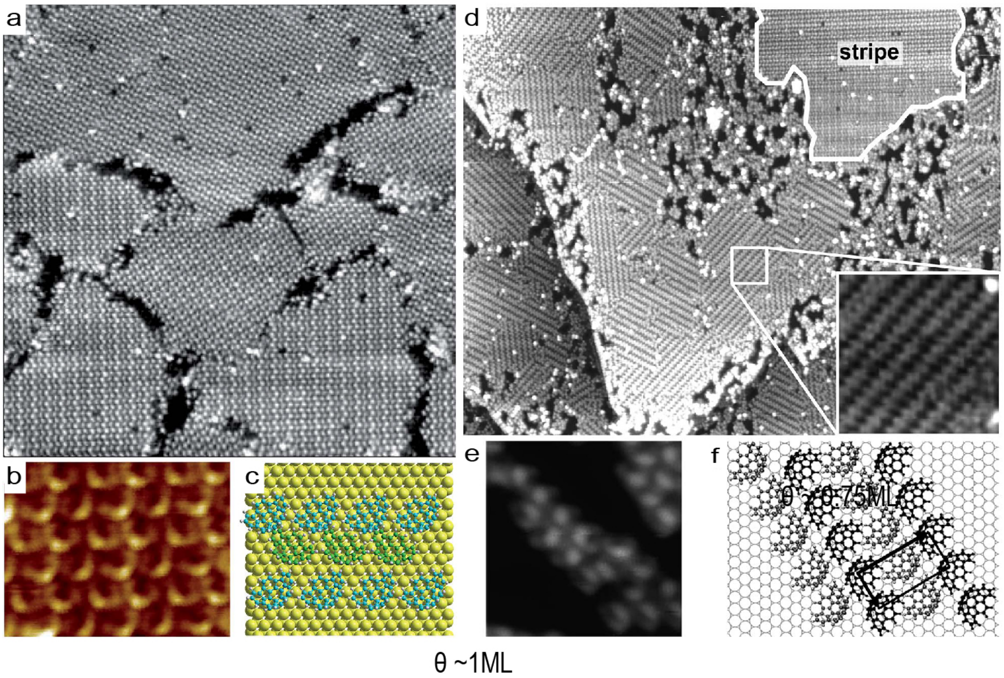

Figure 94: STM images and corresponding model of the two structures formed by TpC close to saturated ML coverage on Cu(111). (a-c) Stripes structure made of tilted molecules aligned in the same direction in very second row. From one row to the next, the molecule tilt by 60°. (d-f) The stripe structure together with a second structure with a double row pattern are observed (d). A double row is made of tilted molecules aligned face to face (e-f). (Measuring parameters: a: 80 nm × 80 nm, –1.2 V, 140 pA; d: 200 nm × 160 nm, 1.2 V, 137 pA; e: 7 nm × 7 nm, –671 mV, 79 pA)

3.4 Conclusion

Three different buckybowls were studied by means of STM. Due to a complex balance between vdW and Pauli interactions between molecules and surface as well as intermolecular CH-π interactions, MiC adsorbs at ML coverage with a tilted configuration. The molecules form ordered zigzag lines of molecules. A pronounced charge redistribution and a large interface dipole are observed at the organic/metal interface as for PiC on Cu(100) and influence the tilt angle of the molecule. No charge-transfer was involved. Such a large interface dipole, on the order of what is found for adsorption of alkali metal on metal surfaces, was never observed for planar PAH but already reported for curved PAH.

The study of $C_{38}H_{14}$ showed an uncommon example of self-assembly with buckybowls adsorbing with an opening down configuration, induced by strong lateral attractive interactions (π-π and CH-π bonding) at low coverage.

By studying TpC on Cu(111), it was observed that the addition of three benzo groups at the rim of corannulene modifies the molecular adsorption footprint from a position with the bowl axis almost perpendicular to the surface to a position where the axis is almost parallel to the surface. This footprint is so stable that it is observed at all coverage, independently of the π-π and CH-π interactions between the molecules close to saturation coverage

All these results were justified using modelling techniques based on quantum mechanics (EHT or DFT) for the adsorption footprints. MM encountered limitations in the modelling of the surface to molecules interactions because of it cannot consider Pauli repulsion and polarization effects which play an important role for the buckybowls adsorption on metal. MM was however helpful to identify weak non-covalent interactions between the molecules.

V. General conclusions and outlook

V.1. Chiral PAH

In the first half of this work, the on-surface self-assembly and thermally-induced chemical reactions of helicenes were investigated. *Rac*-[5]H on Cu(111) was compared to [7]H. The larger interplanar angle of [5]H favored the formation of homochiral dimers, which are also energetically preferred in 3D[125], instead of the heterochiral dimers formed by [7]H. The modification of the short-ordered structure had considerable impacts on the self-assembly. An heterochiral to homochiral transition in the first-layer was induced by second-layer nucleation. This effect was caused by an intrinsic enantiomeric excess created locally by the transport of molecules from the first to the second layer and favored by a limited diffusion of the molecules. Such effect was previously observed for [7]H, but only at enantiomeric excess. The tunability of the first-layer properties, induced by a small excess in coverage, could be interesting to achieve different functionalization for applications, e.g. in organic electronics in order to tune the molecular structure at electrode interfaces of devices. It would be interesting to study the same mechanism on functionalized pentahelicenes such as dicyano[5]H which has polar groups.

Enantiopure *(M)*-1-aza[6]H was studied at low coverage on two different samples, Cu(100) and Au(111), inducing different adsorption footprints. On both surfaces, the short-range ordered structures formed by *(M)*-aza[6]H and [7]H were similar. This implied a small influence of a missing benzene ring and of the aza-group on the intermolecular interactions. The structures formed at low coverage by *(M)*-amino[6]H on Cu(100) looked alike but were completely different on Au(111), inducing a different self-assembly on this surface. This implied a stronger influence of the polar amino group compared to the aza group on the intermolecular interactions, especially when the substrate/molecules interactions are weak. Mixing experiment could also be investigated as aza[6]H can be prepared in enantiopure and a racemic fashion. Sergeant-and-soldiers and majority rule have only been investigated on non-functionalized helicenes so far.

The self-assembly of bis[7]H(sol), synthetized in solution prior sublimation was also studied in ordered to be compared with the self-assembly of bis[7]H synthetized on surface. On Au(111) and Cu(111) the molecules formed identical structures, due to the similar geometry of the templates and despite a small difference in their unit cells' size. One structure was built with rows of homochiral bishelicenes with alternating handedness and the other was made of heterochiral bis[7]H. The surface was overall racemic and both homochiral and heterochiral bis[7]H were observed on the surface as expected by the randomness and efficiency of the synthesis method used in solution.

Two kinds of thermally induced on-surface chiral chemical reactions were then performed on helicenes. At first, Ullmann coupling was performed to determine if stereochemical effects can be induced during chemical reactions of chiral molecules in 2D due to the up-down asymmetry of the surface. Diastereoselectivity was observed after C-C coupling of *rac*-Br[4]H on copper. A diastereoselectivity was induced by the low racemization barrier at room temperature. On both, Au(111) and Cu(111), the C–C coupling of Br[7]H was successful but conducted differently. When evaporated at room temperature, the molecules formed a self-assembly made of organometallic dimers on Cu. On Au, Br[7]H form heterochiral dimers arranged into zigzag rows, as observed for *rac*-[7]H on Au(111), Cu(111) and Ag(111). It shows the weak impact of the Br atom on the intermolecular interactions. However, for Br[7]H, a larger spacing between the rows is observed, leading to a better ordering on Au(111). After annealing, C-C coupling was obtained on both Au and Cu but the presence of Br prevented the self-assembly of the produced bis[7]H (surf) on Cu(111). On Au(111), self-assembly was observed, but one of the ordered-structure was different than the one observed in the self- assembly of bis[7]H (sol). XPS measurements confirmed that the presence of Br atoms on the surface was not responsible for this modification. It could either be due to a reconstruction of the Au(111) surface or to a structural modification of the molecules during coupling. The formation of different conformers on the surface, compared to the those formed during adsorption of already synthetized molecules, could be another explanation. The work on Ullmann coupling reveals that diastereoselectivity is not induced during the reaction but can be induced later, by an inversion of the molecules, which adopt the most energetically favorable configuration for close packing. In addition, due to the various values mentioned in the literature for the desorption temperatures of halogen, the Br desorption was studied carefully with TPD and XPS. As observed previously for DBBA[191], Br only leaves the surface in the form of HBr and therefore requires the dehydrogenation of the molecules. The partial dehydrogenation or cyclodehydrogenation processes being favored by steric overcrowding, explains the specificity of the halogen desorption process and the broad range of temperatures observed in the literature. This also occurs for helicenes(sol) synthetized by solution chemistry. This result is important, not only for the understanding of the Ullmann process but also because Br desorption can often involve a structural modification of the molecule under study, an effect too often neglected by the surface science community, because they are hardly observed with standard STM and XPS techniques.

The second on-surface reaction which was investigated is the decomposition of PAH on oxygen-reconstructed copper. In this experiment, the first surface explosion of oxygen-free molecules was presented. The PAH tested all produced H_2O and CO_2 during their decomposition. The autocatalytic flash decomposition depends on the formation of vacancies in the oxygen layer which act as active surface sites and trigger the autocatalytic decomposition. The initialization is induced by thermal activation. However, flash autocatalytic decomposition was not observed for all PAH. This study showed that two ingredients were needed: the possibility of easy dehydrogenation by steric overcrowding and the presence of a Br in the molecule. When at least one of these two factors is missing, the decomposition is not autocatalytic. On O/Cu(100), the released hydrogen can react with the oxygen layer and creates a first vacancy which initiates the autocatalytic decomposition process. This hypothesis is supported by our work on the desorption of Br during Ullmann coupling of Br[7]H: different explosion temperatures are indeed observed for different PAHs and we showed that these PAHs have different partial dehydrogenation temperatures which would then involve different initiation temperatures of the explosion process. The second important ingredient of surface explosion is the presence of a molecular anchoring to the surface due to debromination well before explosion. Without anchoring, e.g. for [7]H, no surface explosion occurs. Because of the weakening of C-C bonds adjacent to an organometallic C-Cu bond, "anchoring" might allow the destabilization of the stability of benzene rings leading to easier dissociation of CO_2 production and flash autocatalytic decomposition. However, many experiments still need to be performed in the future to improve our understanding of this effect on strained PAH. The first one is about the nature of the decomposition products: carbon is indeed still present on surface after the reaction as confirmed by XPS. Surface explosion could be used to produce certain compounds in addition to CO_2 and H_2O which could even be chiral such as in ref.[198]. The observation of surface explosion of Br-terminated PAH with strain in their molecular backbone raises a number of questions and permits novel experiments. For instance, other halogens and functional groups may also permit the explosion and the nature of the metal surface or the purity of the molecular compounds might have a considerable influence on the reaction. Despite those unsolved questions, the impacts of this study are numerous. At first, it should increase the awareness on the easy reduction capability of certain metal-oxides such as copper: in the race for surface functionalization for new devices, many chemical and coupling reactions are now studied on surfaces but this aspect is often neglected. In addition, the present work opens the path for many other experiments which could develop the current understanding of autocatalytic reactions but also of heterogeneous catalysis.

V.2. Curved PAH

PiC was studied at different coverages on Cu(100) for which different adsorption footprints were observed. At low coverage, when intermolecular interactions are negligible, PiC adsorbs bowl opening-up with its bowl axis perpendicular to the surface. However, at saturated monolayer coverage, CH-π and π-π intermolecular interactions induce a tilt of the molecules. The assembly is similar to what was observed for MiC which has only one indeno group instead of five. PiC adsorbs with two indeno groups parallel to the surface instead of one for the MiC on Cu(100).

Using EHT, MM or DFT computations, the adsorption configuration and the self-assemblies formed by MiC, $C_{38}H_{14}$ and TpC on Cu(111), observed with STM could be determined. In particular, assumptions concerning the nature of the different interactions (π-π, CH-π…) responsible for the different observed motifs could be justified. As for PiC, MiC adopted a tilted configuration at saturated ML coverage but with a different ordered-structure than on Cu(100) due to the different substrates symmetries. This configuration is due, as for PiC, to a complex balance between vdW and Pauli interactions between molecules and surface as well as intermolecular CH-π interactions. A large interface dipole without charge-transfer was also observed. Such large charge redistribution might be interesting to tune the injection properties of metalloorganic interfaces in optoelectronic devices. The asymmetry of TpC induced a tilt of the bowl at all coverages with the bowl axis literally parallel to the surface. The self-assembly observed at saturated ML coverage was justified the attractive π-π and CH-π non-covalent bonding forces between the molecules. Intermolecular interactions induced the uncommon bowl-opening-down adsorption footprint for some of the $C_{38}H_{14}$ in the self-assembly formed by these molecules at medium coverage. These results were justified using EHT, MM or DFT. The computationally depending, quantum-based DFT was compared with MM based on classical-mechanics. The motivation to compare both modelling techniques came from the pentahelicene case (paragraph III.2) where both gave a really similar final molecular configuration on Cu(111)[67]. Unfortunately, for buckybowls strong charge-induced polarization effects induced by the adsorption of curved PAH on metals need to be considered. MM is based on classical mechanics which does not consider the electrons explicitly and is not able to account for polarization and charge redistribution and therefore cannot compute the exact adsorption footprint of buckybowls. However, it can consider the weak non-covalent interactions between the molecules. Note that the DFT method used in this work uses functionals which consider polarization effects but it still have limitations. DFT predicted for example, a tilted adsorption footprint for PiC at low coverage but the experimental results indicated that this configuration is only observed when at least two molecules interact with each other.

Thermally induced on-surface chemistry was performed using PiC on Cu(100) in order to form new species. The low coverage case ($\theta < 0.3$ ML) was particularly interesting because annealing at 503 K led to the formation of flat star-shaped molecules probably induced by copper catalyzed C-C bonds breaking in order to optimize the contact area between the molecules and the metal surface. The stars could however be use as a precursor for growing 2D materials such as graphene or nanoribbons. It could also be interesting to form functional layers on surface by trying to deposit compounds (such as fullerenes) in the bowls or between two PiC. They could also be used as a precursor for endofullerene formation. At higher coverage (0.3 ML < θ < 0.7 ML), annealing leads to the formation of rows of molecules fitting into one another. PiC should be investigated on other metal surfaces such as Ag and Au to determine the catalytic influence of the surface on the reaction products of the thermally-induced reaction. Other buckybowls should also be annealed to determine what parameters, e.g. the bowl curvature, lead to a flattening of the molecules. The formation of a nanotube cap starting from flat precursors was already observed[29] but the PiC show the exact opposite phenomenon.

V.3. General remarks and outlook

In addition to the individual results obtained for each case study, this thesis sheds light upon more general behaviors of PAH. For instance, all studied molecules, when adsorbed on metal surfaces encountered strong Pauli repulsion, an effect which was stronger for curved PAH, leading to a strong charge redistribution at the PAH/metal interface. It induced the presence of a strong interface dipole. For curved PAH, self-assembled motifs were mostly induced by π-π and CH-π non-covalent intermolecular interactions. These interactions can be quite strong and induce a different footprint on the surface when the molecules interact with each other with respect to the footprint of a single molecule. This effect was not observed for chiral PAH for which the footprint determined by the substrate was only weakly disturbed by the intermolecular interactions: all helicenes adsorb with their lowest three first C_6 rings parallel to the surface.

Moreover, this work showed that the small structural modification consisting of additional benzene rings on the molecular backbone has already important incidences for non-planar PAH. It can revolutionize the intermolecular interaction and self-assembly, induce a change in the adsorption footprint or influence the reaction products of a coupling reaction.

This thesis also reveals the important role played by hydrogen in on-surface chemistry. For Ullmann coupling, Br desorption was induced by dehydrogenation of the molecules leading to a structural modification of the reaction products. Similarly, partial dehydrogenation of helicenes induced by steric overcrowding was one of the necessary requirements to observes autocatalytic decomposition. The H-induced chemical reactions should not be underestimated.

Various surface sensitive techniques were employed to gain useful information about the chemical composition, the structural molecular arrangement, the desorption of reaction products, the thermodynamics, etc. For instance, the sub-molecular resolution of STM successfully allowed the discrimination of absolute configuration of single molecules and thus the study of molecular recognition in monolayers. Despite being slow, STM could also provide insights into fundamental processes of crystallization.

Surface chemistry has a huge economic impact due to its applications in today's world: medical devices, optoelectronics, chemicals production, fuels or new materials and interfaces design. The constant development of new technologies and their 'nanoisation' calls for molecular-level understanding of surface chemistry in complex environments. This work demonstrates how surface science tools facilitates the investigation of problems posed currently and to set fundamental knowledge about molecular-level interactions at the interfaces and about on-surface chemistry and their thermodynamics in various conditions, leading to the new technological advances and industrial processes of tomorrow.

References

1. O'Connor, John, Sexton, Brett, Smart, R. (Eds. . *Surface Analysis Methods in Materials Science*. (Springer, 2003). doi:10.1007/978-3-662-05227-3
2. Wandelt, K. *Surface and Interface Science and vol. 1: Concepts and Methods*. (Wiley-VCH, 2014). doi:10.1002/9783527680535
3. Somorjai, G. A. & Li, Y. Impact of surface chemistry. *PNAS* **108,** 917–924 (2011).
4. Goiri, E., Borghetti, P., El-Sayed, A., Ortega, J. E. & de Oteyza, D. G. Multi-Component Organic Layers on Metal Substrates. *Adv. Mater.* **28,** 1340–1368 (2016).
5. Filatov, A. S., Scott, L. T. & Petrukhina, M. A. π−π Interactions and Solid State Packing Trends of Polycyclic Aromatic Bowls in the Indenocorannulene Family: Predicting Potentially Useful Bulk Properties. *Cryst. Growth Des.* **10,** 4607–4621 (2010).
6. Schmidt, W. G. *et al.* Organic molecule adsorption on solid surfaces: chemical bonding, mutual polarisation and dispersion interaction. *Appl. Phys. A* **85,** 387–397 (2006).
7. Fasel, R., Parschau, M. & Ernst, K.-H. Amplification of chirality in two-dimensional enantiomorphous lattices. *Nature* **439,** 449–452 (2006).
8. Parschau, M. *et al.* Buckybowls on Metal Surfaces: Symmetry Mismatch and Enantiomorphism of Corannulene on Cu(110). *Angew. Chemie Int. Ed.* **46,** 8258–8261 (2007).
9. Hemsley, A. R., Collinson, M. E., Kovach, W. L., Vincent, B. & Williams, T. The Role of Self-Assembly in Biological Systems: Evidence from Iridescent Colloidal Sporopollenin in Selaginella Megaspore Walls. *Philos. Trans. R. Soc. B Biol. Sci.* **345,** 163–173 (1994).
10. Xi, M. & Bent, B. E. Iodobenzene on Cu(111): formation and coupling of adsorbed phenyl groups. *Surf. Sci.* **278,** 19–32 (1992).
11. Xi, M. & Bent, B. E. Mechanisms of the Ullmann Coupling Reaction in Adsorbed Monolayers. *J. Am. Chem. Soc.* **115,** 7426–7433 (1993).
12. Mhatre, B. S. *et al.* A window on surface explosions: Tartaric acid on Cu(110). *J. Phys. Chem. C* **117,** 7577–7588 (2013).
13. Purushotham, U. & Sastry, G. N. Conjugate acene fused buckybowls: evaluating their suitability for p-type, ambipolar and n-type air stable organic semiconductors. *Phys. Chem. Chem. Phys.* **15,** 5039 (2013).
14. Yao, Y. *et al.* Effects of C_{70} derivative in low band gap polymer photovoltaic devices: Spectral complementation and morphology optimization. *Appl. Phys. Lett.* **89,** 153507 (2006).
15. Shrotriya, V. Organic photovoltaics: Polymer power. *Nat. Photonics* **3,** 447–449 (2009).
16. Mack, J., Vogel, P., Jones, D., Kaval, N. & Sutton, A. The development of corannulene-based blue emitters. *Org. Biomol. Chem.* **5,** 2448 (2007).
17. Burroughes, J. H. *et al.* Light-emitting diodes based on conjugated polymers. *Nature* **347,** 539–541 (1990).
18. Dimitrakopoulos, C. D. & Malenfant, P. R. L. Organic Thin Film Transistors for Large Area Electronics. *Adv. Mater.* **14,** 99–117 (2002).
19. Chassé, T., Wu, C.-I., Hill, I. G. & Kahn, A. Band alignment at organic-inorganic semiconductor interfaces: α-NPD and CuPc on InP(110). *J. Appl. Phys.* **85,** 6589 (1999).
20. Bloom, C. J., Elliott, C. M., Schroeder, P. G., France, C. B. & Parkinson, B. A. Low Work Function Reduced Metal Complexes as Cathodes in Organic Electroluminescent Devices. *J. Phys. Chem. B* **107,** 2933–2938 (2003).
21. Koller, G., Blyth, R. I. R., Sardar, S. A., Netzer, F. P. & Ramsey, M. G. Band alignment at the organic-inorganic interface. *Appl. Phys. Lett.* **76,** 927 (2000).

22. Scott, J. C. Metal–organic interface and charge injection in organic electronic devices. *J. Vac. Sci. Technol. A Vacuum, Surfaces, Film.* **21,** 521–531 (2003).
23. Denis, P. A. Investigation of H_2 Physisorption on Corannulene ($C_{20}H_{10}$), Tetraindenocorannulene ($C_{44}H_{18}$), Pentaindenocorannulene ($C_{50}H_{20}$), C_{60}, and their Nitrogen Derivatives. *J. Phys. Chem. C* **112,** 2791–2796 (2008).
24. Denis, P. A. Design and characterization of two strong fullerene receptors based on ball–socket interactions. *Chem. Phys. Lett.* **591,** 323–327 (2014).
25. Mattarella, M., Garcia-Hartjes, J., Wennekes, T., Zuilhof, H. & Siegel, J. S. Nanomolar cholera toxininhibitors based on symmetrical pentavalent ganglioside GM1os-sym-corannulenes. *Org. Biomol. Chem.* **11,** 4333–4339 (2013).
26. Kishi, N. *et al.* Wide-Ranging Host Capability of a Pd II -Linked M 2 L 4 Molecular Capsule with an Anthracene Shell. *Chem. - A Eur. J.* **19,** 6313–6320 (2013).
27. Olson, A. J., Hu, Y. H. E. & Keinan, E. Chemical mimicry of viral capsid self-assembly. *Proc. Natl. Acad. Sci.* **104,** 20731–20736 (2007).
28. Turchanin, A. & Gölzhäuser, A. Carbon nanomembranes from self-assembled monolayers: Functional surfaces without bulk. *Prog. Surf. Sci.* **87,** 108–162 (2012).
29. Sanchez-Valencia, J. R. *et al.* Controlled synthesis of single-chirality carbon nanotubes. *Nature* **512,** 61–64 (2014).
30. Petrukhina, M. A. & Scott, L. T. *Fragments of Fullerenes and Carbon Nanotubes*. (John Wiley & Sons, Inc., 2011). doi:10.1002/9781118011263
31. Yu, Z. Q., Wang, C. M., Du, Y., Thevuthasan, S. & Lyubinetsky, I. Reproducible tip fabrication and cleaning for UHV STM. *Ultramicroscopy* **108,** 873–877 (2008).
32. Binnig, G. & Rohrer, H. Scanning Tunneling Microscopy. *Surf. Sci.* **126,** 236–244 (1983).
33. Ernst, K.-H. in *Supramolecular Chirality* **265,** 209–252 (Springer-Verlag, 2006).
34. Feynmann, R. P., Leighton, R. B. & Sands, M. *The Feynmann lectures on physics. Vol. III: quantum mechanics*. (Addison-Wesley Publ. Co., 2014).
35. Morgenstern, K., Lorente, N. & Rieder, K.-H. Controlled manipulation of single atoms and small molecules using the scanning tunnelling microscope. *Phys. status solidi* **250,** 1671–1751 (2013).
36. Chaika, A. N. *et al.* Fabrication of [001]-oriented tungsten tips for high resolution scanning tunneling microscopy. *Sci. Rep.* **4,** 1–6 (2014).
37. Mohn, F., Gross, L., Moll, N. & Meyer, G. Imaging the charge distribution within a single molecule. *Nat. Nanotechnol.* **7,** 227–231 (2012).
38. Hofer, W. A., Foster, A. S. & Shluger, A. L. Theories of scanning probe microscopes at the atomic scale. *Rev. Mod. Phys.* **75,** 1287–1331 (2003).
39. Besenbacher, F. Scanning tunnelling microscopy studies of metal surfaces. *Rep. Prog. Phys.* **59,** 1737–1802 (1996).
40. Gross, L. Recent advances in submolecular resolution with scanning probe microscopy. *Nat. Chem.* **3,** 273–278 (2011).
41. Vickerman, J. C. & Gilmore, I. S. *Surface Analysis– The Principal Techniques*. (John Wiley & Sons, Ltd, 2009). doi:10.1002/9780470721582
42. Einstein, A. Über einen die Erzeugung und Verwandlung des Lichtes betreffenden heuristischen Gesichtspunkt. *Ann. Phys.* **322,** 132–148 (1905).
43. Moulder, J. F., Stickle, W. F., Sobol, P. E. & Bomben, K. D. *Handbook of x-ray photoelectron spectroscopy: a reference book of standard spectra for identification and interpretation of XPS data*. (Physical Electronics Division, Perkin-Elmer Corp, 1992).
44. Hüfner, S. *Photoelectron spectroscopy: principles and applications*. (Springer-Verlag, 1995).
45. Redhead, P. A. Thermal desorption of gases. *Vacuum* **12,** 203–211 (1962).

46. Carter, G. Thermal resolution of desorption energy spectra. *Vacuum* **12,** 245–254 (1962).

47. Allemann, O., Duttwyler, S., Romanato, P., Baldridge, K. K. & Siegel, J. S. Proton-Catalyzed, Silane-Fueled Friedel-Crafts Coupling of Fluoroarenes. *Science (80-.).* **332,** 574–577 (2011).

48. Weimar, M., Correa da Costa, R., Lee, F.-H. & Fuchter, M. J. A Scalable and Expedient Route to 1-Aza[6]helicene Derivatives and Its Subsequent Application to a Chiral-Relay Asymmetric Strategy. *Org. Lett.* **15,** 1706–1709 (2013).

49. Wu, T.-C., Chen, M.-K., Lee, Y.-W., Kuo, M.-Y. & Wu, Y.-T. Bowl-Shaped Fragments of C 70 or Higher Fullerenes: Synthesis, Structural Analysis, and Inversion Dynamics. *Angew. Chemie Int. Ed.* **52,** 1289–1293 (2013).

50. Wäckerlin, C. *et al.* Surface-assisted diastereoselective Ullmann coupling of bishelicenes. *Chem. Commun.* **52,** 12694–12697 (2016).

51. Born, M. & Oppenheimer, R. Zur Quantentheorie der Molekeln. *Ann. Phys.* **389,** 457–484 (1927).

52. Chong, D. P. *Recent Advances in Density Functional Methods (Part II)*. (World Scientific Publishing Co.Pte.Ltd., 1997).

53. Bartók-Pártay, A. *The Gaussian Approximation Potential*. (Springer Berlin Heidelberg, 2010). doi:10.1007/978-3-642-14067-9

54. Howard, A., McIver, J. & Collins, J. *HyperChem Computational Chemistry Part 2: Theory and Methods*. (1996).

55. Parr, R. G. & Weitao, Y. *Density Functional Theory of Atoms and Molecules*. (Oxford University Press, 1994).

56. Koch, W. & Holthausen, M. C. *A Chemist's Guide to Density Functional Theory*. (Wiley-VCH Verlag GmbH, 2001). doi:10.1002/3527600043

57. Carlos Fiolhais, Fernando Nogueira, Miguel Marques, E. E. A Primer in Density Functional Theory. *Mater. Today* **6,** 59 (2003).

58. Hohenberg, P. & Kohn, W. Inhomogeneous Electron Gas. *Phys. Rev.* **136,** B864–B871 (1964).

59. Kohn, W. & Sham, L. J. Self-Consistent Equations Including Exchange and Correlation Effects. *Phys. Rev.* **140,** A1133–A1138 (1965).

60. Cohen, A. J., Mori-Sánchez, P. & Yang, W. Challenges for Density Functional Theory. *Chem. Rev.* **112,** 289–320 (2012).

61. Perdew, J. P., Ruzsinszky, A., Constantin, L. A., Sun, J. & Csonka, G. I. Some Fundamental Issues in Ground-State Density Functional Theory: A Guide for the Perplexed. *J. Chem. Theory Comput.* **5,** 902–908 (2009).

62. Carrasco, J., Liu, W., Michaelides, A. & Tkatchenko, A. Insight into the description of van der Waals forces for benzene adsorption on transition metal (111) surfaces. *J. Chem. Phys.* **140,** 084704 (2014).

63. Dion, M., Rydberg, H., Schröder, E., Langreth, D. C. & Lundqvist, B. I. Van der Waals Density Functional for General Geometries. *Phys. Rev. Lett.* **92,** 246401 (2004).

64. Hoffmann, R. An Extended Hückel Theory. I. Hydrocarbons. *J. Chem. Phys.* **39,** 1397–1412 (1963).

65. Whangbo, M.-H. in *Theoretical Chemistry Accounts* 252–256 (Springer Berlin Heidelberg, 2001). doi:10.1007/978-3-662-10421-7_26

66. Leach, A. R. *Molecular Modelling: Principles and Applications, second edition*. (Pearson Education EMA, 2001).

67. Mairena, A. *et al.* Heterochiral to Homochiral Transition in Pentahelicene 2D Crystallization Induced by Second-Layer Nucleation. *ACS Nano* **11,** 865–871 (2017).

68. Stöckl, Q. S., Hsieh, Y.-C., Mairena, A., Wu, Y.-T. & Ernst, K.-H. Aggregation of C 70 -Fragment Buckybowls on Surfaces: π–H and π–π Bonding in Bowl Up-Side-Down Ensembles. *J. Am. Chem. Soc.* **138,** 6111–6114 (2016).

69. Zoppi, L. *et al.* Pauli Repulsion Versus van der Waals: Interaction of Indenocorannulene with a Cu(111) Surface. *J. Phys. Chem. B* **122,** 871–877 (2018).
70. Jensen, F. *Introduction to Computational Chemistry, 2nd Edition*. (Wiley, 2006).
71. Cornell, W. D. *et al.* A Second Generation Force Field for the Simulation of Proteins, Nucleic Acids, and Organic Molecules. *J. Am. Chem. Soc.* **117,** 5179–5197 (1995).
72. Allinger, N. L. Conformational analysis. 130. MM2. A hydrocarbon force field utilizing V1 and V2 torsional terms. *J. Am. Chem. Soc.* **99,** 8127–8134 (1977).
73. Weiner, S. J., Kollman, P. A., Nguyen, D. T. & Case, D. A. An All Atom Force Field for Simulations of Proteins and Nucleic Acids. *J. Comput. Chem.* **7,** 230–252 (1986).
74. Ernst, K.-H. Molecular chirality at surfaces. *Phys. status solidi* **249,** 2057–2088 (2012).
75. Moss, G. P. Basic terminology of stereochemistry (IUPAC Recommendations 1996). *Pure Appl. Chem.* **68,** 2193–2222 (1996).
76. Lord Kelvin. *Baltimor Lectures on Molecular Dynamics and the Wave Theory of Light*. *The MIT Press* (C.J. Clay and Sons, 1904).
77. Bentley, R. Chiral: A confusing etymology. *Chirality* **22,** 1–2 (2010).
78. George, J. C. *et al.* Age and growth estimates of bowhead whales (Balaena mysticetus) via aspartic acid racemization. *Can. J. Zool.* **77,** 571–580 (1999).
79. Pasteur, L. Recherches sur les relations qui peuvent exister entre la forme cristalline, la composition chimique et le sens de la polarisation rotatoire. *Ann. Chim. Phys.* **24,** 442–459 (1848).
80. Ernst, K. Molecular chirality in surface science. *Surf. Sci.* **613,** 1–5 (2013).
81. Gal, J. in *Differentiation of Enantiomers I* **340,** 1–20 (Springer International Publishing, 2013).
82. Yang, B. *et al.* Direct Observation of Enantiospecific Substitution in a Two-Dimensional Chiral Phase Transition. *J. Am. Chem. Soc.* **132,** 10440–10444 (2010).
83. Dunitz, J. D. Are crystal structures predictable? *Chem. Commun.* **5,** 545–548 (2003).
84. Ernst, K.-H. Expression and Amplification of Chirality in Two-Dimensional Molecular Crystals. *Chim. Int. J. Chem.* **62,** 471–475 (2008).
85. Blaser, H.-U., Jalett, H.-P., Müller, M. & Studer, M. Enantioselective hydrogenation of α-ketoesters using cinchona modified platinum catalysts and related systems: A review. *Catal. Today* **37,** 441–463 (1997).
86. Pérez-García, L. & Amabilino, D. B. Spontaneous resolution under supramolecular control. *Chem. Soc. Rev.* **31,** 342–356 (2002).
87. Dutta, S. & Gellman, A. J. Enantiomer surface chemistry: conglomerate *versus* racemate formation on surfaces. *Chem. Soc. Rev.* **46,** 7787–7839 (2017).
88. Ortega Lorenzo, M., Baddeley, C. J., Muryn, C. & Raval, R. Extended surface chirality from supramolecular assemblies of adsorbed chiral molecules. *Nature* **404,** 376–379 (2000).
89. Kühnle, A., Linderoth, T. R., Hammer, B. & Besenbacher, F. Chiral recognition in dimerization of adsorbed cysteine observed by scanning tunnelling microscopy. *Nature* **415,** 891–893 (2002).
90. Mark, A. G., Forster, M. & Raval, R. Recognition and Ordering at Surfaces: The Importance of Handedness and Footedness. *ChemPhysChem* **12,** 1474–1480 (2011).
91. Shen, Y. & Chen, C.-F. Helicenes: Synthesis and Applications. *Chem. Rev.* **112,** 1463–1535 (2012).
92. Cahn, R. S., Ingold, C. & Prelog, V. Specification of Molecular Chirality. *Angew. Chemie Int. Ed. English* **5,** 385–415 (1966).
93. Weitzenböck, R. & Klingler, A. Synthese der isomeren Kohlenwasserstoffe 1, 2-5, 6-Dibenzanthracen und 3, 4-5, 6-Dibenzphenanthren. *A. Monatshefte für Chemie* **39,** 315–323 (1918).
94. Takeda, Y., Okazaki, M., Maruoka, Y. & Minakata, S. A facile synthesis of functionalized 7,8-

diaza[5]helicenes through an oxidative ring-closure of 1,1′-binaphthalene-2,2′-diamines (BINAMs). *Beilstein J. Org. Chem.* **11,** 9–15 (2015).

95. Goedicke, C. & Stegemeyer, H. Resolution and racemization of pentahelicene. *Tetrahedron Lett.* **11,** 937–940 (1970).

96. Martin, R. H. & Marchant, M. J. Resolution and optical properties ([α]max, ord and cd) of hepta-, octa- and nonahelicene. *Tetrahedron* **30,** 343–345 (1974).

97. Grimme, S. & Peyerimhoff, S. D. Theoretical study of the structures and racemization barriers of [n]helicenes (n = 3–6, 8). *Chem. Phys.* **204,** 411–417 (1996).

98. Gingras, M. One hundred years of helicene chemistry. Part 3: applications and properties of carbohelicenes. *Chem. Soc. Rev.* **42,** 1051–1095 (2013).

99. Görner, H., Stammel, C. & Mattay, J. Excited state behaviour of pentahelicene dinitriles. *J. Photochem. Photobiol. A Chem.* **120,** 171–179 (1999).

100. Markey, M. D. & Kelly, T. R. Troubleshooting a molecular motor: a remarkably stable N-acyl pyridinium salt. *Tetrahedron* **64,** 8381–8388 (2008).

101. Kelly, T. R. *et al.* Progress toward a Rationally Designed, Chemically Powered Rotary Molecular Motor. *J. Am. Chem. Soc.* **129,** 376–386 (2007).

102. Dinescu, L. & Wang, Z. Y. Synthesis and photochromic properties of helically locked 1,2-dithienylethenes. *Chem. Commun.* **24,** 2497–2498 (1999).

103. Ben Hassine, B., Gorsane, M., Pecher, J. & Martin, R. H. Synthèses et Synthèses Enantiosélectives D'Epoxydes Derivant du (E)-Stilbène et de L'α-Méthylstyrène Par la Méthode de Payne. *Bull. des Sociétés Chim. Belges* **95,** 557–566 (1986).

104. Anger, E. *et al.* Synthesis and chiral recognition ability of helical polyacetylenes bearing helicene pendants. *Polym. Chem.* **5,** 4909 (2014).

105. Nuckolls, C. *et al.* Circular Dichroism and UV−Visible Absorption Spectra of the Langmuir−Blodgett Films of an Aggregating Helicene. *J. Am. Chem. Soc.* **120,** 8656–8660 (1998).

106. Reetz, M. T. & Sostmann, S. 2,15-Dihydroxy-hexahelicene (HELIXOL): synthesis and use as an enantioselective fluorescent sensor. *Tetrahedron* **57,** 2515–2520 (2001).

107. Fasel, R. *et al.* Orientation of chiral heptahelicene $C_{30}H_{18}$ on copper surfaces: An x-ray photoelectron diffraction study. *J. Chem. Phys.* **115,** 1020–1027 (2001).

108. Koschel, H., Birkenheuer, U., Held, G. & Steinrück, H.-P. Correlation between chemical properties and electronic structure of pseudomorphic Cu monolayers on Ni(1 1 1) and Ru(0 0 0 1). *Surf. Sci.* **477,** 113–125 (2001).

109. Ernst, K.-H. Stereochemical Recognition of Helicenes on Metal Surfaces. *Acc. Chem. Res.* **49,** 1182–1190 (2016).

110. Ernst, K.-H. *et al.* Pasteur's Experiment Performed at the Nanoscale: Manual Separation of Chiral Molecules, One by One. *Nano Lett.* **15,** 5388–5392 (2015).

111. Parschau, M., Fasel, R. & Ernst, K.-H. Coverage and Enantiomeric Excess Dependent Enantiomorphism in Two-Dimensional Molecular Crystals. *Cryst. Growth Des.* **8,** 1890–1896 (2008).

112. Seibel, J., Parschau, M. & Ernst, K.-H. Two-Dimensional Crystallization of Enantiopure and Racemic Heptahelicene on Ag(111) and Au(111). *J. Phys. Chem. C* **118,** 29135–29141 (2014).

113. Seibel, J., Zoppi, L. & Ernst, K.-H. 2D conglomerate crystallization of heptahelicene. *Chem. Commun.* **50,** 8751 (2014).

114. Seibel, J., Allemann, O., Siegel, J. S. & Ernst, K.-H. Chiral Conflict among Different Helicenes Suppresses Formation of One Enantiomorph in 2D Crystallization. *J. Am. Chem. Soc.* **135,** 7434–7437 (2013).

115. Parschau, M. & Ernst, K.-H. Disappearing Enantiomorphs: Single Handedness in Racemate

Crystals. *Angew. Chemie Int. Ed.* **54,** 14422–14426 (2015).

116. Stöhr, M. *et al.* Self-Assembly and Two-Dimensional Spontaneous Resolution of Cyano-Functionalized [7]Helicenes on Cu(111). *Angew. Chemie Int. Ed.* **50,** 9982–9986 (2011).
117. Shchyrba, A. *et al.* Chirality Transfer in 1D Self-Assemblies: Influence of H-Bonding vs Metal Coordination between Dicyano[7]helicene Enantiomers. *J. Am. Chem. Soc.* **135,** 15270–15273 (2013).
118. Ascolani, H. *et al.* Van der Waals interactions in the self-assembly of 5-amino[6]helicene on Cu(100) and Au(111). *Chem. Commun.* **50,** 13907–13909 (2014).
119. Fuhr, J. D. *et al.* Chiral expression of adsorbed (MP) 5-amino[6]helicenes: from random structures to dense racemic crystals by surface alloying. *Chem. Commun.* **53,** 130–133 (2017).
120. Balandina, T. *et al.* Self-assembly of an asymmetrically functionalized [6]helicene at liquid/solid interfaces. *Chem. Commun.* **49,** 2207 (2013).
121. Taniguchi, M., Nakagawa, H., Yamagishi, A. & Yamada, K. STM observation of thia[11]heterohelicene on gold(111) and gold(110) surface. *Surf. Sci.* **507–510,** 458–462 (2002).
122. Taniguchi, M., Nakagawa, H., Yamagishi, A. & Yamada, K. Molecular chirality on a solid surface: Thiaheterohelicene monolayer on gold imaged by STM. *Surf. Sci.* **454,** 1005–1009 (2000).
123. Taniguchi, M., Nakagawa, H., Yamagishi, A. & Yamada, K. STM observation of molecular chirality and alignment on solid surface. *J. Mol. Catal. A Chem.* **199,** 65–71 (2003).
124. Goretta, S. *et al.* Expeditive Syntheses of Functionalized Pentahelicenes and NC-AFM on Ag(001). *Org. Lett.* **11,** 3846–3849 (2009).
125. Amemiya, R. & Yamaguchi, M. Chiral recognition in noncovalent bonding interactions between helicenes: right-handed helix favors right-handed helix over left-handed helix. *Org. Biomol. Chem.* **6,** 26–35 (2008).
126. Mutasem Omar Sinnokrot, Edward F. Valeev & Sherrill, C. D. Estimates of the Ab Initio Limit for π−π Interactions: The Benzene Dimer. *J. Am. Chem. Soc.* **124,** 10887–10893 (2002).
127. Larsson, J. A. *et al.* Orientation of individual C_{60} molecules adsorbed on Cu(111): Low-temperature scanning tunneling microscopy and density functional calculations. *Phys. Rev. B* **77,** 115434 (2008).
128. Merz, L. *et al.* Reversible Phase Transitions in a Buckybowl Monolayer. *Angew. Chemie Int. Ed.* **48,** 1966–1969 (2009).
129. Smerdon, J. A., Bode, M., Guisinger, N. P. & Guest, J. R. Monolayer and bilayer pentacene on Cu(111). *Phys. Rev. B* **84,** 165436 (2011).
130. Toyoda, K. *et al.* First-principles study of the pentacene/Cu(111) interface: Adsorption states and vacuum level shifts. *J. Electron Spectros. Relat. Phenomena* **174,** 78–84 (2009).
131. Kuroda, R. Crystal and molecular structure of [5]helicene: crystal packing modes. *J. Chem. Soc. Perkin Trans. 2* 789–794 (1982).
132. Duschek, R. *et al.* The adsorption of aromatics on sp-metals: benzene on Al(111). *Chem. Phys. Lett.* **318,** 43–48 (2000).
133. Bagus, P. S., Hermann, K. & Wöll, C. The interaction of C_6H_6 and C_6H_{12} with noble metal surfaces: Electronic level alignment and the origin of the interface dipole. *J. Chem. Phys.* **123,** 184109 (2005).
134. Bagus, P. S., Staemmler, V. & Wöll, C. Exchangelike Effects for Closed-Shell Adsorbates: Interface Dipole and Work Function. *Phys. Rev. Lett.* **89,** 096104 (2002).
135. Caputo, R., Prascher, B. P., Staemmler, V., Bagus, P. S. & Wöll, C. Adsorption of Benzene on Coinage Metals: A Theoretical Analysis Using Wavefunction-Based Methods. *J. Phys. Chem. A* **111,** 12778–12784 (2007).
136. Bagus, P. S., Käfer, D., Witte, G. & Wöll, C. Work Function Changes Induced by Charged Adsorbates: Origin of the Polarity Asymmetry. *Phys. Rev. Lett.* **100,** 126101 (2008).

137. Witte, G., Lukas, S., Bagus, P. S. & Wöll, C. Vacuum level alignment at organic/metal junctions: "Cushion" effect and the interface dipole. *Appl. Phys. Lett.* **87,** 263502 (2005).

138. Campbell, C. T. Bimetallic Surface Chemistry. *Annu. Rev. Phys. Chem.* **41,** 775–837 (1990).

139. Gerlach, R. L. & Rhodin, T. N. Binding and charge transfer associated with alkali metal adsorption on single crystal nickel surfaces. *Surf. Sci.* **19,** 403–426 (1970).

140. Lee, S. B., Weiss, M. & Ertl, G. Adsorption of potassium on iron. *Surf. Sci.* **108,** 357–367 (1981).

141. Merz, L. & Ernst, K.-H. Unification of the matrix notation in molecular surface science. *Surf. Sci.* **604,** 1049–1054 (2010).

142. Ernst, K.-H. On the Validity of Calling Wallach's Rule Wallach's Rule. *Isr. J. Chem.* **57,** 24–30 (2017).

143. Brock, C. P., Schweizer, W. B. & Dunitz, J. D. On the validity of Wallach's rule: on the density and stability of racemic crystals compared with their chiral counterparts. *J. Am. Chem. Soc.* **113,** 9811–9820 (1991).

144. Böhringer, Schneider & Berndt. Real Space Observation of a Chiral Phase Transition in a Two-Dimensional Organic Layer. *Angew. Chem. Int. Ed. Engl.* **39,** 792–795 (2000).

145. Gopakumar, T. G. *et al.* Coverage Driven Formation of Homochiral Domains of an Achiral Molecule on Au(111). *J. Phys. Chem. C* **114,** 18247–18251 (2010).

146. Vidal, F. *et al.* Chiral Phase Transition in Two-Dimensional Supramolecular Assemblies of Prochiral Molecules. *J. Am. Chem. Soc.* **127,** 10101–10106 (2005).

147. Romer, S., Behzadi, B., Fasel, R. & Ernst, K.-H. Homochiral Conglomerates and Racemic Crystals in Two Dimensions: Tartaric Acid on Cu(110). *Chem. - A Eur. J.* **11,** 4149–4154 (2005).

148. Seibel, J., Parschau, M. & Ernst, K.-H. From Homochiral Clusters to Racemate Crystals: Viable Nuclei in 2D Chiral Crystallization. *J. Am. Chem. Soc.* **137,** 7970–7973 (2015).

149. Humblot, V., Ortega Lorenzo, M., Baddeley, C. J., Haq, S. & Raval, R. Local and Global Chirality at Surfaces: Succinic Acid versus Tartaric Acid on Cu(110). *J. Am. Chem. Soc.* **126,** 6460–6469 (2004).

150. Parschau, M., Romer, S. & Ernst, K.-H. Induction of Homochirality in Achiral Enantiomorphous Monolayers. *J. Am. Chem. Soc.* **126,** 15398–15399 (2004).

151. Nobelprize.org. Nobel Media AB 2014. Web. The Nobel Prize in Chemistry 2010. Available at: http://www.nobelprize.org/nobel_prizes/chemistry/laureates/2010/. (Accessed: 30th January 2017)

152. Bäckvall, J.-E. *Scientific Background on the Nobel Prize in Chemistry 2010: Palladium-Catalyzed Cross Couplings in Organic Synthesis*. (The Royal Swedish Academy of Sciences, 2010).

153. Negishi, E.-I. Palladium-or Nickel-Catalyzed Cross Coupling. A New Selective Method for Carbon-Carbon Bond Formation. *Acc. Chem. Res* **15,** 340–348 (1982).

154. Johansson Seechurn, C. C. C., Kitching, M. O., Colacot, T. J. & Snieckus, V. Palladium-Catalyzed Cross-Coupling: A Historical Contextual Perspective to the 2010 Nobel Prize. *Angew. Chemie Int. Ed.* **51,** 5062–5085 (2012).

155. Beletskaya, I. P. & Cheprakov, A. V. Copper in cross-coupling reactions: The post-Ullmann chemistry. *Coord. Chem. Rev.* **248,** 2337–2364 (2004).

156. Eichhorn, J. *et al.* On-surface Ullmann polymerization via intermediate organometallic networks on Ag(111). *Chem. Commun.* **50,** 7680–7682 (2014).

157. Zint, S. *et al.* Imaging Successive Intermediate States of the On-Surface Ullmann Reaction on Cu(111): Role of the Metal Coordination. *ACS Nano* **11,** 4183–4190 (2017).

158. Ruffieux, P. *et al.* On-surface synthesis of graphene nanoribbons with zigzag edge topology. *Nature* **531,** 489–492 (2016).

159. Fan, Q. *et al.* Confined Synthesis of Organometallic Chains and Macrocycles by Cu–O Surface Templating. *ACS Nano* **10,** 3747–3754 (2016).

160. Grill, L. *et al.* Nano-architectures by covalent assembly of molecular building blocks. *Nat. Nanotechnol.* **2,** 687–691 (2007).

161. Lackinger, M. Surface-assisted Ullmann coupling. *Chem. Commun.* **53,** 7872–7885 (2017).

162. Björk, J., Hanke, F. & Stafström, S. Mechanisms of Halogen-Based Covalent Self-Assembly on Metal Surfaces. *J. Am. Chem. Soc.* **135,** 5768–5775 (2013).

163. Gutzler, R. *et al.* Ullmann-type coupling of brominated tetrathienoanthracene on copper and silver. *Nanoscale* **6,** 2660–2668 (2014).

164. Basagni, A. *et al.* On-surface photo-dissociation of C–Br bonds: towards room temperature Ullmann coupling. *Chem. Commun.* **51,** 12593–12596 (2015).

165. Wang, W., Shi, X., Wang, S., Van Hove, M. A. & Lin, N. Single-Molecule Resolution of an Organometallic Intermediate in a Surface-Supported Ullmann Coupling Reaction. *J. Am. Chem. Soc.* **133,** 13264–13267 (2011).

166. Dong, L., Liu, P. N. & Lin, N. Surface-Activated Coupling Reactions Confined on a Surface. *Acc. Chem. Res.* **48,** 2765–2774 (2015).

167. Basagni, A. *et al.* Molecules–Oligomers–Nanowires–Graphene Nanoribbons: A Bottom-Up Stepwise On-Surface Covalent Synthesis Preserving Long-Range Order. *J. Am. Chem. Soc.* **137,** 1802–1808 (2015).

168. Saywell, A. *et al.* Manipulating the Conformation of Single Organometallic Chains on Au(111). *J. Phys. Chem. C* **118,** 1719–1728 (2014).

169. Eichhorn, J. *et al.* On-surface Ullmann polymerization *via* intermediate organometallic networks on Ag(111). *Chem. Commun.* **50,** 7680–7682 (2014).

170. Pham, T. A. *et al.* Comparing Ullmann Coupling on Noble Metal Surfaces: On-Surface Polymerization of 1,3,6,8-Tetrabromopyrene on Cu(111) and Au(111). *Chem. Eur. J.* **22,** 5937–5944 (2016).

171. Schulze Icking-Konert, G., Giesen, M. & Ibach, H. Decay of Cu adatom islands on Cu(111). *Surf. Sci.* **398,** 37–48 (1998).

172. Li, J. *et al.* On-Surface Metalation and 2D Self-Assembly of Pyrphyrin Molecules Into Metal-Coordinated Networks on Cu(111). *Helv. Chim. Acta* **100,** e1600278 (2017).

173. Röckert, M. *et al.* Insights in Reaction Mechanistics: Isotopic Exchange during the Metalation of Deuterated Tetraphenyl-21,23D -porphyrin on Cu(111). *J. Phys. Chem. C* **118,** 26729–26736 (2014).

174. Röckert, M. *et al.* Coverage- and Temperature-Dependent Metalation and Dehydrogenation of Tetraphenylporphyrin on Cu(111). *Chem. - A Eur. J.* **20,** 8948–8953 (2014).

175. Treier, M. *et al.* Surface-assisted cyclodehydrogenation provides a synthetic route towards easily processable and chemically tailored nanographenes. *Nat. Chem.* **3,** pages 61–67 (2011).

176. Ikeda, T., Iijima, T., Sekiya, R., Takahashi, O. & Haino, T. Cooperative Self-Assembly of Carbazole Derivatives Driven by Multiple Dipole–Dipole Interactions. *J. Org. Chem.* **81,** 6832–6837 (2016).

177. Kunkel, D. A. *et al.* Self-assembly of strongly dipolar molecules on metal surfaces. *J. Phys. Chem.* **142,** 101921 (2015).

178. Tran, B. V., Pham, T. A., Grunst, M., Kivala, M. & Stöhr, M. Surface-confined [2 + 2] cycloaddition towards one-dimensional polymers featuring cyclobutadiene units. *Nanoscale* **9,** 18305–18310 (2017).

179. Hammer, B. & Norskov, J. K. Why gold is the noblest of all the metals. *Nature* **376,** 238–240 (1995).

180. Fan, Q. *et al.* Covalent, Organometallic, and Halogen-Bonded Nanomeshes from Tetrabromo-Terphenyl by Surface-Assisted Synthesis on Cu(111). *J. Phys. Chem. C* **118,** 13018–13025 (2014).

181. Chen, M. *et al.* Combined Photoemission and Scanning Tunneling Microscopy Study of the Surface-Assisted Ullmann Coupling Reaction. *J. Phys. Chem. C* **118,** 6820–6830 (2014).

182. Batra, A. *et al.* Quantifying through-space charge transfer dynamics in π-coupled molecular systems. *Nat. Commun.* **3,** 1086 (2012).

183. Fan, Q., Gottfried, J. M. & Zhu, J. Surface-Catalyzed C-C Covalent Coupling Strategies toward the Synthesis of Low-Dimensional Carbon-Based Nanostructures. *Acc. Chem. Res.* **48,** 2484–2494 (2015).

184. Cai, J. *et al.* Atomically precise bottom-up fabrication of graphene nanoribbons. *Nature* **466,** 470–473 (2010).

185. Buchner, F. *et al.* Diffusion, Rotation, and Surface Chemical Bond of Individual 2H - Tetraphenylporphyrin Molecules on Cu(111). *J. Phys. Chem. C* **115,** 24172–24177 (2011).

186. Björk, J. *et al.* STM fingerprint of molecule–adatom interactions in a self-assembled metal–organic surface coordination network on Cu(111). *Phys. Chem. Chem. Phys.* **12,** 8815 (2010).

187. Seibel, J. Two-Dimensional Crystallization of Helical Aromatic Hydrocarbons on Metal Surfaces. (University of Zurich, 2014).

188. Suarez, S. A. *et al.* Br...Br and van der Waals interactions along a homologous series: crystal packing of 1,2-dibromo-4,5-dialkoxybenzenes. *Acta Crystallogr. Sect. B Struct. Sci. Cryst. Eng. Mater.* **72,** 693–701 (2016).

189. Lieberman, H. F., Davey, R. J. & Newsham, D. M. T. Br···Br and Br···H Interactions in Action: Polymorphism, Hopping, and Twinning in 1,2,4,5-Tetrabromobenzene. *Chem. Mater.* **12,** 490–494 (2000).

190. Eichhorn, J. *et al.* On-Surface Ullmann Coupling: The Influence of Kinetic Reaction Parameters on the Morphology and Quality of Covalent Networks. *ACS Nano* **8,** 7880–7889 (2014).

191. Bronner, C., Björk, J., Tegeder, P., Bjö Rk, J. & Tegeder, P. Tracking and Removing Br during the On-Surface Synthesis of a Graphene Nanoribbon. *J. Phys. Chem. C* **119,** 486–493 (2015).

192. Simonov, K. A. *et al.* Effect of Substrate Chemistry on the Bottom-Up Fabrication of Graphene Nanoribbons: Combined Core-Level Spectroscopy and STM Study. *J. Phys. Chem. C* **118,** 12532–12540 (2014).

193. Batra, A. *et al.* Probing the mechanism for graphene nanoribbon formation on gold surfaces through X-ray spectroscopy. *Chem. Sci.* **5,** 4419–4423 (2014).

194. Giovannantonio, M. Di *et al.* Insight into Organometallic Intermediate and Its Evolution to Covalent Bonding in Surface-Confined Ullmann Polymerization. **7,** 8190–8198 (2013).

195. Sun, J. T. *et al.* Surface reconstruction transition of metals induced by molecular adsorption. *Phys. Rev. B* **83,** 115419 (2011).

196. Corso, M., Fernández, L., Schiller, F. & Ortega, J. E. Au(111)-Based Nanotemplates by Gd Alloying. *ACS Nano* **4,** 1603–1611 (2010).

197. Zhang, H. *et al.* Surface Supported Gold-Organic Hybrids: On-Surface Synthesis and Surface Directed Orientation. *Small* **10,** 1361–1368 (2014).

198. Stetsovych, O. *et al.* From helical to planar chirality by on-surface chemistry. *Nat. Chem.* **9,** 213–218 (2017).

199. Xue, X. & Scott, L. T. Thermal Cyclodehydrogenations To Form 6-Membered Rings: Cyclizations of [5]Helicenes. *Org. Lett.* **9,** 3937–3940 (2007).

200. De Oteyza, D. G. *et al.* Substrate-Independent Growth of Atomically Precise Chiral Graphene Nanoribbons. *ACS Nano* **10,** 9000–9008 (2016).

201. Smykalla, L., Shukrynau, P., Korb, M., Lang, H. & Hietschold, M. Surface-confined 2D polymerization of a brominated copper-tetraphenylporphyrin on Au(111). *Nanoscale* **7,** 4234–4241 (2015).

202. Gadgil, C. J. & Kulkarni, B. D. Autocatalysis in biological systems. *AIChE J.* **55,** 556–562 (2009).

203. McCarty, J., Falconer, J. & Madix, R. J. Decomposition of formic acid on Ni(110): I. Flash decomposition from the clean surface and flash desorption of reaction products. *J. Catal.* **30,**

235–249 (1973).

204. Falconer, J. L., McCarty, J. & Madix, R. J. The Explosive Decomposition of Formic Acid on Ni(110).pdf. *J. Appl. Phys. Suppl.* **2,** 525–528 (1974).

205. Falconer, J. L., McCarty, J. G. & Madix, R. J. Surface explosion: HCOOH on Ni <110>. *Surf. Sci.* **42,** 329–330 (1974).

206. Behzadi, B., Romer, S., Fasel, R. & Ernst, K. H. Chiral recognition in surface explosion. *J. Am. Chem. Soc.* **126,** 9176–9177 (2004).

207. Gellman, A. J. *et al.* Superenantioselective chiral surface explosions. *J. Am. Chem. Soc.* **135,** 19208–19214 (2013).

208. Lorenzo, M. O. *et al.* Chemical Transformations, Molecular Transport, and Kinetic Barriers in Creating the Chiral Phase of (R, R)-Tartaric Acid on Cu(110). *J. Catal.* **205,** 123–134 (2002).

209. Callen, B. W., Griffiths, K., Norton, P. R. & Harrington, D. A. Autocatalytic decomposition of water on nickel (110). *J. Phys. Chem.* **96,** 10905–10913 (1992).

210. Schmidt, M. W. L. and L. D. The NO + CO reaction on Pt(100). *Surf. Sci.* **155,** 215–240 (1985).

211. Alas, S. J. & Vicente, L. Kinetic study of the "surface explosion" phenomenon in the NO+CO reaction on Pt(100) through dynamic Monte Carlo simulation. *J. Chem. Phys.* **128,** 134705 (2008).

212. Christmann, K., Chehab, F., Penka, V. & Ertl, G. Surface reconstruction and surface explosion phenomena in the nickel (110)/hydrogen system. *Surf. Sci.* **152–153,** 356–366 (1985).

213. Makeev, A. G. & Nieuwenhuys, B. E. Mathematical modeling of the NO+H_2/Pt(100) reaction: "Surface explosion," kinetic oscillations, and chaos. *J. Chem. Phys.* **108,** 3740 (1998).

214. Vicente, L. & Caballero, F. V. Modeling of surface explosion of NO+H_2 reaction on Pt(1 0 0): Mean-field analysis and dynamic Monte Carlo simulations. *J. Mol. Catal. A Chem.* **272,** 118–127 (2007).

215. Li, Z., Gao, F. & Tysoe, W. T. Surface chemistry of acetic acid on clean and oxygen-covered Pd(100). *Surf. Sci.* **602,** 416–423 (2008).

216. Falconer, J. L., Craigburger, L., Corfa, I. P. & Wilson, K. G. Temperature-Programmed Decomposition of Deuterated Formic Acid on Ni/Si02. *J. Catal.* **104,** 424–433 (1987).

217. Bowker, M. & Cassidy, T. J. Decomposition of Acetate Groups on an Alumina-Supported Rhodium Catalyst. *J. Catal.* **174,** 65–71 (1998).

218. Cassidy, T. J., Allen, M. D., Li, Y. & Bowker, M. From surface science to catalysis: Surface explosions observed on Rh crystals and supported catalysts. *Catal. Letters* **21,** 321–331 (1993).

219. Kangas, T., Laasonen, K., Puisto, A., Pitkänen, H. & Alatalo, M. On-surface and sub-surface oxygen on ideal and reconstructed Cu(1 0 0). *Surf. Sci.* **584,** 62–69 (2005).

220. Jensen, F., Besenbacher, F., Laegsgaard, E. & Stensgaard, I. Dynamics of oxygen-induced reconstruction of Cu(100) studied by scanning tunneling microscopy. *Phys. Rev. B* **42,** 9206–9209 (1990).

221. Nowakowski, J. *et al.* Porphyrin metalation providing an example of a redox reaction facilitated by a surface reconstruction. *Chem. Commun.* **49,** 2347–2349 (2013).

222. Rieger, A., Schnidrig, S., Probst, B., Ernst, K.-H. & Wäckerlin, C. Identification of On-Surface Reaction Mechanism by Targeted Metalation. *J. Phys. Chem. C* **121,** 27521–27527 (2017).

223. Kovács, I. Thermal and photo-induced oxidation of CH2 on Cu(100). *J. Mol. Catal. A Chem.* **141,** 31–38 (1999).

224. Simonov, K. A. *et al.* From Graphene Nanoribbons on Cu(111) to Nanographene on Cu(110): Critical Role of Substrate Structure in the Bottom-Up Fabrication Strategy. *ACS Nano* **9,** 8997–9011 (2015).

225. Zhang, Y.-Q. *et al.* Homo-coupling of terminal alkynes on a noble metal surface. *Nat. Commun.* **3,** 1286 (2012).

226. Schulman, J. M. & Disch, R. L. Aromatic Character of [n]Helicenes and [n]Phenacenes. *J. Phys. Chem. A* **103,** 6669–6672 (1999).

227. Shen, Y. *et al.* Chiral Self-Assembly of Nonplanar 10,10′-Dibromo-9,9′-bianthryl Molecules on Ag(111). *Langmuir* **33,** 2993–2999 (2017).

228. Sánchez-Sánchez, C. *et al.* Purely Armchair or Partially Chiral: Noncontact Atomic Force Microscopy Characterization of Dibromo-Bianthryl-Based Graphene Nanoribbons Grown on Cu(111). *ACS Nano* **10,** 8006–8011 (2016).

229. Gottardi, S. *et al.* Comparing Graphene Growth on Cu(111) versus Oxidized Cu(111). *Nano Lett.* **15,** 917–922 (2015).

230. Wong, Y.-T. & Hoffmann, R. Theoretical Study of Chemisorption of Acetylene on the Cu(l00) Surface. *J. Chem. Soc. Faraday Trans.* **86,** 553–559 (1990).

231. Overend, J. The equilibrium bond lengths in acetylene and HCN. *Trans. Faraday Soc.* **56,** 310 (1960).

232. Jensen, F., Besenbacher, F., Laesgaard, E. & Stensgaard, I. Surface reconstruction of Cu(110) induced by oxygen chemisorption. *Phys. Rev. B* **44,** 10233 (1990).

233. Ma, L., Zhang, J. & Xu, K. Structural and electronic properties of atomic oxygen adsorption on Cu(111) surface: A first-principles investigation. *Sci. China Physics, Mech. Astron.* **56,** 573–580 (2013).

234. Spitzer, A. & Lüth, H. The adsorption of oxygen on copper surfaces: II. Cu(111). *Surf. Sci.* **118,** 136–144 (1982).

235. Josa, D., Rodríguez-Otero, J. & Cabaleiro-Lago, E. M. Fullerene recognition with molecular tweezers made up of efficient buckybowls: a dispersion-corrected DFT study. *Phys. Chem. Chem. Phys.* **17,** 13206–13214 (2015).

236. Barth, W. E. & Lawton, R. G. Dibenzo[ghi,mno]fluoranthene. *J. Am. Chem. Soc.* **88,** 380–381 (1966).

237. Kroto, H. W., Heath, J. R., O'Brien, S. C., Curl, R. F. & Smalley, R. E. C_{60}: Buckminsterfullerene. *Nature* **318,** 162–163 (1985).

238. Bauert, T. *et al.* Quadruple Anionic Buckybowls by Solid-State Chemistry of Corannulene and Cesium. *J. Am. Chem. Soc.* **135,** 12857–12860 (2013).

239. Zoppi, L., Bauert, T., Siegel, J. S., Baldridge, K. K. & Ernst, K.-H. Pentagonal tiling with buckybowls: pentamethylcorannulene on Cu(111). *Phys. Chem. Chem. Phys.* **14,** 13365 (2012).

240. Stöckl, Q., Bandera, D., Kaplan, C. S., Ernst, K.-H. & Siegel, J. S. Gear-Meshed Tiling of Surfaces with Molecular Pentagonal Stars. *J. Am. Chem. Soc.* **136,** 606–609 (2014).

241. Stöckl, Q. S. Modification of surfaces with buckybowls : Fivefold symmetry and two-dimensional self-assembly. (University of Zürich, 2014).

242. Bauert, T. *et al.* Building 2D Crystals from 5-Fold-Symmetric Molecules. *J. Am. Chem. Soc.* **131,** 3460–3461 (2009).

243. Saunders, M. *et al.* Incorporation of helium, neon, argon, krypton, and xenon into fullerenes using high pressure. *J. Am. Chem. Soc.* **116,** 2193–2194 (1994).

244. Eliseeva, M. N. & Scott, L. T. Pushing the Ir-Catalyzed C–H Polyborylation of Aromatic Compounds to Maximum Capacity by Exploiting Reversibility. *J. Am. Chem. Soc.* **134,** 15169–15172 (2012).

245. Bauert, T. *et al.* Large Induced Interface Dipole Moments without Charge Transfer: Buckybowls on Metal Surfaces. *J. Phys. Chem. Lett.* **2,** 2805–2809 (2011).

246. Zhang, R., Duan, T., Ling, L. & Wang, B. CH4 dehydrogenation on Cu(111), Cu@Cu(111), Rh@Cu(111) and RhCu(111) surfaces: A comparison studies of catalytic activity. *Appl. Surf. Sci.* **341,** 100–108 (2015).

247. Bebensee, F. *et al.* Adsorption and dehydrogenation of tetrahydroxybenzene on Cu(111). *Chem.*

Commun. **49,** 9308 (2013).

248. Hou, J. G. *et al.* Surface science: Topology of two-dimensional C_{60} domains. *Nature* **409,** 304–305 (2001).

249. Lewis, E. A. *et al.* Controlling selectivity in the Ullmann reaction on Cu(111). *Chem. Commun.* **53,** 7816–7819 (2017).

250. Li, H., Li, Y., Koper, M. T. M. & Calle-Vallejo, F. Bond-Making and Breaking between Carbon, Nitrogen, and Oxygen in Electrocatalysis. *J. Am. Chem. Soc.* **136,** 15694–15701 (2014).

251. Matei, D. G. *et al.* Functional Single-Layer Graphene Sheets from Aromatic Monolayers. *Adv. Mater.* **25,** 4146–4151 (2013).

252. Meyer, E. A., Castellano, R. K. & Diederich, F. Interactions with Aromatic Rings in Chemical and Biological Recognition. *Angew. Chemie Int. Ed.* **42,** 1210–1250 (2003).

253. Umadevi, D. & Sastry, G. N. Impact of the Chirality and Curvature of Carbon Nanostructures on Their Interaction with Aromatics and Amino Acids. *ChemPhysChem* **14,** 2570–2578 (2013).

254. Bauert, T., Baldridge, K. K., Siegel, J. S. & Ernst, K.-H. Surface-assisted bowl-in-bowl stacking of nonplanar aromatic hydrocarbons. *Chem. Commun.* **47,** 7995 (2011).

255. Jaafar, R. *et al.* Bowl Inversion of Surface-Adsorbed Sumanene. *J. Am. Chem. Soc.* **136,** 13666–13671 (2014).

256. Sakurai, H., Daiko, T. & Hirao, T. A synthesis of sumanene, a fullerene fragment. *Science* **301,** 1878 (2003).

257. Dunitz, J. D. Intermolecular atom-atom bonds in crystals? *IUCrJ* **2,** 157–158 (2015).

258. Dunitz, J. D., Gavezzotti, A. & Rizzato, S. "Coulombic Compression", a Pervasive Force in Ionic Solids. A Study of Anion Stacking in Croconate Salts. *Cryst. Growth Des.* **14,** 357–366 (2014).

259. Wsol, V., Skalova, L. & Szotakova, B. Chiral Inversion of Drugs: Coincidence or Principle? *Curr. Drug Metab.* **5,** 517–533 (2004).

260. Meldrum, F. C. & Cölfen, H. Controlling Mineral Morphologies and Structures in Biological and Synthetic Systems. *Chem. Rev.* **108,** 4332–4432 (2008).

261. Gingras, M. One hundred years of helicene chemistry. Part 1: non-stereoselective syntheses of carbohelicenes. *Chem. Soc. Rev.* **42,** 968–1006 (2013).

262. Gingras, M., Félix, G. & Peresutti, R. One hundred years of helicene chemistry. Part 2: stereoselective syntheses and chiral separations of carbohelicenes. *Chem. Soc. Rev.* **42,** 1007–1050 (2013).

263. Hermann, K. *Crystallography and Surface Structure*. (Wiley-VCH Verlag GmbH & Co. KGaA, 2011). doi:10.1002/9783527633296

264. Wood, E. A. Vocabulary of Surface Crystallography. *J. Appl. Phys.* **35,** 1306–1312 (1964).

265. Bieri, M. *et al.* Two-Dimensional Polymer Formation on Surfaces: Insight into the Roles of Precursor Mobility and Reactivity. *J. Am. Chem. Soc.* **132,** 16669–16676 (2010).

266. Lin, J.-L. *et al.* Reactions of CH2═CHBr and CH3 CHBr2 on Cu(100) and O/Cu(100). *J. Phys. Chem. C* **121,** 17990–17998 (2017).

267. Priyakumar, U. D. & Sastry, G. N. Heterobuckybowls: A Theoretical Study on the Structure, Bowl-to-Bowl Inversion Barrier, Bond Length Alternation, Structure-Inversion Barrier Relationship, Stability, and Synthetic Feasibility †. *J. Org. Chem.* **66,** 6523–6530 (2001).

268. Wu, Y.-T. & Siegel, J. S. Aromatic Molecular-Bowl Hydrocarbons: Synthetic Derivatives, Their Structures, and Physical Properties. *Chem. Rev.* **106,** 4843–4867 (2006).

269. Lipkowitz, K. Abuses of Molecular Mechanics: Pitfalls to Avoid. *J. Chem. Educ.* **72,** 1070 (1995).

270. Boyd, D. B. & Lipkowitz, K. B. Molecular mechanics: The method and its underlying philosophy. *J. Chem. Educ.* **59,** 269 (1982).

271. Zoppi, L. *et al.* Pauli Repulsion Versus van der Waals: Interaction of Indenocorannulene with a

Cu(111) Surface. *J. Phys. Chem. B* **122,** (2018).

272. Stöckl, Q. S., Wu, T.-C., Mairena, A., Wu, Y.-T. & Ernst, K.-H. Erecting buckybowls onto their edge: 2D self-assembly of terphenylcorannulene on the Cu(111) surface. *Faraday Discuss.* **204,** 429–437 (2017).

Acknowledgements

I keep very good memories of this PhD at Empa in the challenging field of surface science. I encountered difficulties during the course of my doctoral studies but thanks to the encouragements and help of coworkers, friends and family, I could overcome them.

First and foremost, I would like to thank my PhD advisor, Prof. Karl-Heinz Ernst, for giving me a lot of freedom in my research project but also for being always available when I needed to discuss the results. He was always pushing me to grow scientifically in our exciting field, for example through the attendance of international conferences, where he presented me to many experts from the field. He also encouraged me to take part in many projects beyond the scope of this PhD (measurements at the SLS synchrotron, molecular modelling, experiments with spin polarized electrons at LBNL Berkeley). His constant support was very much appreciated.

I would like to thank Prof. Karl Gademann, Prof. Anthony Linden who were part of my promotion committee and followed my work and Prof. Andrew Gellman who accepted to be an external examiner of my thesis. I am also grateful for the help of Oliver Gröning who volunteered to teach me Extended Hückel Theory simulations with the computational package 'Igor' and was always available to answer my questions. The support from the Graduate School of Chemical and Molecular Sciences Zurich (CMSZH) was also really appreciated.

I would also like to express my gratitude to Manfred Parschau and Christian Wäckerlin for the technical help they provided, for teaching me so much about the experiments and helping me understand my results. Manfred taught me everything about the VT-STM and vacuum systems in general and was always there to help (always with a smile!) when I needed it. Christian always took time to answer the many, many questions I had, to discuss the results and to teach me how to write papers, to read my thesis and to advise me. Both of you with your humor and your endless problem-solving skills contributed a lot to the success of my PhD.

Thousand thanks to Gitgit who was there from the first day on to embark with me on our PhD rollercoaster. She always supported me, both at work and in my personal life, and I keep countless happy memories from our trips, ski retreats etc. during those three and a half years together. I also would like to thank the other members of the Nanoscale Materials Laboratory at Empa and especially my fellow PhD students and postdocs for providing such a nice and fun working environment and for the nice moments shared together outside from work. Many thanks the rest of the girls' gang, Alex, Chrysa and Jingyi for the fun we had together in the office, for our dinners and all the nice memories we created together. Big thank you also to Mirko for being such a priceless friend in and outside Empa and to Aarati for her advices, friendship and constant happy mood. Thanks also to Boran for the nice time spent together at Empa and at Minimum. You all made Zürich feel like home.

I cannot thank all my friends and family members individually, but I could not have done it without them. Thank you to Benoit, Jé, and Mauro who in addition to be my closest friends, read my posters and some parts of my thesis, gave their opinions on my talks and lived with me the ups and downs of the PhD journey. Thanks to Thibaut, my former assistant, for advising me in my scientific career, always believing in me and being my favorite Apero partner in Zürich when things went wrong with the experiment. Many thanks to Cristina, my favorite synthetic chemist, for reading the entire thesis, giving me such good feedbacks and also for being such a valuable friend. Thanks to Steffi, my incredible tandem partner, for the help with all German related matters including the Zusammenfassung and for being always so interested about my work. Thanks also to the Germines, for being an inspiration and for believing in me so much during all these years studying physics.

Last but not least, thanks to Guillaume, Alexis and my parents for their constant encouragements. Big thank you to Guigui who was here for me all along, for his invaluable support, for reading the entire thesis and listening so much to my talks that he could almost give them himself. My parents provided everything I needed to be able to study at EPFL and have the chance to undertake a PhD. A special thank you to my mum, who never studied sciences but was always interested and curious about my PhD. She lived with me the difficult times (e.g. when the machine was broken) and the happy moments (e.g. when I published my papers). I could not hope for a better support.

Thank you all!

Appendix

A.Additional results

A.1. Pentahelicene

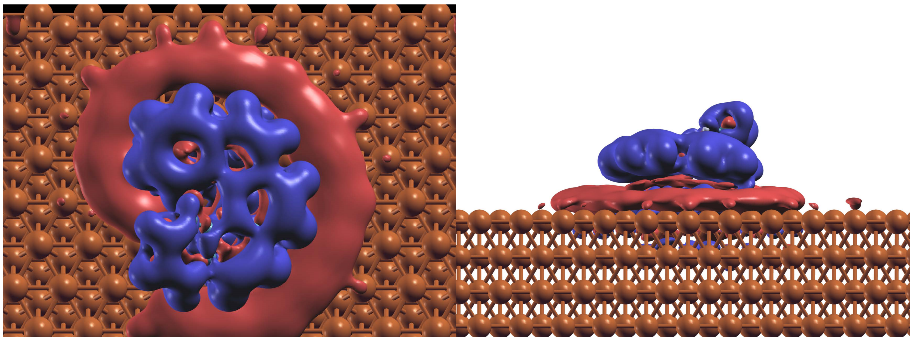

Figure A. 1: Top and side views of the charge redistribution induced by the adsorption of [5]H on Cu(111) as calculated with DFT by Dr. Laura Zoppi. Red shows the accumulation of charge and blue the depletion.

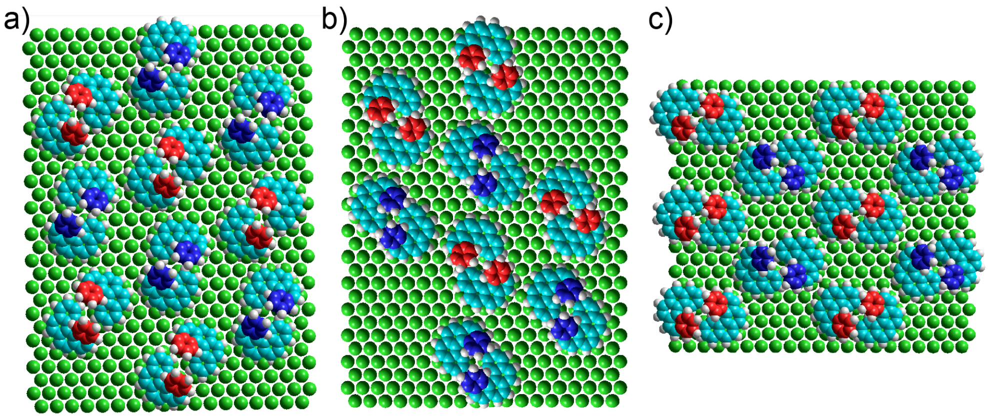

Figure A. 2: Ball models of the three checkerboard rotational domains formed by *rac*-[5]H on Cu(111). The red and dark blue rings highlight the uppermost ring of a *(P)*-[5]H and a *(M)*-[5]H respectively. a, b and c correspond respectively to ε, β, and δ of the Figure 16.

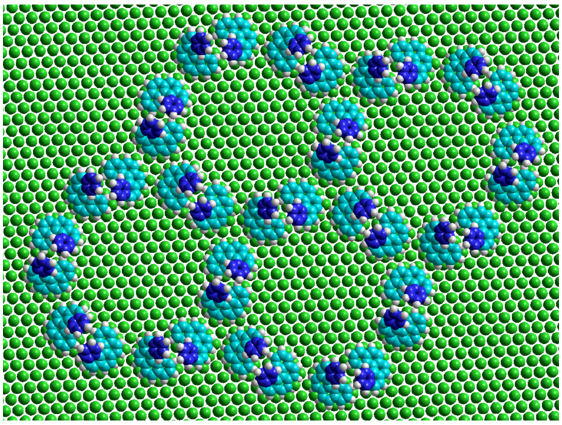

Figure A. 3: Ball models of a domain of the honeycomb structure formed by *rac*-[5]H on Cu(111). A dark blue ring highlights the uppermost ring of a *(M)*-[5]H.

A.2. Bisheptahelicene

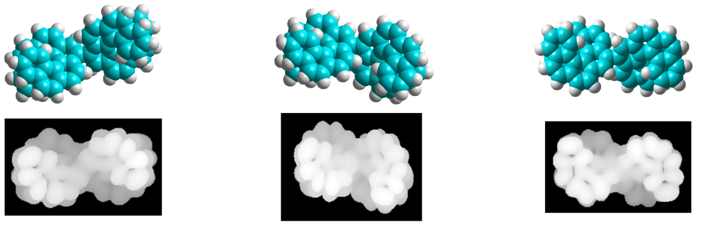

MM-9,9-bis[7]H MM-9,10-bis[7]H MM-10,10-bis[7]H

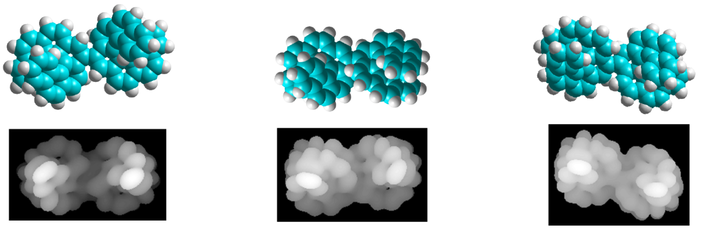

MM-9,9-bis[7]H-B MM-9,10-bis[7]H-B MM-10,10-bis[7]H-B

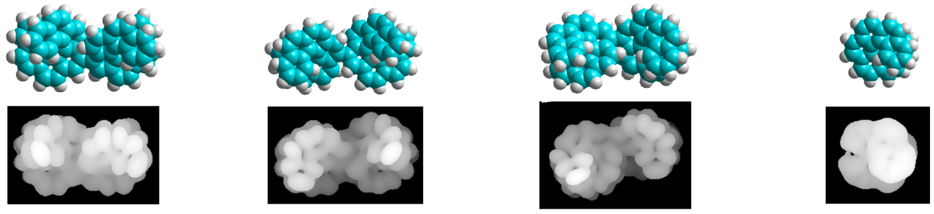

PM-9,9-bis[7]H PM-9,10-bis[7]H PM-10,10-bis[7]H M-[7]H

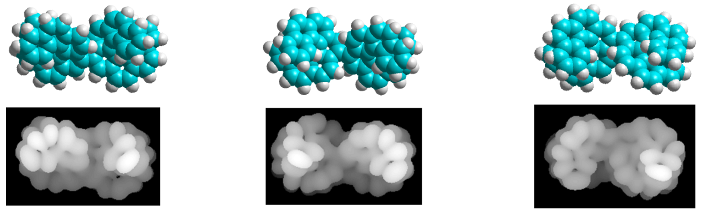

PM-9,9-bis[7]H-B PM-9,10-bis[7]H-B PM-10,10-bis[7]H-B

Figure A. 4: Electron density maps of the frontier orbitals close to the LUMO (LUMO to LUMO+4, states 138 to 142 Extended Hückel) for all possible configurations of the bis[7]H, after geometric optimization on a Cu(111) slab with AMBER force field. In the case of homochiral configurations, only the M case is presented, the P configuration can be obtained by reflection. For each configuration, there are two possible cases: one where the left part of the molecule is on top of the other one and one where the left part is below. They share the same name but a "B" is added to the name in the second case.

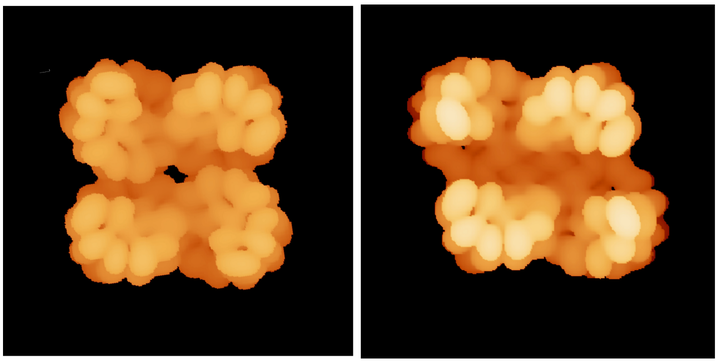

MM-9,10-bis[7]H PM-9,9-bis[7]H-B

Figure A. 5: Models of the parallelogram structure based on the EHT STM simulations (states 138-142 Ext. Hückel, LUMO to LUMO+4) of two *(M,M)*-9,10′-bis[7]H (left) and two *(P,M)*-9,9′-bis[7]H-B (right) respectively.

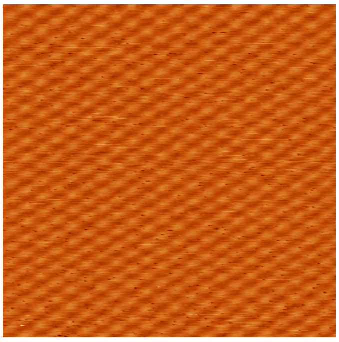

Figure A. 6: STM image of the clean Cu(111) template (5 nm×5 nm, 280 mV, 1.6 nA). The $[1\bar{1}0]$ direction of the Cu(111) is rotated by 9 ± 3° (counter-clockwise) with respect to the vertical direction.

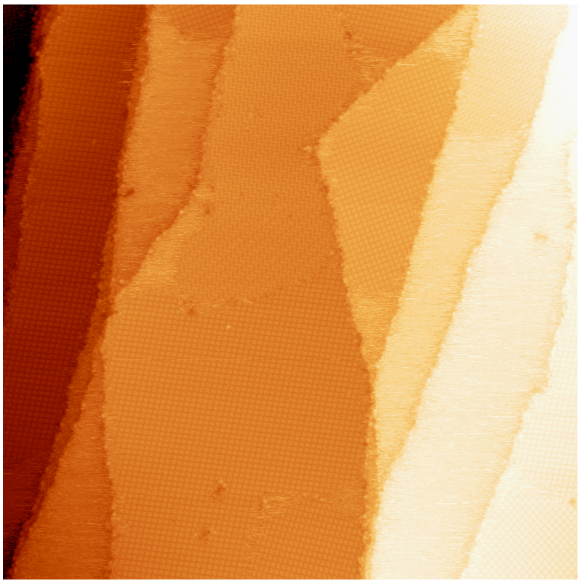

Figure A. 7: Same large scale STM image (200 nm × 200 nm, 29 pA, 1.575 V) of bis7[h]on Cu(111) as in the Figure 1. There is no parabolic filtering in this case. The real height difference between the steps is observed.

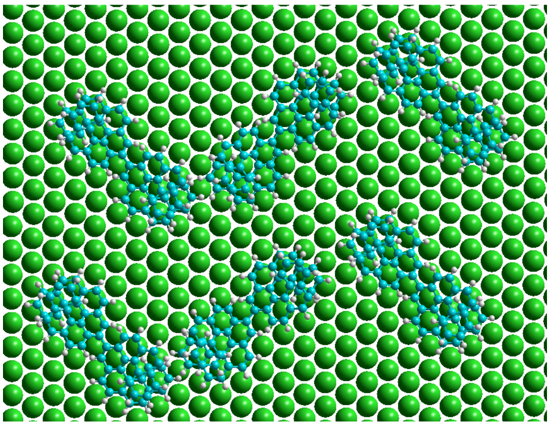

Figure A. 8: Ball & stick representation of the molecular model on Cu(111) (matrix notation: (7, −1; 5, 15)) of the Figure 31.

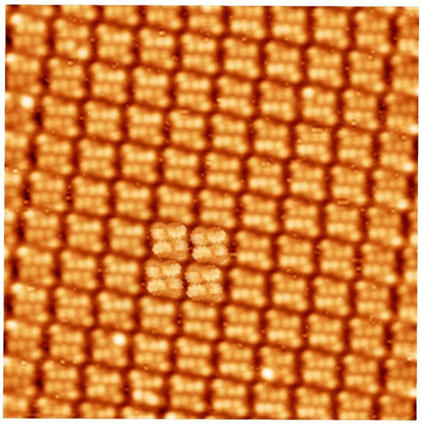

Figure A. 9: STM image of the parallelogram structure on Cu(111) (20 nm × 20 nm, 1.85 V, 25 pA). ETH electron density maps (states 138-142 Ext. Hückel, LUMO to LUMO+4) of *(P,M)*-9,9'-bis[7]H are superimposed on the STM image. Both contrasts of the model and measured STM data correspond.

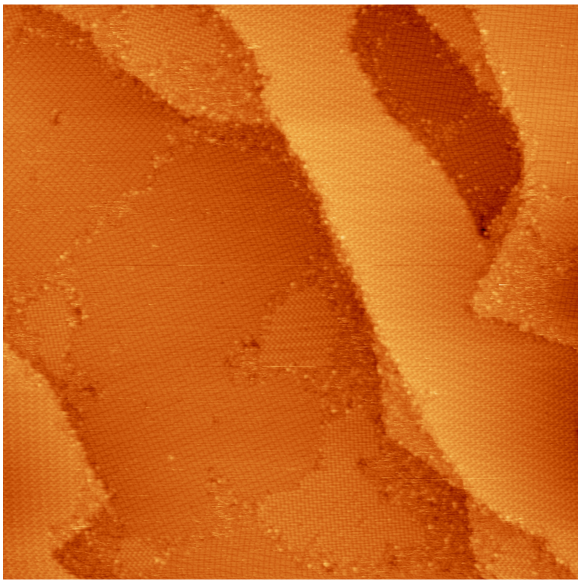

Figure A. 10: Large scale STM image (200 nm × 200 nm, 25 pA, 2.05 V) of bis7[H] on Cu(111) showing the coexistence of the zigzag and parallelogram structure around monolayer (ML) coverage.

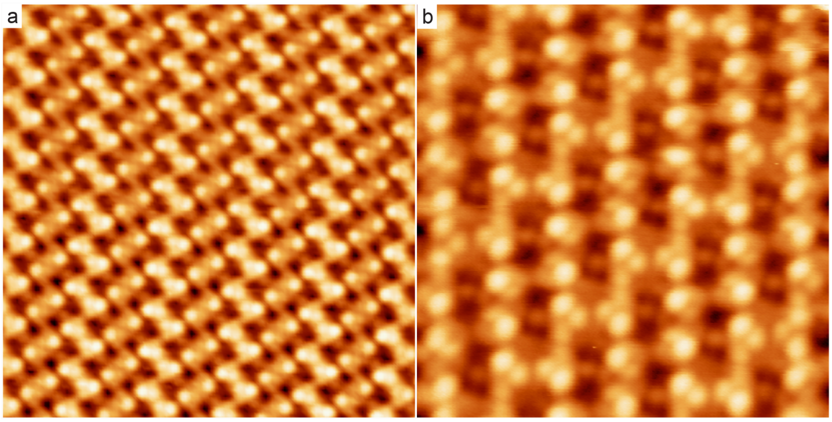

Figure A. 11: STM images (a: 16.8 nm × 16.8 nm, 31 pA, 1.93 V; b: 10 nm×10 nm, 28 pA, 2.09 V) of the zigzag structure on Cu(111). (a) *(M,M)*-bis[7]H are brighter than *(P,P)*-bis[7]H. (b) It is a mirror domain of (a), rotated by 60° in the clockwise direction. *(P,P)*-bis[7]H are the brightest in this domain.

A.3. Bromoheptahelicene

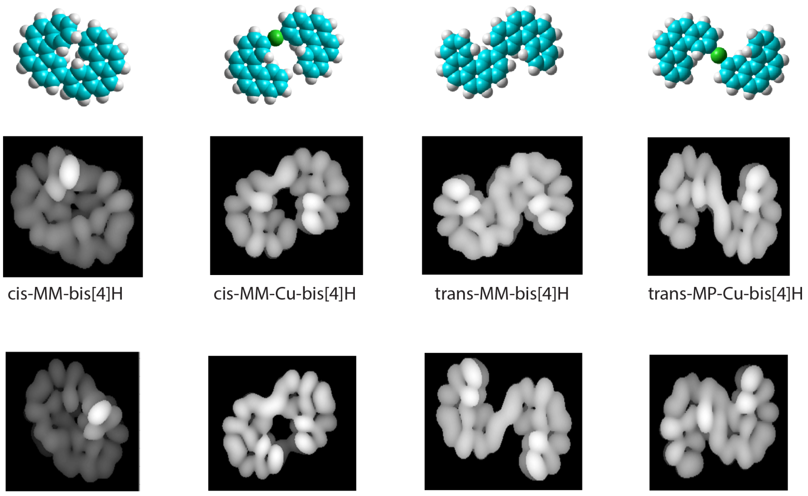

cis-MM-bis[4]H · cis-MM-Cu-bis[4]H · trans-MM-bis[4]H · trans-MP-Cu-bis[4]H

cis-MP-bis[4]H · cis-MP-Cu-bis[4]H · trans-MM-Cu-bis[4]H · trans-MP-bis[4]H

Figure A. 12: Electron density maps of the frontier orbitals of different organometallic (levels 90-92, Ext. Hückel) and organic (levels 84-86, Ext. Hückel) bis[4]H that could possibly be obtained after Ullmann coupling of 2-Br[4]H on copper. EHT calculations were performed on molecules which were optimized on a fixed 4-layer Cu(100) slab using AMBER force field calculation. To compare with the STM images (positive bias: tunneling into unoccupied states of the sample), only the states close to the LUMO (LUMO to LUMO+3) were considered.

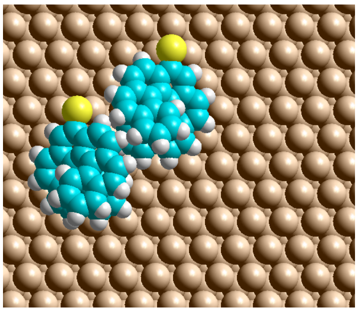

Figure A. 13: Minimum-energy configuration of a heterochiral Br[7]H dimer, obtained from MM calculations (AMBER force-field), computed from 287 initial configurations. The four-layer Au(111) slab was constrained and the two molecules were free to relax.

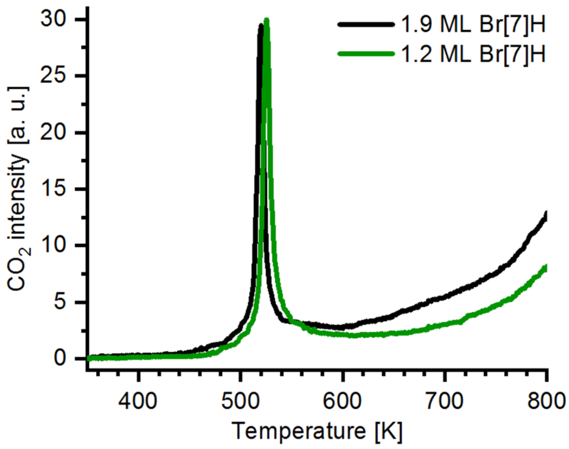

Figure A. 14: TDS graph showing the autocatalytic decomposition of different nominal coverages (above 1 ML) of Br[7]H on 1 ML of oxygen on Cu(100). The heating rate is 1 K/s.

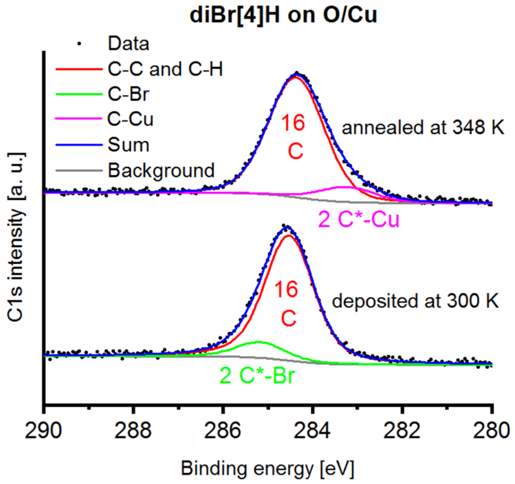

Figure A. 15: C1s XP spectra for 1 ML of diBr[4]H deposited on O/Cu at 300 K and after annealing at 348 K. Before annealing, the C1s spectrum exhibits a shoulder at 285.2 eV, indicative of C-Br. This shoulder is replaced by a shoulder at lower binding energy (283.3 eV) after annealing. Such low binding energy C1s species are characteristic for organometallic C-metal bonds.[222,224,225] The fits have been performed while keeping the relative intensities of the C-Br and C-Cu species fixed to 1/8, as expected for the stoichiometry of diBr[4]H.

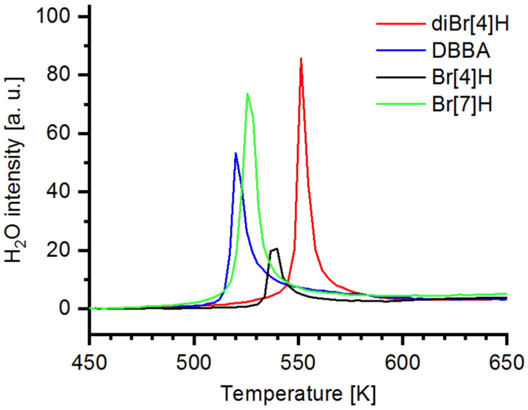

Figure A. 16: TDS graph showing the autocatalytic decomposition of Br[7]H, diBr[4]H, Br[4]H and diBrbianthracene. The H_2O (18 amu) signal was measured for a heating rate of 3 K/s. The signal for Br[4]H is truncated because the mass spectrometer was saturated (too high sensitivity).

A.4. Pentaindenocorannulene

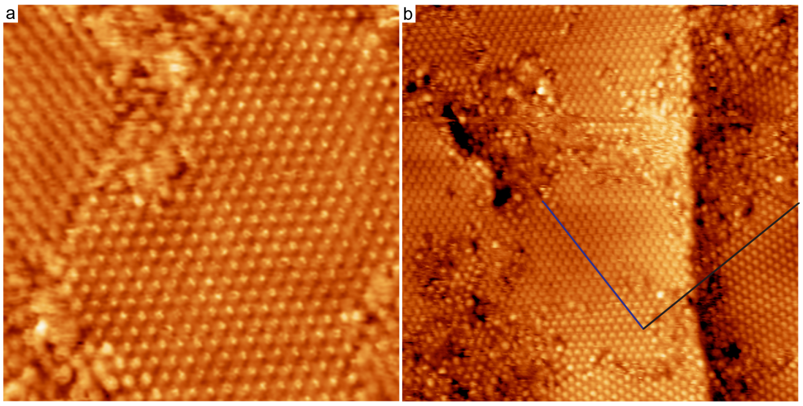

Figure A. 17: STM images of PiC on Cu(100) showing ordered structures at ML coverage. (a) In a domain, single molecules arrange in row. Each molecule has a round shape with a brighter protrusion on one side (24.5 nm × 24.5

nm, –2.62 V, 22 pA, annealing 15 min at 473 K). (b) The molecules arrange in rotational domains which are perpendicular to each other (30 nm×30 nm, 2.05 V, 31 pA, annealing 15 min at 473 K).

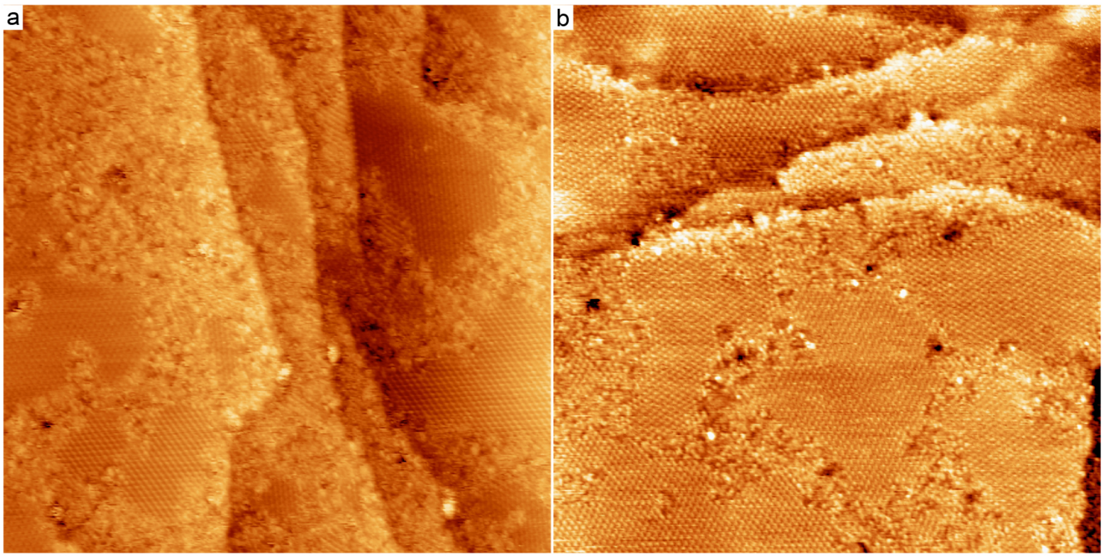

Figure A. 18: STM images (a: 89.8 nm × 89.8 nm, –2.62 V, 22 pA, annealing 15mn at 473 K; b: 86.4 nm × 86.4 nm, 25 pA, 3.08 V, no annealing). In both images, the ordered domains are made of rows of molecules. Two different orientations of the rows are observed both at θ = 0.7 ML (a) and θ = 1.0 ML (b).

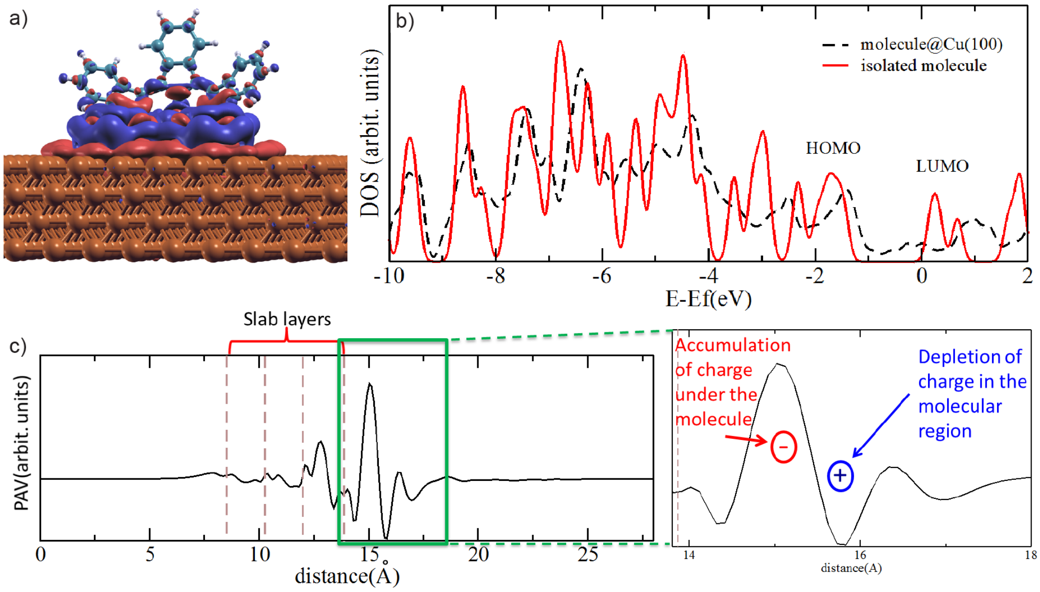

Figure A. 19: (a) Side view of the charge redistribution after adsorption of PiC on Cu(100). Red shows the accumulation of charge and blue the depletion. (b) Density of states of an isolated PiC and for the molecule on the Cu(100) substrate. All electronic states of the adsorbate match the components of the isolated molecule. (c) Planar linear electron density perpendicular to the surface. The depletion of charge in the molecules and the accumulation of electrons at the surface is more clearly observed in the inset.

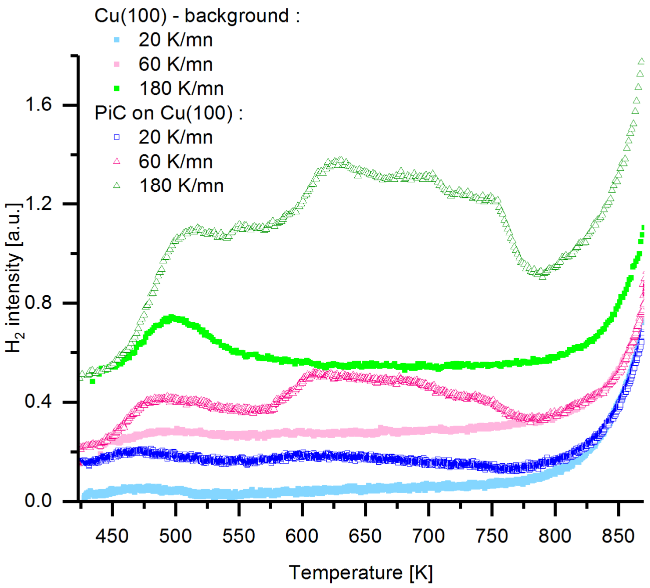

Figure A. 20: TD spectrum of PiC on Cu(100) (empty symbols) for different heating rate (0.33, 1, and 3 K/s). Spectra of the clean Cu(100) are also displayed (filled symbols) as a comparison. The spectra were offset for clarity.

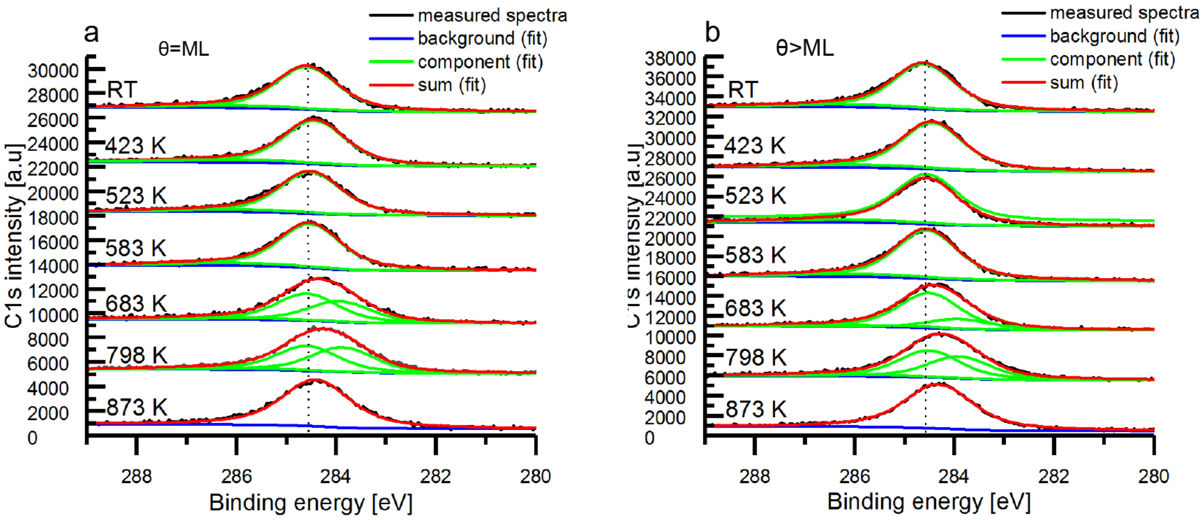

Figure A. 21: XP spectra of 1 ML (a) and 1.21 ML (b) of PiC on Cu(100) after annealing for 15 min at different temperatures. In both cases, the C1s peak observed at 284.6 eV after molecular adsorption shifts to lower energy value due to the C-H bond breaking and the stronger binding of the molecules with the surface or with copper adatoms (formation of organometallic species) [224,225]. At 873 K, the peak switches back to higher energy due to the formation of graphene[251]. The spectra were offset for clarity.

A.5. Monoindenocorannulene

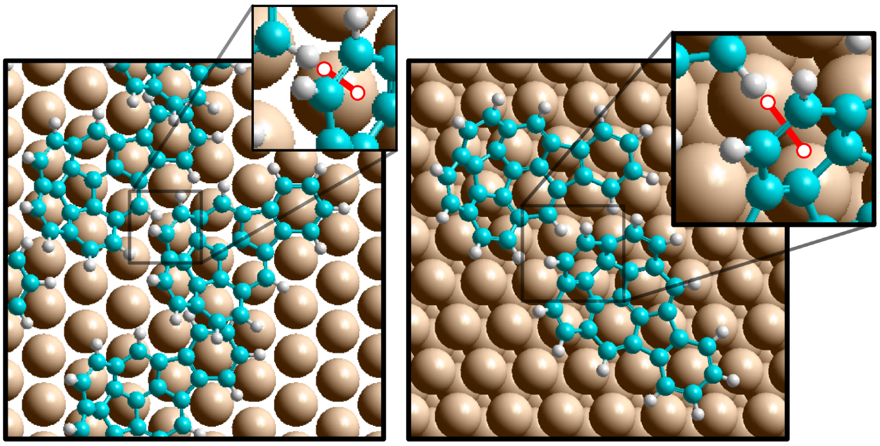

Figure A. 22: Left: Details of the modelled structure of MiC on Cu(111) presented in Figure 87. Right: lowest-energy dimers computed with AMBER-force field geometry optimization from 288 initial configurations. CH-π bonds are indicated with red lines.[69]

A.6. $C_{38}H_{14}$

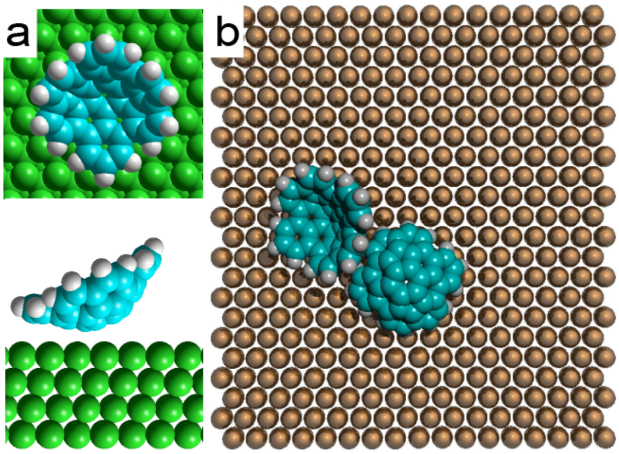

Figure A. 23: MM models of $C_{38}H_{14}$ on Cu(111). (a) Optimized configuration of a single molecule obtained after optimization of 108 initial configurations. Without constraints, the bowl adopts an opening-up configuration which diverges with the STM results. (b) Optimized configuration of a dimer sticking in a local energy minimum and interacting via the naphthalene group of the tilted molecule. This motif is 1.45 kcal/mol higher in energy than the configuration shown in Figure 88c, d.

Curriculum Vitae

Anaïs MAIRENA

Date of birth: 9th November 1991
Nationality: French
E-mail: anais.mairena@gmail.com

Scientific Experience

Doctoral researcher

Empa - Swiss Federal Laboratories for Materials Science and Technology, Dübendorf, Switzerland | 10. 2014 - present

Researcher at the Nanoscale Materials Science Laboratory

Chairwoman of the organizing committee of the PhD students' symposium

Empa, Dübendorf, Switzerland | 2016

Organizer of a scientific conference (~110 participants)

R&D intern

Centre Suisse d'Électronique et de Microtechnique, Basel, Switzerland | 2013 – 2014

Researcher at the Integrated Light Management Group of the Thin Film Optics Division

Project: "Transparent organic light emitting diodes"

Education

PhD, Doctor of Sciences in Chemical and Molecular Sciences

University of Zürich, Zürich, Switzerland | 2014 – 2018

PhD thesis: "Chemistry of non-planar polycyclic aromatic hydrocarbons on metal surfaces" in the Molecular Surface Science group headed by Prof. Dr. Karl-Heinz Ernst

Master of Science in Applied Physics (average grade: 5.43/6, 124/120 ECTS)

École Polytechnique Fédérale de Lausanne (EPFL), Lausanne, Switzerland | 2012 - 2014

Master thesis: "Electrochemically promoted catalysis of dispersed Pt and Pd clusters on solid ion-conductors" in the Laboratory of Nanostructures at Surfaces headed by Prof. Dr. Harald Brune

Bachelor of Science in Physics

EPFL, Lausanne, Switzerland | 2009 - 2012

French baccalaureate in sciences (passed with highest honors)

Lycée la Versoie, Thonon-les-bains, France | 2006 - 2009

List of publications, awards and conference contributions

Publications

As of March 2018, the following publications have arised from this work:

- Laura Zoppi, Quirin Stöckl, Anaïs Mairena, Oliver Allemann, Jay S Siegel, Kim K Baldridge, Karl-Heinz Ernst
  Pauli Repulsion Versus van der Waals: Interaction of Indenocorannulene with a Cu(111) Surface. *J. Phys. Chem. B* **122,** 871–877 (2018)

- Anaïs Mairena, Laura Zoppi, Johannes Seibel, Alix F Tröster, Konstantin Grenader, Manfred Parschau, Andreas Terfort, Karl-Heinz Ernst
  Heterochiral to Homochiral Transition in Pentahelicene 2D Crystallization Induced by Second-Layer Nucleation. *ACS Nano* **11,** 865–871 (2017)

- Quirin S Stöckl, Tsun-Cheng Wu, Anaïs Mairena, Yao-Ting Wu, Karl-Heinz Ernst
  Erecting buckybowls onto their edge: 2D self-assembly of terphenylcorannulene on the Cu(111) surface. *Faraday Discuss.* **204,** 429–437 (2017)

- Quirin S Stöckl, Ya-Chu Hsieh, Anaïs Mairena, Yao-Ting Wu, Karl-Heinz Ernst
  Aggregation of C70-Fragment Buckybowls on Surfaces: π–H and π–π Bonding in Bowl Up-Side-Down Ensembles. *J. Am. Chem. Soc.* **138,** 6111–6114 (2016)

- Christian Wäckerlin, Jingyi Li, Anaïs Mairena, Kévin Martin, Narcis Avarvari, Karl-Heinz Ernst
  Surface-assisted diastereoselective Ullmann coupling of bishelicenes. *Chem. Commun.* **52,** 12694–12697 (2016)

- Anaïs Mairena, Martin Wienke, Kévin Martin, Narcis Avarvari, Andreas Terfort, Karl-Heinz Ernst, Christian Wäckerlin
  Stereospecific autocatalytic surface explosion chemistry of polycyclic aromatic hydrocarbons. *J. Am. Chem. Soc.* (2018), accepted for publication

The following four publications are in preparation:

- Anaïs Mairena, Samuel Lampart, Laura Zoppi, Kim Baldridge, Jay S. Siegel, Karl-Heinz Ernst
  Modification of a copper surface with pentaindenocorannulene

- Anaïs Mairena, Samuel Lampart, Jay S. Siegel, Christian Wäckerlin, Karl-Heinz Ernst
  Thermally induced chemistry of pentaindenocorannulene on a copper surface

- Anaïs Mairena, Manfred Parschau, Laura Zoppi, Martin Wienke, Andreas Terfort, Karl-Heinz Ernst
  Diastereoslective self-assembly of bisheptahelicene on Cu(111)

- Anaïs Mairena, Christian Wäckerlin, Manfred Parschau, Laura Zoppi, Martin Wienke, Andreas Terfort, Karl-Heinz Ernst
  Diastereoslective self-assembly and on-surface synthesis of 9,9′-bisheptahelicene on Au(111)

Awards

The following prizes were received based on this work :

- 2016 Travel Award of the Chemical and Molecular Sciences Zürich (CMSZH)
- 2017 Chemistry Travel Award of the Swiss Academy of Sciences (SCNAT) and Swiss Chemical Society (SCS)
- 2017 Travel Awards of the Chemical and Molecular Sciences Zürich (CMSZH)
- 2018 Swiss Working Group for Surface and Interface Science (SAOG) Charmey Poster Prize: 1st place

Conference contributions

In addition to internal seminars, this work on the chemistry of non-planar cyclic aromatic hydrocarbons was presented and discussed in external conferences in Switzerland but also in international congresses. A list of these presentations is given below, mentioning the type of contribution between brackets.

- 255th American Chemical Society (ACS) National Meeting, New-Orleans, USA, 03.2018 (Two oral contributions)
- SAOG 2018, Fribourg, Switzerland, 02.2018 (Poster)
- Empa PhD Symposium 2017, Dübendorf, Switzerland, 11.2017 (Poster)
- 16th International conference on chiroptical spectroscopy- CD 2017, Rennes, France, 06.2017 (Poster)
- DPG Spring Meeting of the Condensed Matter Section 2017, Dresden, Germany, 03.2017 (Oral contribution)
- Gordon Research Conference: Chemical reactions at Surfaces, Lucca, Italy, 02.2017 (Poster)
- Gordon Research Seminar: Chemical reactions at Surfaces, Lucca, Italy, 02.2017 (Oral contribution)
- 33rd Annual Meeting of the Swiss Working Group for Surface and Interface Science (SAOG), Fribourg, Switzerland, 01.2015 (Poster)
- AVS, 63rd International Symposium and Exhibition, Nashville, USA, 11.2016 (Oral contribution)
- Doktorandentag of the CMSZH Graduate School, Schloss Au, Switzerland, 06.2016 (Poster)
- Empa PhD Symposium 2015, Dübendorf, Switzerland, 12.2015 (Poster)
- Chirality at the Nanoscale 2015, Leuven, Belgium, 11.2015 (Poster)
- 79th Annual Meeting of the DPG and DPG Spring Meeting, Berlin, Germany, 03.2015 (Oral contribution)
- 2015 Annual meeting of the Swiss “molecules at surfaces” research community (MolCHSurf), Bern, Switzerland, 06.2015 (Oral contribution)
- 31st Annual Meeting of the SAOG, Fribourg, Switzerland, 01.2015 (Poster)